Fossil Energy Program Annual Progress Report

Oak Ridge National Laboratory
MANAGED BY UT-BATTELLE FOR THE DEPARTMENT OF ENERGY

ORNL 2002-031194/vlc

ORNL/TM-2003/119

Fossil Energy Program Annual Progress Report for April 2002 Through March 2003

Roddie R. Judkins
Program Manager

Paul T. Carlson
Technical Assistant

June 2003

Prepared for the
DOE Office of Fossil Energy
(AA, AB, AC, AW, AZ, SA)

Prepared by the
OAK RIDGE NATIONAL LABORATORY
Oak Ridge, Tennessee 37831-6285
managed by
UT-BATTELLE, LLC
for the
U.S. DEPARTMENT OF ENERGY
under Contract DE-AC05-00OR22725

CONTENTS

CONTENTS

CONTENTS

We would like to thank the ORNL Creative Media Solutions group for its assistance in this project. Vickie Conner, in Graphics Services, designed the cover; Sandra Lyttle, in Publishing Services, formatted the papers and created the PDF file.

FOSSIL ENERGY PROGRAM ANNUAL PROGRESS REPORT FOR APRIL 2002 THROUGH MARCH 2003[1]

Roddie R. Judkins, Program Manager
Paul T. Carlson, Technical Assistant
Oak Ridge National Laboratory

INTRODUCTION

The mission of the Fossil Energy Program is to conduct research and development that contribute to the advancement of fossil energy technologies. The Oak Ridge National Laboratory Fossil Energy Program research and development activities, performed for the Department of Energy Assistant Secretary for Fossil Energy, cover the areas of coal, clean coal technology, gas, petroleum, and support to the Strategic Petroleum Reserve.

Projects on the ORNL Fossil Energy Program are supported by the U.S. Department of Energy Office of Fossil Energy, the DOE National Energy Technology Laboratory, the DOE Fossil Energy Clean Coal Technology Program, the DOE National Petroleum Technology Office, and the DOE Fossil Energy Office of Strategic Petroleum Reserve.

The ORNL Fossil Energy Program shares with DOE Oak Ridge Operations technical management responsibility for all activities on the DOE Fossil Energy Advanced Research Materials Program. The Advanced Research Materials Program includes research at other DOE and government laboratories, at universities, and at industrial organizations.

[1]Research sponsored by the U.S. Department of Energy, Office of Fossil Energy, under contract DE-AC05-000R22725 with UT-Batttelle, LLC.

CORROSION RESISTANT COATINGS FOR CERAMICS

B. L. Armstrong, M. P. Brady, K. M. Cooley, J. A. Haynes, H-T. Lin, and S.B. Waters
Oak Ridge National Laboratory

INTRODUCTION

Advanced fossil energy processes have hostile environments that can contain sulfur, nitrogen, trace heavy metals, alkali salts, steam and/or temperatures up to 1400°C. Silicon based ceramics such as silicon carbide (SiC) or SiC/SiC composites are attractive for use in these environments for applications such as hot-gas filters, heat exchangers, and other devices for advanced energy producing systems. Silicon based ceramics are candidates due to their higher temperature capability relative to metals, high thermal conductivity, retention of mechanical properties at operating temperatures, and excellent thermal shock resistance. A slow growing, silica scale is the typical protection mechanism for the SiC material. This scale limits oxygen diffusion and thus prevents further attack of the substrate. A major drawback of SiC ceramics is the susceptibility of the silica scale to volatilization and corrosion by alkali salts such as Na_2SiO_4 and steam at high temperatures, which limits the applicability for extended service in many fossil energy conversion and combustion system environments. Thus, the use of protective coatings or the development of material with improved stability in these harsh environments becomes necessary. To address this issue, the development of novel coatings for SiC ceramics utilizing low-cost slurry based processing methods such as dip coating is being pursued. Several materials including mullite, doped alumino-silicates, and zircon were deposited on to SiC substrates and were evaluated for feasibility, specifically the thickness and thickness variation, density, microstructure and stability of the coating. Additionally, a processing approach is being developed for materials that form other types of protective scales such as the direct conversion of metal coatings to form alumina scales. Interim results for all of these approaches will be discussed.

The purpose of this program is to develop an understanding of the advantages and disadvantages of using these materials in fossil environments and from that understanding develop ceramic coatings with enhanced corrosion resistance through improvements in the composition and processing of the coating. Processing innovations will focus on aqueous coating development including such techniques as dip coating. In addition, materials that form scales other than silica will be evaluated. Candidate materials will be exposed in facilities at ORNL and will be characterized to identify the most promising materials for specific applications.

SLURRY COATING DEVELOPMENT

This program has been investigating several approaches to improving the environmental stability of SiC. The challenge of developing any coating system for application in a fossil environment is that the resulting coating must be adherent to the substrate, must be stable and protective in high temperature water vapor, have a close thermal expansion match with the substrate (SiC), be compatible with the substrate such that mechanical properties or thermal resistance is not reduced, is easily densified without interaction or degradation of the substrate, and utilize a cost effective processing method for application. The further challenge of developing any coating system is being able to separate the efficacy of the coating material with the efficacy of the process.

This program has been divided into parallel efforts to first identify and test the effectiveness of alternative coating materials and second to develop three-dimensional coating technologies to apply these materials without the degradation of the substrate. Work continues on the testing and evaluation of the alternative coating material system without the contribution of the substrate. Work this year has focused on the synthesis and evaluation of calcium aluminate ($CaAl_4O_7$). The material was synthesized in-house, pellets were fabricated for thermal cycling tests, weight loss, phase and microstructure evaluation. Testing is on-going. Coatings of the materials have also been screen printed on to hexaloy SASiC substrates, and evaluation of the resulting coatings is in process.

The second effort that is being taken to develop 3D coatings utilizes low cost, slurry based coating techniques to coat the surface of a hexaloy SiC substrate. There are numerous slurry-based approaches including dip coating, screen-printing, spin coating, spray coating, and vacuum coating. Two coating methods were selected for evaluation; a near term, materials evaluation approach, screen-printing, and a long term, system evaluation approach, dip coating. Screen-printing was selected such that the candidate material systems could be quickly “screened” for efficacy while minimizing processing set-up times and parameters. Once the material issues are evaluated, development of a dip coating system will be initiated to demonstrate processing feasibility. Most of the development work has focused on the candidate material system, mullite, however, other materials are also being evaluated such as barium strontium doped alumino-silicate, zirconium doped alumino-silicate, and zircon. Mullite was selected based on thermal expansion match to SiC and relative corrosion resistance to fossil environments as demonstrated by J. Hurley at University of North Dakota-Energy & Environmental Research Center (UND-EERC) (1).

Examples of coatings of zircon (Aldrich) and mullite (Washington Mills) are shown in Fig. 1A and 1B, respectively. The zircon coating was prepared using the screen-printing process, and the mullite coatings were deposited using a dip coating process. The screen-printed coating of zircon was densified on to the surface of a SiC substrate using a non-traditional sintering technique called High Density Infrared Sintering Process or HDI. The resulting coating had an average thickness of approximately

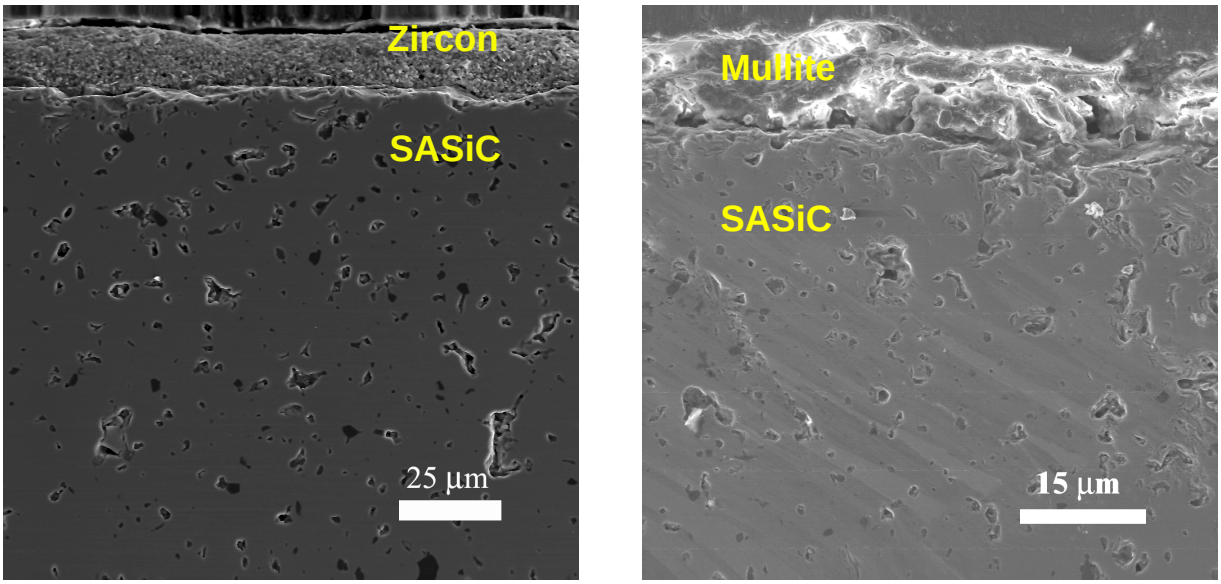

1A **1B**

Fig. 1. (A) Zircon coating deposited on to SASiC substrate by screen printing. Sintered using the High Density Infrared Sintering Process (HDI). (B) Mullite coating deposited on to SASiC substrate by dip coating. Sintered at 1600°C in nitrogen for 2 hours.

20 microns. The dip coated mullite coating, shown in Fig. 1B, was densified at 1600°C in a nitrogen environment using traditional sintering processes. The coating thickness varied across the substrate due to flow of the slurry in the dip direction. The average thickness was approximately 15–20 microns. The importance of the effect of processing on the resulting microstructure and ultimately the effectiveness of the coating is illustrated in these figures. If the process is not optimized, the resulting coating microstructure will be affected through thickness variation and density, and ultimately performance of the coating. The development of an improved dip process continues.

SURFACE ALLOY DEVELOPMENT FEASIBILITY STUDY

One challenge in the densification of a slurry coating is the prevention of fast growing -silica formation at the coating—substrate interface. Oxygen will diffuse to the substrate during the sintering process until densification is complete. Even if steps are taken to limit the oxygen diffusion during this densification process, the formation of a silica layer at the coating—substrate interface can still occur if the coating does not completely prevent oxygen transport. Thus, the development of a sacrificial coating that oxidizes and/or diffuses via a heat treatment or in-situ to form a volatility barrier have been proposed to address this concern. Thus, the concept of looking at the use of a thin metallic precursor layer as a route to form a self-graded oxide surface layers that can act as volatility barriers to protect against aggressive species that would degrade a silica layer was proposed. In this approach, the metal layer would completely convert to ceramic by an oxidation pretreatment.

It was proposed to evaluate the well-characterized alumina-forming intermetallic systems, yttrium doped chrome aluminide (Cr_2AlY), titanium/yttrium doped chrome aluminide (TiCrAlY), hafnium doped nickel aluminide (NiAlHf), chromium/yttrium doped nickel aluminide (NiCrAlY), and chrominum/ yttrium doped iron aluminide (FeCrAlY). These compositions were selected with a range of coefficient of thermal expansion (CTE), high temperature strength properties in the metal layer, and base metal component chemistries in order to explore what the key issues are regarding the conversion of the metal layer to ceramic and the formation of a dense, adherent oxide after oxidation pretreatment. It is anticipated that the oxide layer formed will be a duplex layer with an outer layer of alumina and an inner layer consisting of a graded oxide layer of the base metal of the aluminide, Si and Al, as depicted in Fig. 2

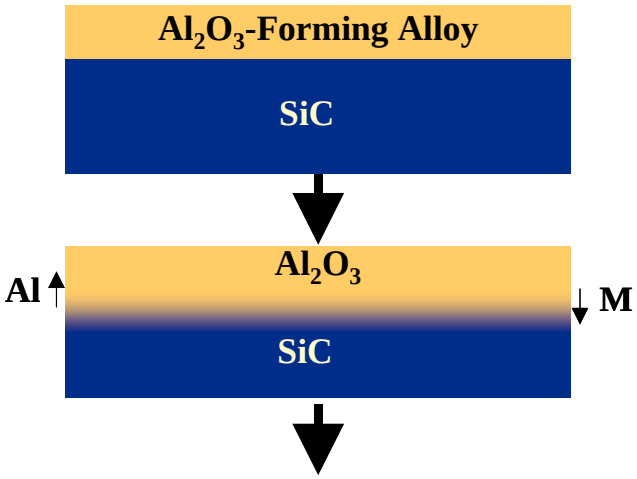

Fig. 2. Schematic of a Sacrificial Self-Grading Alumina-Forming Precursor.

The initial feasibility experiments used TiCrAlY coatings due to its low CTE versus other alumina-forming materials. It was surmised that if this material would survive thermal cycling in laboratory air without spalling off the substrate, then further investigation of this approach was warranted. Feng Huang and Mark L. Weaver of the University of Alabama, Tuscaloosa sputtered a 2–3 micron coating of nominal composition Ti-51Al-12Cr (atom percent) on to a SASiC substrate. The substrate was then exposed to ten, 100 hour cycles to 1100°C in laboratory air. Excellent adherence was seen as no spallation occurred. As shown in Fig. 3, the alumina layer that formed at the surface was not continuous which indicated that the coating composition was not optimized. In spite of that, the excellent adherence that was demonstrated suggested that the concept of sacrificial metallic layers was worth more investigation.

Thus, the University of Alabama sputtered NiAlHf, Cr_2AlY, NiCrAlY, and FeCrAlY on to Hexaloy SASiC substrates. The resulting substrates were exposed to 1150°C in flowing oxygen for 0.5 hour to convert the coating to alpha alumina prior to stability testing. All of the coatings were adherent in spite of the thermal expansion coefficient mismatch from the starting materials. However, the full conversion to alpha alumina was not seen. Raman spectroscopy showed evidence of transient aluminas in all of the preheat-treated samples. The contribution of the coating and its interaction with the substrate was noted in the different alumina morphologies produced after pretreatment. Both the NiAl(Hf) and NiCrAlY coatings showed needle like morphology with some overall porosity. The Cr_2AlY and FeCrAlY had a

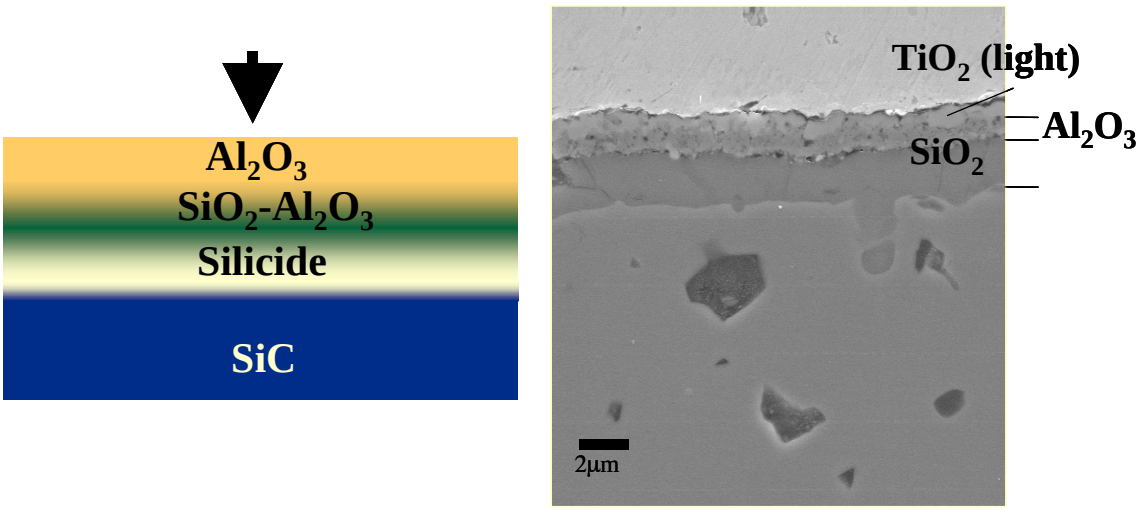

Fig. 3.Exposure of 3 mm sputtered Ti-51Al-12Cr on SiC showed excellent adherence after ten, 100 hour cycles to 1100°C in laboratory air. No spallation occurred.

more spherical morphology as expected with alpha alumina, but the overall density of the coating was still poor. The substrates were subsequently exposed to 72 hours at 1000°C in 100% humidity, and analysis is currently being completed.

CHARACTERIZATION OF SAMPLES: TESTING AT NETL-CERF

Since virtually no data exists on the response of advance alloys and ceramics in realistic coal combustion environments under well-controlled conditions, the dedication of a combustor at the National Energy Technology Laboratory (NETL) was established to provide the long exposure times for a large number of specimens. Over 139 samples were submitted for testing including six ceramic and 11 metal alloy compositions. Combined Prader Creek Coal was used for this study. The combustor had six temperature profiles: 1500–1600°F, 1700–1800°F, 1900–2000°F, 2000–2100°F, 2100–2200°F, and 2300–2400°F. The samples were exposed for either 350, 650, or 1000 hours at a designated temperature profile. Examination of the ceramic samples submitted for this test will be reported as a part of the program, and analysis is on-going. As stated previously, six ceramic compositions were submitted for testing; mullite foams made by two separate techniques (Oak Ridge National Laboratory's gelcasting and the University of Dayton Research Institute's sol-gel process), Honeywell SiC/SiC composites, chemical vapor deposition (CVD) mullite coated SiC, Honeywell plasma spray coatings on SiC, COI's alumina/alumina silicate laminates, and COI's alumina-silicate/alumino-silicate laminates. The ceramic compositions are currently being cut and polished for scanning electron microscopy (SEM) and electron microprobe analysis. Only some of the results will be shown in this report.

J. A. Haynes and S. Zemskova at ORNL fabricated the CVD mullite coatings on SASiC. Two sample sets were tested. The first set was exposed for 650 and 1000 hours at 1900–2000°F and the second set for 350 and 1000 hours at the same temperature profile. The average coating thickness (before and after exposure) was 3–5 microns. The coatings were visually intact upon removal. The coatings showed no apparent surface microcracking and were adherent. Porosity was evident in the exposed mullite coating cross-sections shown in Fig. 4, but this is a typical microstructural characteristic in these CVD mullite coatings. Some silica was evident at the interface between the mullite coating and the SASiC substrate. The Al/Si ratio decreases from the exposed surface of the mullite to the interface of the mullite and the SiC after moderate exposure, and the silica layer thickness increases with exposure time at a constant temperature zone.

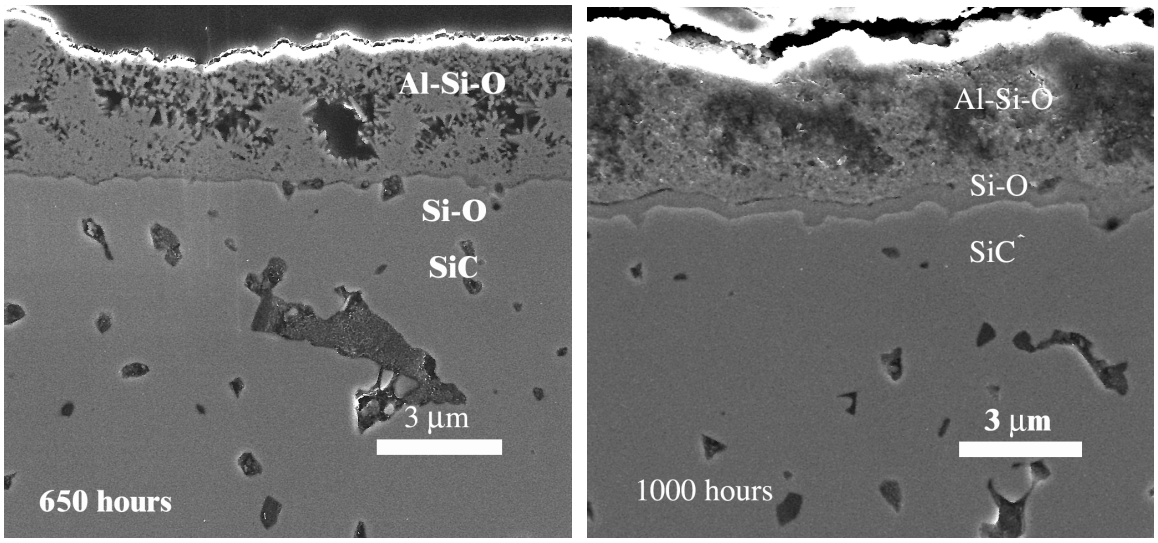

Fig. 4. Exposure of CVD mullite on SiC after exposure at 650 and 1000 hours at 1900–2000°F in the CERF combustor at NETL.

Honeywell fabricated plasma spray coatings on SASiC. The samples were exposed for 350 and 1000 hours at 2100–2200°F. The average coating thickness after exposure was 30–60 microns depending upon the sample. The coatings were visually intact upon removal with no apparent surface microcracking and the coatings were adherent. The exposed cross-sections shown in Fig. 5 show a dense coating, but delamination of the coating is evident in the samples probably due to thermal expansion mismatch between the coating and the SASiC substrate. Silica is also evident at the interface between the coating and the SiC. The silica layer thickness is similar regardless of exposure time at a constant temperature zone.

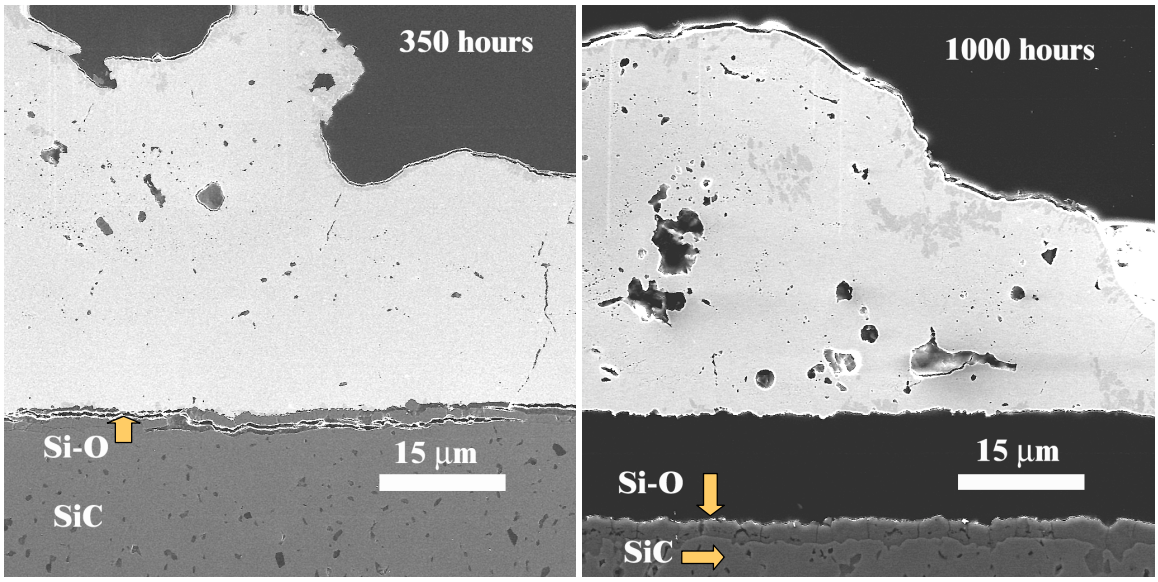

Fig. 5.Exposure of Honeywell's plasma sprayed coating on SiC after exposure at 350 and 1000 hours at 2100–2200°F in the CERF combustor at NETL.

SUMMARY

Two approaches were taken to address the development of novel, protective coatings for SiC ceramics for use in harsh fossil environments. The first approach utilized a low cost aqueous based slurry method. Work continues on the improvement of dip coated mullite coatings on SASiC substrates. Cyclic testing at elevated temperatures is on-going to demonstrate the feasibility of this process. The second approach that was proposed was a sacrificial coating that oxidizes via a heat treatment to form a volatility barrier. The feasibility of the concept was demonstrated using a thin metallic precursor layer. Four alumina-forming alloys were chosen and were tested first at 1150°C for 30 minutes in flowing oxygen and subsequently at 1000°C for 72 hours in 100% water environment. Evaluation is on-going. Evaluation of the ceramic samples submitted for testing in the NETL combustor is also on-going. Initial data was reported on the ORNL CVD mullite and Honeywell plasma sprayed coatings on SASiC substrates.

REFERENCE

1. "Support Services for Ceramic Fiber-Ceramic Matrix Composites: Final Annual Technical Progress Report," J. P. Hurley and C. R. Crocker, September 28, 2001.

CHEMICALLY VAPOR DEPOSITED YTTRIA-STABILIZED ZIRCONIA (YSZ) FOR THERMAL AND ENVIRONMENTAL BARRIER COATING

V. G. Varanasi, T. M. Besmann, and J. L. Lothian
Oak Ridge National Laboratory
W. Xu and T. L. Starr
University of Louisville

INTRODUCTION

Yttria-stabilized zirconia (YSZ) is used as a thermal barrier coating (TBC) to protect super-alloy blades such as Mar-M247 or Rene-N5 during engine operation. The current method for YSZ fabrication for TBC applications is by air-plasma spraying (APS) or electron beam-physical vapor deposition (EB-PVD) (Haynes 1997). APS gives reasonable deposition rates, but has a limited life and aging effects due to its porous and lamellar structure. The EB-PVD coatings are more stable and can accommodate thermomechanical stresses due to their characteristic strain-tolerant, columnar microstructure. EB-PVD, however, is primarily line-of-sight, which often leaves "hidden areas" uncoated, has low throughput, and has high capital cost. The process of metal-organic chemical vapor deposition (MOCVD) is investigated here as an economical alternative to EB-PVD and APS, with the potential for better overall coverage as well as the ability to produce thick (100–250 μm), strain-tolerant, columnar coatings.

MOCVD of YSZ involves the use of zirconium and yttrium organometallic precursors reacting with an oxygen source. Previous researchers have used β-diketonate or chloride precursors and oxygen (Wahl et al. 2001a, Wahl et al. 2001b, Yamane and Harai 1989). These precursors have low transport rates due to their low carrier solvent solubility (Varanasi et al. 2003). Solvated zirconium and yttrium butoxide precursors were investigated here due to their higher vapor pressures and high solvent solubility. This work uses predictive equilibrium modeling and experiments involving butoxide precursors for tetragonal YSZ fabrication.

EQUILIBRIUM ANALYSIS

In this work an equilibrium analysis was used to determine the minimum oxygen requirement needed to efficiently deposit YSZ. Since a large portion of the precursors is carbon, it will also be necessary to ensure that the deposit does not a carbon phase. The overall reaction is

$$Y(C_4H_9O)_3\text{:toluene}+Zr(C_4H_9O)_4\text{:n-butanol} \rightarrow YO_{1.5}\text{-}ZrO_2+\text{waste organics} \quad (1)$$

We focused on preparing 4 mole percent Y_2O_3, tetragonal YSZ. For ease of control it is desirable to obtain the same coating Y/(Y+Zr) ratio as that of the inlet Y/(Y+Zr) ratio.

The thermochemical properties (Barin 1989, Kubaschewski et al. 1996, Sundman 1985) and solid solution model (Du et al. 1992) were collected and organized into a ThermoCalc database. Figure 1 shows the effect of the temperature and inlet O/(Y+Zr) ratio. If no oxygen was added to the system, a minimum inlet O/(Y+Zr) ratio of five was imposed on the system since oxygen is present in the precursors at this ratio. Two more restrictions imposed on this system are the mole fraction of hydrogen and carbon, which are introduced solely through the precursors. Thus, the carbon to metal ratio (C/(Y+Zr)) and the inlet hydrogen to metal ratio (H/(Y+Zr) were fixed at 30 and 60, respectively. In Fig. 2, it can be seen that as long as the temperature is 950°C and the inlet O/(Y+Zr) ratio is greater than 30, carbon will not form with tetragonal YSZ.

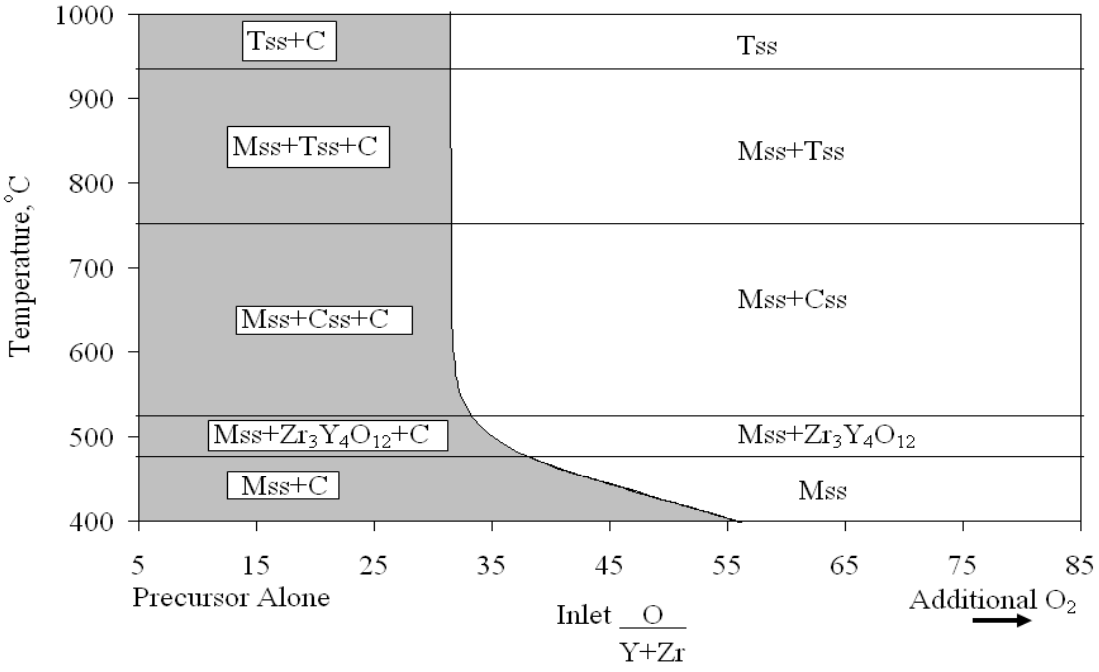

Fig. 1. Equilibrium analysis of using Y- and Zr-butoxide precursors.

EXPERIMENTAL

From the equilibrium analysis a minimum of 18 moles per minute of molecular oxygen is required for every mole per minute of Y-butoxide + Zr-butoxide (O/(Y+Zr)=35) to ensure formation of tetragonal YSZ at 950°C. To assure full oxidation, the oxygen flow rate was selected to be twice the minimum, O/(Y+Zr)=72.

The YSZ was deposited in the stagnation flow MOCVD reactor shown in Fig. 2. Substrates included alpha-alumina (99.6% purity: Coors) and Rene-N5 (Howmet). The precursors were Y- and Zr-tert butoxides dissolved in toluene and n-butanol, respectively. The precursors were pre-solvated and their

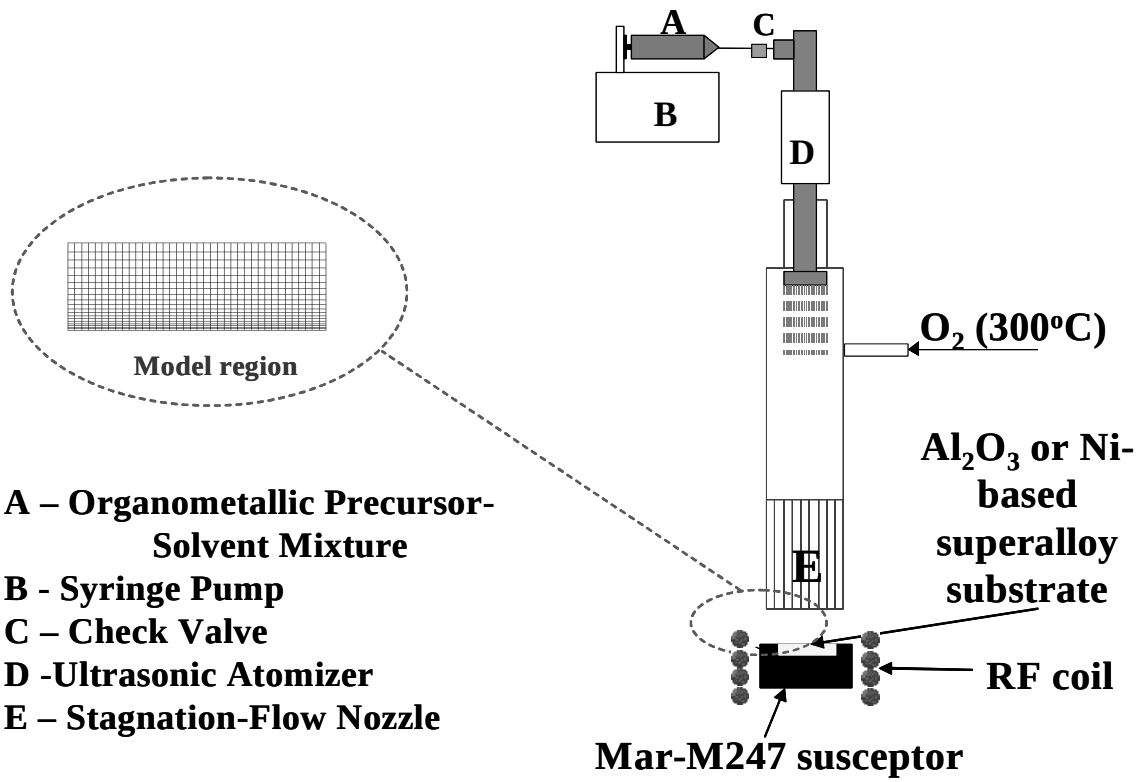

Fig. 2. MOCVD reactor developed at Oak Ridge National Laboratory.

solubility was 0.5 M Y in toluene and 2.23 M Zr in n-butanol. From the as-delivered batches, the reactants were mixed together based on their solubility and the desired coating composition. The solution was delivered continuously by a syringe pump through a poppet-seal relief valve into the deposition chamber. To ensure efficient vaporization, the solution was then misted using an ultrasonic atomizing nozzle. The misted solution was carried by 300°C O_2 at 1200 sccm to the substrate through a stainless-steel stagnation flow nozzle. The substrate was inductively heated using a Mar-M247 susceptor. The CVD chamber wall and susceptor holder were made of fused silica glass. A thermocouple was placed within the susceptor to control the susceptor temperature, while the substrate temperature was read using an optical pyrometer. Samples were then analyzed using X-ray diffraction (XRD) to identify the phases. Scanning electron microscopy (SEM) revealed coating thickness and microstructure. In addition, electron probe microanalysis (EPMA) was used to determine the relative homogeneity of yttrium and zirconium throughout the as-deposited coating.

RESULTS AND DISCUSSION

Figure 3 shows a YSZ deposit with a columnar microstructure on an alpha-alumina substrate. In this electron micrograph, initial lamellar layers of YSZ form, and then the columnar structure forms. To the

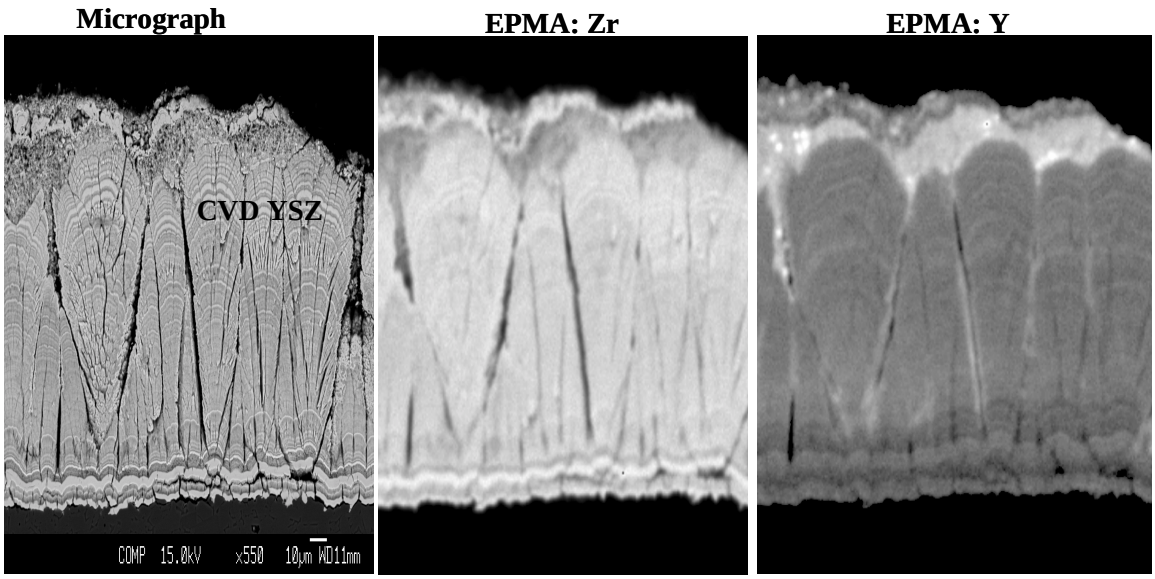

Fig. 3. Micrograph of YSZ with EPMA intensity maps for Zr and Y as-deposited on alpha-alumina substrate.

right of the electron micrograph are EPMA intensity maps. The lighter the region, the higher the concentration of the atom in that region. In this case, there is reasonable uniformity of Y and Zr atoms in the columnar coating. The banded layers show varying intensity of Y and Zr atoms relative to the columnar structure, indicating some non-uniformity. At the top of the coating, areas of high Zr or Y appears to be the result of powder formation. The powder formation may be indicative of separate zirconia and yttria phases being produced.

Figure 4 shows the YSZ coating on a Ni-based super-alloy substrate. Although the coatings are predominantly columnar, powder may be trapped within the columnar regions and within the gaps between columnar grains. This was attributed to pre-reaction of the precursors due to a failure to maintain cooling oil to the injector. There also appears to be a porous YSZ layer formed near the interface between the substrate and YSZ. This porous initial YSZ layer may have resulted from insufficient scale growth prior to deposition. Again banding is seen within the coating layers, which may be due to non-uniformity of yttrium and zirconium composition.

X-ray diffraction (XRD) results can be seen in Fig. 5. The peaks represent the CVD YSZ coating and positions of the standard peaks for 3.25 mole percent yttria YSZ are shown below the pattern. The standard and the coating peaks match reasonably well.

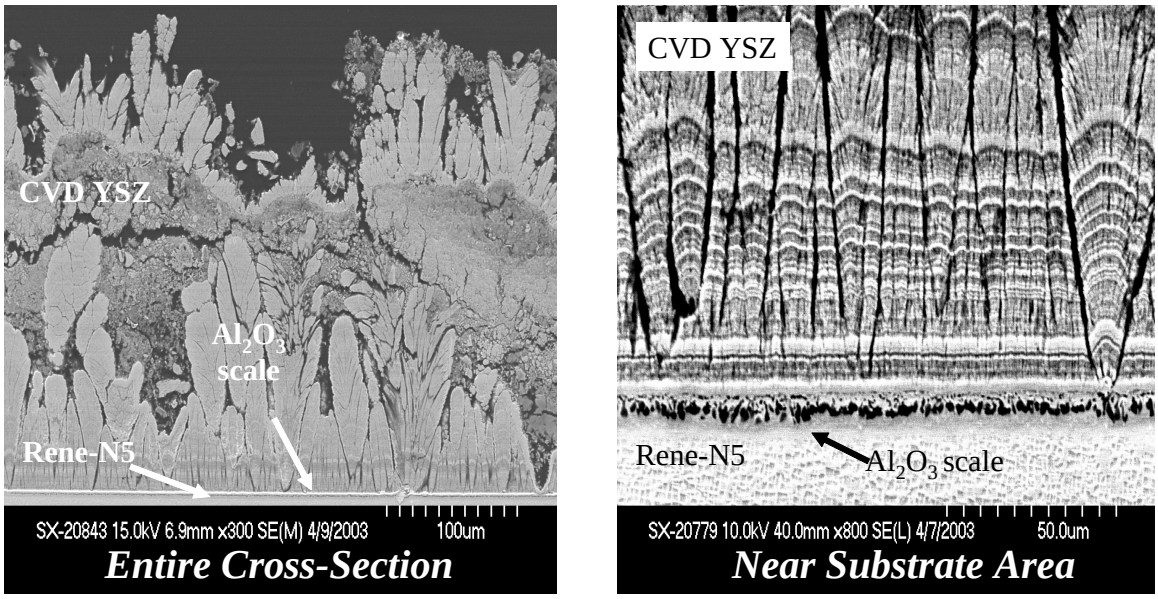

Fig. 4. SEM micrograph of YSZ as-deposited on Rene-N5, Ni-based superalloy substrate.

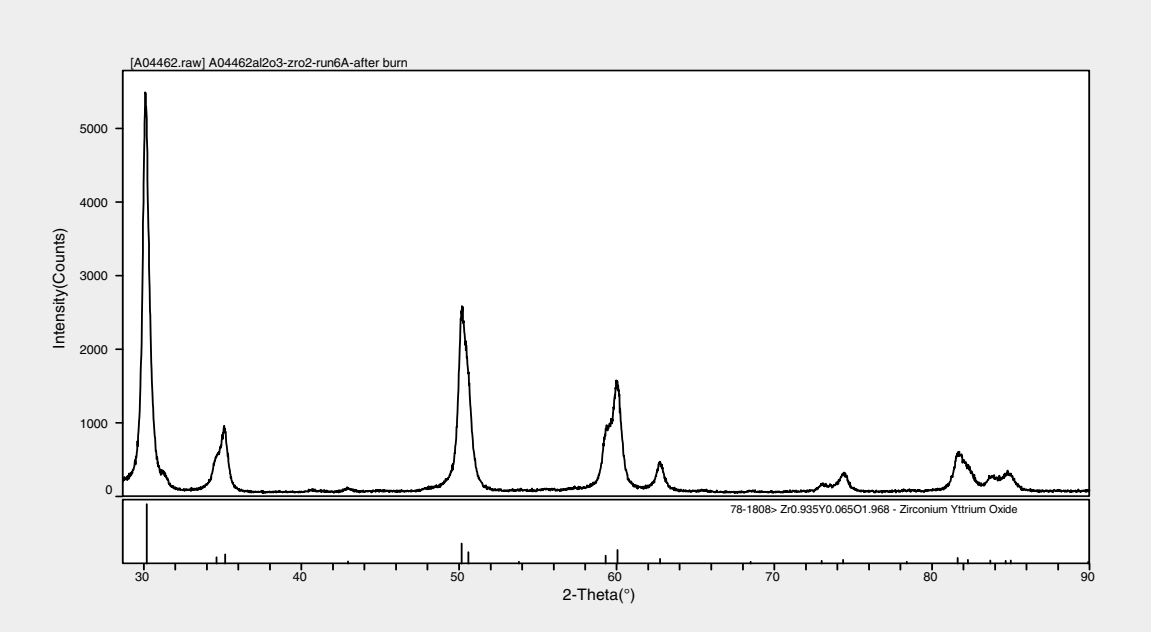

Fig. 5. XRD of tetragonal YSZ coating (at 3.25 wt% Y_2O_3) on Ni-based superalloy.

SUMMARY

Results of equilibrium modeling predicted carbon-free tetragonal YSZ formation and experiments demonstrated tetragonal YSZ formation with columnar grain structures and high deposition rates (~45 μm hr^{-1}). These coatings showed reasonable Y and Zr uniformity throughout the columnar region, although were not entirely uniform. Future work will include parametric studies to improve the coatings quality followed by scale-up to larger substrate and blade geometries.

REFERENCES

Barin, I., F. Sauert, et al. (1989). *Thermochemical Data of Pure Substances*. Germany, VCH Verlagsgesellschaft.

Du, Y., Z. Jin, et al. (1992). "Thermodynamic Calculation of the ZrO_2-$YO_{1.5}$-CaO Phase Diagram." *CALPHAD* 16(4): 355–362.

Haynes, J. A. (1997). Oxidation and Degradation of Thermal Barrier Coating Systems. *Material Science and Engineering*. Tuscaloosa, University of Alabama**:** 277.

Kubaschewski, O., C. B. Alcock, et al. (1996). *Materials Thermochemistry*. Oxford, Pergamon Press.

Sundman, B., B. Janson, et al. (1985). "The ThermoCalc Databank System." *CALPHAD: Computational Coupling Phase Diagram Thermochemistry* 9(121): 153–190.

Varanasi, V. G., T. M. Besmann, et al. (2003). "Parametric Study of the Chemical Vapor Deposition of Yttria-Stabilized Zirconia From Organometallic Precursors." *Proceedings of the Electrochemical Society: Chemical Vapor Deposition XVI and EuroCVD 14*. Vol. 2, p. 783.

Wahl, G., W. Nemetz, et al. (2001a). "Chemical Vapor Deposition of TBC: An Alternative Process for Gas Turbine Components." *Transactions of the ASME* **123**: 520–524.

Wahl, G., C. Metz, et al. (2001b). "Thermal Barrier Coatings." *Proceedings: Thirteenth European Conference on Chemical Vapor Deposition*: Pr3-835-846.

Yamane, H. and T. Hirai. (1989). "Yttria Stabilized Zirconia Transparent Films Prepared by Chemical Vapor Deposition." *Journal of Crystal Growth* 94: 880–884.

MULTI-PHASE Cr-BASED ALLOYS FOR AGGRESSIVE HIGH TEMPERATURE ENVIRONMENTS

M. P. Brady, C. T. Liu, P. F. Tortorelli, P. Sachenko, L. R. Walker, C. A. Carmichael, and J. L. Wright
Oak Ridge National Laboratory

INTRODUCTION

The objective of this work is to develop and characterize a new family of Cr-based alloys for structural use in aggressive 900–1300°C corrosion environments. The potential advantages of Cr are high melting point, moderate density, and good high-temperature corrosion resistance in many environments [1]. However, these are currently negated by inadequate high-temperature strength, ambient-temperature brittleness, and susceptibility to environmental embrittlement at elevated-temperatures by rapid nitride subscale formation [1]. Over the course of this effort, two distinct approaches to overcoming these problems have been pursued: Cr_2Ta-reinforced Cr and MgO-dispersed Cr. The Cr_2Ta-reinforced Cr alloys are based on the Cr-Cr_2Ta eutectic structure and contain a Cr solid solution matrix phase reinforced with lamellar Cr_2Ta Laves phase. They exhibit an attractive combination of high-temperature strength (tensile fracture strengths of 340–550 MPa at 1200°C), high-temperature ductility (15–40% tensile elongation above 1000°C), creep resistance (creep rupture life in excess of 1000 hours at 138 MPa loading at 1000°C in air), and oxidation resistance (comparable to that of commercial chromia-forming alloys in 1100°C, 1000 h cyclic oxidation screenings in air) [2]. However, no room-temperature ductility has been achieved and extensive microalloying and microstructural control efforts have 1ed to only modest room-temperature fracture toughness of 12–14 MPa√m.

In contrast, the MgO-dispersed Cr alloys [3,4] exhibit tensile elongations of greater than 10% and fracture toughness in the 20–25 MPa√m range at room temperature. These alloys are based on Cr-(3-6) MgO wt.%. and are made by powder metallurgical processes, typically sintering or hot pressing and extrusion. They consist of a Cr matrix phase with MgO and $MgCr_2O_4$ spinel (formed during powder consolidation) dispersions at the grain boundaries. Although ductile at room temperature, the yield strength of these alloys is only 200–240 MPa at room temperature, and efforts to improve strength have resulted in a concomitant reduction in ductility. Both classes of alloys exhibit excellent high-temperature corrosion resistance in many molten salt and slag environments, although they remain susceptible to nitride subscale formation. During this year, the development effort has focused on two key areas: (1) evaluation of the high-temperature corrosion behavior of baseline alloy compositions in coal combustion environments relevant to fossil energy power generation systems and (2) the effect of macroalloying additions of transition metals to further improve mechanical and corrosion resistance

properties. Some success in improving toughness and environmental resistance was achieved with additions of transition metal(s). A patent application is forthcoming, for this report these additions are referred to as “X”

DISCUSSION OF CURRENT ACTIVITIES

HIGH-TEMPERATURE CORROSION BEHAVIOR

Coupons of Cr-9Ta-5Mo-2Si-0.15La-0.1Ti atomic percent (at.%), a baseline Cr-Cr_2Ta alloy, and Cr-6MgO-0.75Ti weight percent (wt.%), a baseline MgO-dispersed Cr alloy, were submitted to the Combustion and Environmental Research Facility at the National Energy Technology Laboratory for exposure under coal combustion conditions. (Cr-Cr_2Ta alloys are reported in at.% and Cr-MgO in wt.%). The tests were conducted using Prader Creek coal; the Cr-Cr_2Ta alloy coupons were exposed at temperature ranges of 1149–1204°C and 1260–1316°C for 350, 650, and 1000 h. The Cr-MgO alloy coupons were exposed at temperature ranges of 1038–1098°C and 1093–1149°C for 350 and 1000 h. After exposure, the coupons were analyzed by optical microscopy, scanning electron microscopy (SEM), and electron probe microanalysis (EPMA).

Figure 1 shows Cr-9Ta-5Mo-2Si-0.15La-0.1Ti after exposure for 1000 h at 1260–1316°C. A significant fraction of the coupon broke away as a result of the exposure (Fig. 1a). Cross-section analysis revealed that a Cr_2O_3-based scale was formed, however extensive subscale nitridation of the Cr matrix phase (to form Cr_2N) and the Laves phase (to form mixed Cr-Ta-N/Cr_2N) also occurred. The failure of the coupon is attributed to the low fracture toughness of this alloy (~12 MPa-$m^{1/2}$ at room temperature) and embrittlement of the Cr matrix phase by the subscale nitridation. Previous work had shown that the Cr_2Ta Laves phase could selectively getter some incoming nitrogen, limiting nitridation of the adjacent Cr matrix phase, however, these results indicate that the gettering effect is overwhelmed during long term, high temperature exposures.

Figure 2 shows Cr-6MgO-0.75Ti after a 1000 h exposure at 1093–1149°C in the coal combustion environment. In contrast to the Cr-9Ta-5Mo-2Si-0.15La-0.1Ti alloy, the coupon remained intact and, further, showed good corrosion resistance over the course of the exposure. However, cross-section analysis revealed evidence of preferential subscale nitridation along the Cr matrix grain boundaries. Collectively, the coal combustion exposures suggest that the Cr-Cr_2Ta and Cr-MgO alloys exhibit good inherent resistance to ash deposit attack in oxidizing coal combustion environments; however, this resistance is negated by susceptibility to subscale nitrogen penetration.

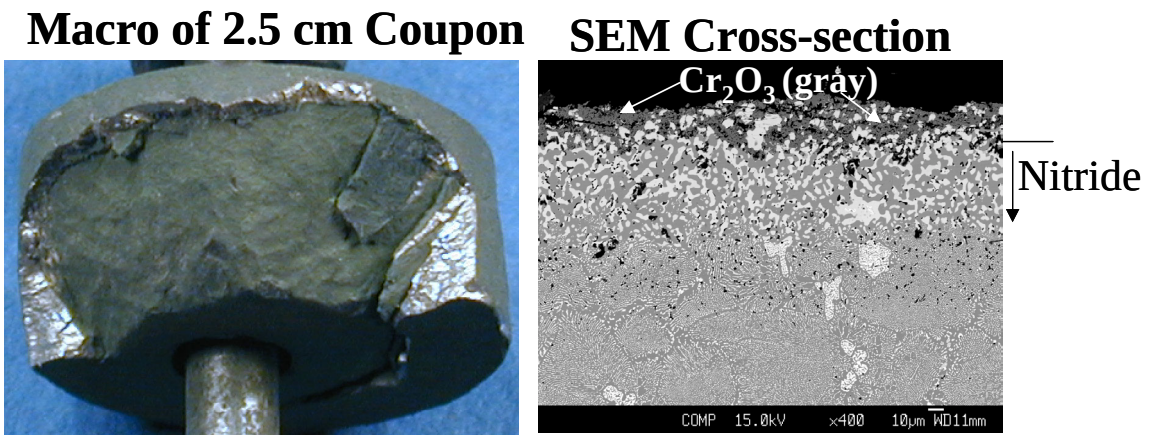

Fig. 1. Cr-9Ta-5Mo-2Si-0.15La-0.1Ti after 1000 h coal combustion test at 1260–1316°C. Cr solid solution (dark), Cr_2Ta Laves (light).

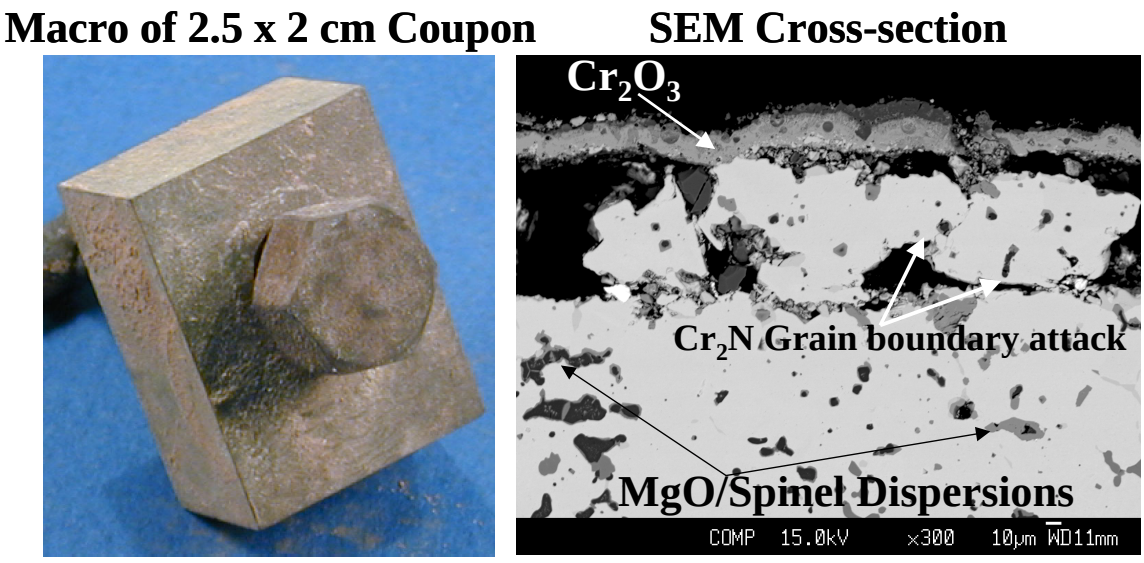

Fig. 2. Cr-6MgO-0.75Ti after the 1000 h coal combustion test at 1093–1149°C.

MACROALLOYING EFFECTS

Macroalloying was initially investigated for the Cr_2Ta-reinforced Cr alloys in order to improve room temperature fracture toughness. Additions of X were found to be particularly effective, with substitution of 25–35 at.% X for Cr yielding values greater than 15 MPa-$m^{1/2}$. When combined with a reduction in Ta level to maintain the eutectic structure (the X additions shifted the Cr-Cr_2Ta eutectic from about 9.5 at.% to the 5.5–7.5 at.% Ta range), room temperature fracture toughness in the 20 MPa-$m^{1/2}$ range was achieved. A summary of room temperature fracture toughness trends over the course of this program is shown in Fig. 3.

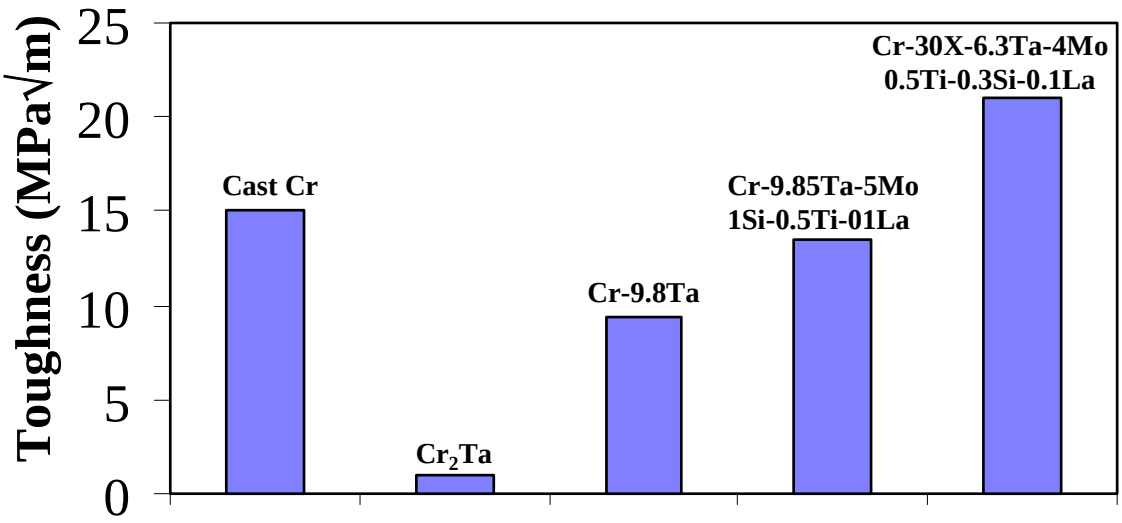

Fig. 3. Summary of room temperature fracture toughness trends. The fracture toughness values were obtained using subsized chevron-notched three-point bend samples and should be considered semiquantitative (modulus of 300 GPa used for Cr and 250GPa for all other alloys, see reference 5 for further details of this technique).

Somewhat unexpectedly, the addition of X was also found to significantly retard subscale nitridation on elevated temperature exposure in air. Figure 4 shows an SEM cross-section of Cr-35X-5.5Ta-4Mo-0.5Ti-0.3Si-0.1La at.% after eleven, 100 h cycles (1100 h total) at 1100°C in air. EPMA analysis of the zone underneath the Cr_2O_3 scale showed no evidence of nitride/nitrogen in the Cr matrix phase. Further, the Laves phase beneath the scale was selectively internally oxidized rather than internally nitrided, as is typical for Cr-Cr_2Ta alloys without X additions [6]. The apparent prevention of, or at least significant retardation of subscale nitridation is a key finding. Cr_2O_3 scales are generally permeable to nitrogen and subscale nitridation of Cr to form Cr_2N occurs at a faster rate than Cr_2O_3. The rapid formation of nitride subscales has been a major barrier to the use of Cr and Cr matrix alloys at elevated temperatures in nitrogen containing environments [e.g., 1]. It is not yet known whether the X additions act by making the Cr_2O_3 scale or the Cr(X) matrix phase impermeable (or at least much less permeable) to nitrogen, modifying the permeability of Cr(X) to oxygen, relative to nitrogen, or if they otherwise alter the relative reactivity of Cr_2O_3 vs Cr_2N formation by the alloy such that the nitride is not formed.

The levels of X additions needed to impart the improved toughness and limit/prevent subscale nitridation also depress the melting point of the alloy such that high-temperature strength is degraded. This is illustrated in Fig. 5, which shows yield strength at 1000°C as a function of X additions. Partial substitution of Co for X (5–10 at.% Co range) was investigated in an attempt to improve high temperature strength, however it was not effective, with a further decrease in strength at 1000°C, although tensile elongation at 1000°C was significantly increased (5% for Cr-30X-6.3Ta-4Mo-0.5Ti-0.3Si-0.1La vs 33%

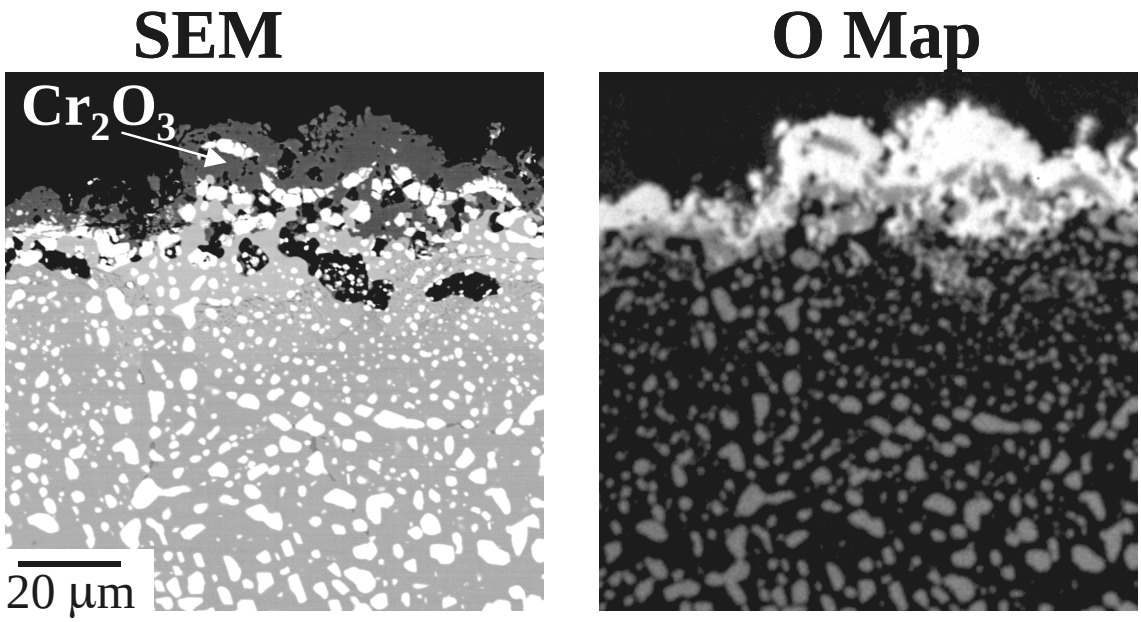

Fig. 4. Cross-section of Cr-35X-5.5Ta-4Mo-0.5Ti-0.3Si-0.1La at.% after eleven, 100 h cycles (1100 h total) at 1100°C in air. Cr solid solution (dark), Laves (light).

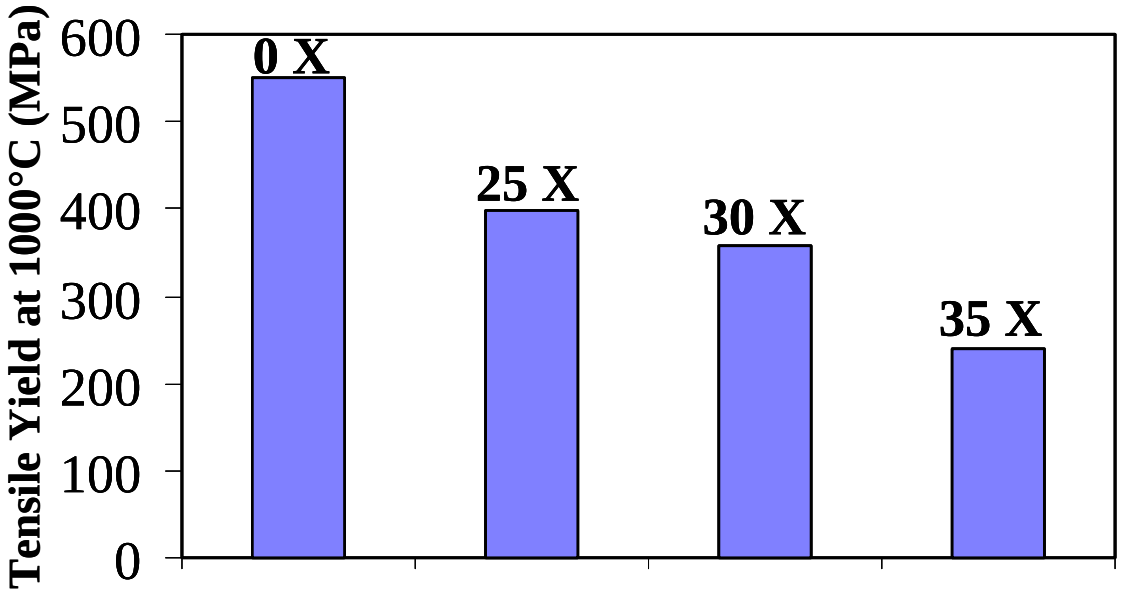

Fig. 5. Tensile yield strength at 1000°C for Cr-8Ta-5Mo-0.1La (0 X hypoeutectic alloy) and as a function of X content for Cr-X-Ta-4Mo-0.5Ti-0.3Si-0.1La at.% (Ta level adjusted to yield eutectic: 25X/6.8Ta; 30X/6.3Ta; 35X/5.7Ta). The data was obtained using sheet tensile samples ~0.6–0.7 mm thick with a gage length of 12.7 mm prepared to a 600 grit surface finish. The crosshead speed was 2.54mm/minute (initial strain rate of 3.3×10^{-3}/s). The samples were heated to 1000°C in air for testing in approximately 5 minutes.

for Cr-20X-10Co-6.3Ta-4Mo-0.5Ti-0.3Si-0.1La). The best balance of room temperature toughness and high temperature strength was found for additions of 30 at.% X, with Cr-30X-6.3Ta-4Mo0.5Ti-0.3Si-0.1La exhibiting an attractive combination of over 20 MPa-$m^{1/2}$ toughness at room-temperature and 350 MPa yield strength at 1000°C.

Macroalloying with X was also investigated for the MgO-dispersed Cr alloys in an attempt to eliminate susceptibility to subscale nitridation. Short term oxidation tests indicated a similar positive effect, with no subscale nitridation observed for Cr-44X wt.% with 6 wt.% MgO after a 120 h screening exposure at 1100°C in air (Fig. 6). (Cr-6MgO exhibited subscale Cr_2N formation under these conditions). The X additions also significantly increased room-temperature yield strength, from 200 MPa for Cr-6MgO to nearly 700 MPa for Cr-44X + 6 MgO, while preserving a small (1–2%) amount of tensile ductility at room-temperature. However, the high strength was not well retained at elevated temperature, with a yield strength of only 90 MPa obtained at 900°C.

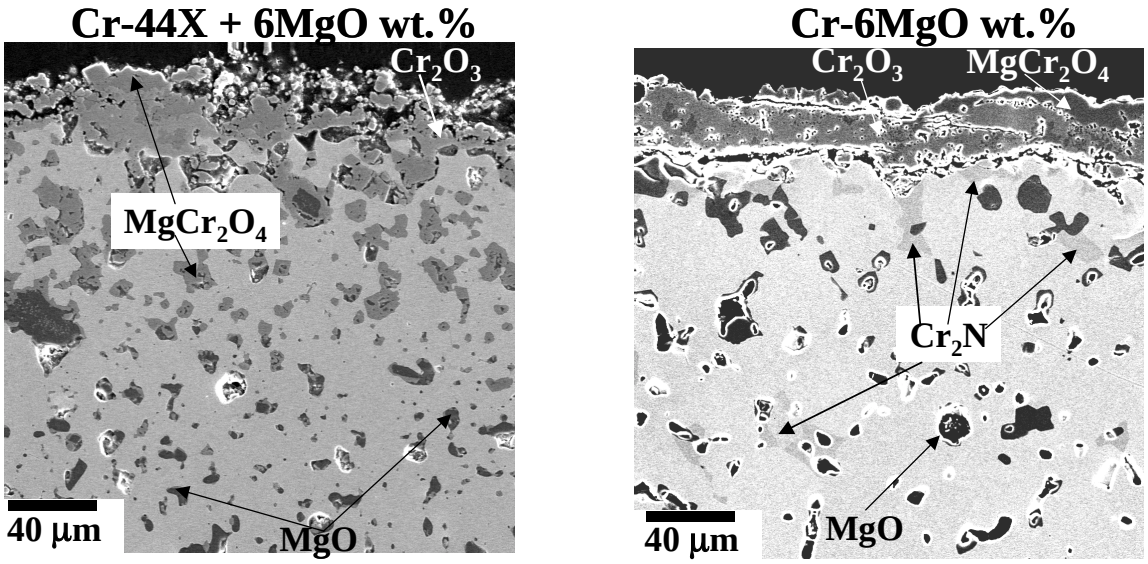

Fig. 6. SEM cross-sections after 120 h at 1100°C in air. No subscale nitridation was observed for the Cr-44X base alloy, although the Mg-based oxide dispersions were completely converted to $MgCr_2O_4$ underneath the scale (identification based solely on EPMA data).

FUTURE PLANS

Collectively, this development program has succeeded in identifying approaches capable of mitigating the key limiting phenomena of Cr-based alloys (inadequate high-temperature strength, room-temperature brittleness, and embrittling nitride subscale formation). However, it does not appear possible to achieve them all in a single alloy. The alloys developed under this program will be spun off to an applied development effort for black liquor gasification in the paper and pulp industry, to take advantage of the excellent molten salt corrosion resistance of Cr. The understanding of the manipulation of multi-phase microstructures gained under this program will be transitioned to other alloy systems. Initial efforts will focus on intermetallic strengthened ferritic and austenitic alloys for improved elevated temperature strength in applications such as superheater tubes.

REFERENCES

1. W. D. Klopp, NASA TM X-1867, September 1969.
2. M. P. Brady, J. H. Zhu, C. T. Liu, P. F. Tortorelli, L. R. Walker, C. G. McKamey, J. L. Wright, C. A. Carmichael, D. J. Larson, M. K. Miller, and W. D. Porter, *Mate. High Temp.*, vol. 16, no. 4, pp. 189–193 (1999).
3. D. M. Scruggs, "Ductile Chromium Composition," U.S. Patent 3, 175, 279 (Mar. 30, 1965).
4. M. P. Brady, I. M. Anderson, M. L. Weaver, H. M. Meyer, L. R. Walker, M. K. Miller, D. J. Larson, I. G. Wright ,V. K. Sikka, A. Rar, G. M. Pharr, J. R. Keiser, and C. A. Walls, *Mater. Sci. Eng. A* (in press 2003).
5. J. H. Schneibel, C. A. Carmichael, E. D. Specht, and R. Subramanian, *Intermetallics*, 5, p. 61 (1997).
6. M. P. Brady, J. H. Zhu, C. T. Liu, P. F. Tortorelli, and L. R. Walker, *Intermetallics*, 8, 9–11, pp. 1111–1118 (2000).

ACKNOWLEDGEMENTS

This research was sponsored by the U.S. Department of Energy, Fossil Energy Advanced Research Materials (ARM) Program. Oak Ridge National Laboratory is managed by U.T.-Battelle, LLC for the U.S. Department of Energy.

WELDING AND WELD REPAIR OF SINGLE CRYSTAL GAS TURBINE ALLOYS

J. M. Vitek, S. A. David, S. S. Babu, and J.-W. Park
Oak Ridge National Laboratory

INTRODUCTION

The cost-effective commercial use of single crystal nickel-based superalloys for land-based turbine engine components such as blades and vanes requires that they can be repair welded to improve as-cast yields or to refurbish worn or failed components after intermediate service intervals. This program addresses this vital need by determining the welding behavior and weldability of single crystal nickel-based superalloys in order to develop an understanding and methodology for weld repair of critical components in advanced gas turbine systems. A two-pronged approach is being undertaken. First, the problem of stray grain formation in single crystal welds is being examined in detail. Their formation must be avoided in order to achieve optimum properties in single crystal welds. Thermodynamic, thermal, and solidification modeling as well as examination of model alloys and filler metal composition modifications are being carried out in order to identify the necessary conditions for the elimination of stray crystal formation in weldments. Second, a variety of fusion welding techniques, including electron and laser beam welding, and transient liquid phase bonding, are being utilized on commercial alloys in order to identify process conditions that are amenable to producing crack-free welds. Complementary thermo-mechanical modeling and simulation testing are used to identify weld cracking behavior. The welds are being evaluated by advanced characterization techniques in order to understand the microstructural development and cracking behavior, and to tailor the weld procedures to yield sound welds that meet microstructure and anticipated property requirements prior to, and after, long-term service. The program is being coordinated with an industry-university consortium that provides in-kind support and direction to the program.

BACKGROUND

In order to achieve performance goals for gas turbine engines, high-temperature operation is required. At such high temperatures, creep must be kept to a minimum and for many metallic components, adequate creep properties can only be achieved with the use of single crystals. Such single crystals are routinely used in aircraft turbine engines. However, due to the increase in size of land-based turbine engines compared to comparable aircraft turbine engines, component cost will be increased dramatically and component quality will be a major manufacturing concern. Consequently, current casting yields need to be improved to make the costs manageable. The problem of improving casting yields is exacerbated by the fact that the larger component size increases the likelihood of having defects. One solution is to

develop a reliable repair process that can be used to refurbish defective castings and thereby improve the net yield. Similarly, a technology for repairing parts is essential since replacement costs will be prohibitive. Such a repair technology will be needed for worn parts as well as failed components.

Earlier work at ORNL has shown that it is possible to weld polycrystalline nickel-based superalloys under limited conditions using electron or laser beam welding (1). However, routine commercial welding of single crystal nickel-based superalloys has three major hurdles that need to be surmounted in order to make refurbishment and repair feasible. First, the single crystal nature of the nickel-based superalloys is easily lost during welding due to stray grain formation (2). Second, nickel-based superalloys are very prone to cracking during welding. Finally, non-equilibrium solidification, elemental partitioning, and subsequent solid state transformation can yield microstructures that are not ideal and will not produce material with the needed properties (3,4). In addition to fusion welding, there is a need for the surface buildup of worn components through arc, electron-beam, or laser-beam deposition processes. For such surface deposition, published work by Gaumann et al (5) has shown that the conditions that favor epitaxial growth versus nucleation and growth are related to the temperature gradients, solidification velocities and heat-treatment processes (5).

The three major hurdles for welding of single-crystal nickel superalloys (stray grain formation, cracking, and non-equilibrium microstructure formation) are interdependent. It is the objective of this proposal to investigate the potential for weld refurbishment and repair of components by concentrating on these three effects and to determine processes, process conditions, and alloy compositions that will make such weld processing possible.

RESULTS AND DISCUSSION

MATERIALS

Commercial nickel-based superalloys were generously provided by several members of the industry-university consortium that was established for this project. In particular, a single-crystal slab of commercial alloy Rene N5 was provided by GE Power Systems and single-crystal slabs of PWA 1483 and CMSX4 were provided by Siemens-Westinghouse Corporation. Single crystal rods of model alloys based on an Fe-15Cr-15Ni composition were provided by PCC Airfoils Corporation. These materials were used in the studies described below.

STRAY GRAIN FORMATION IN MODEL ALLOYS

Previous work has shown that commercial nickel-based superalloys are extremely prone to stray grain formation (2). In contrast, stray grain formation in a model, high purity stainless steel alloy (Fe-15Cr-15Ni) was rare (6). It has been proposed that stray grain formation is related to the extent of constitutional supercooling ahead of the advancing solidification front (2,7). Detailed examination of stray grain formation as a function of welding conditions was not possible in commercial alloys or the high-purity model alloys. This is because in the former, excessive stray grain formation was found regardless of the welding conditions while in the latter, no stray grains were found under any conditions. Since the extent of constitutional supercooling, and hence the tendency to form stray grains during welding, is proportional to the solidification temperature range, model alloy compositions with larger solidification temperature ranges were identified by ORNL and prepared by PCC Airfoils. The alloy compositions and the calculated solidification temperature ranges are shown in Table 1, along with calculated values for the high-purity model alloy and typical nickel-based superalloys.

Table 1: Model alloy compositions and corresponding (calculated) solidification temperature ranges.

Alloy Composition (wt %)	Calculated Solidification Temperature Range (°C)
Fe-15Cr-15Ni (high purity alloy)	7.9
Fe-15Cr-15Ni-1Al	11.9
Fe-15Cr-15Ni-3Al	29.4
Fe-15Cr-15Ni-1Si	27.9
Fe-15Cr-15Ni-1Ti	33.6
Typical Ni-based single crystal superalloys	40–50

Electron beam welds were made on the experimental alloys at two different speeds to assess the sensitivity of stray grain formation in these model alloys to welding conditions. A comparison of the grain structure in the high-purity alloy and one of the new model alloys is shown in Fig. 1. The results show that the new alloys are indeed vulnerable to stray grain formation. Furthermore, results showed that the extent of stray grain formation was affected by the welding conditions. These promising results will be followed by more extensive weld runs in order to identify the relationship between welding conditions and stray grain formation.

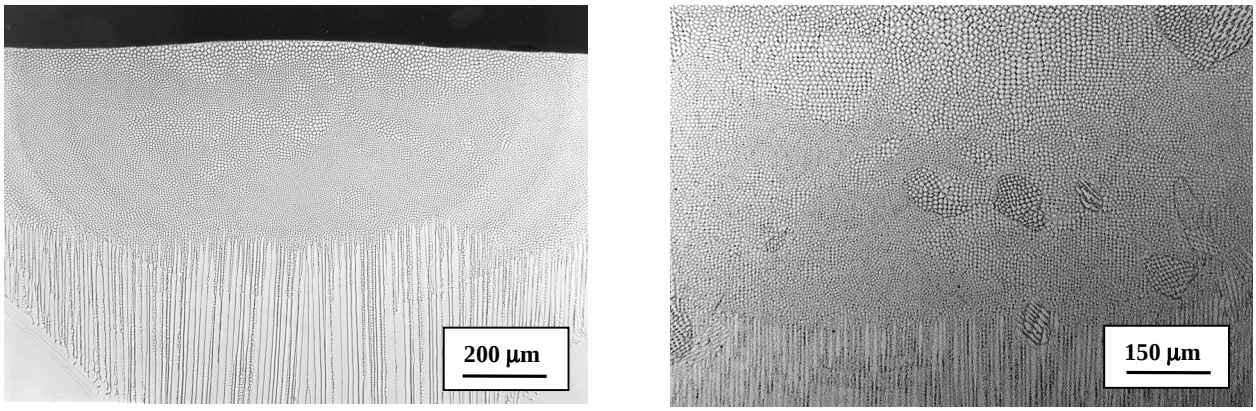

Fig. 1. Transverse view micrographs of electron-beam welded single crystals welded along [100] direction and on (001) plane at same speed of 4.2 mm/s. The alloy on the left is high-purity Fe-15Cr-15Ni and shows a complete absence of stray grains. The alloy on the right is Fe-15Cr-15Ni-1Si and shows numerous stray grains.

STRAY GRAIN FORMATION IN COMMERCIAL ALLOYS

A series of autogenous laser welds were made on the Rene N5 single crystal alloy at different weld speeds and weld powers. The weld direction was along the axis of the slab from which the specimens were machined, and the surface normal was the same as that of the slab. X-ray analysis indicated that the weld direction was 15° from [100] and the surface normal was 22° from [001]. It was found that the extent of stray grain formation in these welds was influenced by the welding conditions. Low speed welds tended to maintain the single crystal nature of the base material while high speed welds resulted in more extensive stray grain formation. Furthermore, since the weld direction and sample surface normal were not along symmetric crystallographic orientations, there was a marked difference in the grain structure on either side of the weld centerline. Orientation Imaging Microscopy (OIM) was used to reveal the extent of stray grain formation.

Thermal modeling was used to identify the weld pool shape in these welds as a function of welding conditions. The modeled weld pool shape was combined with the crystallographic orientation data and the weld conditions to determine the dendritic growth velocities as a function of position in the weld pool, using a geometrical model developed earlier (8). The thermal modeling also allowed for a determination of the thermal gradient as a function of position along the solid-liquid interface. These results were used to evaluate the extent of constitutional supercooling as a function of weld conditions and weld position. The results showed that the conditions leading to the greatest constitutional supercooling corresponded very well with the experimental results on stray grain formation. Further details may be found in a publication that is presently being prepared (9).

WELD CRACKING BEHAVIOR IN COMMERCIAL ALLOYS

Nickel-based superalloys are extremely prone to weld cracking (1). Experiments were conducted to determine the influence of welding conditions on cracking behavior. Two types of experiments were conducted. Autogenous gas tungsten arc (GTA) and laser welds were made on Rene N5 sheet samples for different welding conditions. All GTA welds showed cracking, although the extent of cracking was less for lower speed welds. Low speed laser welds did not show any cracking, but as the speed was increased, cracking became more prevalent. The cracking behavior was closely related to the extent of stray grain formation. Cracks tended to follow along stray grain boundaries. This is shown in Fig. 3.

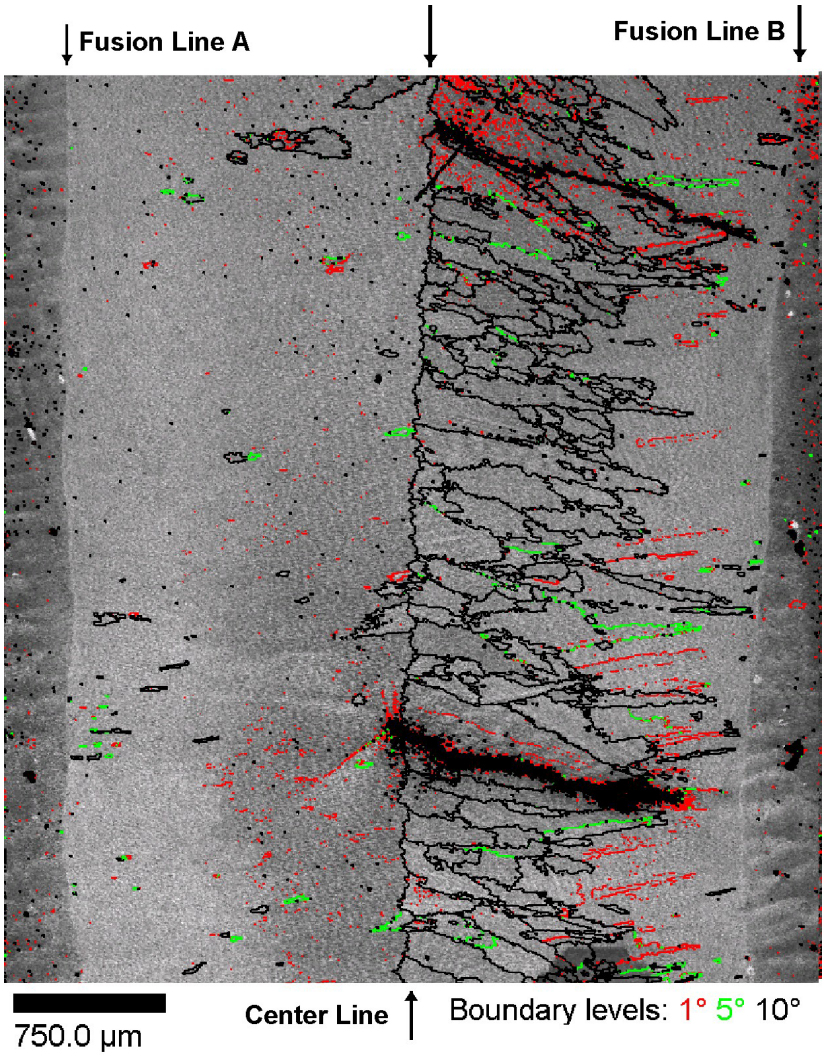

Fig. 2. Optical micrograph of the top surface of laser welded Rene N5 with grain boundaries (as determined by OIM) superimposed. The results show the formation of high-angle grain boundaries (>10° misorientation) near the center of the weld on only one side of the weld.

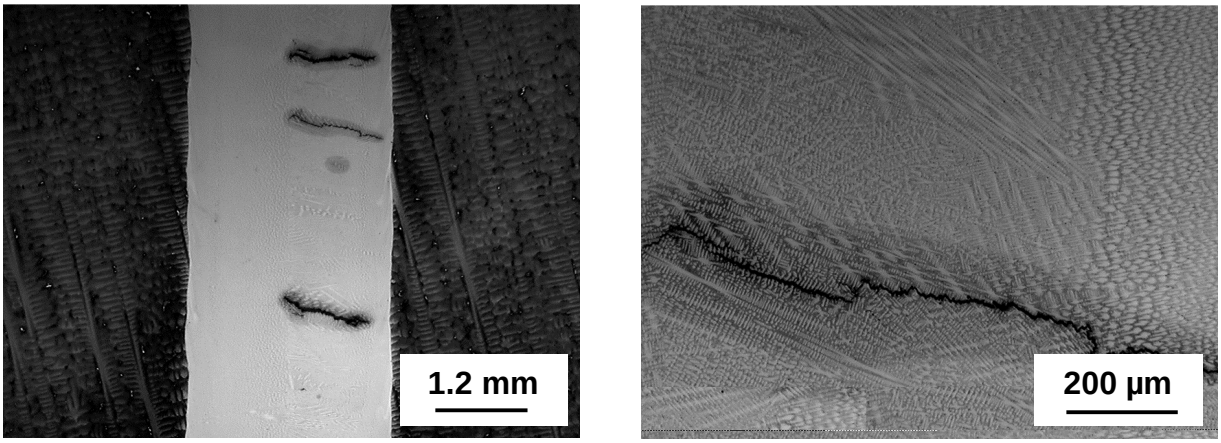

Fig. 3. Top view of laser welded Rene N5 showing cracking behavior (left) on only one side, where stray grains were found (see Fig. 2) and higher magnification view (right) showing cracks follow along stray grain boundaries.

Additional welds were made on Rene N5 by Honeywell Aerospace Services (a consortium member in this project) using their powder laser deposition process. Welds were made for two different geometries (groove and clad) with different filler metals. The results showed extensive cracking for the groove geometry. Cracking was most severe when the filler metal was a high-strength, high gamma prime content alloy, which is comparable to the single crystal alloys. The clad geometry was less susceptible to cracking.

Extensive modeling studies have been initiated to model the development of stresses during welding. These modeling results will be used to determine the effect of welding conditions on the magnitude of the stresses encountered during welding and to interpret the experimental results. The calculations will also be used to identify preferred welding conditions that minimize stresses and reduce the extent of cracking.

REFERENCES

1. S. A. David, J. M. Vitek, S. S. Babu, L. Boatner, and R. W. Reed, “Welding of Nickel-Base Superalloy Single Crystals,” *Sci. Technol. Welding and Joining*, Vol. 2, 1997, pp. 79–88.
2. J. M. Vitek, S. A. David, and L. A. Boatner, “Microstructural Development in Single Crystal Nickel-Base Superalloy Welds,” *Sci.. Technol. Welding and Joining*, Vol. 2, 1997, pp. 109–118.
3. S. S. Babu, S. A. David, and M. K. Miller, “Microstructural Development in PWA 1480 Electron Beam Welds—An Atom-Probe Filed-Ion Microscope Study,” *Applied Surface Science*, Vol. 94/95, 1996, pp. 280–287.
4. S. S. Babu, S. A. David, J. M. Vitek, and M. K. Miller, “Atom-Probe Field Ion Microscopy Investigation of CMSX-4 Ni-Base Superalloy Laser Beam Welds,” *J. de Physique IV*, Vol. 6, 1996, pp. C5-253–258.

5. M. Gaumann, S. Henry, F. Cleton, J.-D. Wagniere, and W. Kurz, “Epitaxial Laser Metal Forming: Analysis of Microstructure Formation,” *Mat. Sci. Eng*., Vol. A271, 1999, pp. 232–241.
6. M. Rappaz, S. A. David, J. M. Vitek, and L. A. Boatner, “Analysis of Solidification Microstructures in Fe-Ni-Cr Single Crystal Welds,” *Metall. Trans. A*, Vol. 21A, 1990, pp. 1767–1782.
7. M Gaumann, R Trivedi, and W Kurz, “Nucleation Ahead of the Advancing Interface in Directional Solidification,” *Mat. Sci. Eng.*, Vol. A226-228, 1997, pp. 763–769.
8. M. Rappaz, S. A. David, J. M. Vitek, and L. A. Boatner, “Development of Microstructures in Fe-15Ni-15Cr Single Crystal Electron Beam Welds,” *Metall. Trans. A*, Vol. 20A, 1989, pp.1125–1138.

HIGH TEMPERATURE OXIDATION PERFORMANCE OF ALUMINIDE COATINGS

B. A. Pint, Y. Zhang, † J. A. Haynes and I. G. Wright

Metals and Ceramics Division
Oak Ridge National Laboratory
Oak Ridge, TN 37831-6156

†Department of Mechanical Engineering
Tennessee Technological University
Cookeville, TN 38505-0001

INTRODUCTION

Aluminide coatings are of interest for many high temperature applications because of the possibility of improving the oxidation resistance of structural alloys by forming a protective external alumina scale.[1-5] Steam and exhaust gas environments are of particular interest because alumina is less susceptible to the accelerated attack due to hydroxide formation observed for chromia- and silica-forming alloys and ceramics.[6-13] For water vapor testing, one ferritic (Fe-9Cr-1Mo) and one austenitic alloy (304L) have been selected as substrate materials and CVD coatings have been used in order to have a well-controlled, high purity coating. It is anticipated that similar aluminide coatings could be made by a higher-volume, commercial process such as pack cementation. Previous work on this program has examined as-deposited coatings made by high and low Al activity CVD processes and the short-term performance of these coatings.[5,14,15] The current work is focusing on the long term behavior in both diffusion tests[16] and oxidation tests of the thicker, high Al activity coatings. For long-term coating durability, one area of concern has been the coefficient of thermal expansion (CTE) mismatch between coating and substrate.[5] This difference could cause cracking or deformation that could reduce coating life. Corrosion testing using thermal cycling is of particular interest because of this potential problem and results are presented where a short exposure cycle (1h) severely degraded aluminide coatings on both types of substrates.

To further study the potential role of aluminide coatings in fossil energy applications, several high creep strength Ni-base alloys were coated by CVD for testing in a high pressure (20atm) steam-CO_2 environment for the ZEST (zero-emission steam turbine) program. Such alloys would be needed as structural and turbine materials in this concept. For Ni-base alloys, CVD produces a ≈50μm β-NiAl outer layer with an underlying interdiffusion zone. Specimens of HR160, alloy 601 and alloy 230 were tested with and without coatings at 900°C and preliminary post-test characterization is reported.

EXPERIMENTAL PROCEDURE

The substrates used in this study include Fe-9Cr-1Mo, type 304L stainless steel (Fe-18Cr-9Ni nominally), HR160 (Ni-30Co-28Cr-2.8Si-2Fe), alloy 601 (Ni-22.5Cr-14Fe-1.4Al) and alloy 230 (Ni-23Cr-12W-1.5Fe-1.4Mo). The laboratory-scale CVD reactor and coating process have been described elsewhere.[5,15] For the Fe-base alloys, the higher Al activity was achieved by including Cr-Al alloy pellets in the reactor during deposition for 4h at 1050°C.[15] Characterization of the as-deposited coatings has been provided elsewhere.[14-16] The Ni-base alloys were coated in the same reactor for 6h at 1100°C using a procedure developed for monocrystal Ni-base superalloys.[17,18] Mass gains for the coatings on HR160 averaged

2.4mg/cm^2 which was lower than that observed for alloy 230 (4.2mg/cm^2) or alloy 601 (3.8mg/cm^2).

For the Fe-base alloys, the oxidation testing focuses on 700°C where the substrate alloys are adversely affected by environmental effects but some strength is retained. Cyclic oxidation testing in air with 10±0.5 vol.%H_2O was conducted two ways: (1) in a vertical automated test rig with the specimens suspended from alumina rods using Pt-Rh wire and a cycle consisting of 1h at temperature and 10min cooling at room temperature or (2) in a horizontal tube furnace with the specimens in an alumina boat, the cycle consisting of 100h at temperature with the specimens cooled and weighed after each cycle. In each case, both ends of the high-purity alumina reaction tube were closed and the water vapor was controlled in the carrier gas by a water injection system described elsewhere.[19] For the Ni-base alloys, the high pressure tests were conducted at 2.1 GPa (300 psi) in an alloy 230 reaction tube using a steam-10%CO_2 atmosphere in one of the ORNL Keiser rigs.[20,21] The testing in laboratory air was conducted in box furnaces with the specimens contained in alumina crucibles with lids.[22]

Before and after exposures, specimens were weighed on a Toledo-Mettler model AG245 balance. Selected specimens were examined by light microscopy, field emission gun, scanning electron microscopy (SEM) equipped with energy dispersive x-ray analysis (EDXA) and electron probe microanalysis (EPMA) using wavelength dispersive x-ray. For cross-sections, the surface reaction product was protected by Cu-plating the specimen prior to mounting in epoxy.

RESULTS AND DISCUSSION

Fe-BASE ALLOYS TESTED AT 700°C

Previous testing of CVD coatings on Fe-base substrates for up to 1000, 1h cycles at 700°C in air with 10vol% H_2O had shown excellent coating performance.[14] Without a coating, 304L and Fe-9Cr-1Mo were severely attacked after short exposures in this environment, Figure 1. However, small cracks were noted by SEM in the surface of the thicker coatings after 1000h, Figures 2a and 2b. Limited spallation of the external scale was noted on 304L but not on Fe-9Cr-1Mo where deeper cracks in the coating were observed. Therefore, the test was continued to 2000h. After 2000h, the coated 304L specimen showed a significantly higher mass gain while the coated Fe-9Cr-1Mo specimen began to show an increase towards the end of the second 1000 cycles, Figure 1. Examination of the specimens after 2000 cycles revealed even more extensive macroscopic damage to the coating, Figures 2c and 2d, so the test was stopped and the coatings were sectioned.

Figure 3a shows the entire thickness of the Fe-9Cr-1Mo coated specimen revealing large cracks through the coating and, in one location, the coating had been penetrated and oxidation of the substrate had begun. At higher magnification, Figure 4a, a crack appears to extend from the outer layer deep into the inner coating layer. For the coated 304L specimen, Figure 3b shows similar cracking and degradation where the coating had been breached at the specimen edge. At higher magnification, Figure 4b, the cracks generally appeared to remain in the outer, Al-rich layer. More pores were observed in this coating than in the ferritic specimen.

The cracks in the coatings are attributed to the CTE mismatch between the coating and substrates. Two pieces of evidence support this hypothesis. First, similar coated specimens were isothermally exposed for 2000h at 700°C in air. After exposure, no deformation or cracking was observed, e.g., Figure 3c, and

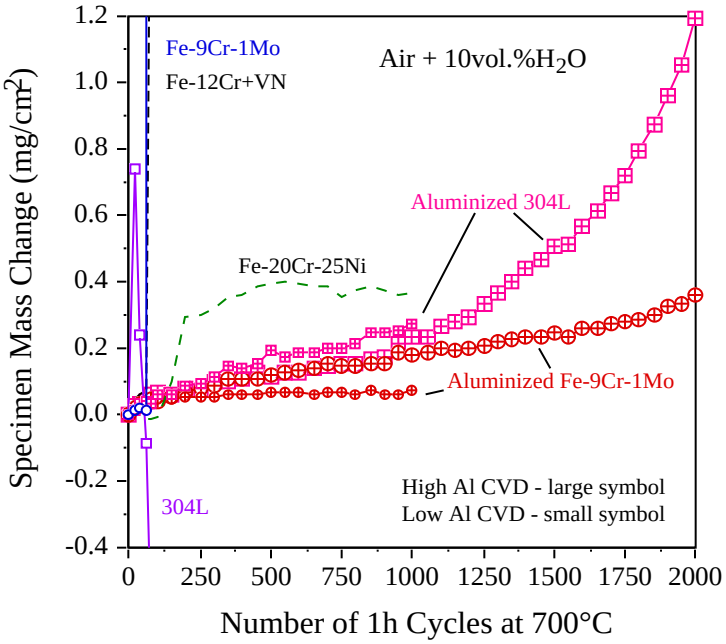

Figure 1. Specimen mass changes during 1h cycles at 700°C in air+10%H_2O. Results are shown for specimens coated with both the high (larger symbol) and low (smaller symbol) Al activity processes.

examination of the Al content of coatings exposed in dry air and humid air showed little depletion compared to the as-deposited coating, Figure 5a. (Some variation in the starting Al content and thickness may explain the slightly higher Al content in the coating exposed in humid air.) Second, coated specimens are currently being tested in 100h (rather than 1h) cycles at 700°C in air + 10%H_2O and no accelerated attack has been observed after 2000h of testing, Figure 5b. Both of these results suggest that the thermal cycling causes the cracking in the coating and an accumulation of cyclic damage is needed to compromise the oxidation resistance of the coatings. Because of the limited Al diffusion after 2000h, it is anticipated

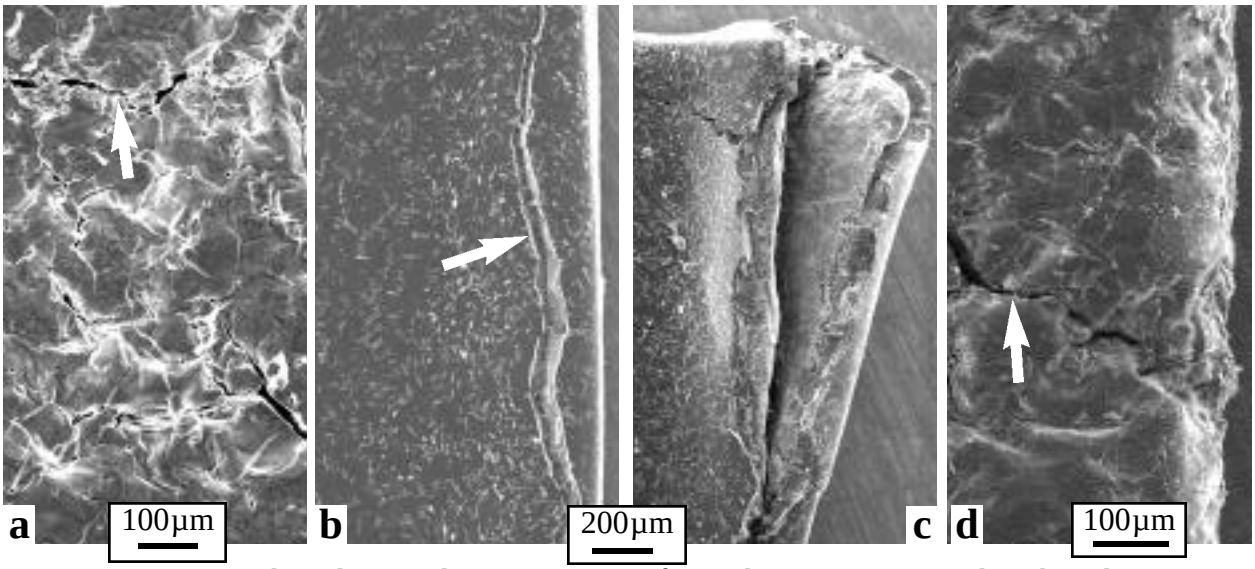

Figure 2. SEM secondary electron plan-view images of coated specimens exposed in 1h cycles at 700°C in humid air; (a) Fe-9Cr-1Mo after 1000 cycles, (b) 304L after 1000 cycles, (c) 304L after 2000 cycles and (d) Fe-9Cr-1Mo after 2000 cycles. Arrows point to cracks in the coating.

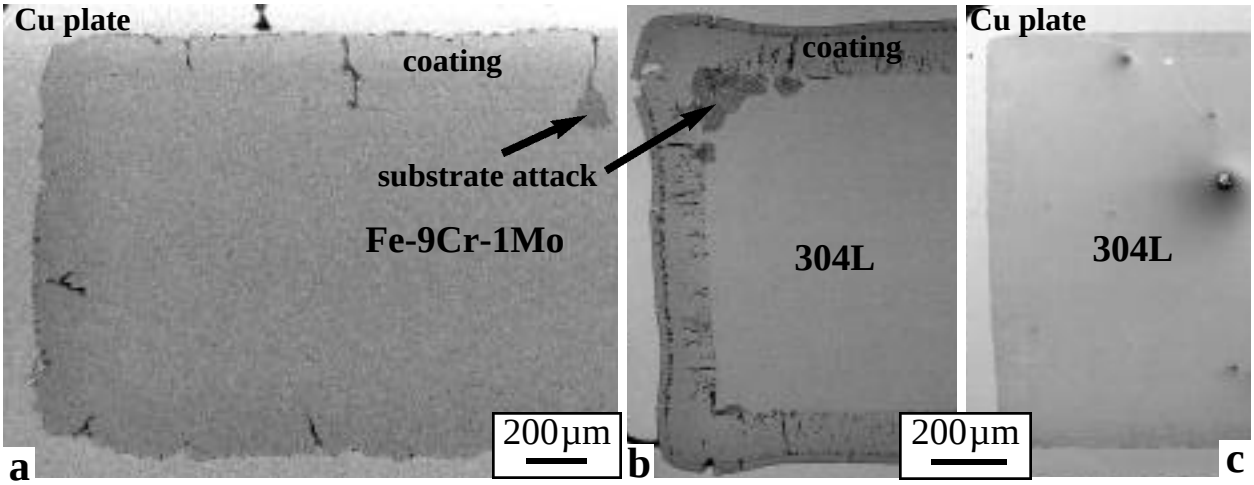

Figure 3. SEM secondary electron cross-sectional images of the coated specimens (a) Fe-9Cr-1Mo and (b) 304L after 2000, 1h cycles at 700°C in humid air, and (c) 304L after an isothermal 2000h exposure at 700°C in laboratory air.

that the coatings in the 100h cycle test may have a significantly longer lifetime than those in the 1h cycle test. The thermal cycling damage to the coating was more severe on the 304L specimen than the Fe-9Cr-1Mo. One explanation for this is that 304L retains more strength at this temperature than the ferritic alloy. A weaker substrate may allow more stress relaxation in the coating layer compared to a stronger substrate. Another possible reason is that the diffusion of Al into the 304L substrate may have caused the inner coating layer to become ferritic. This would result in three different CTE's in the three layers resulting in more strain during each cycle. In the case of the coating on the ferritic substrate, both the substrate and the inner coating layer would remain ferritic.

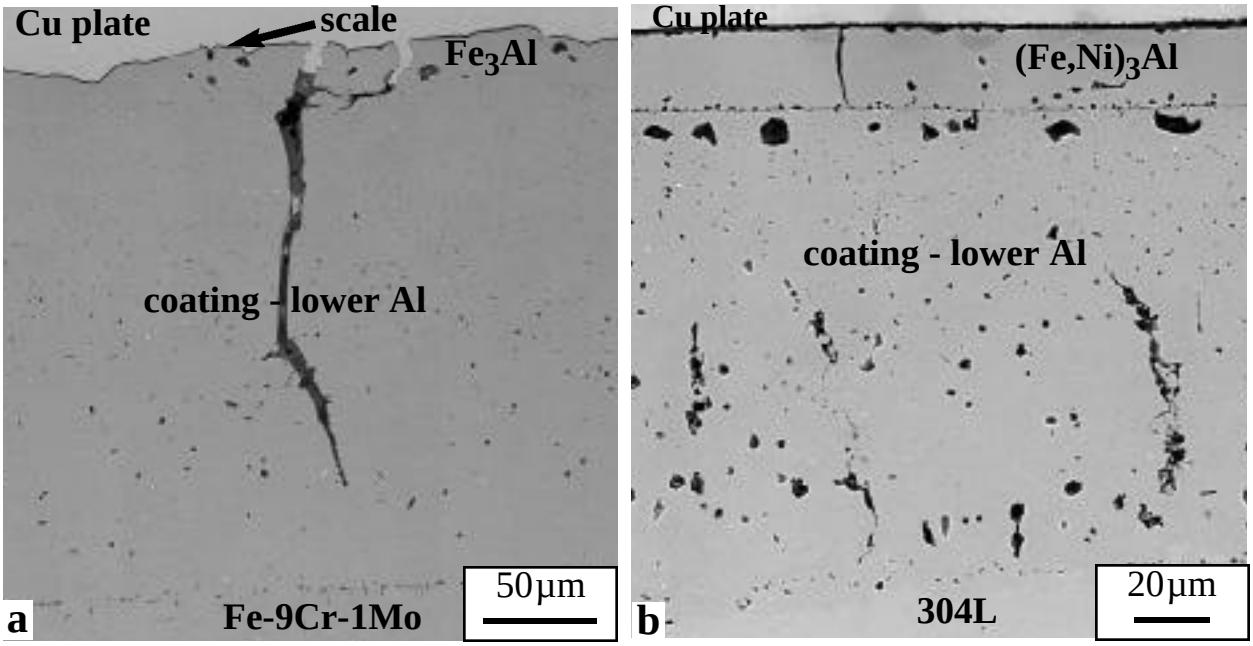

Figure 4. SEM secondary electron cross-sectional images of the coated specimens after 2000, 1h cycles at 700°C in humid air, (a) Fe-9Cr-1Mo and (b) 304L. The coatings consist of an outer Al-rich layer and an inner, thicker layer with a gradually declining Al content.

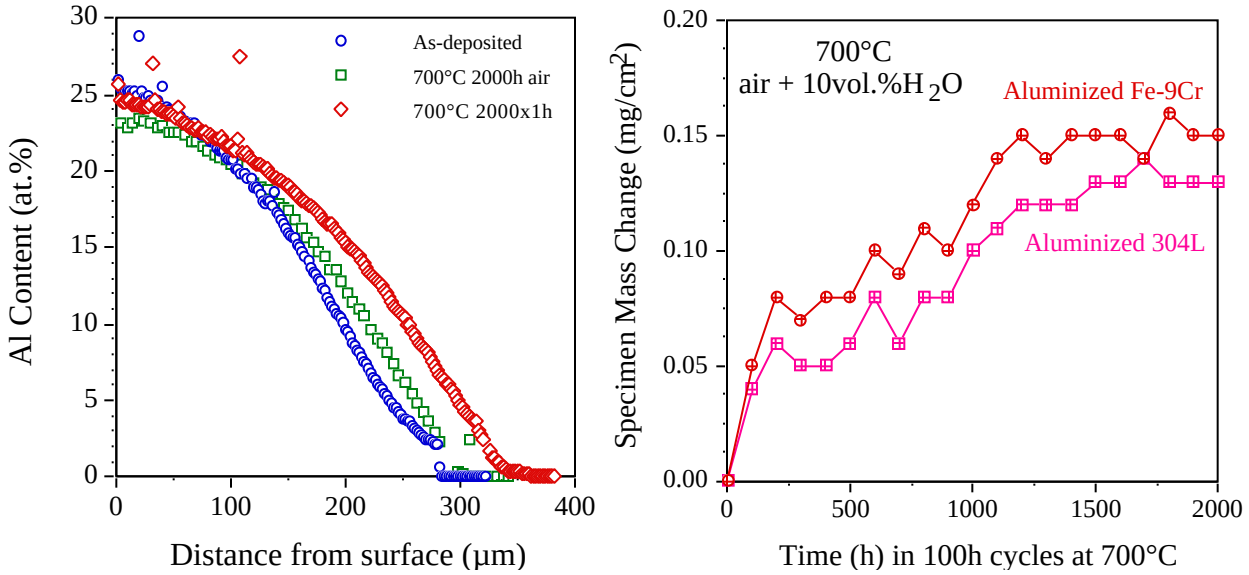

Figure 5. (a) EPMA Al profiles from an as-deposited coating, a coating exposed for 2000h in air and the coating exposed for 2000 1h cycles in humid air. (b) specimen mass gains for coatings exposed in 100h cycles at 700°C in humid air.

Ni-BASE ALLOYS AT 900°C

In order to evaluate the potential environmental problems for hot section materials in ZEST, three Ni-base alloys were tested with and without aluminide coatings at 900°C and 1135°C in the anticipated high-temperature, high-pressure ZEST environment (steam-10%CO_2). The full range of results will be reported elsewhere.[21] A summary of the mass change data at 900°C is given in Figure 6. Figure 6a shows that specimen mass gain of the coated and uncoated Ni-base alloys, 601, HR160 and 230, after 2, 500h cycles in the high pressure ZEST test. In each case, the aluminized specimens (arrows) showed less mass change than the uncoated alloys. For comparison, the performance of two alumina-forming alloys, MA956 (FeCrAl) and alloy 214 (NiCrAl), and type 310 stainless steel (Fe-25Cr-20Ni) also are included. In general, the aluminized specimens and alumina-forming alloys showed low mass gains for the test whereas the chromia-forming alloys tended to show higher mass gains due to the formation of faster growing chromia scales or mass losses due to scale spallation and/or volatilization. Figure 6b compares the performance of the same alloys after 500h (1 cycle) at 900°C in the ZEST test conditions and in laboratory air. The aluminized alloys showed similar behavior in air and in the high pressure steam-CO_2 environment. In contrast, the uncoated Ni-base alloys showed higher mass gains or losses in the ZEST test conditions, suggesting a susceptibility to the steam-CO_2 environment. In order to obtain long-term performance data on the aluminized Ni-base alloys, one specimen of each composition is being oxidized in air at 900°C in 500h cycles, Figure 7. After up to 3000h of exposure, the coated specimens are all showing low mass gains and no spallation. The mass gains for the coated specimens after 3000h in air are lower than the uncoated alloys after 500h.

The surface scale was examined on the aluminized specimens after 2, 500h cycles at 900°C in the ZEST test conditions. Figure 8 shows plan-view SEM images of the scale formed on aluminized alloy 601 that were typical of all three coated specimens. The slight ridges in Figure 8a mark coating grain boundaries and are typical of the surface morphology of CVD aluminide coatings. At higher magnification, Figure 8b, some larger oxide grains were observed that were rich in Ni. The formation of transient Ni-rich oxide

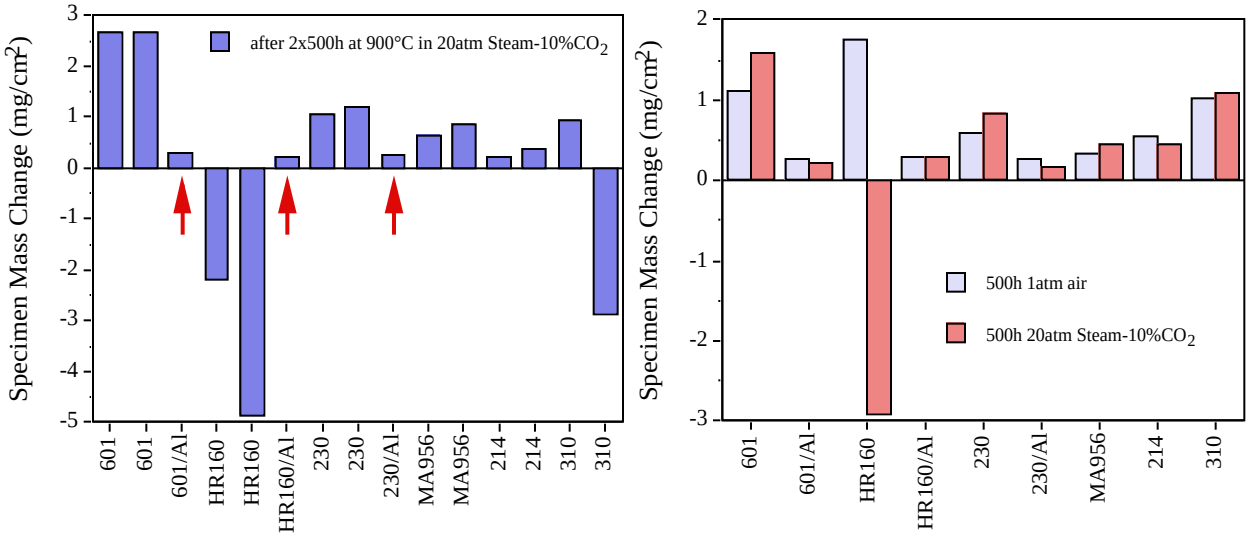

Figure 6. Specimen mass changes (a) after 2, 500h cycles at 900°C in the ZEST test (steam-10%CO_2 at 20atm) and (b) after 500h at 900°C in air and ZEST test.

has not been observed in previous work on aluminized Ni-base superalloys in air at 1100°-1200°C.[17-18] The formation may be due to the lower oxidation temperature or the environment. In cross-section, Figure 9, the coatings showed several common features typical of aluminide coatings: a thin, adherent surface oxide, a uniform β-(Ni,Al) coating with some lighter phases (likely lower Al content γ'-Ni_3Al) and an underlying interdiffusion layer. One unusual feature was noted on alloy 230, where voids were observed in the interdiffusion zone, Figure 9c. These may have occurred as a result of diffusion during the aluminization process or may reflect some type of coating penetration during the test. One troubling aspect of these cross-sections is the nearly single-phase, Cr-rich interdiffusion zone. The interdiffusion zone becomes enriched in refractory elements when Ni diffuses out to form the NiAl coating. However,

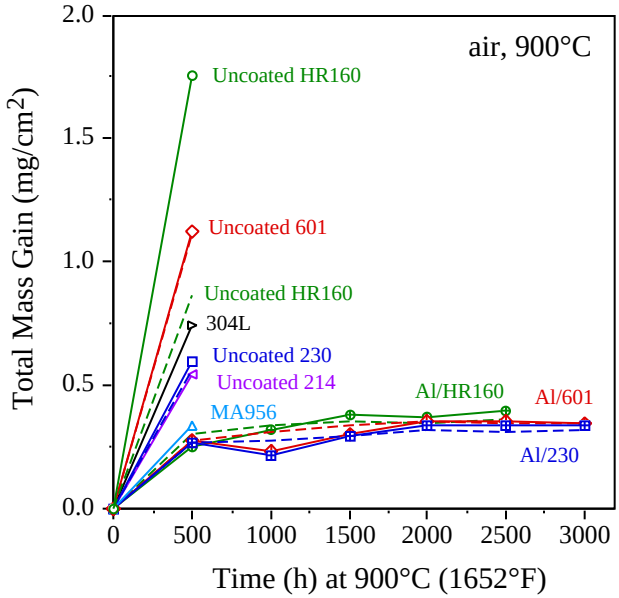

Figure 7. Specimen mass changes during 500h cycles at 900°C in air with and without aluminide coatings. The solid lines show the total mass gain and the dashed lines show the specimen mass gains.

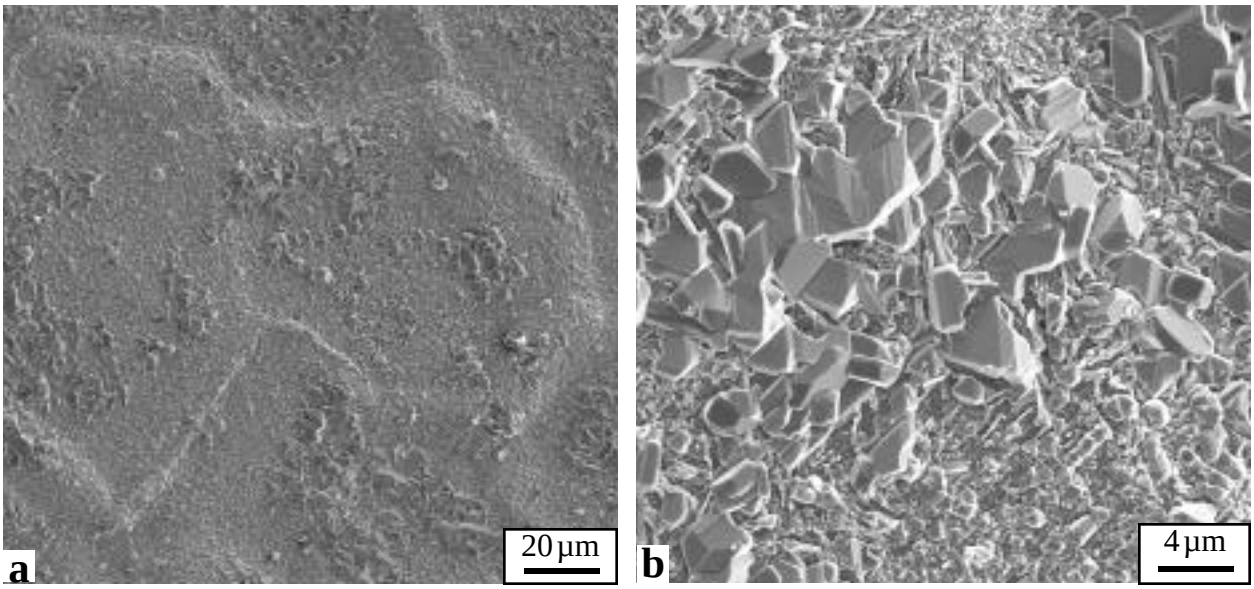

Figure 8. SEM secondary electron plan view images of the scale formed on aluminized alloy 601 after 2, 500h cycles at 900°C in steam-10%CO_2 at 20atm.

monocrystal superalloys with lower Cr contents (6-8wt.%) form an interdiffusion zone which is a mixture of refractory-rich topologically close-packed (TCP) phases and a Ni-base γ matrix.[18] The Cr-rich layer, which is likely a TCP phase, may have poor high temperature fatigue resistance or be susceptible to environmental embrittlement. More work is needed to clarify these issues. However, a MCrAlY-type overlay coating may be more appropriate to protect these alloys for ZEST-type environments.

SUMMARY

Long-term testing of CVD aluminide coatings on one ferritic (Fe-9Cr-1Mo) and one austenitic (304L) Fe-base substrate showed that high frequency cycling caused failure after less than 2000h at 700°C in air+10%H_2O. The deformation and cracking could not be attributed to the environment or the loss of Al due to corrosion or back diffusion. The most likely cause is the thermal expansion mismatch between the Fe_3Al outer coating and the substrate. Initial testing of aluminized Ni-base alloys in a high pressure, high

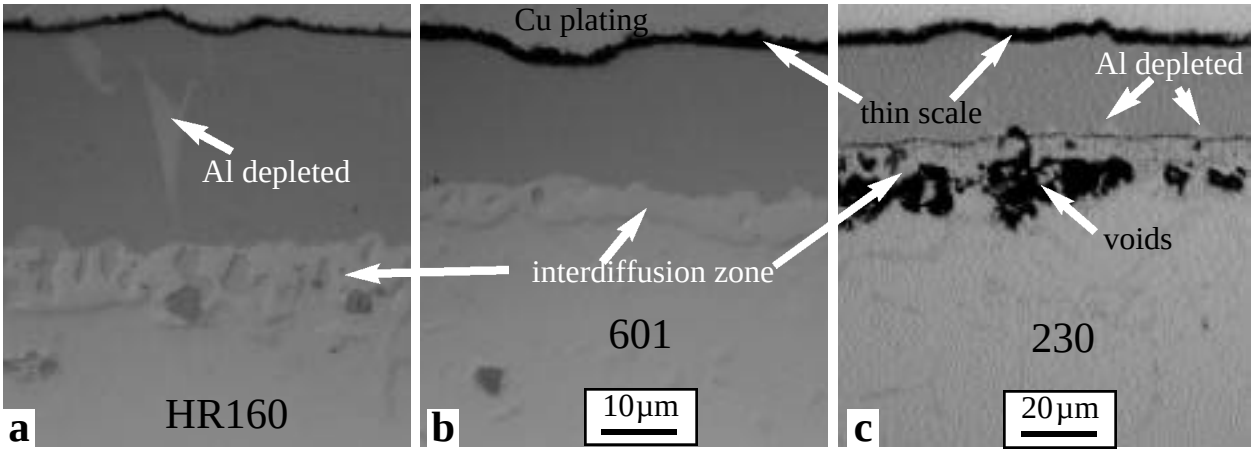

Figure 9. Light microscopy of polished cross-sections of aluminide coatings after 2, 500h cycles at 900°C in the ZEST test: (a) HR160 (b) alloy 601 and (c) alloy 230.

temperature ZEST-type environment showed good performance of the coatings under these conditions.

ACKNOWLEDGMENTS

The authors would like to thank K. Cooley, L. D. Chitwood, G. Garner, K. S. Reeves and H. Longmire at ORNL for assistance with the experimental work and C. G. McKamey and P. F. Tortorelli at ORNL for their comments on the manuscript. This research was sponsored by the U.S. Department of Energy, Fossil Energy Advanced Materials Research Program under contract DE-AC05-00OR22725 with UT-Battelle, LLC. R. Bishop and J. Farmer at LLNL provided specimens and funding for the oxidation exposures under the ZEST program.

REFERENCES

1. P. F. Tortorelli and K. Natesan, *Mater. Sci. Eng*., A258 (1998) 115.
2. P. F. Tortorelli, J. H. DeVan, G. M. Goodwin, M. Howell in: *Elevated Temperature Coatings: Science and Technology I,* Eds. N. B. Dahorte, J. M. Hampikian, J. J. Stiglich; TMS, Warrendale, PA, 1995, p.203.
3. F. D. Geib and R. A. Rapp, *Oxid. Met.*, 40 (1993) 213.
4. M. Zheng and R. A. Rapp, *Oxid. Met.*, 49 (1998) 19.
5. B. A. Pint, Y. Zhang, P. F. Tortorelli, J. A. Haynes and I. G. Wright, *Mater. High Temp.*, 18 (2001) 185.
6. G. C. Wood, I. G. Wright, T. Hodgkiess, D. P. Whittle, *Werk. Korr*., 21 (1970) 900.
7. J. Shen, L. Zhou and T. Li, *Oxid. Met.*, 48 (1997) 347.
8. H. Nickel, Y. Wouters, M. Thiele and W. J. Quadakkers, *Fresenius J. Anal Chem.*, 361 (1998) 540.
9. H. Asteman, J.-E. Svensson, L.-G. Johansson and M. Norell, *Oxid. Met.*, 52 (1999) 95.
10. E. J. Opila and N S Jacobson in: *Fundamental Aspects of High Temperature Corrosion*, Eds. D A Shores, R A Rapp, and P Y Hou; Proc. Vol.96-26, Electrochemical Society, Pennington, NJ, 1996, p.344.
11. N. S. Jacobson, *J. Am. Ceram. Soc.*, 76 (1993) 3.
12. E. J. Opila and R. E. Hann Jr., *J. Am. Ceram. Soc.*, 80 (1997) 197.
13. K. L. More, P. F. Tortorelli, M. K. Ferber, and J. R. Keiser, *J. Am. Ceram. Soc.*, 83 (2000) 211.
14. B. A. Pint, Y. Zhang, P. F. Tortorelli, J. A. Haynes and I. G. Wright in: *Proc. Sixteenth Annual Conf. Fossil Energy Materials*, R. R. Judkins (comp.), U. S. Department of Energy, 2002.
15. Y. Zhang and B. A. Pint in: *Proc. Sixteenth Annual Conf. Fossil Energy Materials*, R. R. Judkins (comp.), U. S. Department of Energy, 2002.
16. Y. Zhang and B. A. Pint in: *Proc. Seventeenth Annual Conf. Fossil Energy Materials*, R. R. Judkins (comp.), U. S. Department of Energy, 2003.
17. W. Y. Lee, Y. Zhang, I. G. Wright, B. A. Pint and P. K. Liaw, *Met. Trans.*, 29A (1998) 833.
18. Y. Zhang, J. A. Haynes, W. Y. Lee, I. G. Wright, B. A. Pint, K. M. Cooley and P. K. Liaw, *Met. Trans.*, 32A (2001) 1727.
19. B. A. Pint and J. M. Rakowski, NACE Paper 00-259, Houston, TX, presented at NACE Corrosion 2000, Orlando, FL, March 2000.
20. J. R. Keiser, M. Howell, J. J. Williams, and R. A. Rosenberg, NACE International Paper 96-140, Houston, TX, presented at NACE Corrosion 1996.
21. I. G. Wright, B. A. Pint, Y. Zhang and R. Bishop, to be presented at NACE Corrosion 2004.
22. B. A. Pint, P. F. Tortorelli and I. G. Wright, *Oxid. Met.*, 58 (2002) 73.

Mo-Si-B ALLOY DEVELOPMENT

J. H. Schneibel
Oak Ridge National Laboratory

Jamie J. Kruzic and Robert O. Ritchie
Lawrence Berkeley National Laboratory

INTRODUCTION

Nickel-base superalloys have outstanding oxidation and mechanical properties at elevated temperatures, but their service temperatures are inherently limited to temperatures around 1000˚C. Oxide dispersion strengthened materials, with solidus temperatures as high as 1480°C [1], can operate above 1000°C. However, their creep strengths are relatively low. For example, the nickel-base ODS alloy MA754 has a 1000 h rupture strength of 78 MPa at 1150°C and the iron-base ODS alloy MA956 has a 100 h rupture strength of 51 MPa at 1100°C [1]. Also, these ODS alloys have high stress exponents which makes them prone to catastrophic fracture in creep since a small increase in stress can result in a dramatic increase in the creep rate. In order to increase the thermodynamic efficiency of fossil energy systems, strong, tough and oxidation resistant materials capable of service temperatures much higher than 1000°C are needed. While refractory elements such as Nb, Mo, Ta, and W have very high melting points, they lack oxidation resistance. One way to improve their oxidation resistance is to form silicides. A prime example is $MoSi_2$ that is widely used in heating elements for resistance furnaces. Its good oxidation resistance is due to the formation of a protective silica glass scale. However, $MoSi_2$ is very brittle with a room temperature fracture toughness on the order of 3 MPa $m^{1/2}$ [2]. Also, it is very weak at high temperatures [2]. If the Si concentration is reduced below that of $MoSi_2$, phases such as Mo_5Si_3, Mo_3Si, and α-Mo (Mo solid solution) form. These phases will have a lower oxidation resistance, but their fracture toughness may be higher. As indicated in the schematic ternary phase diagram in Fig. 1, two main alloy systems have been examined to date. In the first one, which was pioneered by Akinc and collaborators [3–5], intermetallic alloys consisting of Mo_5Si_3, the T2 phase Mo_5SiB_2, and the A15 phase Mo_3Si were investigated. They exhibit excellent oxidation resistance at elevated temperatures (e.g., 1300°C). The boron additions are crucial for providing the observed oxidation resistance [4,5], as already hinted at in an early study of the ternary Mo-Si-B phase diagram by Nowotny et al. [6]. The second system is the focus of this paper and was pioneered by Berczik et al. [7,8].

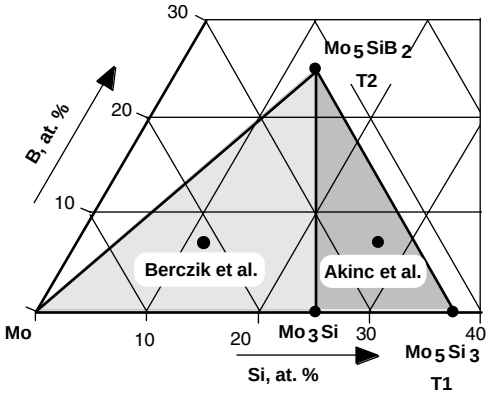

Fig. 1. Schematic illustration of the Mo-rich section of the ternary Mo-Si-B phase diagram.

Berczik investigated alloys consisting of α-Mo, Mo_3Si, and T2. While these alloys are not as oxidation resistant as Mo_5Si_3-T2-Mo_3Si alloys, they contain a ductile phase, α-Mo. Depending on its volume fraction and distribution, the α-Mo can improve the room and high temperature fracture toughness significantly. The fracture toughness increases with increasing α-Mo volume fraction. For a given α-Mo volume fraction, the fracture toughness is expected to be higher if the α-Mo forms a continuous matrix instead of individual particles [9]. The fracture toughness is also expected to increase if the microstructural scale of the α-Mo increases [10]. The oxidation resistance, on the other hand, is increased by decreasing the α-Mo volume fraction and by distributing the α-Mo in the form of isolated particles, instead of a continuous matrix. Clearly, then, the optimization of Mo-Mo_3Si-T2 alloys requires a trade-off between fracture toughness on the one hand, and oxidation resistance on the other.

The creep resistance of Mo-Mo_3Si-T2 alloys is governed by several factors. Mo_3Si and Mo_5SiB_2 are all very strong at elevated temperatures [11–13]. Since it can be safely assumed that the creep strength of α-Mo is lower than that of Mo_3Si and T2, the creep strength of Mo-Mo_3Si-T2 alloys is likely to decrease as the α-Mo volume fraction increases. The creep strength will also depend on the microstructural morphology—if the α-Mo is distributed as a continuous matrix or "binder" phase instead of isolated particles, the creep strength may be relatively low. However, the microstructural scale is also important. By way of example, nickel-base superalloys consist of narrow (100 nm) γ solid solution channels between γ' (Ni_3Al) particles. Their creep strength is determined by dislocation motion in the channels. It may therefore be beneficial for the creep strength of Mo-Mo_3Si-T2 intermetallics if the continuous α-Mo "channels" are very narrow, e.g., 100 nm. Such narrow channels might also be beneficial for room temperature toughening. Many bcc materials such as Mo or FeAl tend to fracture in a relatively brittle manner by cleavage. However, if the size scale of the FeAl phase is small enough, e.g., on the order of 1 μm, ductile failure is observed in FeAl/TiC composites [14]. This is because the dislocation pile-ups in the FeAl ligaments cannot become long enough to nucleate cleavage fracture. Molybdenum ligaments in Mo-Mo_3Si-T2 materials may behave in the same manner if they are sufficiently thin.

This introduction shows that many different factors need to be considered in the design of Mo-Mo_3Si-T2 intermetallics. While oxidation resistance is a very important factor in their design, this particular paper will focus exclusively on the design of the mechanical properties by controlling the scale and topology of the microstructure, as well as by improving the mechanical properties of the toughening α-Mo phase.

EXPERIMENTAL

The alloys in this work were prepared by arc-melting of elemental starting materials in a partial pressure of argon (70 kPa) on a water-cooled copper hearth. The purity of the starting materials Mo, Si and B was

99.95, 99.99, and 99.5 weight % (wt%), respectively. Some alloys were microalloyed with high-purity Ti or Zr. Unless stated otherwise, alloy compositions will be stated in atomic % (at. %). The alloys were re-melted several times in order to improve their homogeneity. Some alloys were drop-cast into cylindrical water-cooled copper molds with diameters of 12.5 or 25 mm. When the alloys were examined in the cast and annealed condition, their annealing treatment was 24 hours at 1600°C in vacuum at a pressure of approximately 10^{-4} Pa. Several as-cast alloys were crushed into powders with sizes ranging from <50 to 230 μm. In a recently developed approach, the surfaces of the crushed Mo-Si-B powders were "coated" with a thin (e.g., 10 μm) layer of Mo by removing Si via vacuum annealing [15]. The powders were consolidated by hot isostatic pressing (HIPing) in evacuated Nb cans. The HIPing conditions were 4h at a temperature of 1600°C and a pressure of 200 MPa.

Metallography specimens were prepared by grinding, mechanical polishing, and etching in Murakami's reagent. Microstructural examination was carried out by optical microscopy as well as scanning electron microscopy (SEM). The phases were identified by a combination of energy dispersive spectroscopy (EDS) in an SEM, by wavelength-dispersive spectroscopy (microprobe), and powder x-ray diffraction. Images were typically obtained in the backscattered electron (BSE) mode in order to maximize the contrast between the different phases.

Compression specimens with a diameter of 3 mm and a height of 6 mm were electro-discharge machined. Their creep strengths were evaluated from constant displacement rate tests with an initial strain rate of 10^{-5} s^{-1} in flowing argon at 1300°C in an Instron testing machine equipped with a $MoSi_2$ furnace. Button-head tensile specimens with gage diameters and lengths of 3.2 and 12.5 mm, respectively, were machined by grinding to a #8 finish.

For the purpose of screening tests, the fracture toughness K_q was determined from flexure tests with chevron-notched flexure bars with a cross-section of 3×4 mm and a span of 20 mm (see also Fig. 2):

$$K_q = [EG/(1-\nu^2)]^{1/2} \quad , \qquad (1)$$

where E is Young's modulus, $G=W/A$ is the work W expended during fracture divided by the area A swept out by the crack, and ν = Poisson's ratio. The fracture toughness values determined with this technique tend to be higher than those determined with more rigorous techniques. On the other hand, this technique is very simple to implement and is suitable for comparative purposes.

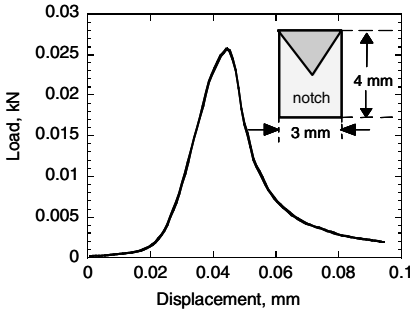

Fig. 2. Determination of K_q from flexure tests with chevron-notched flexure bars.

Precise fracture toughness values were obtained under plane-strain conditions by monotonically loading fatigue-precracked, disk-shaped compact-tension DC(T) specimens to failure. During these tests, crack lengths were periodically monitored using the elastic unloading compliance. Following pre-cracking, specimens were cycled for ~24 hr at the ΔK_{TH} threshold (where there is no discernable crack growth) in an attempt to remove any possible crack bridging in the wake of the pre-crack. The resistance curve (R-curve) behavior was then evaluated by measuring the crack-growth resistance, K_R, as a function of crack extension, Δa.

RESULTS AND DISCUSSION

MICROSTRUCTURES

Figure 3 shows an SEM micrograph of cast and annealed Mo-12Si-8.5B. The α-Mo (bright) has a volume fraction on the order of 40% and appears to be discontinuous.

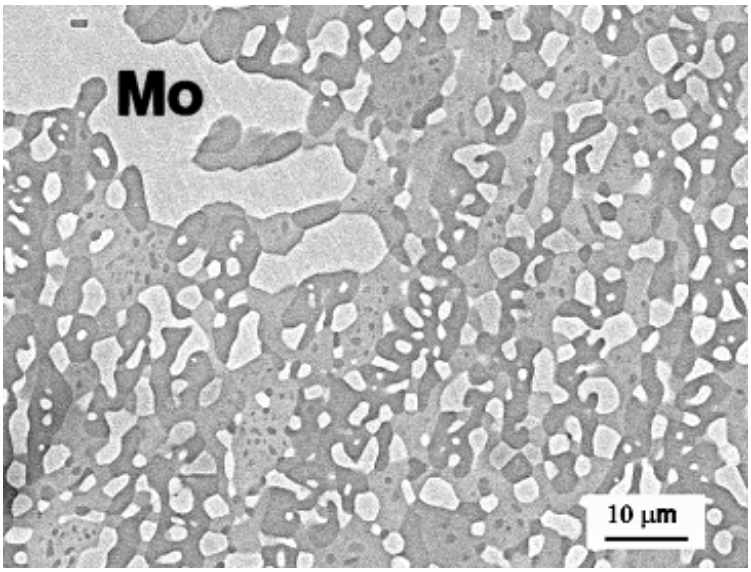

Fig. 3. Cast and annealed Mo-12Si-8.5B. The bright particulate phase is α-Mo.

Table 1 lists the initial powder sizes and the α-Mo volume fraction of four silicide alloys fabricated from Mo-20Si-10B (Mo_3Si/T2) powders by the Si evaporation/HIPing technique [15]. SEM images of the microstructures of the alloys are shown in Fig. 4. In comparing these pictures, it should be kept in mind that their scale markers are different.

Table 1. Mo-Mo_3Si-T2 alloys fabricated by the Si evaporation technique [15].

Specimen designation	Powder size prior to Si removal	α-Mo volume fraction, %
Fine	≤45 μm	34
Medium	45–90 μm	34
Coarse	90–180 μm	49
Medium-low	45–90 μm	5

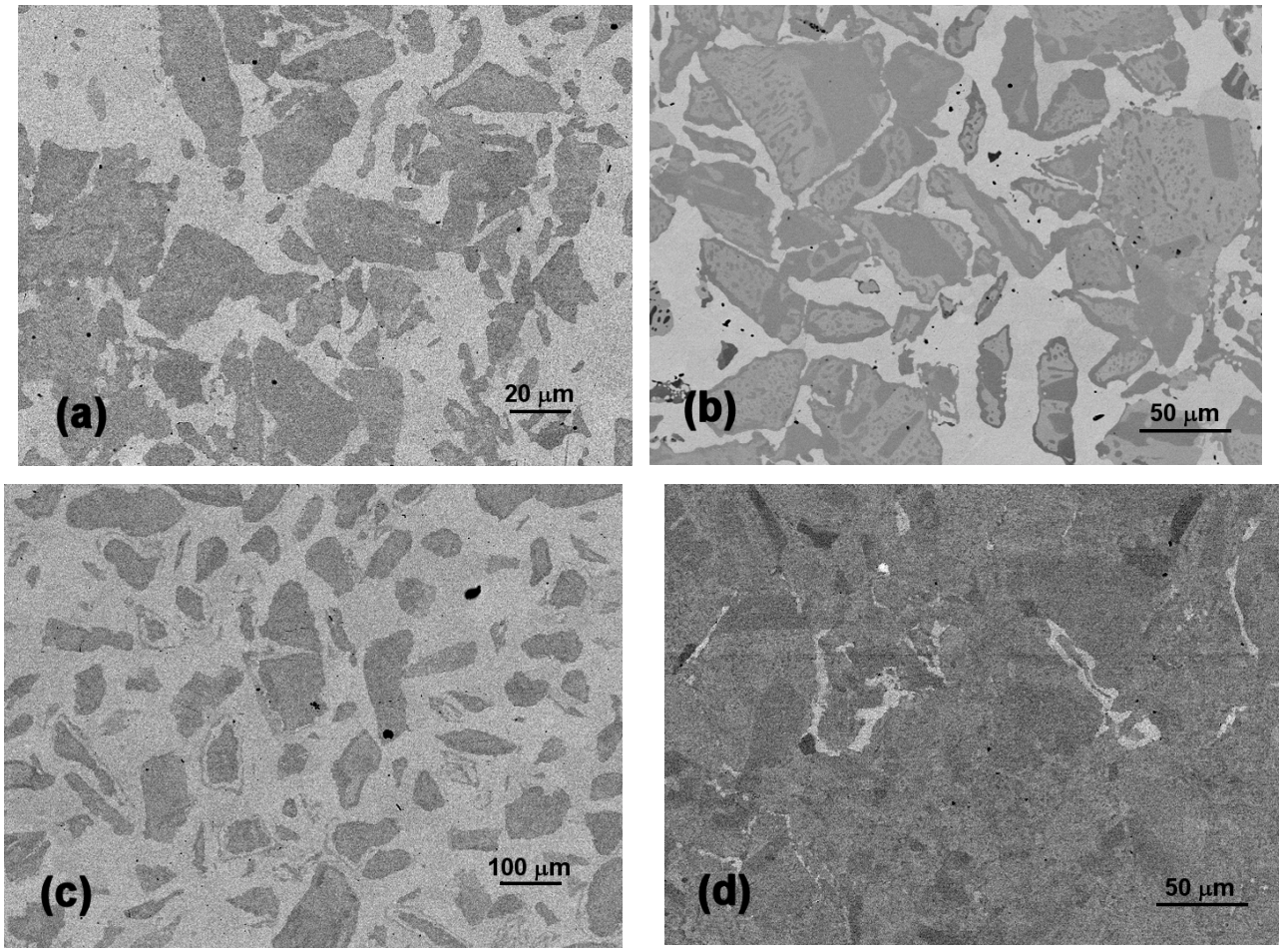

Fig. 4. BSE-SEM micrographs of the Mo-Si-B alloys listed in Table 1: (a) "fine," (b) "medium," (c) "coarse," and (d) "medium-low."

TENSILE STRENGTH AND CREEP STRENGTH

A specimen with the "coarse" microstructure was tested in tension at room temperature. It failed prematurely in a brittle manner at a stress of 140 MPa. At 1200°C in vacuum and an initial strain rate of 3.3×10^{-3} s^{-1}, the 0.2% yield stress was 336 MPa, the maximum stress 354 MPa, and the ductility 1.8%. The low ductility value suggests that the mechanical properties of the α-Mo matrix need to be improved further.

Figure 5 compares the creep strength of cast and annealed Mo-12Si-8.5B with that of the four powder-metallurgically processed alloys. The trends in the data are interpreted as follows. The cast and annealed alloy has the highest creep strength since it exhibits a continuous matrix of strong Mo_3Si/T2. The "fine" alloy is much weaker because of its fine-scale microstructure and the relatively weak continuous α-Mo matrix. Coarsening the microstructure, while keeping the volume fraction constant, improves the creep strength ("medium"). Reducing the α-Mo volume fraction to 5% increases the creep strength only slightly. This result is not well understood since the α-Mo in this alloy ("medium-low") appears to be discontinuous [Fig. 3(d)].

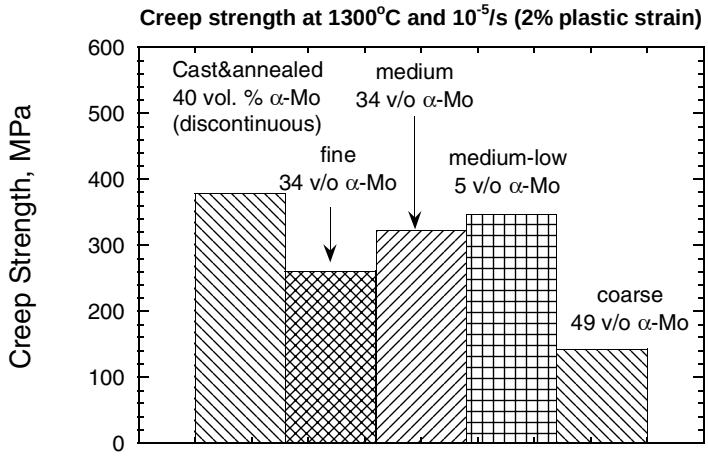

Fig. 5. Creep strength of Mo-Si-B alloys at 1300°C and an initial strain rate of 10^{-5} s^{-1} for different microstructural topologies, scales, and α-Mo volume fractions.

One would therefore expect the creep strength to be higher than that of the cast and annealed alloy with 40 vol.% α-Mo. Finally, the "coarse" alloy is much weaker than any of the other alloys. This is to be expected in view of its high volume fraction of continuous α-Mo.

FRACTURE TOUGHNESS

Figure 6 compares the room temperature R-curves for several Mo-Si-B materials. Cast&annealed Mo-Si-B with an α-Mo volume fraction of approximately 40 vol.% shows only a small increase in crack growth resistance with crack extension. More pronounced R-curve behavior is found for a volume fraction of 34% of continuous α-Mo. This suggests that continuous α-Mo is more effective in providing extrinsic toughening (i.e., crack tip shielding by bridging in the wake of the crack) than discontinuous α-Mo. Finally, when the α-Mo volume fraction is increased to 49%, a high value of the initiation toughness, 12 MPa $m^{1/2}$, and pronounced R-curve behavior are observed. The stress intensity factor reaches a value as high as 21 MPa $m^{1/2}$. This shows clearly that Mo-Si-B alloys with high fracture toughness can be designed.

As pointed out in the introduction, efforts to further increase the fracture toughness (or to maintain a certain value of the fracture toughness while reducing the α-Mo volume fraction) must focus on the mechanical properties of the α-Mo phase. It is well know that microalloying additions of Zr and Ti improve the mechanical properties of Mo alloys. The best-known example is TZM (Mo-0.5Ti-0.1Zr, wt%). Table 2 lists the fracture toughness values of cast and annealed Mo-Si-B alloys in which Mo was partially substituted with additions of Zr (1.5 at. %) do improve the fracture toughness of Mo-Mo_3Si-T2 alloys. Since it is

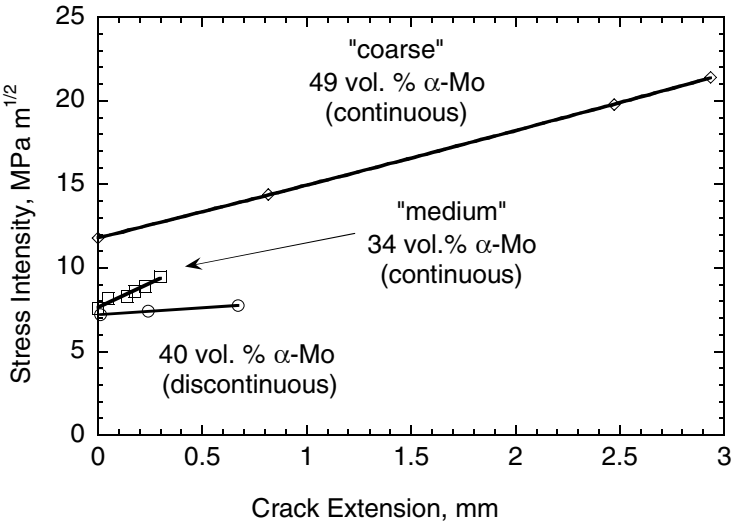

Fig. 6. Room temperature crack growth resistance of Mo-Si-B alloys.

Table 2. Fracture toughness *K*q of Mo-Si-B alloys micro-alloyed with Ti or Zr. K_q was evaluated from Eq. (1) assuming E = 327 GPa and ν = 0.29

	Area of triangle broken during test, mm^2	Absorbed energy, mJ	G, J/m^2	K_q, MPa $m^{1/2}$	K_q, MPa $m^{1/2}$, average ± standard deviation
Mo-12Si-8.5B	2.94	0.68	231	9.1	
"	2.88	0.775	267	9.8	9.0 ± 0.8
"	3.19	0.603	189	8.2	
Mo-12Si-8.5B-1.5Ti	2.86	0.905	317	10.6	10.0 ± 0.8
"	2.81	0.692	246	9.4	
Mo-12Si-8.5B-1.5Zr	3.05	1.575	516	13.6	
"	3.48	1.93	555	14.1	13.5 ± 0.7
"	2.89	1.32	457	12.8	

considered unlikely that the Zr addition improves the fracture toughness of Mo_3Si and T2, Zr acts presumably by improving the mechanical properties of the toughening α-Mo phase.

In the 1960's, Scruggs found that powder-metallurgical Cr is ductilized by addition of MgO particles that transform into $MgCr_2O_4$ spinel particles [16]. Under the Fossil Energy Materials Program, M. P. Brady verified this ductilizing effect [17]. He determined that segregation of detrimental impurities such as nitrogen to the particle-matrix interface is one of the factors responsible for ductilization. Scruggs found that Mo can also be ductilized by adding spinel particles [18]. Nominally pure Mo and Mo-3.4 wt% $MgAl_2O_4$ coupons were prepared by hot-pressing at 1800°C. Figure 7 qualitatively compares their bend ductility. Clearly, the addition of the spinel particles improves the ductility substantially. If Mo-Si-B intermetallics with an α-Mo

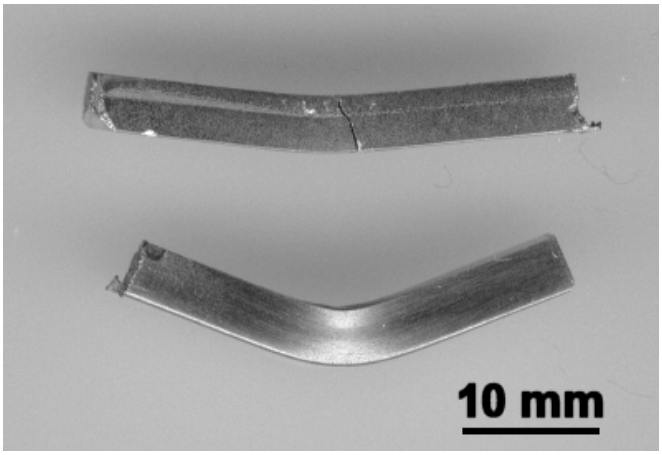

Fig. 7. Qualitative comparison of the room temperature bend ductility of Mo and Mo-3.4 wt% $MgAl_2O_4$.

phase containing spinel particles could be produced, their fracture toughness would be increased due to the increased ductility of the α–Mo phase. It is presently not clear how such a microstructure could be produced. Also, it is not known what particle size and volume fraction would provide the highest ductility increase.

In order to attain satisfactory oxidation resistance, the α-Mo volume fraction in Mo-Si-B intermetallics has to be kept as low as possible. This, in turn, means that the mechanical properties of the α-Mo have to be improved as much as possible. Microalloying with Zr and adding spinel dispersoids present two possible options to achieve that aim.

CONCLUSIONS

Mo-Si-B intermetallics can be processed such that the α-Mo occurs either in the form of discrete particles or as a continuous matrix. The creep strength is seen to depend on the microstructural topology and scale, as well as the α-Mo volume fraction. With 49 vol.% of continuous α-Mo, very high fracture toughness values up to 21 MPa $m^{1/2}$ can be obtained. It is considered very important to further improve the mechanical properties of the α-Mo phase. This will increase its efficiency for providing toughening. In order to achieve a certain value of the fracture toughness, less α-Mo will then be required, with a concomitant improvement in the oxidation resistance. The mechanical properties of α-Mo can be improved by micro-alloying with Zr or by dispersing $MgAl_2O_4$ spinel particles. Future work will examine issues such as the optimum size and volume fraction of the spinel particles and ways to incorporate them in the α-Mo phase of three-phase Mo-Mo_3Si-Mo_5SiB_2 silicides.

ACKNOWLEDGEMENTS

This work was sponsored by the Office of Fossil Energy, Advanced Research Materials (ARM) Program, U.S. Department of Energy, under contract DE-AC05-00OR22725 with Oak Ridge National Laboratory managed by UT-Battelle, LLC. The work of J. J. Kruzic and R. O. Ritchie was supported by the Director, Office of Science, Office of Basic Energy Sciences, Division of Materials Sciences and Engineering of the U.S. Department of Energy under contract No. DE-AC03-76SF00098 with the Lawrence Berkeley National

Laboratory and the multi-National Laboratory program on “Design and Synthesis of Ultrahigh-Temperature Intermetallics” within the DOE Center for Excellence and Processing of Advanced Materials.

REFERENCES

1. www.specialtymetals.com.
2. A. K. Vasudévan and J. Petrovic, “A comparative overview of molybdenum silicide composites,” Mater. Sci. and Engng. A155 (1992) 1–17.
3. M. K. Meyer, M. J. Kramer, and M. Akinca [sic], “Compressive creep behavior of Mo_5Si_3 with the addition of boron,” Intermetallics 4 (1996) 273–281.
4. M. Akinc, M. K. Meyer, M. J. Kramer, A. J. Thom, J. J. Huebsch, and B. Cook, “Boron-doped molybdenum silicides for structural applications,” Intermetallics A261 (1999) 16–23.
5. M. K. Meyer, A. J. Thom, and M. Akinc, “Oxide scale formation and isothermal oxidation behavior of Mo-Si-B intermetallics at 600–1000°C,” Intermetallics 7 (1999) 153–162.
6. H. Nowotny, E. Dimakopoulou, and H. Kudielka, “Untersuchungen in den Dreistoffsystemen: Molybdän-Silizium-Bor, Wolfram-Silizium-Bor und in dem System: VSi_2-$TaSi_2$,” Mh. Chem. 88 (1957) 180–192.
7. D. M. Berczik, United States Patent 5,595,616 (1997), “Method for enhancing the oxidation resistance of a molybdenum alloy, and a method of making a molybdenum alloy.”
8. D. M. Berczik, United States Patent 5,693,156 (1997), “Oxidation Resistant Molybdenum Alloys.”
9. R. Raj and L. R. Thompson, “Design of the microstructural scale for optimum toughening in metallic composites,” Acta Metall. Mater. 42 (1994) 4135–4142.
10. M. F. Ashby, F. J. Blunt, and M. Bannister, “Flow Characteristics of highly constrained Metal Wires,” Acta Metall., 37[7] (1989) 1847–1857.
11. I. Rosales and J. H. Schneibel, “Stoichiometry and mechanical properties of Mo_3Si,” Intermetallics 8 (2000) 885–889.
12. K. Ito, K. Ihara, K. Tanaka, M. Fujikura, and M. Yamaguchi, “Physical and mechanical properties of single crystals of the T2 phase in the Mo-Si-B system,” Intermetallics 9[7] 591–602 (2001).
13. R. D. Field, D. J. Thoma, J. C. Cooley, F. Chu, C. L. Fu, M. H. Yoo, W. L. Hults, and C. M. Cady, “Dislocations in Mo_5SiB_2 T2 Phase,” Intermetallics 9 (2001) 863–868.
14. R. Subramanian and J. H. Schneibel, “The Ductile-Brittle Size Transition of Iron Aluminide Ligaments in an FeAl/TiC Composite,” Acta Materialia, 46[13] (1998) 4733–4741.
15. J. H. Schneibel, M. J. Kramer, and D. S. Easton, “A Mo-Si-B intermetallic alloy with a continuous α-Mo matrix,” Scripta Materialia 46 (3) (2002) pp. 217–221.
16. D. M. Scruggs, L. H. Van Vlack, and W. M. Spurgeon, J. Amer. Ceram. Soc. 51 (1968) 473.

17. M. P. Brady, I. M. Anderson, M. L. Weaver, H. M. Meyer, L. R. Walker, M. K. Miller, D. J. Larson, I. G. Wright, V. K. Sikka, A. Rar, G. M. Pharr, J. R. Keiser, and C. A. Walls, “Nitrogen impurity gettering in oxide dispersion ductilized chromium,” accepted for publication in Materials Science and Engineering A.
18. D. M. Scruggs, “Ductile tungsten composition containing a spinel dispersed uniformly throughout,” United States Patent 3,320,037, Patented May 16, 1967.

UNDERSTANDING DAMAGE MECHANISMS IN FERRITIC/MARTENSITIC STEELS

R. W. Swindeman and P. J. Maziasz
Oak Ridge National Laboratory
M. J. Swindeman
Stress Engineering Services, Inc., Mason, OH

INTRODUCTION

Advanced ferritic/martensitic steels are being used extensively in fossil energy applications. New steels such as 2 1/4Cr-W-V (T23, T24), 3Cr-W-V, 9Cr-Mo-V (T91), 7Cr-W-V, 9Cr-W-V (T92 and T911), and 12Cr-W-V (T122, SAVE 12, and NF12) are examples of tubing being used in boilers and heat recovery steam generators (1). Other products for these new steels include piping, plates, and forgings. There is concern about the high-temperature performance of the advanced steels for several reasons. First, they exhibit a higher sensitivity to temperature than the 300 series stainless steels that they often replace. Second, they tend to be metallurgically unstable and undergo significant degradation at service temperatures in the creep range. Third, the experience base is limited in regard to duration. Fourth, they will be used for thick-section, high-pressure components that require high levels of integrity. To better understand the potential limitations of these steels, damage models are being developed that consider metallurgical factors as well as mechanical performance factors. Grade 91 steel was chosen as representative of these steels for evaluation of cumulative damage models since laboratory and service exposures of grade 91 exceed 100,000 hours.

CUMULATIVE DAMAGE MODEL SELECTION

Of the many cumulative damage models that have been proposed over the years, four were selected for this comparison. The models include the Life Fraction (LF), which is time-based and often identified as Robinson's rule (2), the Monkman-Grant (MG), which makes use of the observed correlation between rupture life and creep rate (3), the API-MPC Omega method (OM), which is based on tertiary creep behavior (4) and is often used for fitness-for-service evaluations (5), and Dyson's Continuing Damage Mechanics (CDM) model, which is representative of models that incorporate specific damage mechanisms (6).

The LF model is, by far, the easiest method to use. One only needs knowledge of the component history and temperature-stress-life relationship derived from uniaxial tests at constant conditions. A damage factor, D_{LF}, ranging from zero to one is calculated by summing the life fraction used at each service condition:

$$D_{LF} = \Sigma\, t_i/tr_i$$

where t_i is the time at any temperature and stress and tr_i is the time to rupture at that temperature and stress. The remaining life fraction is (1-D). The order of summing is not important. The time to rupture for each service condition may be interpolated from isothermal stress-rupture correlations for a specific heat, calculated from a stress-temperature-life parametric fit to the specific heat, or interpolated from parametric curves representing the average strength properties for the steel. A consistent multiaxial stress criterion is necessary but creep rate data are not needed.

The MG model requires that a sample be extracted from the exposed material and subjected to a creep test at a temperature and stress within the range of interest. The observed minimum creep rate (mcr) can then be used to estimate the rupture life, t_r, from a simple correlation for the material:

$$t_r = A\ mcr^p$$

where A and p are experimentally determined materials parameters. Here, it is assumed that A and p do not vary with temperature and stress. A multiaxial stress criterion must be assumed.

The development of the OM model was reviewed by Prager (4) who cites six capabilities of the model that include the prediction of the creep curve, application to specific heats, prediction of remaining life without knowledge of history, generalization to multiaxial stress states, selection of benchmark tests for conditions close to service conditions, and incorporation in finite element analysis. The Omega concept may be expressed in several ways, but to be consistent with the notion of life fraction or damage parameter, D_{OM}:

$$D_{OM} = \dot{e}\ \Omega\ t\ /\ (1 + \dot{e}\ \Omega\ t)\ ,$$

where $\dot{e}$ is creep rate based on true stress and true strain, t is service time, and Ω is a "materials creep damage susceptibility parameter." The Ω parameter represents the combined effect of area change due to deformation, strain-softening, cavitation, and any other mechanism that could lead to an increased creep rate with increasing time or strain such that:

$$\dot{e} = \dot{e}_o \exp(\Omega e)\ ,$$

where $\dot{e}_o$ is the initial creep rate. The integration of this equation produces a rupture life. The OM only considers tertiary creep. If primary creep is observed, the initial creep rate will not correspond to $\dot{e}_o$. It is expected that the API 579 document will provide Ω values for a service exposed material.

THE CDM MODEL

A mechanistic approach to damage has been taken by Dyson (6). His model has been developed to include three categories of damage: strain-induced, thermally-induced, and environmentally-induced. In each category, specific damage mechanisms are identified and formulations for the damage parameter,

damage rate, and strain rate are identified. In the strain-induced damage category, for example, four subcategories are identified: creep-constrained cavity-nucleation, creep-restrained cavity-growth, dynamic subgrain growth, and multiplication of mobile dislocations. In the thermally-induced category, Dyson introduces particle coarsening and the depletion of solid-solution elements. In the environmentally-induced category, two subcategories have been proposed: fracture of surface corrosion products and internal oxidation. In the model, the creep rate at any instant ($\dot{e}$) is given by:

$$\dot{e} = \dot{e}_o \sinh (\sigma/\sigma_0) \ ,$$

where $\dot{e}_o$ and σ_0 are composite parameters that contain several microstructural parameters that reflect up to eight more-or-less independent damage mechanisms. Typical materials parameters that are required to use the DM include grain size, a cavitation constant, subgrain radius, dislocation density, particle spacing, a rate constant for particle coarsening, the concentration of solute strengthen elements, a rate constant for particle precipitation, a rate constant for corrosion, Clearly, for alloys such as Grade 91, several damage mechanisms will be active. The parametric constants for the Dyson model have not been formulated for Grade 91 to date, so this model will not be exercised here.

DAMAGE EVALUATIONS FOR GRADE 91

Three damage conditions were selected for evaluation. The first condition was produced by simple laboratory aging. Here, blocks of material that were exposed to temperatures in the range of 482 to 704C for times in the range of 5,000 to 75,000 hours (7). Specimens from the aged blocks were tested under relatively long time creep conditions and the results evaluated in terms of the predictions of the three of the models mentioned above. The second condition was produced by service exposure in a power boiler. Superheater tubing was removed after 116,000 and 143,000 hours and specimens from the tubing were tested at various stresses and temperatures. The third condition was produced by long-time creep testing that was interrupted for testing at higher temperatures and stresses.

To examine the use of these models, an evaluation was undertaken of the influence of the conditions mentioned above on the rupture life at 600°C and 100 MPa. The material model that formed the basis of the allowable stresses in the ASME Boiler and Pressure Vessel Code sets the average life for 600°C and 100 MPa to be close to 84,000 hours. The first condition examined was a sample aged 10,000 hours at 649°C. Based on the Zener-Hollomon parameter, this condition is comparable to exposure for 100,000 hours at 600°C. The creep life of the aged specimen was estimated as 30,000 hours. The LF damage model would predict no loss in life for aged specimens while results show that 65% of the life was lost just due to thermal aging. The OM damage model estimates life of to be around 33,000 hours. This is a conservative estimate relative to the estimated life based on the trend of ASME Code allowable

stress, and suggests that the OM model accounts for some thermal aging effects. The MG, which is based on the measured creep rate of the aged sample and the MG parametric constants averaged for the as-tempered condition, predicted a life of 26,000 hours. Similar to the OM model, this time is roughly comparable to the actual life of the aged specimen. Turning to the specimens service-exposed for 116,000 hours at 560°C and 34 MPa hoop stress, the damage estimated by all three models is negligible. The post-service uniaxial rupture life was 14870 hours for 600°C and 100 MPa. Again, the LF model estimated 84,000 and the OM model estimated 32,700 hours. The MG model, on the other hand, estimated 12,800 hours. The third condition examined involved long-time laboratory creep tests that are in progress. Specimens of two different heats were each exposed to 538°C and 165 MPa for approximately 85,000 hours. For these conditions, the life is expected to be about 425,000 hours using the Code values and 87,500 from the OM model. Both specimens were then tested at 600°C and 100 MPa. Testing times have exceeded 4,000 hours. The LF model predicts a remaining life of 67,000 hours while the OM model predicts failure in less than 2,000 hours. The MG model predicts 42,000 and 55,000 for the two tests.

It is clear that wide ranges in predicted life can be expected when long-time, high-temperature exposures are evaluated from models that are largely based on short-time test results. Additional testing is underway that involves specimens exposed to long-time creep. Detailed metallurgical characterization is underway to better understand the evolution of the parametric values in the damage equations. As this information develops, the predictions of the Dyson model will be attempted.

REFERENCES

1. R. Viswanathan and W. T. Bakker, *Materials for Ultrasupercritical Fossil Power Plants*, TR-114750, EPRI, Palo Alto, CA, February, 2000.
2. E. L. Robinson, “Effect of Temperature Variation on the Creep Strength of Steel,” *Trans. ASME*, 1938, vol. 60, p. 253–259.
3. F. C. Monkman and N. J. Grant, *Proc. ASTM*, 1956, vol 56, p. 593.
4. M. Prager, “The Omega Method-An Engineering Approach to Life Assessment,” *J. Pressure Vessel Technology*, 2000, Vol. 122, No. 3, 273–280.
5. Anon., *Recommended Practice for Fitness-for-Service, API 579*, American Petroleum Institute, 1220 L Street, N.W., Washington, D.C., USA, 1997.
6. B. Dyson, “The Use of CDM in Materials Modeling and Component Creep Life Prediction,” *J. Pressure Vessel Technology*, 2000, Vol. 122, No. 3, 281–296.

7. C. R. Brinkman, D. J. Alexander, and P. J. Maziasz, “Modified 9Cr-1Mo Steel for Advanced Steam Generator Applications,” paper 90-JPC/NE-8, presented at the *Joint ASME/IEEE Power Generation Conference*, Boston, Massachusetts, USA, October 21–25, 1990.

CONCEPTS FOR SMART PROTECTIVE HIGH-TEMPERATURE COATINGS

P. F. Tortorelli, M. P. Brady, I. G. Wright, and B. A. Pint
Oak Ridge National Laboratory

INTRODUCTION

Environmental resistance is a critical material barrier to the operation of fossil systems with the improved energy efficiencies and environmental performance described by the goals of the Vision 21 concept of the U.S. Department of Energy's Office of Fossil Energy. All fossil fuel-derived processes contain reactive species and high-temperature degradation arising from reactions of solids with gases and condensable products often limits performance or materials lifetimes such that efficiency, emission, and/or economic targets or requirements are not realized. Therefore, historically, the development of materials for fossil-fuel combustion and conversion systems has been closely linked to corrosion studies of alloys and ceramics in appropriate environments. This project is somewhat different from such studies in that it focuses on the feasibility of new routes to controlling the critical chemical and mechanical phenomena that collectively form the basis for environmental protection in relevant fossil environments by exploring compositional and microstructural manipulations and cooperative phenomena that have not necessarily been examined in any detail to date. This can hopefully lead to concepts for "smart" coatings or materials that have the ability to sense and respond appropriately to a particular set or series of environmental conditions in order to provide high-temperature corrosion protection.

The strategies being explored involve cooperative or in-place oxidation or sulfidation reactions of multiphase alloys.[1,2] The first material systems to be evaluated involve silicides as there is some evidence that such materials have enhanced resistance in oxidizing-sulfidizing and sulfidizing environments and in air/oxygen at very high temperatures.[3] In this regard, molybdenum silicides may prove to be of particular interest. Molybdenum is known to sulfidize fairly slowly[4] and there has been recent progress in developing Mo-Si-B systems with improved oxidation resistance at high and intermediate temperatures.[5–11] Consequently, Mo-Si-B alloys with different compositions and phase morphologies were oxidized in dry air at 1200°C under cyclic oxidation conditions. In addition, elevated-temperature oxidation-sulfidation exposures of Mo-Mo_5SiB_2-Mo_3Si alloys were also conducted. In this way, the specific effects of the multiphase nature (composition, morphology) of the Mo-Si-B system on protective product formation are being evaluated.

DISCUSSION OF CURRENT ACTIVITIES

Automated cyclic oxidation exposures were conducted on an α-Mo-Mo_5SiB_2-Mo_3Si alloy (from within the 3-phase field labeled "1" in Fig. 1) in dry, flowing O_2 at 1200°C using a cycle consisting of 60 min at temperature and 10 min out of the furnace. Duplicate specimens of the α-Mo-Mo_5SiB_2-Mo_3Si α-Mo-Mo_5SiB_2-Mo_3Si composition were attached to alumina rods with Pt-Rh wires and mass changes were typically measured after 1, 5, 40, 60, 80, and 100 cycles and then every 100 cycles using a Mettler model AG245 balance. The resulting gravimetric data are shown in Fig. 2, which also contains data from compositions based on the phase fields denoted as "2" and "3" in Fig. 1.[12,13] The specimens containing α-Mo showed a substantial mass loss for the first thermal cycle. Subsequently, only modest changes in specimen mass were measured. In fact, after the first cycle, the rates of mass change of the two α-Mo-Mo_5SiB_2-Mo_3Si specimens were equivalent to and less than those measured for the T1-Mo_5SiB_2-Mo_3Si coupons and not much different than that of the $MoSi_2$-containing alloy (Fig. 2). Such observations suggest a multistage mechanism in which the Mo is rapidly removed by formation of volatile MoO_3 and the resulting near-surface enrichment in silicon and boron facilitate the formation of a protective borosilicate or silica layer that grows laterally to seal the remaining Mo-rich areas of the alloy from the environment.[9] Results from short-term cyclic oxidation experiments were consistent with this interpretation—see, as an example, Fig. 3, which shows that the initial mass loss was dependent on the

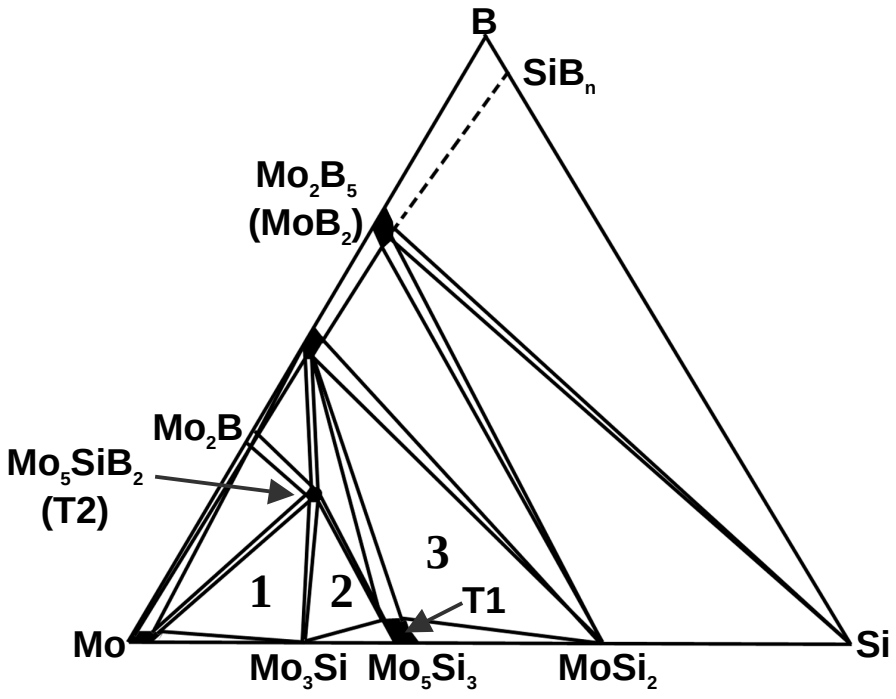

Fig. 1. A schematic Mo-Si-B phase diagram based on Nowotny et al., 1957.

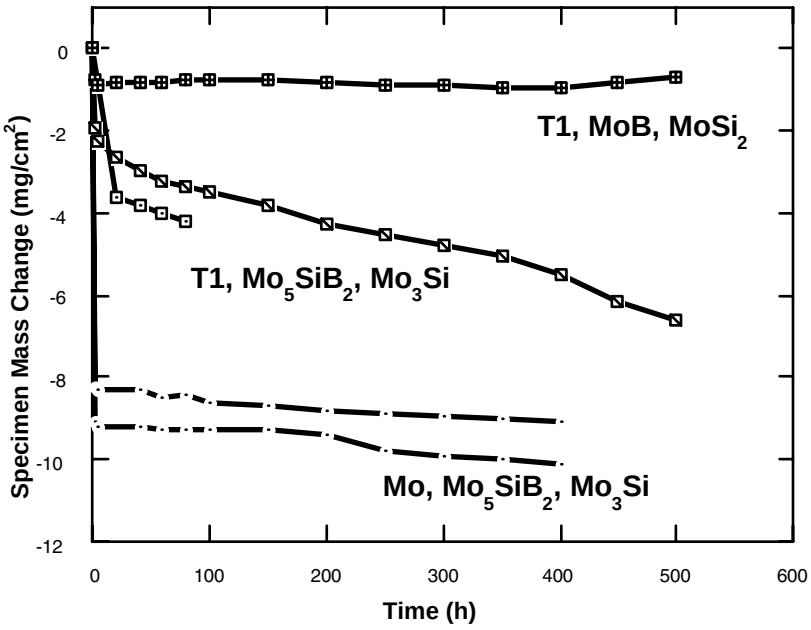

Fig. 2. Specimen mass change of Mo-Si-B alloys as a function of time at 1200°C for 1-h thermal cycles

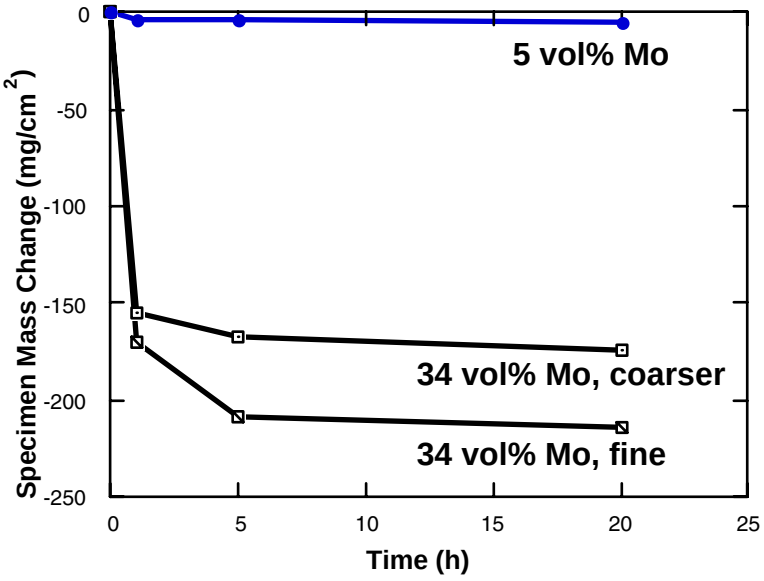

Fig. 3. Specimen mass change of Mo-Si-B alloys as a function of time at 1200°C for 1-h thermal cycles,[10] Fine and coarser refer to size of Mo phase in the 34vol% Mo alloys. See ref. 10 for examples of these microstructures.

starting Mo concentration and that the onset of protective behavior was indeed very rapid. This type of process suggests that the oxidation behavior of this multiphase system can possibly be controlled by finely dispersing not only the most active phase (α-Mo), but also the most Si-rich component, which can act as a source for silicon during oxidation,[11] based on the concepts of cooperative oxidation phenomena.[1,14] In this regard, Mo-Mo_5SiB_2-Mo_3Si alloys with a fine-scale microstructure have been shown to have significantly better oxidation resistance than similar compositions with a coarser phase dispersion.[10,11] However, the cyclic oxidation results shown in Fig. 3 do not show a significant difference between the behavior of two Mo-Mo_5SiB_2-Mo_3Si alloys that have the same Mo content (34%) but a fine and coarser microstructure, respectively. Accordingly, it is not presently clear whether manipulation of phase sizes to increase the oxidation resistance of these Mo-Si-B alloys will be effective (or practical, given that the need for improved fracture toughness appears to necessitate a coarser Mo phase [10]).

A preliminary evaluation of the sulfidation resistance of α-Mo-Mo_5SiB_2-Mo_3Si alloys was conducted by isothermally exposing specimens to an H_2-H_2S-H_2O-Ar gas mixture at 800°C for 100–150 h. At this temperature, the gas composition yielded a p_{S_2} of ~10^{-6} atm and a p_{O_2} of ~10^{-22} atm. This environment represents severe coal gasification conditions, but has been used previously to evaluate the corrosion of the most sulfidation-resistant alloys.[15,16] Furthermore, calculations based on equilibrium thermodynamics predict that Mo-Si alloys should form SiO_2 and MoS_2 under these conditions (Fig.4).

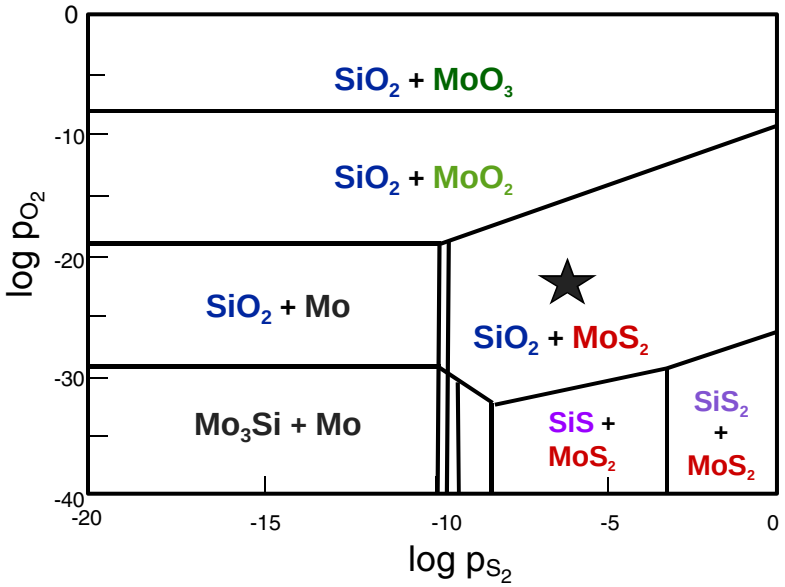

Fig. 4. Calculated product stability diagram for Mo-Si as a function of the partial pressures of oxygen and sulfur. The star represents partial pressures of H_2-H_2S-H_2O-Ar gas mixture used for oxidation-sulfidation exposures at 800°C.

The gravimetric results are shown in Fig. 5, which also includes typical data for a very sulfidation-resistant alloy, Fe_3Al,[15,17] another alumina-former (FeCrAl), and a model austenitic stainless steel (based on the nominal Cr and Ni concentrations of type 310). The different α-Mo-Mo_5SiB_2-Mo_3Si specimens (same Mo concentration, 34 vol%, but differing coarseness of the microstructure) showed similar gravimetric behavior representative of very good sulfidation resistance. Scanning electron microscopy of the as-exposed surfaces indicated only thin corrosion products (Fig. 6). (Little spallation was observed.) Because of the limited volume of these products, x-ray diffraction could not definitively determine their compositions, but it was apparent that some sulfides had formed. Interestingly, as shown in Fig. 6, the various phases appeared to react with the environment independently of each other. It therefore appears that, under the current oxidation-sulfidation exposure conditions, the α-Mo-Mo_5SiB_2-Mo_3Si alloys exhibit the "in-place" (or "independent") mode of multiphase oxidation.[1] Therefore, within the range of phase sizes investigated in this study, it is expected that the coarseness of the phase distribution should not have a major effect on corrosion behavior and this is what is observed in the gravimetric results (Fig. 5b).

If confirmed by more comprehensive analytical work and exposures in aggressive varying environments, the knowledge gained about the different modes of reaction under oxidizing and oxidizing/sulfidation conditions (cooperative versus in-place, see above) will be used to help explore

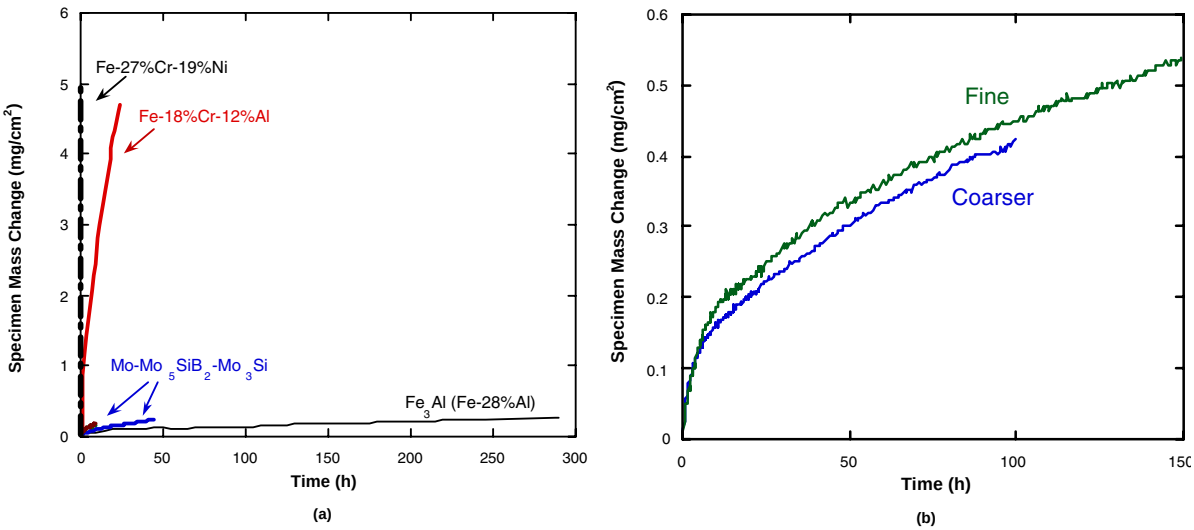

Fig. 5. Mass change versus time for exposures of Mo-Mo_5SiB_2-Mo_3Si, a stainless steel model alloy (Fe-27%Cr-19%Ni), and a FeCrAl (concentrations in at.%) to H_2-H_2S-H_2O-Ar at 800°C. (b) replots Mo-Mo_5SiB_2-Mo_3Si data of (a) with expanded ordinate scale. "Coarser" and "fine" refer to respective sizes of the phases in the Mo-Mo_5SiB_2-Mo_3Si alloys.

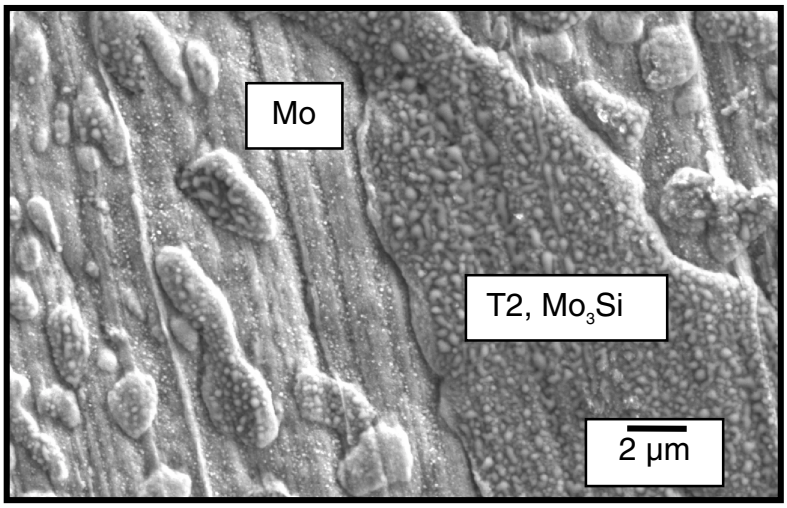

Fig. 6. Scanning electron micrograph of the surface of a specimen of Mo-Mo_5SiB_2-Mo_3Si after exposure to H_2-H_2S-H_2O-Ar at 800°C for 150 h.

phase and composition manipulations in the Mo-Si-B system in order to evaluate the possibilities of developing such alloys as smart protective coatings. Other multiphase alloys will also be examined for such coating applications based on opportunities to improve corrosion resistance through microstructure/geometric effects and alteration of subsurface depletion paths.[2]

SUMMARY

Smart protective coatings may provide one of the breakthrough areas to overcome materials barriers imposed by the requirements of advanced fossil energy systems. To this end, multiphase molybdenum silicides are being examined as the first attempt in evaluating smart coating concepts for high-temperature corrosion resistance in fossil environments. The present work confirmed that Mo-rich, B-containing silicides can have adequate oxidation resistance at high temperature. Also, preliminary results showed that these silicides have excellent high-temperature sulfidation resistance.

REFERENCES

1. F. Gesmundo and B. Gleeson, *Oxid. Met.* **44** (1995) 211–37.
2. M. P. Brady, B. Gleeson, and I. G. Wright, *JOM* **52** (2000) 16–21.
3. M. P. Brady, B. A. Pint, P. F. Tortorelli, I. G. Wright, and R. J. Hanrahan Jr., Chapter 6 in *Corrosion and Environmental Degradation of Materials*, M. Schütze (eds.), Wiley-VCH, Weinheim, Germany, 1999.
4. S. Mrowec, *Oxid. Met.* **44** (1995) 177–209.
5. M. K. Meyer and M. Akinc, *J. Am. Ceram. Soc.* **79** (1996) 938–944.

6. D. M. Berczik, “Oxidation Resistant Molybdenum Alloys,” U.S. Patent, 5,693,156, 1997.
7. M. K. Meyer, A. J. Thom, and M. Akinc, *Intermetallics* **7** (1999) 153–62.
8. K. Natesan and S. C. Deevi, *Intermetallics* **8** (2000) 1147–58.
9. M. G. Mendiratta, T. A. Parthasarathy, and D. M. Dimiduk, *Intermetallics* **10** (2002) 225–32.
10. J. H. Schneibel, P. F. Tortorelli, M. J. Kramer, A. J. Thom, R. O. Ritchie, and J. J. Kruzic, paper BB.2 in *Defect Properties and Related Phenomena in Intermetallic Alloys*, E. P. George, H. Inui, M. J. Mills, and G. Eggeler (eds.), The Materials Research Society, Pittsburgh, 2002.
11. V. Supatarawanich, D. R. Johnson, and C. T. Liu, *Mater. Sci. Eng. A* **344** (2003) 328–39.
12. P. F. Tortorelli, B. A. Pint, K. L. More, A. J. Thom, and M. Akinc, *ORNL Fossil Energy Program Annual Report for April 2000 to March 2001*, R. R. Judkins and P. T. Carlson (eds.), ORNL/TM-2001/89, July 2001, www.ornl.gov/fossil.
13. P. F. Tortorelli, M. P. Brady, I. G. Wright, and B. A. Pint, *ORNL Fossil Energy Program Annual Report for April 2001 to March 2002*, R. R. Judkins and P. T. Carlson (eds.), ORNL/TM-2002/122, July 2002, www.ornl.gov/fossil.
14. G. Wang, B. Gleeson, and D. L. Douglass, *Oxid. Met.* **35** (1991) 333–48.
15. J. H. DeVan and P. F. Tortorelli, *Mater. at High Temp.* **11** (1993) 30–35.
16. K. Natesan and P. F. Tortorelli, pp. 265–80 in *Nickel and Iron Aluminides: Processing, Properties and Applications*, S. C. Deevi, V. K. Sikka, P. J. Maziasz, and R. W. Cahn (eds.), ASM International, Materials Park, OH, 1997.
17. J. H. DeVan, pp. 107–15 in *Oxidation of Intermetallics*, T. Grobstein and J. Doychak (eds.), TMS, Warrendale, PA, 1989.

ODS ALLOY DEVELOPMENT

I. G. Wright, B. A. Pint, and C. G. McKamey
Oak Ridge National Laboratory

INTRODUCTION

The overall goal of this project is to facilitate the exploitation of oxide dispersion-strengthened (ODS) alloys. The main barriers to the wider use of these alloys are the fact that they cannot be joined by conventional techniques; they have highly-directional mechanical properties: in particular, for extruded tubes with present processing the creep strength in the transverse direction typically is significantly lower than that in the axial direction; these alloys have unusual mechanical behavior, in that their high sensitivity to strain rate results in a mode of creep failure that is different from conventional high-temperature alloys; and, because a powder metallurgical route is required for their fabrication, these alloys are expensive.

There are several options being explored to overcome these barriers. For joining, unconventional approaches including inertia welding and transient liquid phase (TLP) bonding are being examined. For modification of the mechanical properties, innovative processing routes are being explored that have the potential to produce the desired microstructure. In addition, the alloy properties and characteristics are being quantified, where possible, so that there are no surprises for designers and engineers looking to use these alloys.

Approaches taken in this project involve studies to understand and quantify all available routes for joining these alloys, including the cases where it is unlikely that the joints will exhibit a very high fraction of the original metal strength. Other studies are aimed at developing a mechanistic understanding of how to control the alloy microstructure, so that the necessary parameters can be readily translated from laboratory to production-sized processing. As a way of quantifying the temperature limits of the alloys, studies are aimed at understanding the mechanism(s) of the oxidation behavior of these alloys to facilitate the development of an analytical life prediction model.

The reason for the interest in ODS alloys is summarized in Fig. 1 which was derived from the data of Starr and Shibli[(1)] and compares the average 100kh stress rupture strength for all available wrought or cast high-temperature alloys with the theoretical maximum rupture strength that could be obtained if the strengthening mechanisms used were fully optimized. The diagram also indicates the range of strength required for ultra-supercritical steam conditions (relatively low temperature, high pressure) and for high-temperature heat exchangers for indirect-fired duty cycles (very high temperatures, relatively low pressures), from which it is seen that the capabilities of the current high-temperature alloys are marginal for both applications. The typical longitudinal stress rupture strength for ODS-FeCrAl alloys, also shown

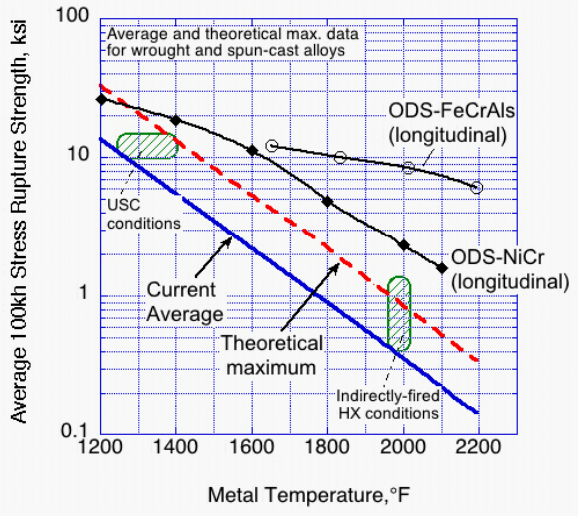

Fig. 1. Schematic comparison of the current average and theoretical maximum creep strength of current high-temperature alloys (after Starr and Shibli, 2000).

on the diagram, illustrates their strength advantage. Essentially, ODS alloys have potential for use to temperatures where otherwise ceramic materials would have to be considered. In addition, the ODS-FeCrAl alloys have excellent oxidation resistance due to the formation of a protective alumina scale, which confers excellent resistant to oxidation in air and steam, and to sulfidation. The efforts reported here are coordinated with those in Office of Fossil Energy's Advanced Research Materials (ARM) programs at the University of California at San Diego,[2] University of Liverpool,[3] and at Foster Wheeler Inc.[4] In addition, the efforts support a Vision 21 program conducted by Special Metals Inc. intended to increase the transverse creep rupture strength of an ODS ferritic alloy, MA956.[5] Approaches taken and results derived from efforts in other programs, in particular the European COST programs,[6] also are noted in planning the effort on this program. The alloys of interest are the commercial ferritic ODS alloys: MA956, MA956H, and PM2000; in addition an ORNL-developed alloy (ODS-Fe_3Al) is included, as well as an alloy used in an earlier European COST program for an externally-fired heat exchanger,[7] Dour Metal ODM751. A non-ODS, powder metallurgy-produced FeCrAl alloy (Kanthal APM) is included in the program as an oxidation comparator. The nominal compositions of these alloys are shown in Table 1.

Table 1. Compositions of the ferritic ODS alloys of interest (in wt%)

Alloy	Fe	Al	Cr	Mo	Ti	Dispersoid
ODS-Fe_3Al	Bal.	15.9	2.2		0.07	Y_2O_3
MA956H	Bal.	5.77	21.66		0.40	Y_2O_3
MA956	Bal.	4.46	19.64		0.39	Y_2O_3
PM2000	Bal.	5.5	20		0.5	Y_2O_3
ODM751	Bal.	4.5	16.5	1.5	0.6	Y_2O_3
Kanthal APM	Bal.	5.5	20		0.03	None

The focus of this paper is on the recent efforts on joining these alloys, as well as identification of their temperature limits in terms of oxidation behavior.

DISCUSSION OF CURRENT ACTIVITIES

JOINING OF ODS ALLOYS

The challenges faced in joining ODS alloys are that the processes used must avoid (1) redistributing the Y_2O_3 dispersed phase, which will float out of the alloy if it is fused, and (2) changing the grain size, shape, and orientation in the alloy microstructure. As a result, fusion processes are probably a last resort, although laser welding (which minimizes the size of the fused zone) has been used successfully for bonding sheet,[8] and brazing has been explored in the European COST-522 program for joining tubes.[6,9] Friction welding was shown earlier in this program[10] to result in distortion of the microstructure in the region of the joints formed on rod-shaped specimens, the effect of which was to degrade the creep strength in that area. Further investigation of a version of friction welding (inertia welding) reported here used tubes of MA956 and was intended to quantify the effect of the more symmetrical distortion of the microstructure expected for tube walls. Diffusion bonding using a TLP approach was successfully demonstrated in the HiPPS program for a Ni-Cr-based ODS alloy that forms a chromia scale.[11] Studies to extend this concept to the more difficult case of the alumina-forming FeCrAl ODS alloys is underway, and preliminary results are reported here. Further, progress has been made in a plasma-assisted diffusion bonding technique by the MER Corporation of Tucson, Arizona, and a detailed characterization of such joints also is reported.

Inertia welding of MA956 tubes: As-extruded, un-recrystallized tubes of MA956, with an outside diameter of 63.5 mm, and 7 mm wall thickness, were supplied to Interface Welding Inc., of Carson City, California for inertia welding trials. In this process, one section of tube is fixed in the hub of a large flywheel, while the section to which it is to be joined is attached to a rigid frame and aligned such that it will mate exactly with the section attached to the flywheel, as the flywheel is advanced. The process involves spinning up of the flywheel to a given speed, after which it is uncoupled from the drive and advanced with a known force until the tube attached to the flywheel encounters the rigidly-held section of tube in the frame. The energy from the momentum of the flywheel is dissipated by friction between the two sections of tube as the flywheel is held with the two tube sections in contact. The processing parameters were determined based on the integrity of the joints as judged in bend tests of coupons cut from the joined tubes. Sequences in the processing are illustrated in Fig. 2. The reproducibility of the parameters measured during joining was found to be excellent, and a number of samples of joined tube was produced for evaluation. A preliminary examination of the microstructure of the joint indicated that the deformation was confined to a relatively small zone near the joint, and that the demarcation between highly-deformed material and material exhibiting the normal microstructure following extrusion was very sharp. This is illustrated in Fig. 3, which shows a cross section at the tube outer surface near the joint for a sample that had been re-crystallized following joining. A more detailed examination of the joints by

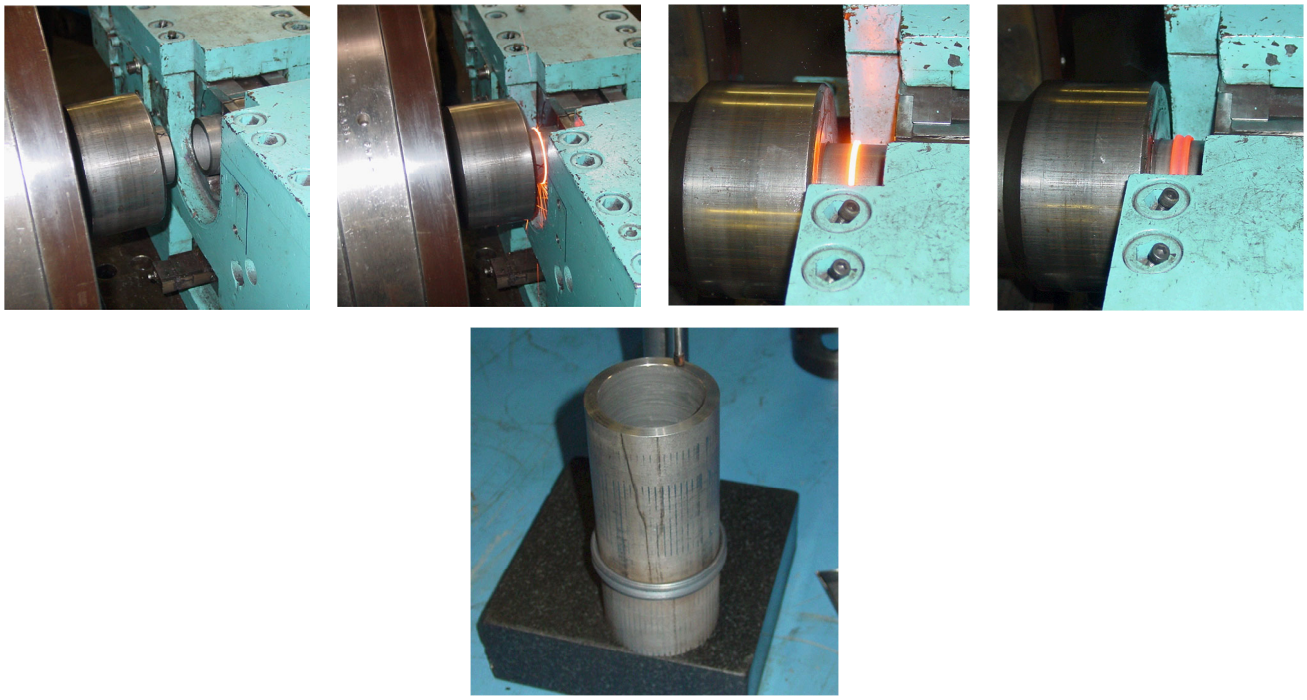

Fig. 2. Sequences in the inertia welding of a MA956 tube.

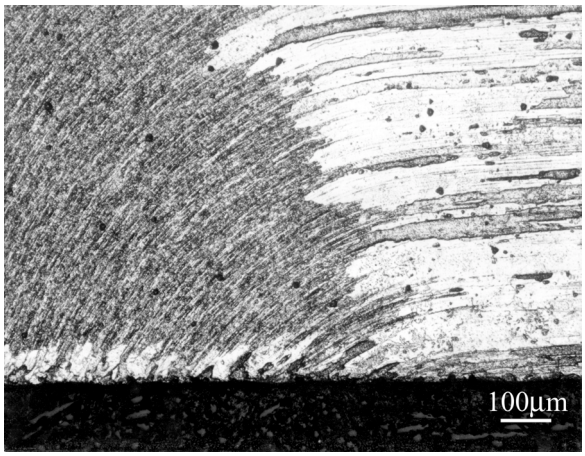

Fig. 3. Microstructure adjacent to joint in an inertia-welded MA956 tube, recrystallized after joining.

transmission electron microscopy (TEM) is in progress, and specimens are being prepared for creep testing of the joints

Plasma-assisted diffusion bonding: Figure 4 shows a cross section of a block of MA956 that was joined by plasma-assisted diffusion bonding (MER Corporation). The etched microstructure of the joint indicates that the bond line appears to be quite clean with essentially no indication of microstructural distortion along it. The appearance of grain continuity across the joint in places should not be interpreted to indicate that grain growth has occurred though the joint, since the alloy specimen had been re-crystallized before joining. The appearance is serendipitous. Examination of the bond by electron probe micro-analysis (EPMA) suggested that there was a collection of dark-appearing (in the back-scattered electron view) along the bond line that appeared to be enriched in Ti, Y, Al, and O, Fig. 5. A Y-enrichment might suggest some local accumulation of the yttria dispersoid as a result of localized melting, while Ti and Al enrichments may suggest accumulation of Ti-Al-rich particles that are normally present throughout the matrix of the

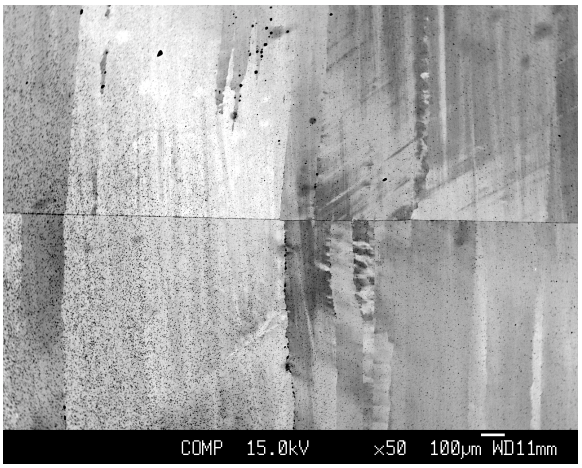

Fig. 4. Joint made by plasma-assisted diffusion bonding in MA956 (joined after recrystallization).

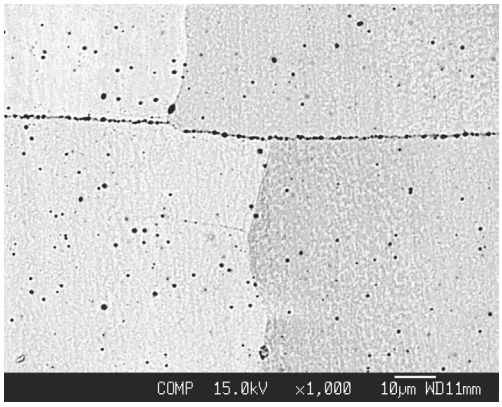

Secondary electron image

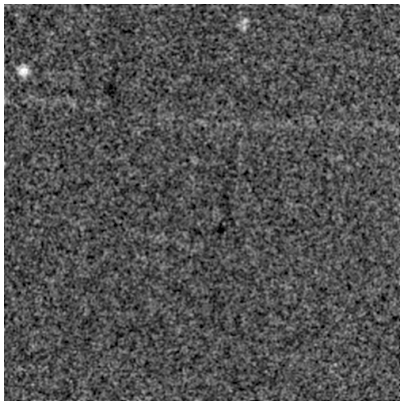

Oxygen X-ray map

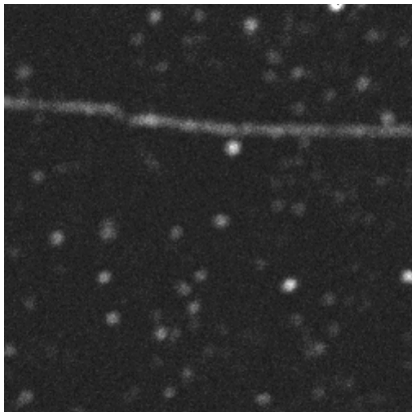

Titanium X-ray map

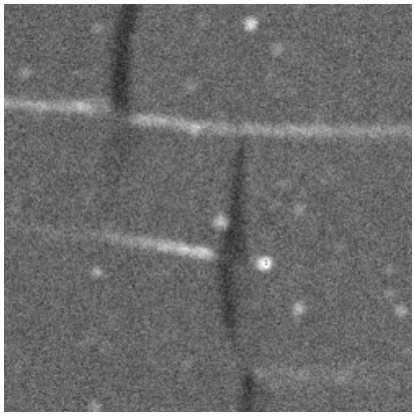

Yttrium X-ray map

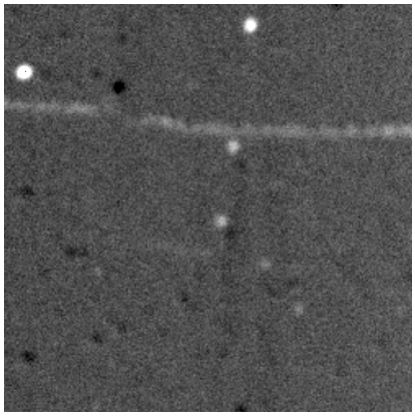

Aluminum X-ray map

Fig. 5. EPMA mapping of the center portion of the joint shown in Fig. 4.

alloy. The relative strength of the X-ray signals suggested that the particles along the bond line were predominately Ti-rich. Transmission electron micrographs of cross sections taken across the joint shown in Fig. 4 are shown in Figs. 6 and 7. In Fig. 6, the bond line has the appearance of an alloy grain boundary, which contains discrete particles but otherwise appears to be very clean. In Fig. 7, one of the larger particles is shown in detail to consist of a mixture of Al_2O_3 and TiC particles. While the sizes of these particles were similar to Ti-rich particles present in the original alloy microstructure, it is not known if the number of such particles along the bond line is similar to or greater than the population of particles in the original matrix.

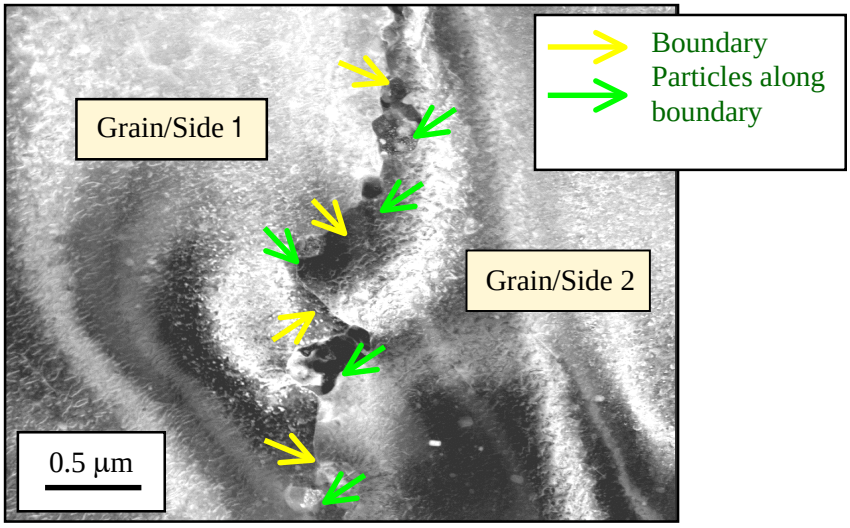

Fig. 6. Transmission electron micrograph across the bond shown in Fig. 5 (bond line runs top- bottom).

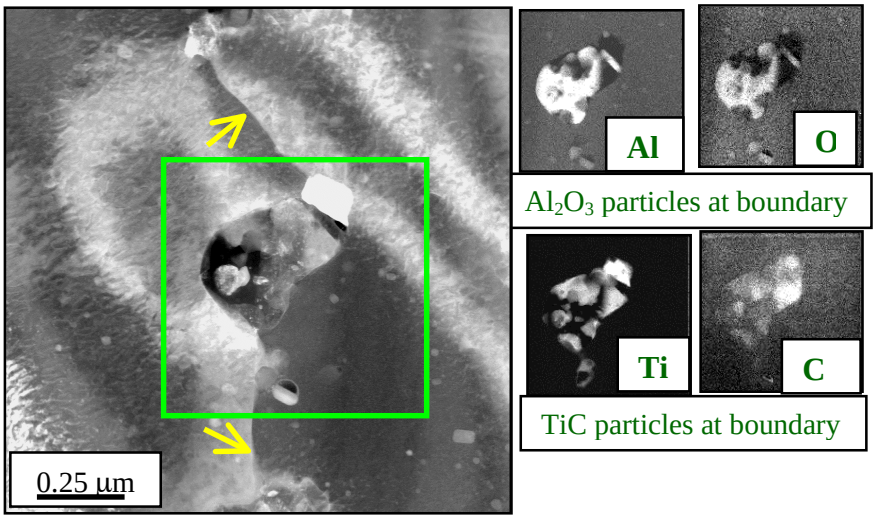

Fig. 7. Transmission electron micrograph of a particle in the bond line shown in Fig. 6 (bond line in indicated by arrows).

Transient liquid phase bonding: As part of a collaborative effort with the Energy & Environmental Research Center, Grand Forks, North Dakota (J. Hurley) and one of the original developers of TLP bonding in the HiPPS program (N. S. Bornstein), a proof-of-principle alloy for use as a transient liquid phase was melted and rolled into foil, and used in initial bonding trials for joining tubes of alloy MA956. A sample cross section of such a joint is shown in Fig. 8, which is an SEM back-scattered image. The bright-appearing particles in the interdiffusion zone on each side of the bond line are rich in the TLP alloy, and the data points indicated on the figure are locations where spot analyses were made using EPMA. The interest here is to develop joining conditions that allow the TLP to wet the surfaces to be joined, and for those surfaces to be in contact under conditions where there is sufficient time at temperature to allow diffusion bonding to occur. During this process, it is essential that the transient liquid phase diffuses away from the joint to the extent that any modification of the composition near the joint due to remaining TLP alloy phases is not detrimental to the mechanical properties. Detailed analysis of this joint by TEM is in progress. Results from the analysis will be compared with data from creep tests of specimens made from these joints and used to guide further development of the bonding conditions.

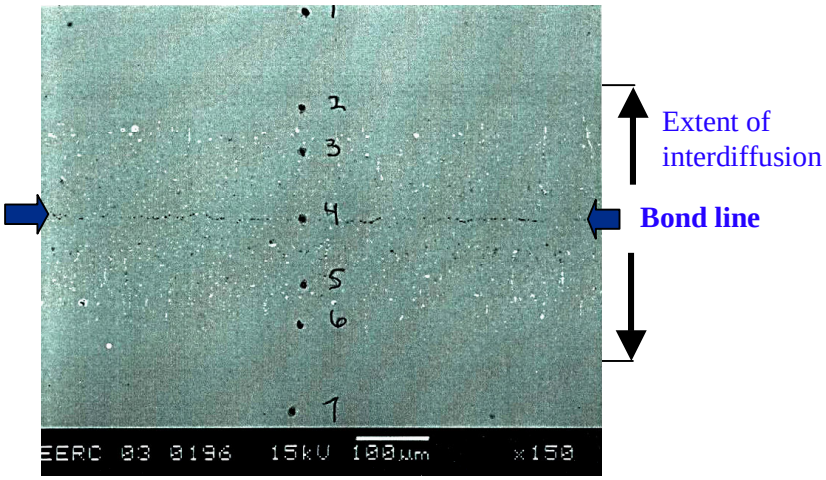

Fig. 8. Scanning electron micrograph of a TLP bond in alloy MA956.

TEMPERATURE LIMITS

It is expected that ODS alloys in service will be subjected to mechanical loading such that their rate of creep would be negligibly slow. As a result, the service life of these alloys is likely to be determined by their oxidation behavior. Further, these alloys form very thin alumina scales which grow very slowly and remain protective until the Al content in the alloy has been essentially exhausted, at which point a non-protective mode of oxidation will ensue (‘breakaway oxidation’). This means that the extent of oxidation attack during protective behavior cannot readily be assessed by the usual methods of measuring section thinning. As a result, there is need for a method for predicting the oxidation-limited lifetimes of such

alloys. Fortunately, for this class of FeCrAl alloys, the basis for such modeling is relatively straightforward since there are several simplifying factors or assumptions involved:

- these alloys form essentially single-phase scales of alumina that are uniform in thickness;
- there is negligible internal attack; and
- the Al concentration gradient in the alloy remains flat until very near the end of life.

As a result, it is possible simply to equate the oxidation lifetime to the rate of consumption of the available Al to form the oxide scale,[12] so that:

Oxidation-limited lifetime = (Al available for oxidation) / (oxidation rate)

The oxidation kinetics of these alloys, in terms of total mass change (total oxygen consumed), have a characteristic shape as indicated in Fig. 9. For the purposes of modeling, the oxidation behavior has been described as involving three stages, defined as:

Stage 1, which involves initial, transient, oxidation is very short for these alloys at the temperatures of interest, and so is ignored for the purposes of modeling.

Stage 2, which involves growth of the oxide according to a parabolic rate law; and

Stage 3, which involves a period of linear mass gain as result of continuing oxide growth, as well as spallation of some of the scale.

As shown in Fig. 9, Stage 3 ends with a rapid increase in the total mass gain due to the formation of a non-protective scale, as breakaway oxidation ensues.

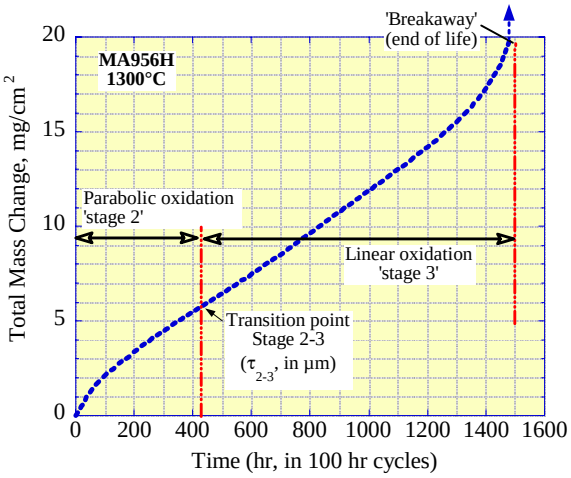

Fig. 9. Typical form of the oxidation kinetics of ferritic ODS alloys.

The current expression of the model based on this approach is:

$$t_b = \{[S*10^{-4}*\rho_A*A_\tau*e^{-Q\tau/(1.987*T)}]^2/(3600*A_2*e^{-Q2/(1.987*T)})\} + \{[1/(3600*M)*(V/A)*(\rho_M/(A_3*e^{-Q3/(1.987*T)}))*$$

$$[(C_{Bo}-C_{Bb}) - M*S*10^{-4}*(A/V)*(\rho_A/\rho_M)*A_\tau*e^{-Q\tau/(1.987*T)}]\} \text{ hours}$$

This is a simple, deterministic, algebraic expression for which the input required consists of:

(a) data about the alloy (density: ρ_M; initial aluminum content: C_{Bo}; Al content at which failure occurs: C_{Bb});

(b) about the oxide (density:ρ_A; constants based on oxide and alloy stoichiometry: M, S); and

(c) alloy oxidation descriptors (essentially Arrhenius data for the various stages of oxidation: A_2, Q_2; A_3, Q_3; A_τ, Q_τ).

Given these data for a given alloy, the only input required to predict oxidation-limited lifetime is the metal temperature (T), and the component size (represented by the volume of the component divided its surface area, V/A). This parameter is useful, since for a tube V/A = d/4, were d is the wall thickness. The oxidation parameters were generated from long-term oxidation exposures in which specimens were taken to failure. Note that Stage 3 kinetics are only experienced for oxide scale thicknesses greater than approximately 20 μm, and that at the lower temperatures of interest (1000, 1100°C), such scale thicknesses are only obtained after many thousands of hours of exposure. In addition, the value of C_{Bb} must be measured experimentally, which requires exposing specimens to failure and then being able to remove them from test immediately upon failure before they are consumed by breakaway oxidation. Using the oxidation data and values of the C_{Bb} measured to date, the lifetime model was exercised for a particular alloy, MA956H, to predict the oxidation-limited lifetimes as a function of wall/section thickness (V/A) and temperature, with the results shown in Fig. 10. Figure 11 shows the correspondence of these predictions with experimentally-observed lifetimes for this alloy: even though the oxidation lifetime axis is logarithmic, the predictions appear to be reasonable.

Because this alloy oxidizes very slowly, data for 1100°C are sparse: the one specimen so far oxidized to failure exhibited a life of 23,400 hours. Figure 12 shows similar predictions and experimentally-observed lifetimes for alloy MA956, which has an oxidation rate significantly faster than MA956H. For this alloy, there are several experimental data points at 1100 and 1200°C, which allow the suggestion that the predictions given by this simple model are reasonable, if optimistic, for temperatures in the range of 1100 to 1300°C. On this basis, and using values of C_{Bb} measured at only two temperatures, the model was exercised to provide comparative lifetimes as a function of temperature and section thickness for all of the ODS alloys of interest. Predictions for 1100°C are shown in Fig. 13, which indicates that all of the alloys (except MA956) are expected to exhibit reasonably similar lifetimes for the thicker sections (V/A > 0.4),

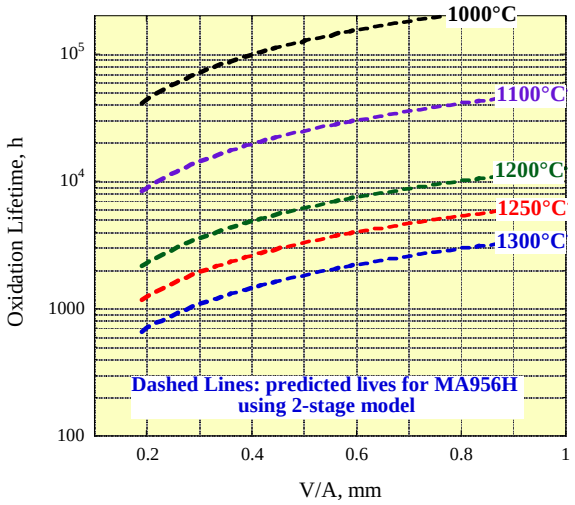

Fig. 10. Predicted oxidation lifetimes for alloy MA956H.

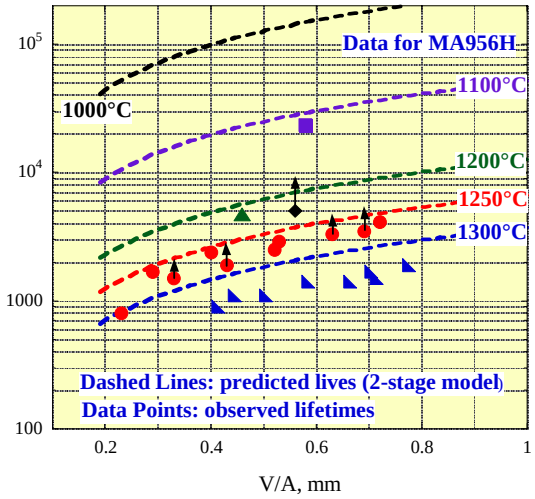

Fig. 11. Comparison of predicted and observed oxidation lifetimes for alloy MA956H.

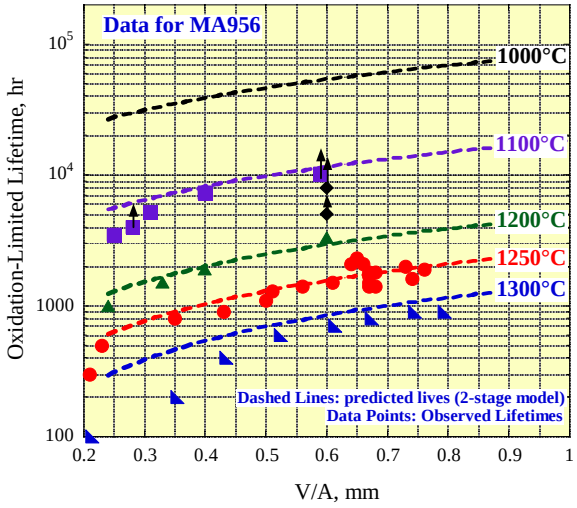

Fig. 12. Comparison of predicted and observed oxidation lifetimes for alloy MA956.

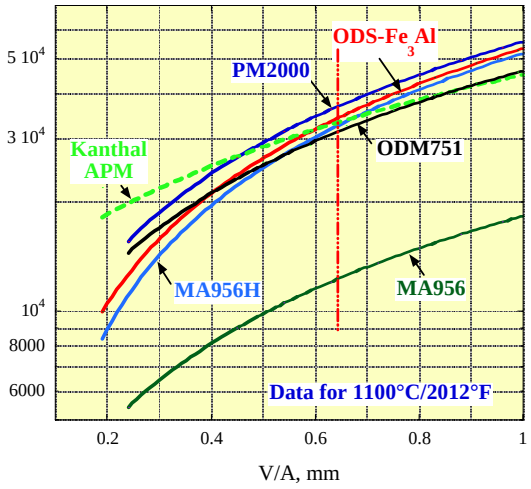

Fig. 13. Comparison of predicted oxidation lifetimes for all the ODS alloys of interest at 1100°C (note that the vertical line denotes the V/A value for a tube of 2.5 mm thickness)

while there is some differentiation among the alloys for thinner sections. Note also that in Fig. 12 there is an increasing divergence between the predicted and the observed lifetimes as the value of V/A decreases from 0.5 to 0.2. Presumably, there is some feature of thinner sections that is not treated correctly by the model.

The difference in oxidation rate, hence oxidation-limited lifetime, between alloys MA956 and 956H is considered surprising since the only major difference in the nominal compositions of these alloys is in Al content, which would be expected to change the total oxidation-limited lifetime (difference in Al

reservoir), but would not have been expected to influence the oxidation rate. Examination of the detailed compositions of these two alloys indicated a higher level of "free" Ti in MA956 (0.3 compared to 0.2 atomic %), where free Ti is that in excess of the amount required to form compounds with the C and N present in the alloy. Incorporation of Ti into the alumina scales formed on ODS-FeCrAl alloys has been shown in some cases to modify the rate of scale growth; however, results for variants of PM2000 indicated an *increase* in life with an increase from 0 to 0.4 at% Ti,[13] which tends to discount the influence of Ti in the current results. TEM cross sections of the scales formed on these two alloys are compared in Figs. 14 and 15 for samples oxidized for 100 hours at 1200°C in air. Both formed scales that exhibited the grain structure expected from reactive element doping[14] (by yttrium in this case) and, while Y was found to be enriched at the oxide grain boundaries as expected, and Ti was enriched at the oxide metal interface, it was not possible to make quantitative comparisons of such enrichments between the two alloys. Other features found in the oxide scale on MA956, shown in Fig. 15, were large inclusions identified as TiC particles, and particles containing Y, Ti, Si, and C (but, apparently, no O). The latter particle in the cross section shown is oriented parallel to the major oxide grain boundaries, so that it might be capable of acting as a rapid diffusion path for oxygen, hence increasing the oxidation rate. Also, it appears to have caused some mechanical disruption of the oxide scale with an obvious void or crack present in the scale above it.

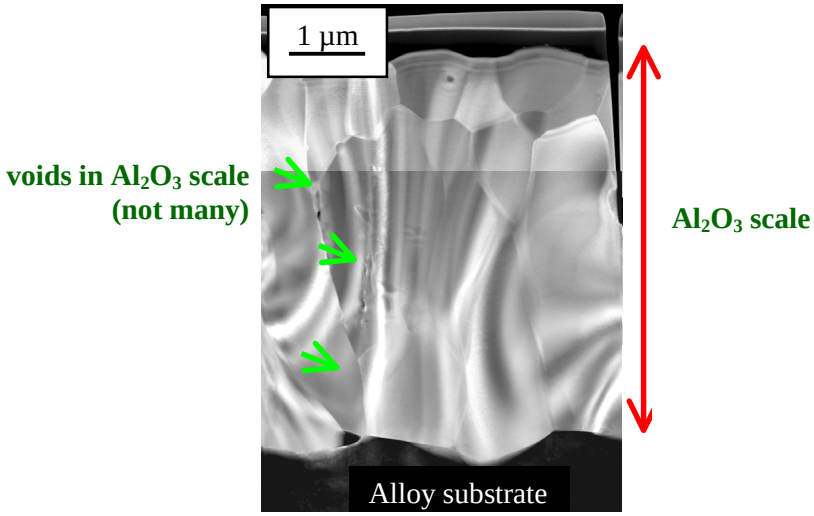

Fig. 14. TEM of a cross section of the oxide scale formed on alloy MA956H oxidized for 2h at 1200°C in air, showing the expected large, columnar-grained structure.

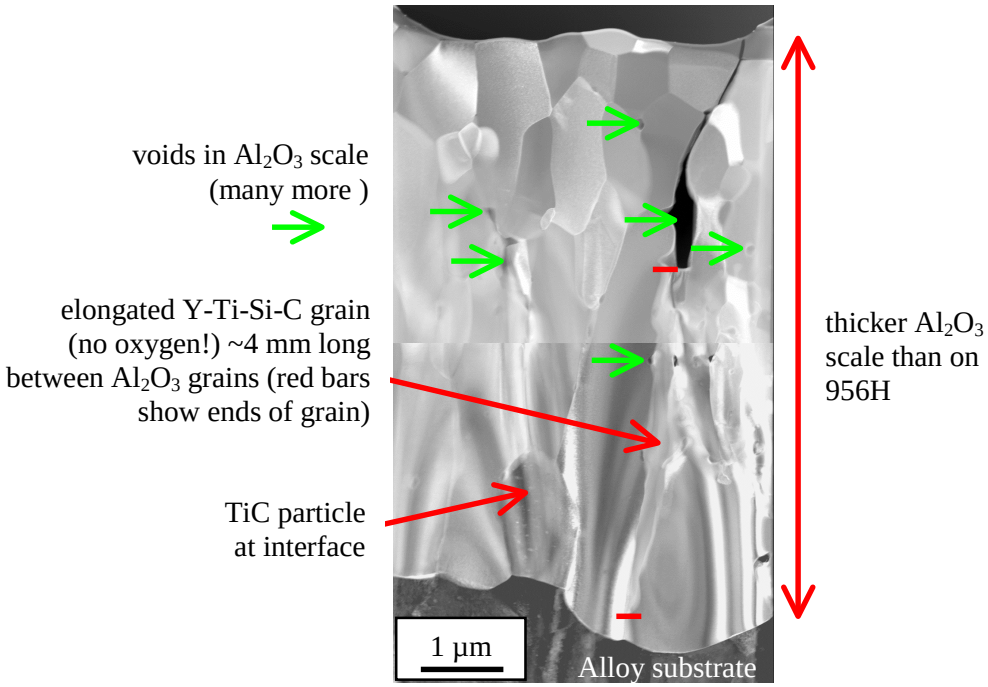

Fig. 15. TEM of a cross section of the oxide scale formed on alloy MA956 oxidized for 2h at 1200°C in air, showing thicker scale than 956H, and inclusions in the scale.

EFFECT OF SPECIMEN SHAPE

One of the obvious shortcomings of the current life prediction model is that it over-predicts lifetime, whereas such predictions should be conservative. Observations from the oxidation exposure tests suggested that the oxidation lifetime, that is, the time to failure, may be influenced by the shape of the specimen used in the laboratory tests. The specimen shapes typically are parallelepipeds or discs of various lengths and thicknesses. While the parameter V/A is a shape factor of sorts, it did not appear to account sufficiently for the difference between predicted and observed lifetimes. Potential sources of over-prediction of the oxidation lifetime include:

- an under-representation of the actual oxidation rates in Stages 2 and 3;
- assumption a larger reservoir of available Al than experienced in practice: this could arise though the use of too low a value of the minimum Al content (C_{Bb}), or from the development of a gradient in the Al concentration profile near the specimen surfaces toward the end of life[15]; and
- lack of a treatment for the acceleration in Al consumption immediately before break away occurs.

These considerations led to the study of the effect of specimen shape on oxidation life involving two sizes of parallelepiped, a disc, and a cylinder. The dimensions were chosen such that the parallelepipeds and the discs had the same thickness; the smaller parallelepiped had the same volume as the disc, as did the standard parallelepiped and the cylinder; and the cylinder and the small parallelepiped had the same

surface area. Note that the V/A parameter was the same for the parallelepipeds, so that it did not discriminate between them.

Figure 16 shows the total mass gain-time curves at 1250°C for the different shapes. In particular, the disc exhibited a longer life than did both the parallelepipeds, presumably reflecting its larger V/A ratio. Also, the larger parallelepiped failed first, significantly earlier than the small parallelepiped. For the disc and parallelepipeds the color of the alumina scale changed from grey to dull pink before any breakaway oxidation was observed, confirming that the available Al in the alloy had been depleted significantly. The large parallelepiped failed at a corner, as shown in Fig. 16, and the demarcation between the protective and the failed oxide was very sharp, as shown in the SEM topograph in Fig. 17a. A cross section of the non-failed corner adjacent to the failed corner shown in Fig. 17b indicated that the protective oxide scale was of essentially uniform thickness around the end of the specimen, with no signs of imminent failure: note also a cluster of large voids (possibly Kirkendall voids) in the center of the specimen thickness near the end, together with internal precipitates, the elongated ones of which were TiN. In contrast, the small parallelepiped appeared to fail essentially at all four corners simultaneously, after which the growth of a non-protective scale proceeded rapidly across the specimen surface in an essentially symmetrical way.

Consideration of the reasons for the early failure of the large parallelepiped led to examination of the conditions prevailing as the point of breakaway oxidation is approached. If a flat Al concentration profile is assumed to persist throughout the oxidation lifetime of the specimen, the point on the alloy surface that will be the first to fall below C_{Bb} and experience breakaway oxidation will that which represents the

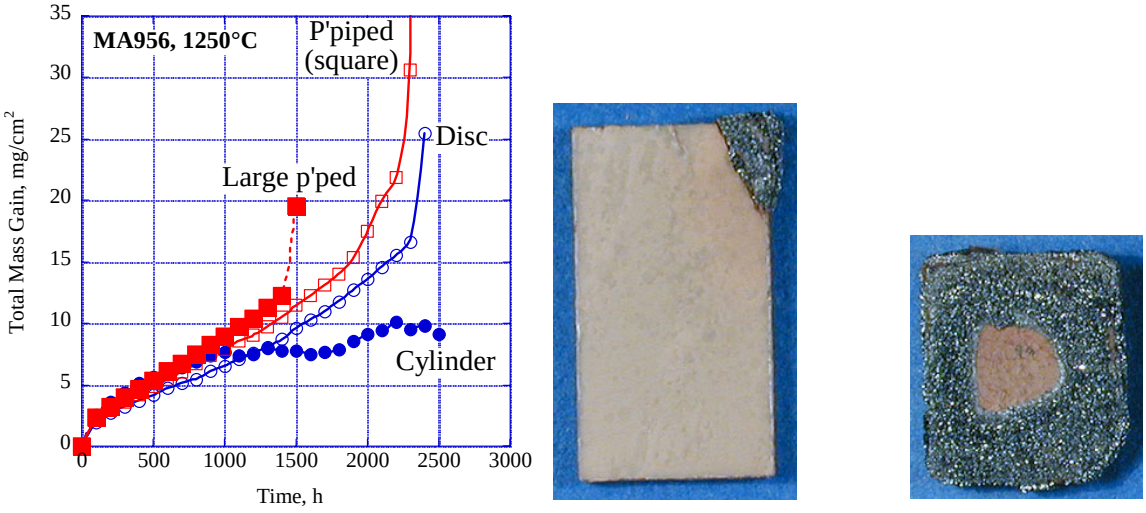

(a) **(b)** **(c)**

Fig. 16. Oxidation behavior of different specimen shapes, MA956, 100h cycles at 1200°C in air. (a) oxidation kinetics, 100h cycles at 1250°C; (b) large parallelepiped showing failure at one corner; (c) small parallelepiped showing symmetrical progression of breakaway oxidation.

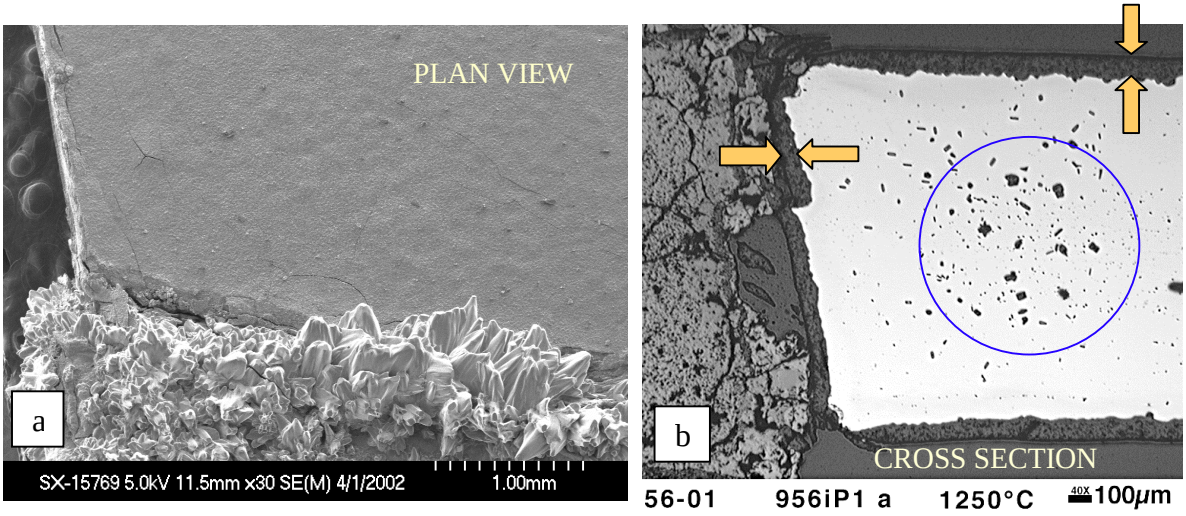

Fig. 17. Mode of failure of a long parallelepiped specimen of MA956 (a) plan view of the corner at which breakaway initiated; (b) cross section of the adjacent corner: the scale shows no sign of imminent breakaway behavior.

longest distance that Al from the center of the reservoir has to travel. With a flat Al concentration profile, the center of that reservoir may be considered to be the center of the alloy thickness, so that the surface of a sphere that touches four sides of the parallelepiped (see Fig. 18) represents the minimum diffusion path length to any surface. The radius of that sphere is half the thickness of the parallelepiped (or d/2), while the distance to an edge is 0.7d, and the distance into the corner is 0.87d. These distances are shown in Table 2, in which w is width; and l is length. Interestingly, these considerations do not suggest a reason for the difference in oxidation lifetimes of the two parallelepipeds (same thickness). This is possibly an indication that the assumption that a flat Al concentration profile persists until breakaway occurs is not sound and, in that case, the center of the Al reservoir would be the center of mass. The longest diffusion distance in a parallelepiped is that from the center of mass to a corner. The formulation for this distance, listed in Table 2, involves all of the dimensions of the parallelepiped, and so holds some promise for discriminating between the behavior parallelepiped sizes.

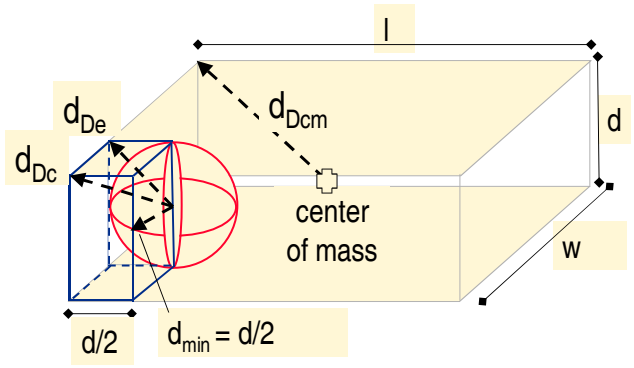

Fig. 18. Schematic representation of diffusion lengths in a parallelepiped.

Table 2. Suggested shape factors: diffusion lengths

Shape	Edge d_{De}	Corner d_{Dc}	Center of Mass d_{Dcm}
P'piped	$0.707 \times d$	$0.866 \times d$	$0.5 \times \text{sqrt}\ (l^2 + w^2 + d^2)$
Cylinder	—	$0.707 \times \text{diam}$	$0.5 \times \text{sqrt}\ (l^2 + \text{diam}^2)$
Disc	$0.707 \times d$	$0.707 \times d$	$0.5 \times \text{sqrt}\ (d^2 + \text{diam}^2)$

CONCLUSIONS

The results reported indicate that progress has been made in the joining of ODS alloys, as well as in determining the temperature limits of this class of alloy. Three routes are being evaluated for joining these alloys: *inertia welding*, where interest is in controlling and understanding the microstructural distortion caused by the process; *plasma-assisted diffusion*, which appears capable of producing clean joints and where interest is centered on determining the source of alumina-titanium carbide particles along the bond line and their influence on mechanical properties: and thirdly *transient liquid phase bonding*, for which the major questions concern the amount of TLP alloy remaining near the bond line, and its effect on alloy properties. The effort to determine the temperature limits of these alloys has involved generating oxidation data for all the available ODS-FeCrAl alloys, including running exposures for very long times until oxidation failure occurs. In addition, an initial working model for prediction of the oxidation-limited lifetime has been developed that appears to give reasonable predictions for alloy lifetimes over the temperature range 1100 to 1300°C. A major concern with this model at present is the fact that it over-predicts the lifetimes of specimens exposed to failure in the laboratory, and analysis is continuing to provide a mathematical description of specimen shapes that would cause the model to better discriminate among different shapes. Nevertheless, given that the predictions of the model are reasonable, it indicates that lifetimes of between 30,000 and 70,000 hours at 1100°C would be expected for typical tube sizes, with wall thicknesses ranging from 2.5 to 6.4 mm.

ACKNOWLEDGMENTS

This research was sponsored by the Fossil Energy Advanced Research Materials (ARM) Program, U.S. Department of Energy, under contract DE-AC05-96OR22464 with UT-Battelle LLC. Program of the U.S. Department of Energy. Mr. L. D. Chitwood was responsible for the oxidation lifetime tests; Mr. L. R. Walker carried out the electron microprobe analyses; and Ms. D. W. Coffey and Dr. K. L. More were responsible for preparing the TEM images.

REFERENCES

1. F. Starr and I. A. Shibli, "Fundamental issues in the development of austenitic and Ni-based alloys for advanced supercritical steam and high-temperature indirect-fired gas turbines," pp. 459–471 in *Proc. Fifth Intl. Charles Parsons Turbine Conference: Advanced Materials for 21st Century Turbines and Power Plant,* A. Strang, W. M. Banks, R. D. Conroy, G. M. McColvin, J. C. Neal, and S. Simpson, Eds., IOM Communications Ltd., Book No. 736 (2000).
2. B. Kad, J. Heatherington, I. G. Wright, and V. K. Sikka, "Optimization of ODS FeCrAl and Fe_3Al properties," *Proc. 17th Annual Conference on Fossil Energy Materials*," Baltimore, Maryland, April 2003.
3. A. R. Jones, J. Ritherdon, and D. J. Prior, "Reduction of defect content in ODS alloys," ibid.
4. J. L. Blough and W. W. Seitz, "Fireside corrosion testing of candidate superheater tube alloys, coatings, and claddings-Phase III," ibid.
5. M. A. Harper, "Improved ODS alloy for heat exchanger tubing," *Proc. 16th Annual Conference on Fossil Energy Materials*," Baltimore, Maryland, April 2002.
6. F. Olsson, S. A. Svensson, and R. Duncan, "Externally-fired gas turbine cycles with high-temperature heat exchangers utilizing Fe-based alloy tubing," pp. 139–153 in *Proc. 15th International Plansee Seminar*, G. Kneringer, P. Rodhammer, and H. Wildner, Eds., Plansee Holding AG, Reutte (2001).
7. F. Starr, A. R. White, and B. Kazimierzak, in *Materials for Advanced Power Engineering 1994*, D. Coutsouradis, et al., Eds. (Kluwer Academic Publishers, 1994) pp. 1393–1412.
8. C. Brown, E. Verghese, D. Sporer, and R. Sellors, "PM2000 honeycomb structures," Paper 98-GT-565, presented at the *43rd AMSE Gas Turbine and Aeroengine Technical Congress*, Exposition, and Users Symposium, Stockholm, Sweden, June 2–5, 1998.
9. S. Holmstrom, M. Siren, L. Heikinheimo, P. Auerkari, J. Varmavuo, and R. Saarinen, "Performance of an iron-based ODS alloy in a boiler environment," pp. 769–777 in *Materials for Advanced Power Engineering 1998*, LeComte-Beckers, F. Schubert, and P. J. Ennis, Eds., Forschungszentrum, Zentralbibliothek, 1998.
10. P. L. Threadgill, *Friction Welding of an Fe_3Al-based ODS Alloy*, Report No. ORNL/Sub/97-SX373/01, July 1998. See, also, B. J. Inkson and P. L. Threadgill, "Friction Welding of Fe-40Al Grade 3 ODS Alloy," *Mat. Sci. and Eng*., **A258**, 313–318 (1998).
11. D. J. Seery and J. Sangiovanni, "Engineering development of a coal-fired high-performance power generating system," Paper No. 1.7 in *Proc. of the Advanced Coal-Based Power and Environmental Systems'98 Conference*, Morgantown, West Virginia, July 21–23, 1998, DOE/FETC-98/1072.
12. W. J. Quadakkers, K. Bongartz, F. Schubert, and H. Schuster, in *Materials for Advanced Power Engineering 1994*, D. Coutsouradis, et al., Eds. (Kluwer Academic Publishers, 1994) pp. 1533–1542.

13. W. J. Quadakkers, D. Clemens, and M. J. Bennett, “Measures to improve the oxidation limited service life of Fe-based ODS alloys,” pp.195–206 in S. B. Newcomb and J. A. Little, (Eds.), *Microscopy of Oxidation 3*, Institute of Metals, London, U.K. (1997).
14. B. A. Pint, “Study of the reactive element effect in ODS iron-base alumina-formers,” *Mater. Sci. Forum*, **251–254**, 397–404 (1997).
15. B. A. Pint, L. R. Walker, and I. G. Wright, “Characterization of the breakaway Al content in alumina-forming alloys,” *Proc. 5th International Conference on the Microscopy of Oxidation*, Limerick, Ireland (2002).

TRADE STUDY FOR INTEGRATING NUMEROUS SECA SOFC MODULES

B. Ozpineci, L. M. Tolbert, and D. J. Adams
Oak Ridge National Laboratory

INTRODUCTION

Under the Department of Energy's Solid State Energy Conversion Alliance program, solid oxide fuel cell (SOFC) modules are being developed in the 3–10 kW range for residential applications. For applications requiring higher power than 10 kW, several modules can be connected, e.g., 25 10-kW modules for a 250-kW hospital. This study proposes ways to connect numerous fuel cell modules using power electronics converters.

TASKS ACCOMPLISHED

A literature review was conducted for fuel cells, their characteristics, models, and power converter interfaces for fuel cells with an emphasis on SOFCs. This review also included the ganging of multiple energy sources using power converters; however, only a few publications on this latter subject were found.

To integrate numerous SOFC modules, five different approaches are proposed in this report: series, multilevel, cascaded multilevel, dc distribution, and high-frequency ac (hfac) distribution. Each of these configurations will be described in the following subsections.

A. Series configuration: The simplest way of integrating fuel cells is to connect them in series and feed the output to a power converter as shown in Fig. 1.

The power converter consists of a dc-dc voltage regulator and an inverter. The reason for the voltage regulator is that the fuel cell output voltage decreases with increasing current, but a dc-dc voltage regulator maintains a stiff dc link voltage for the inverter input (Fig. 2). Depending on how many fuel cell modules are connected in series, this regulator can be of the buck or boost type. Moreover, it can be of the high-frequency link type or chopper type.

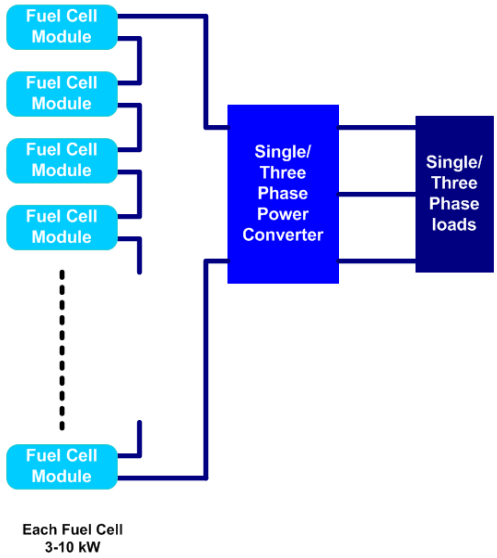

Fig. 1. Block diagram of the series configuration.

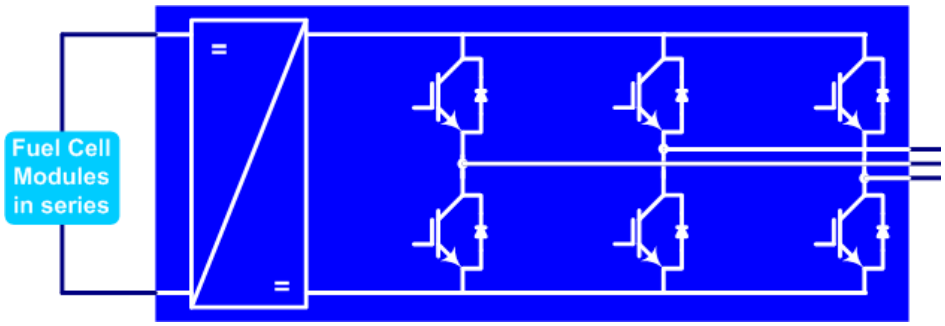

Fig. 2. Dc/dc voltage regulator and a three-phase inverter.

B. Cascaded multilevel configuration: Another approach is to couple each fuel cell module with its own power converter module, as shown in Fig. 3, and connect the power converter outputs in series. The power converter module consists of a voltage regulator and a single-phase H-bridge inverter. This configuration is similar to the cascaded multilevel inverter shown in Fig. 4.

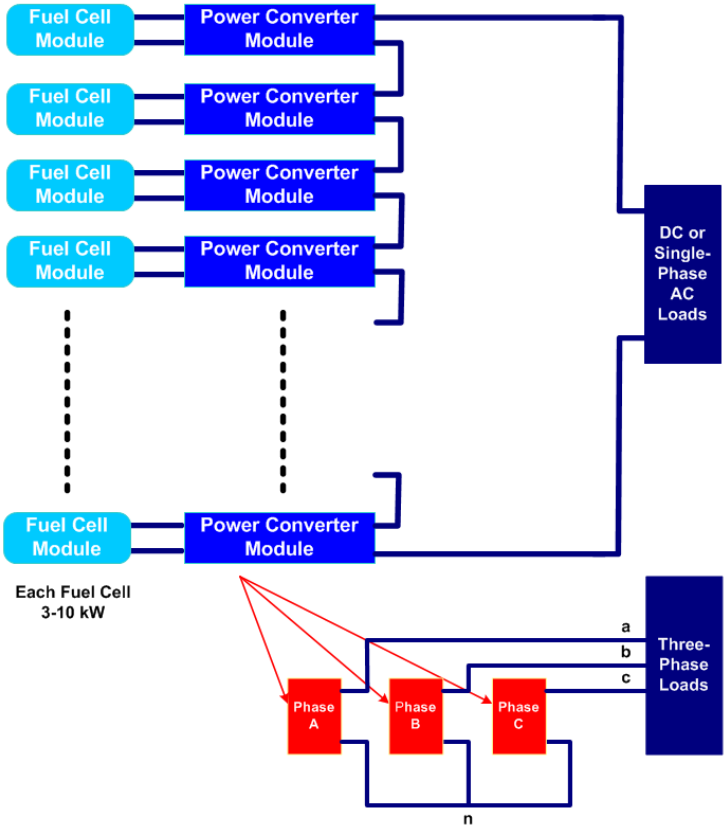

Fig. 3. Block diagram of the cascaded multilevel configuration.

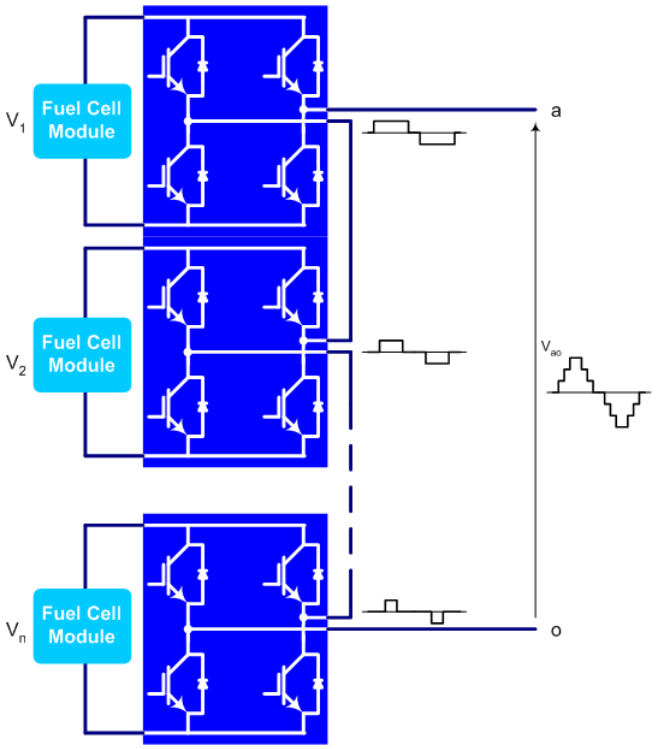

Fig. 4. One phase of a cascaded multilevel inverter.

Each fuel cell and power converter module produces a single-phase three-level ac voltage, as shown in Fig. 5. These voltages are added in series to form a single-phase multilevel output voltage. Three of these single-phase voltages can be connected to form a three-phase supply (Fig. 3).

The voltage regulator can be eliminated if the multilevel inverter control senses the voltages and operates the power converters accordingly.

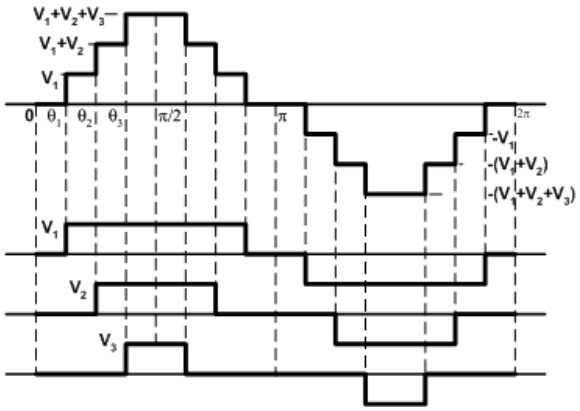

Fig. 5. One phase of a cascaded multilevel inverter.

C. Multilevel configuration: Similar to the cascaded multilevel converter configuration, SOFCs can be connected to one single-phase/three-phase multilevel inverter as shown in Fig. 6. In this case, there might not be a need for a voltage regulator, as in approaches A and B, if the multilevel inverter control senses the fuel cell voltages at all times.

There are many types of multilevel inverters. One typical type, the diode clamped multilevel inverter, is shown in Fig. 7 with four fuel cell modules.

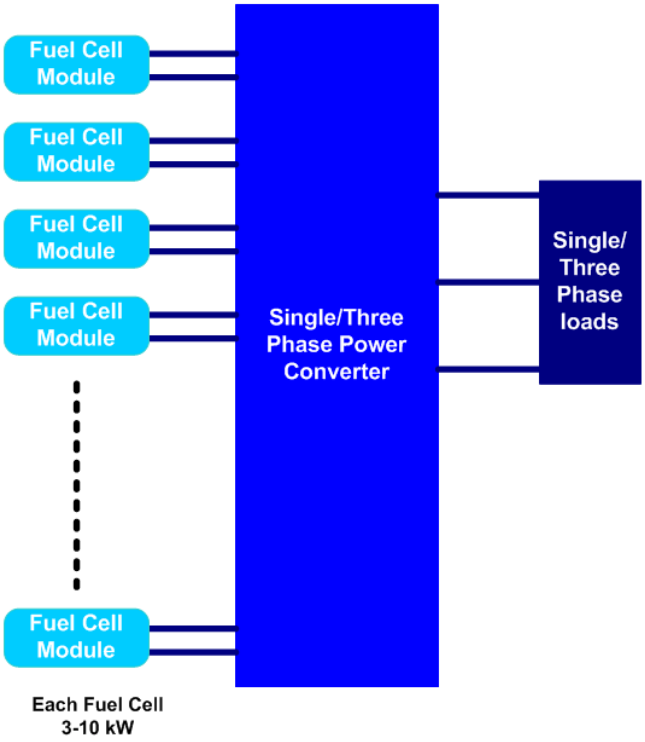

Fig. 6. Block diagram of the multilevel configuration.

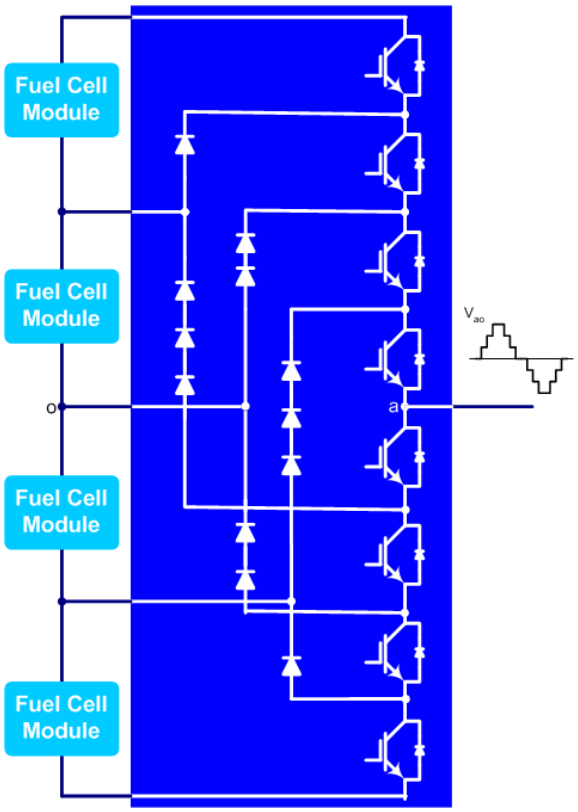

Fig. 7. One phase of a diode clamped multilevel inverter.

D. dc distribution configuration: In this configuration, as in the cascaded multilevel case, each fuel cell module has its own power converter module; however, unlike in that case, each power converter is a dc-dc converter and their outputs are connected in parallel instead of series (Fig. 8). These dc-dc converters have to be of the boost type since the fuel cell module voltage will typically be less than the dc distribution/link voltage.

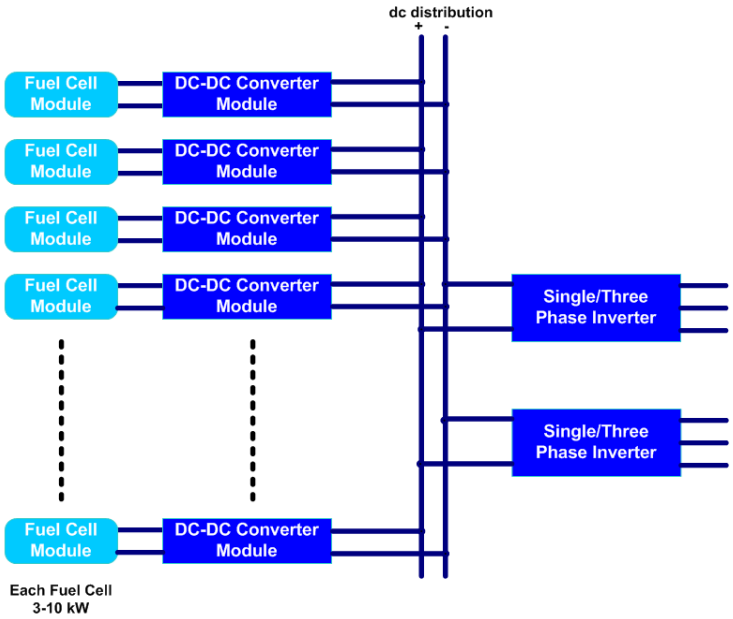

Fig. 8. Block diagram of the dc distribution configuration.

The advantage of dc distribution is that other power sources or loads can be connected to the dc link through a power converter without disturbing the rest of the system. However, connecting power converters in parallel causes problems with circulating currents that need to be carefully addressed.

E. hfac distribution configuration: In this approach, each fuel cell is connected to an H-bridge inverter, which converts the dc input to hfac voltage, typically at more than 20 kHz (Fig. 9). Each fuel cell and dc-hfac inverter module is connected to a transformer primary tap. The transformer boosts the input voltage and feeds single-phase to single-phase/three-phase power converters.

The transformer brings the advantages of isolation, voltage boost, and the capability of adding other power sources and loads through a power converter. Additionally, because of the high frequency, it is much smaller than a utility frequency transformer. However, it also has the disadvantages of higher expense and the possibility of saturation.

The power converter in the secondary of the transformer can either be a single-phase to three-phase cycloconverter or a rectifier and a three-phase inverter.

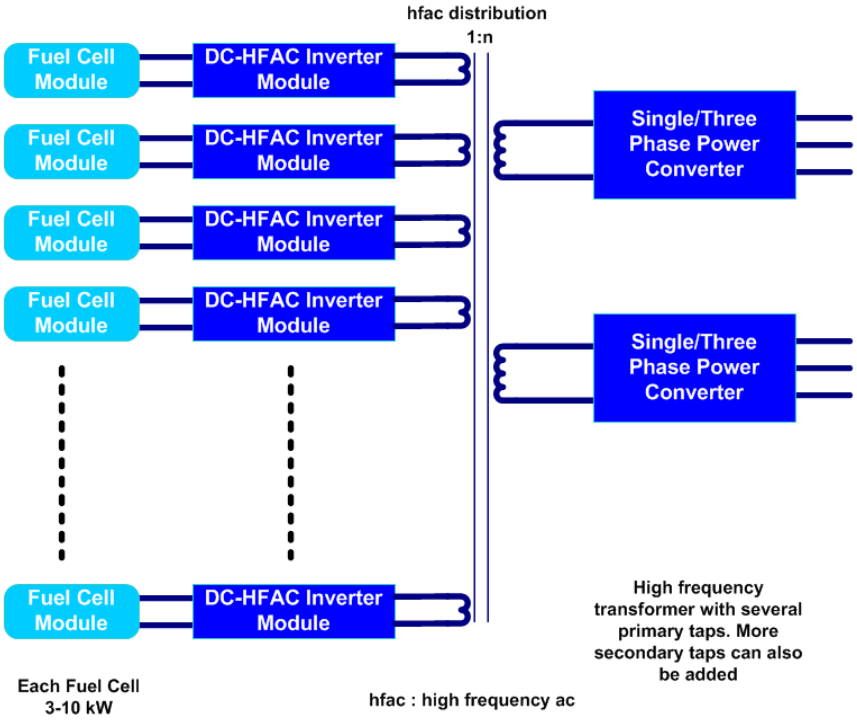

Fig. 9. Block diagram of the hfac distribution configuration.

FUTURE WORK

The five configurations described will be evaluated for

- relative cost (capital and operating),
- control complexity and stability (ease of operation and customization),
- reliability,
- maintainability and availability (at power system and device levels),
- service life,
- fault tolerance,
- modularity (ability to accommodate isolation of portions of system for service or addition of generation capacity while other portions of complete system continue functioning),
- energy conversion efficiency,
- cooling system cost and energy consumption,
- impact of trends in power device developments (benefits of new devices in the research and development pipeline), and
- ease of mass customization to enable mass production to drive down costs.

ECONOMICAL FABRICATION OF MEMBRANE MATERIALS

T. R. Armstrong, B. L. Armstrong, C. A. Walls, R. D. Ott, and C. A. Blue
Oak Ridge National Laboratory

INTRODUCTION

The objective of this project is to develop novel approaches for the fabrication of membranes for hydrogen and oxygen separation. In past years this project has focused on the development of high densify infrared processing to rapidly sinter thin support membranes. This year the project has undertaken a new focus. The approach is two-fold: (1) continue the development and use of high density infrared processing as warranted and (2) initiate development of thin ceramic membranes supported on metallic supports. Initial studies are being carried out on novel proton conducting ceramic materials deposited on supported produced by Pall Corporation.

RAPID DENSIFICATION OF CERAMIC MATERIALS

ORNL has investigated the use of both a high density infrared and low density infrared process. The high density process utilizes a unique technology to produce extremely high-power densities of up to 3.5 kW/cm^2 with a single lamp, instead of using an electrically heated resistive element to produce radiant energy; controlled and contained plasma is utilized. The lamp consists of a 3.175-cm-diam quartz tube, which can be 10.16, 20.32, or 38.1 cm long. The lamp is sealed at the ends where the cathode and anode are located. Deionized water mixed with argon or nitrogen gas enters at the cathode side through high-velocity jets impinging at a given angle. Due to the high velocities and pressure, the de-ionized water is impelled to the wall of the quartz tube and spirals down the length of the tube in a uniform 2- to 3-mm-thick film. This water film serves two purposes: (1) to cool the quartz wall and (2) to remove any tungsten particulate that may be expelled from the electrodes. The gas moves in a spiral fashion through the center of the tube, and a capacitive circuit initiates the plasma. The plasma, which has a temperature in excess of 10,000 K, is stable and produces a radiant spectrum from 0.2 to 1.4 microns. The spectrum is primarily in the infrared (0.78 to 1.00 μm), although substantial energy is released in the visible wavelength, similar to the appearance of natural sunlight in energy distribution and color rendition. In contrast, the spectrum at a CO_2 laser with wavelengths near 10.6 microns is absorbed with much lower efficiency. The powder coatings discussed here are highly absorbing because the open areas act like black bodies. The low density light source is a tungsten halogen lamp which require no special cooling or facility for its use.

The samples sintered included both yttrium doped barium cerate (proton conductor for hydrogen separation) and a solid oxide fuel cell membrane composed yttria stabilized zirconia supported on a thick anode (NiO/yttria stabilized zirconia). These samples were prepared by tape casting to produce a porous

support followed by screen printing thick film membranes on its surface. In the case of barium cerate, both the support and membrane were composed of barium cerate.

The high density infrared process demonstrated that samples could easily be sintered to full density. In fact, thin films were fully densified on porous supports without interaction with the support in the case of the fuel cell or densification of the porous support. The sintering process was carried out very rapidly with the round trip cycle time (room temperature to sintering temperature to room temperature) taking no more than 60 minutes. In the case of 1 cm^2 no thermal shock or mechanical failure within the samples was noted. Examples of the samples are shown in Fig. 1.

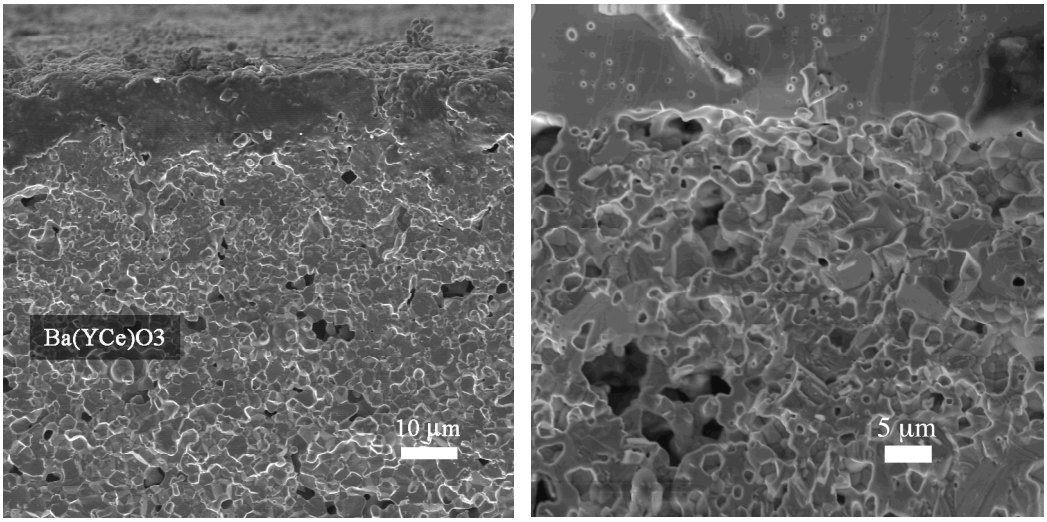

Fig. 1. Examples of barium cerate and a solid oxide fuel cell component sintered using the high density infrared process.

The high density infrared sintering process uses a high voltage power supply to generate the plasma used in sintering. This power supply consumes a great deal of energy during the sintering process that greatly impacts the efficiency and cost effectiveness of the process. In order to improve the economics of the process a low power density tungsten lamp set setup and used to sinter the same set of samples shown in Fig. 1. In order to qualify this process the heat flux of the low density lamp was measured using a heat flux sensor. This analysis determined that the heat flux of the low density lamp could only reach an equivalent heat of 1200°C. This level of heat is too low to sinter the samples shown in Fig. 1. Continued analysis indicated that only the high density lamp produced by Vortek is capable of producing the level of heat to full sintering the samples under investigation.

METALLIC SUPPORTED MEMBRANES STRUCTURES

Metallic supported membranes offer unique opportunity to solve problems with seals and mechanical integrity plaguing all ceramic planar and tubular devices. The use of a metallic support allows seals to be easily made using brazes technology. However, their use is not without the need to technological development. For example, several development issues need to be addressed:

1. Thermal expansion mismatch between the support and electrolyte
2. Creep of the metallic support
3. Potential oxidation depending on use
4. SiO_2 formation under the scale if used for fuel cells
5. Membrane deposition
6. Sintering to avoid oxidation of the metal

ANALYSIS OF POTENTIAL ISSUES

Metallic supports that best match the thermal expansion to materials like cerates are ferritic stainless steels that forms a chromia (Cr_2O_3) scale upon oxidation. These materials are potential candidate supports due to their close, but not exact, thermal expansion match to potential membrane materials. A large number of off-the-shelf ferritic stainless steels are available as the support material; however, their thermal expansions are not closely matched to candidate membrane materials. Figure 2 shows the thermal

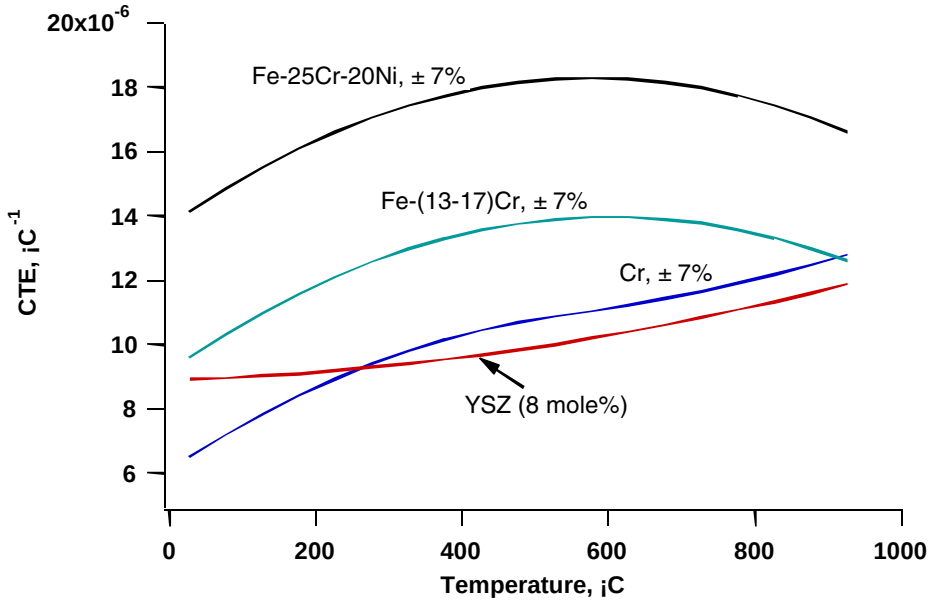

Fig. 2. Schematic overview of CTE data for austenitic Fe-25Cr-20Ni wt%, ferritic Fe-(13-17)Cr, pure Cr, and yttria stabilized zirconia [data from Thermophysical Properties of Matter, Volume 12, Y. S. Touloukian, R. K. Kirby, R. E. Taylor, and P. D. Desai, eds., 1979].

expansion of YSZ compared to several ferritic steels. Chrome concentrations in these alloys typically have to be in excess of 13 wt% to achieve a coherent chromia scale. One chromia-forming alloy of interest would be the Plansee Cr-5Fe-1Y_2O_3 wt% alloy, which was designed to match the thermal expansion characteristics of the YSZ electrolyte. However, because Cr-5Fe-1Y_2O_3 is brittle at room temperature, it is extremely expensive to machine and is currently not economically feasible at this point in time. Near net shaped powder processing is being pursued in order to reduce machining costs of this material.

One of the primary concerns with porous metals used at elevated temperatures is creep. Very little data has been collected on creep of porous materials, however, one fact is certain, it is significantly higher than that of a dense metallic sample. Microstructural engineering through controlled processing can reduce creep.

Two additional concerns with the use of ferritic stainless steels as the support if used for fuel cells are: (1) oxidation during processing of the air electrode and (2) oxidation during operation in the presence of a buffered gas (H_2, CO_2, H_2O). Figure 3 shows the parabolic rate constant for ferritic stainless steels as a function of temperature. At 1200°C the corresponding diffusion coefficient for oxygen diffusion into ferritic stainless steel is in the range 10^{-8} to 10^{-11} cm^2/sec. During sintering of the air electrode, this range of diffusion coefficients indicates that for a 1 hour (3600 seconds) soak in air the chromia scale will range from approximately 1 μm to 60 μm.

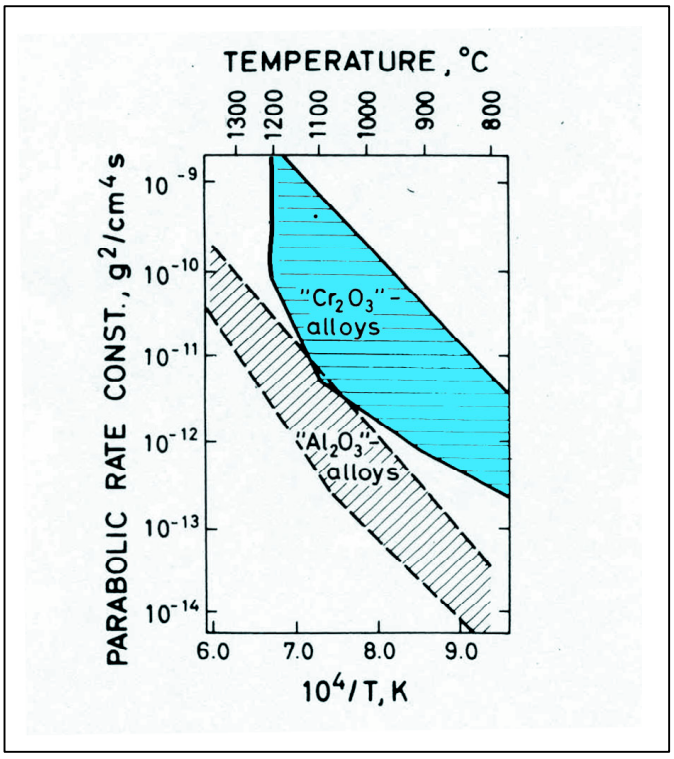

Fig. 3. Scatter bands for literature values of the parabolic rate constants for formation of chromia scales on binary chromium alloys. [P. Kofstad, High Temperature Corrosion, Elsevier Applied Science, New York 1988.]

The stability of chrome oxide was determined using the Ellingham diagram as a function of temperature and environment. The Ellingham diagram clearly indicates that any scale formed during processing will be stable in the operating environment of the fuel cell at all temperatures.

The diagram also indicates that a fuel environment with steam is quite oxidizing, and it would be expected that chromia scale would continue to grow during fuel cell operation at 700°C, albeit at a very

slow rate. Literature [C. T. Fujii and R. A. Meussner, *J. Electrochem. Soc*., **111** 1215 (1964)] data clearly indicates that Fe-Cr alloys, with up to 15% Cr, oxidize in Ar-H_2O environments. Additional data [K. Przyblski and G. J. Yurek, *Materials Science Forum*, **63** 1–74 (1989)] indicate the growth rate of chromia is independent of oxygen partial pressure at 800 and 900°C from 1 atm to 10^{-22} atm in a H_2-H_2O atmosphere. Lower oxygen partial pressures will reduce the iron content in the scale that may alter the conductivity of the scale.

A final concern with the use of ferritic stainless steels is the residual Si level in the alloy. It is well established that minor additions of Si (0.5–2 wt% range) to Cr_2O_3-forming alloys such as ferritic steels result in near continuous or continuous SiO_2 formation at the alloy/scale interface [B. Ahmad and P. Fox, *Oxid. Met*., **52**, 113 (1999)]. Although usually beneficial for oxidation resistance, such SiO_2 would significantly degrade the electrical conductivity of the scale, making the alloy unsuitable for use in SOFC applications. It has recently been shown [M. P. Brady, B. A. Pint, D. T. Hoelzer, I. W. Wright, and T. R. Amrstrong, submitted to *Electrochemical and Solid State Letters*] by cross-section transmission electron microscopy (TEM) that a Si impurity level of only 0.05 wt% resulted in the formation of a nearly continuous amorphous SiO_2 layer, up to 0.5 micron thick in some regions, at the alloy scale interface in Y_2O_3 dispersion strengthened Fe-13Cr wt% exposed for 10,000 h at 700°C in air (Fig. 4). This level of Si is well within the impurity range present in commercially available Cr_2O_3 forming ferritic steels. It is likely that many Cr_2O_3 forming alloys evaluated for performance in fuel cell environments contained similar or even higher levels of Si impurities, and that their electrical performance was adversely effected by SiO_2 at the alloy/scale interface. Unless specifically characterized in cross-section by TEM or other high resolution techniques, the presence of the SiO_2 would be missed.

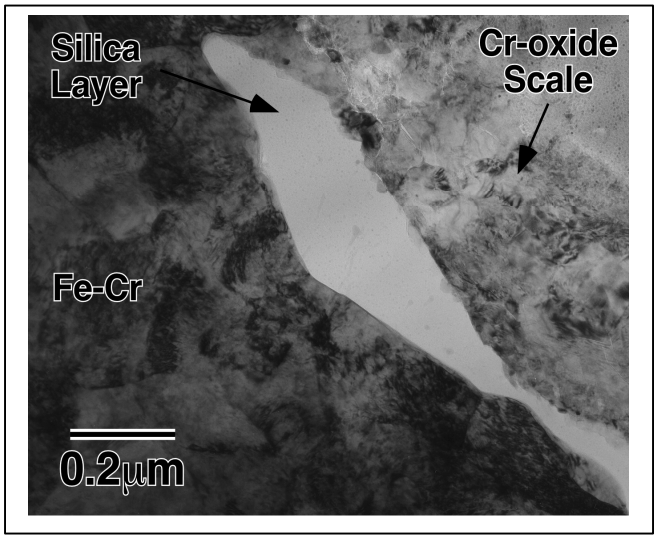

Fig. 4. TEM cross-section micrograph of Y_2O_3 dispersion strengthened Fe-13Cr wt% exposed for 10,000 h at 700°C in air showing SiO_2 formation at the alloy/Cr_2O_3 interface.

CONCLUSIONS

The use of metallic supports for thick film ceramic membranes has the potential to solve several key development issues- robustness and sealing. ORNL is pursuing the development of proton conducting membranes supported on 0.5 mm thick stainless steel supports. The membranes are being deposited using

slurry deposition processes and sintering processes have been developed that prevent oxidation of the support material. Microstructures of the membranes and test data on the flux of hydrogen through the membranes will be determine later this year and reported on later.

DEVELOPMENT OF INORGANIC MEMBRANES FOR HYDROGEN SEPARATION

Brian L. Bischoff, Roddie R. Judkins, K. Dale Adcock, and Lawrence E. Powell
Oak Ridge National Laboratory

INTRODUCTION

This paper presents information and data relative to recent advances in the development at Oak Ridge National Laboratory of porous inorganic membranes for high-temperature hydrogen separation. The Inorganic Membrane Technology Laboratory, which was formerly an organizational element of Bechtel Jacobs Company, LLC, was formally transferred to Oak Ridge National Laboratory on August 1, 2002, as a result of agreements reached between Bechtel Jacobs Company, the management and integration contractor at the East Tennessee Technology Park (formerly the Oak Ridge Gaseous Diffusion Plant or Oak Ridge K-25 Site); UT-Battelle, the management and operating contractor of Oak Ridge National Laboratory; and the U.S. Department of Energy (DOE) Oak Ridge Operations Office.

Research emphasis during the last year has been directed toward the development of high-permeance (high-flux) and high-separation-factor metal-supported membranes. Performance data for these membranes are presented and are compared with performance data for membranes previously produced under this program and for membranes produced by other researchers. New insights into diffusion mechanisms are included in the discussion. Fifteen products, many of which are the results of research sponsored by the DOE Fossil Energy Advanced Research Materials Program, have been declared unclassified and have been approved for commercial production.

Inorganic membranes with pore sizes less than 1 nm offer many advantages over thin-film palladium membranes and ion-transport membranes for the separation of hydrogen from a mixed-gas stream. In microporous membranes, the flux is directly proportional to the pressure, whereas in palladium membranes it is proportional to the square root of the pressure. Therefore, microporous membranes become the more attractive option for systems that operate at increased pressure. An added feature of the microporous membranes is that their permeance increases dramatically with temperature. Consequently, inorganic membranes have the potential to produce very high fluxes at elevated temperatures and pressures. The membranes can be fabricated from a variety of materials (ceramics and metals) because the separation process is purely physical, not ion transport. Proper material selection can ensure that the membrane will have a long lifetime while maintaining high flux and selectivity. One further advantage is the relatively low cost of microporous membranes. Because their fabrication does not require the use of exotic materials or precious metals, such as palladium, the cost of producing microporous membranes should be low compared with that for palladium membranes.

One disadvantage of microporous inorganic membranes is that they are porous. They can never produce 100% pure gas streams as can thin-film-palladium or ion-transport membranes. However, when microporous membranes are coupled with pressure swing adsorption (PSA), the combined system can produce 100% hydrogen. In this scenario, PSA would only be required to separate the final 1% of the impurities, and the coupling of the two technologies should result in a very compact and efficient separation system.

MEMBRANE FABRICATION

The permeance of a homogeneous membrane is inversely proportional to the membrane thickness. To be effective for gas separations, the mean pore diameter should be 2 nm or less. With such small pores, the membrane must be very thin, preferably less than 2 μm, in order to have the highest flux at the lowest pressure drop. Such a thin membrane is too weak to support itself and it must be applied as a layer onto a strong, porous support material, either metal or ceramic. It is preferable that the separative layer be applied to the inside of the tube for its protection. Metal is preferred for the support tube for several reasons. For example, metal tubes are easier to incorporate into a module. Also, ceramic support tubes can be prone to catastrophic failure. If a tube fails, the broken pieces can result in a cascading effect, causing others to break.

The primary or separative membrane layer can be applied directly to the support tube or to an intermediate layer. A layer having an intermediate pore size applied to the support tube first can provide a better surface for the primary separative layer, resulting in a thinner and more uniform membrane. The primary layer should have a mean effective pore diameter of 10 nm or less and preferably as small as 2 nm. Once the primary layer is in place, various chemical treatments can be used to reduce the effective pore diameter to the desired value (as low as 0.5 nm).

It is extremely difficult to fabricate a membrane with absolutely no defects. Fabricated membranes are evaluated by combining measurements made on them with a model[1] to estimate the percentage of flow through the defects and to estimate the amount that the separation factor would be lowered by their presence. Because a defect can allow the unimpeded flow of both the desired product gas and the undesired gases, the number of defects must be minimized in order to achieve a high separation factor. Several methods have been developed to reduce the effective pore diameter of a defect or to eliminate the defect altogether. These defect repair methods do not significantly reduce the number of small pores and thus do not lower the flux rate of hydrogen through the membrane.

MEMBRANE CHARACTERIZATION AND TESTING

The two most important characteristics of inorganic membranes are permeance and separation factor. Permeance is a measure of the gas flow rate per unit area per unit pressure difference. A more fundamental unit is permeability, which is the permeance multiplied by the thickness of the membrane. In most cases, the thickness of the membrane is not known very accurately and so permeance is a more practical unit.

The separation factor is meaningful only with respect to a mixture of two gases. The ideal separation factor is the ratio of the permeance of the two gases measured at zero pressure, where there is no interaction or momentum exchange between them. Each gas flows through the membrane as if the other gas were not there. The ideal separation factor for a given temperature can be estimated by measuring the permeance of each gas separately as a function of average pressure and extrapolating the permeance to zero average pressure. The ideal separation factor is then the ratio of the zero-pressure permeances.

The transport of gases through membranes behaves differently as the pore diameter is reduced. Gas transport can also be affected by temperature, and a change in temperature can affect diffusion differently at different pore diameters. However, measuring pore diameters that are smaller than 2 nm is extremely difficult. Therefore, it is critically important to be able to follow the changes in the transport mechanisms of different gases during pore-diameter reduction to help determine the extent to which pores have been reduced. A detailed protocol is followed to help follow the changes in transport mechanisms.

Several theoretically based models have been developed to help understand the transport mechanisms. One of the most important is the Hard Sphere Model,[2,3] which combines the effect of the size of the gas molecule with Knudsen diffusion. Separation by Knudsen diffusion generally treats gas molecules as points having no molecular dimensions. In reality, the diameter of a pore appears to the molecule to be the pore diameter minus its own diameter (or its equivalent hard sphere). Without taking into account the molecular diameter, the separation factor for free molecule diffusion (Knudsen flow) is the square root of the molecular weight ratio. With the molecular diameter consideration, the separation factor for free molecule diffusion (Knudsen flow) is the square root of the molecular weight ratio (Knudsen separation factor) multiplied by the cube of the ratio of the difference between the pore diameter and the molecular diameter for each molecule. The effects that the molecular diameter and molecular size have on the theoretical separation factor are demonstrated in Fig. 1 with several gas pairs. This model provides a mathematical formula for what is essentially a bridge between the Knudsen separation factor and the molecular sieve separation factor. When the pore diameter becomes equal to or less than the larger of the two molecules, the larger molecule cannot pass through the membrane and the separation factor becomes infinite (as in a molecular sieve). As can be seen in Fig. 1, the larger the difference in the molecular diameters, the larger the pore diameter can be where the separation factor becomes infinite, as is the case

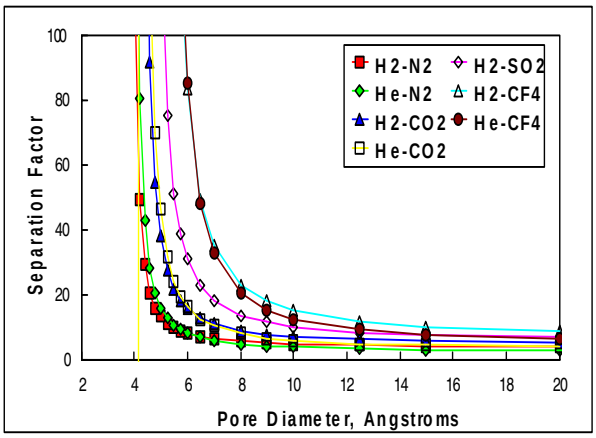

Fig. 1 Separation factors for gas pairs with different relative sizes as a function of pore diameter obtained by using the Hard Sphere Transport Model.

with hydrogen/CF_4 and helium/CF_4. The effective hard sphere diameters, in angstroms, of the molecules used in the calculations for Fig. 1, are as follows: helium 2.58, hydrogen 2.97, nitrogen 3.68, carbon dioxide 3.99, carbon tetrafluoride 4.7, and sulfur dioxide 4.11. The information in Fig. 1 clearly shows that there is a potential for achieving very large separation factors, even at pore diameters larger than the molecular sieve pore diameter, when there is a difference in the molecular diameters of the gas pair.

Free molecule diffusion is not the only transport mechanism. The next most important transport mechanism is surface flow. Surface flow occurs when there is significant adsorption of a gas on the walls of the membrane. While the molecules are adsorbed on the membrane surfaces, they are in motion and can diffuse along the surface. In general, the heavier the molecule or the larger the interaction potential between the membrane surface and the molecule, the larger the adsorption and the more surface flow occurs. Since this transport mechanism favors the heavier molecule, it tends to decrease the separation factor. Surface flow has been included in the full mathematical transport model.[3] However, adsorption and surface flow measurements are required to evaluate constants in the mathematical formulation. To date, these measurements have only been completed for carbon dioxide and an alumina membrane at 25°C. Model calculations were then made for the binary pair (helium and carbon dioxide). Zero surface flow for helium was assumed. The results of these calculations are shown in Fig. 2. As the pore diameter decreases, the gas-phase diffusion decreases and the surface flow increases, primarily because the amount of surface area increases relative to the pore volume. This decrease in flow causes the separation factor to decrease until the pore diameter approaches the diameter of carbon dioxide, at which point the transport of the carbon dioxide decreases sharply while the separation factor increases sharply. The calculation was based on the flow of the

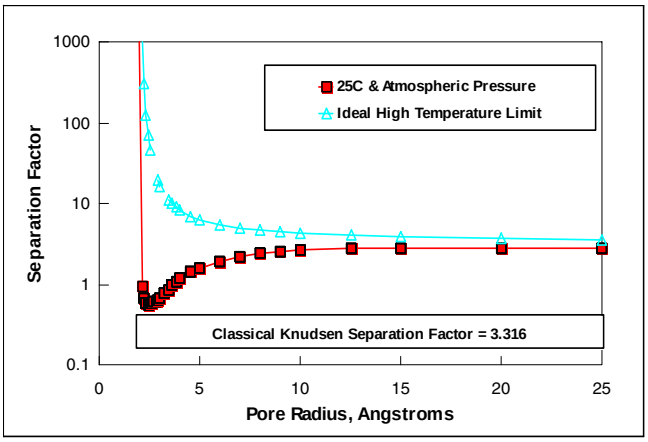

Fig. 2. He-CO_2 separation factors at 25°C calculated from the Full Transport Model compared with the Hard Sphere Free Molecule Diffusion Model.

individual pure gases. It does not take into account the fact that adsorbed carbon dioxide molecules may decrease the effective size of the pore diameter and may thus impede the flow of the helium molecules. Therefore, in a mixed-gas separation, the separation factor may be even smaller than is shown in Fig. 2. It should be pointed out that the separation factor drops below unity and becomes less than one under certain conditions, which means that the carbon dioxide permeance is larger than the helium permeance.

PERMEANCE MEASUREMENTS

Rapid and highly accurate permeance measurements are the heart and soul of our membrane development management protocol. Single-point permeance measurements are of little value. Permeance is measured as a function of average pressure. A linear regression of permeance vs average pressure provides valuable information (we use the sum of the feed pressure and permeate pressure, which is twice the average pressure, and refer to it as Σ P or pressure summation). Initial testing is performed with air at room temperature. A series of 5 to 25 permeance measurements is made over an average pressure range from about 50 to 200 cm Hg. A linear regression is calculated, and then calculations are made of zero permeance, a permeance deviation factor, and the permeance at an average pressure of 75 cm Hg. The permeance deviation factor is the ratio of the slope of the linear regression to the zero-pressure permeance. A positive value may indicate viscous flow from defects in the membrane. These measurements are made on the membrane at every stage of development.

Membranes that show promise, by having a small permeance deviation factor, go to the next level of permeance testing, where permeance measurements are made over the same average pressure range but at more than one temperature, typically 25, 150, and 250°C. This series of measurements is made with three or four pure gases selected from helium, hydrogen, oxygen, argon, carbon dioxide, carbon tetrafluoride, and sulfur hexafluoride. A linear regression with pressure summation (sum of feed and permeate pressure) is made at each temperature and for each gas. The ideal separation factor for each gas with respect to helium is calculated from the zero-pressure permeances. The ideal separation factor is extrapolated to $1/T = 0$. At infinite temperature ($1/T = 0$), no adsorption would be expected. Therefore, the flow is primarily free molecule diffusion. The equation used to calculate the results in Fig. 1 can be used with the ideal separation factor at $1/T = 0$ and the molecular diameters to calculate a mean pore diameter for the membrane. While the accuracy of this pore diameter calculation is unknown, it does provide a parameter to track the progress in reducing the membrane pore diameter.

RESULTS

Helium has been found to behave similarly to hydrogen in microporous membranes and is much safer to use in the laboratory. Therefore, most of our preliminary testing has employed helium as a surrogate

for hydrogen. Because much of our testing is completed at temperatures less than 250°C and because sulfur hexafluoride is more inert than most hydrocarbons or carbon dioxide, sulfur hexafluoride is often employed to simulate larger hydrocarbons that may be present in a gas stream.

Only the membranes that showed promise (i.e., small permeance deviation factor) in the testing with air at room temperature were subject to testing with multiple gases at higher temperatures. Results of selected membranes from recent membrane development work are presented in Tables 1, 2, and 3. Table 1 lists the permeance of helium, oxygen, carbon dioxide, and sulfur hexafluoride at two temperatures. The data is listed in reverse chronological order with the most recent work at the top of table and the data at the bottom of the table being from early in 2002. Ideal separation factors were calculated from the data for each of the gas pairs (He/O_2, He/CO_2, and He/SF_6) at both temperatures and are presented in Table 2. Of special note is how much better the most recent membranes perform. Recent membranes were found to have ideal separation factors of helium from sulfur hexafluoride over 30 at room temperature and over 100 at 250°C. Work earlier in the year resulted in He/SF_6 separation factors

Table 1. Permeance data of three gases for a series of membranes at room temperature and at 250ºC ($scm^3/cm^2 \cdot s \cdot cm\ Hg$)

Tube	He Permeance		O_2 Permeance		CO_2 Permeance		SF_6 Permeance	
	23°C	250°C	23°C	250°C	23°C	250°C	23°C	250°C
25227a	6.71e-04	3.20e-03	2.48e-04	6.56e-04	9.42e-04	1.04e-03	6.58e-05	7.77e-05
2528b	8.77e-04	5.03e-03	2.79e-04	1.16e-03	1.20e-03	1.76e-03	1.86e-05	3.65e-05
5021b	5.93e-04	3.22e-03	2.67e-04	8.27e-04	1.86e-03	1.28e-03	1.66e-05	2.39e-05
5022a	1.67e-03	5.71e-03	1.19e-03	1.83e-03	6.77e-03	2.88e-03	1.26e-04	1.32e-04
2527b	5.30e-04	3.36e-03	1.24e-04	6.46e-04	5.29e-04	9.35e-04	2.86e-05	3.93e-05
2527a	1.22e-03	4.36e-03	6.00e-04	1.04e-03	2.78e-03	1.54e-03	7.29e-05	8.85e-05
5021a	1.59e-03	4.44e-03	1.10e-03	1.40e-03	5.43e-03	2.14e-03	2.42e-04	1.57e-04
25221a	5.11e-04	2.96e-03	2.79e-04	6.86e-04	1.41e-03	1.06e-03	7.27e-05	5.61e-05
25210a	1.56e-03	4.62e-03	8.72e-04	1.23e-03	4.57e-03	1.82e-03	8.35e-05	1.17e-04
2525a	1.93e-03	5.79e-03	1.89e-03	1.86e-03	1.04e-02	2.85e-03	1.67e-04	9.47e-05
108b	2.46e-04	6.51e-04	8.37e-05	1.06e-04	7.50e-05	9.61e-05	4.35e-05	5.01e-05
60b	4.06e-04	4.10e-04	1.54e-04	1.45e-04	1.49e-04	1.24e-04	9.47e-05	7.15e-05
106a	1.24e-03	2.49e-03	1.09e-03	1.79e-03	1.96e-03	2.14e-03	7.96e-04	8.76e-04
108a	1.15e-03	3.19e-03	4.55e-04	7.65e-04	6.46e-04	7.83e-04	2.94e-04	3.05e-04
5426a	4.52e-05	6.37e-05	1.83e-05	1.82e-05	3.06e-05	1.84e-05	1.06e-05	9.30e-06
54212A	1.05e-03	2.32e-03	1.78e-03	2.07e-03	9.61e-03	3.10e-03	7.74e-04	7.05e-04
12305422B	8.70e-05	1.30e-04	3.37e-05	4.85e-05	3.48e-05	4.25e-05	1.76e-05	2.14e-05
12305429A	1.40e-03	4.39e-03	1.12e-03	1.65e-03	6.39e-03	2.59e-03	4.62e-04	2.57e-04
1230530-94A	2.20e-02	2.65e-02	8.35e-03	8.40e-03	9.13e-03	7.42e-03	5.00e-03	3.68e-03
1230530-109A	3.13e-03	4.54e-03	1.82e-03	1.43e-03	7.96e-03	2.02e-03	2.76e-04	2.31e-04
1230530-89B	1.39e-02	1.78e-02	6.45e-03	5.93e-03	1.16e-02	5.65e-03	4.44e-03	2.45e-03
1230530-89A	2.07e-02	2.59e-02	1.06e-02	1.31e-02	1.72e-02	1.31e-02	8.07e-03	5.66e-03
1230530-86a	9.74e-03	1.54e-02	5.61e-03	6.19e-03	1.22e-02	6.58e-03	3.63e-03	2.36e-03
1230530-16A	4.25e-02	4.92e-02	4.16e-02	4.48e-02	5.06e-02	4.39e-02	5.11e-02	4.13e-02

Table 2. Ideal separation factors for He and a second gas at two temperatures

Tube	Ideal Separation Factor for He/Gas					
	O_2		CO_2		SF_6	
	23°C	250°C	23°C	250°C	23°C	250°C
25227a	2.70	4.87	0.71	3.08	10.20	41.16
2528b	3.15	4.33	0.73	2.85	47.18	137.85
5021b	2.22	3.89	0.32	2.51	35.68	134.86
5022a	1.40	3.12	0.25	1.98	13.18	43.36
2527b	4.28	5.20	1.00	3.59	18.54	85.46
2527a	2.03	4.20	0.44	2.83	16.72	49.32
5021a	1.45	3.18	0.29	2.08	6.56	28.30
25221a	1.83	4.31	0.36	2.79	7.03	52.70
25210a	1.78	3.74	0.34	2.54	18.63	39.39
2525a	1.02	3.10	0.19	2.03	11.58	61.14
108b	2.93	6.11	3.27	6.77	5.65	12.99
60b	2.64	2.82	2.73	3.32	4.28	5.74
106a	1.14	1.39	0.63	1.16	1.55	2.84
108a	2.53	4.17	1.79	4.08	3.92	10.47
5426a	2.46	3.51	1.48	3.47	4.25	6.87
54212A	0.59	1.12	0.11	0.75	1.36	3.28
12305422B	2.58	2.68	2.50	3.06	4.94	6.06
12305429A	1.25	2.66	0.22	1.69	3.03	17.06
1230530-94A	2.64	3.15	2.41	3.57	4.40	7.21
1230530-109A	1.72	3.18	0.39	2.25	11.37	19.66
1230530-89B	2.15	3.00	1.20	3.15	3.13	7.28
1230530-89A	1.95	1.98	1.20	1.98	2.56	4.58
1230530-86a	1.74	2.49	0.80	2.34	2.69	6.54
1230530-16A	1.02	1.10	0.84	1.12	0.83	1.19

mostly in the single digits and often less than would be expected from Knudsen diffusion. The large improvement in the separation factor is believed to be attributable to a recent improvement in the process to eliminate defects. For ideal free molecule diffusion, the ratios of the permeances predict Knudsen separation factors of 3.316 for He/CO_2, 2.827 for He/O_2, and 6.041 for He/SF_6. An ideal separation factor greater than this indicates a higher-than-expected separation factor than would be predicted if Knudsen diffusion alone were the mechanism governing gas flow through these fine pores.

Table 1 also shows how the permeance consistently increased as the temperature increased for all gases except the carbon dioxide. Depending on the membrane, the permeance of carbon dioxide sometimes increased and sometimes decreased with increasing temperature. This is believed to be a function of the amount of surface flow occurring along the walls of the pores at room temperature. An increase in permeance with temperature is contrary to what would be predicted if transport were governed by Knudsen diffusion. This phenomenon is believed to be caused by a thermally activated diffusion process that is not well understood at this time. One interesting feature of this mechanism is that it does not seem to affect all gases in the same way. With the most recent membranes (e.g., 2528b and 5021b),

Table 3. Pore diameter of membrane calculated from measured separation factors of helium and each gas and the Hard Sphere Model (angstroms)

Tube	CO_2	SF_6	O_2
25227a	5.50	6.69	5.19
2528b	5.74	6.34	6.34
5021b	5.04	6.24	5.70
5022a	5.18	6.82	5.49
2527b	5.60	6.30	6.28
2527a	5.13	6.83	5.14
5021a	5.27	6.87	5.50
25221a	5.00	6.25	4.88
25210a	5.08	7.36	5.29
2525a	4.93	6.36	4.87
108b	5.70	8.95	4.69
60b	13.66	30.71	34.51
106a	–46.89	273.62	–3.25
108a	6.29	9.00	5.73
5426a	6.57	15.76	7.16
54212A	6.97	20.45	–24.93
12305422B	15.75	36.74	–395.96
12305429A	5.35	6.98	6.05
1230530-94A	9.04	14.85	11.13
1230530-109A	5.45	8.84	6.09
1230530-89B	6.47	10.99	8.68
1230530-89A	17.94	22.48	–5.28
1230530-86a	6.84	11.25	11.04
1230530-16A	–4.58	–3.69	–0.26

the permeance of helium increased by a factor of between five and six when the temperature was increased to 250°C while the permeance of sulfur hexafluoride only increased by a factor of less than two. It may be possible to take advantage of this phenomenon, which only appears to occur in very fine pores (or at least is much more pronounced in fine pores). Adjustment of the temperature may result in both an increase in hydrogen flux rate and an increase in the separation factor.

The separation factors extrapolated to $1/T = 0$ and the Hard Sphere Model were used to calculate pore diameter (see Table 3). It is clear from the results that the Hard Sphere Model does not always accurately describe the transport of molecules through these small pores. The model does not incorporate surface diffusion, nor does it account for the increase in permeance that was found when the temperature was increased. More work will be needed to better understand these mechanisms so that they can be incorporated into an expanded, more comprehensive predictive model.

CONCLUSIONS

Much of the work during the past year has been directed toward increasing membrane permeance, achieving repeatability with defect-free membranes, and using materials and techniques that can be approved by the DOE review process and manufactured on a large scale. Significant progress has been made in all these areas. We are significantly expanding our understanding of gas transport in inorganic membranes. Recent results have shown ideal separation factors for helium over sulfur hexafluoride of more than 45 at 23°C and more than 140 at 250°C. Also, it has been observed that the permeance of helium increases significantly with increasing temperature. As a result, even higher permeance and separation factors should be attainable at higher operating temperatures.

Future work will include testing some of the new membranes that have shown high ideal separation factors for helium over sulfur hexafluoride with hydrogen to confirm that our results also apply to hydrogen. Also, efforts will be made to test the best membranes at temperatures approaching 600°C to empirically determine how much the permeance and separation factors increase with increasing temperature. Finally, the membranes need to be evaluated under simulated coal-derived synthesis gas conditions to determine their actual separation performance and long-term stability.

ACKNOWLEDGMENTS

This research was sponsored by the U.S. Department of Energy, Office of Fossil Energy Advanced Research Materials Program, DOE/FE AA1510100, and Work Breakdown Structure Element IMTL-3 (B). Oak Ridge National Laboratory is managed by UT Battelle, LLC, for the U. S. Department of Energy under contract DE-AC05-00OR22725. Accordingly, the U.S. Government retains a nonexclusive, royalty-free license to publish or reproduce the published form of this contribution, or allow others to do so, for U.S. Government purposes.

REFERENCES

1. D. E. Fain and G. E. Roettger, *Effects of Leaks on Gas Separation Performance of A Nano Pore Size Membranes*, K/TSO-24, Lockheed Martin Energy Systems, Inc. Oak Ridge, K-25 Site, Oak Ridge, Tennessee, October 1996.
2. D. E. Fain and G. E. Roettger, "Development of Ceramic Membranes for Gas Separation," *Proceedings for the Fourth Annual Conference on Fossil Energy Materials*, Oak Ridge, Tennessee, May 15–17, 1990, pp. 183–94.
3. D. E. Fain, G. E. Roettger, and D. E. White, "Development of Ceramic Membranes for High Temperature Hydrogen Separation," *Proceedings for the Fifth Annual Conference on Fossil Energy* Materials, Oak Ridge, Tennessee, May 14–16, 1991, pp. 55–64.

DEVELOPMENT OF NOVEL ACTIVATED CARBON COMPOSITES

O. O. Omatete, T. D. Burchell, A. W. Gabbard, M. R. Rogers, and R. R. Judkins
Oak Ridge National Laboratory

INTRODUCTION

The development of a novel activated carbon composite, carbon fiber composite molecular sieve (CFCMS), at the Oak Ridge National Laboratory has been discussed in earlier reports. Here, we report the investigation of CO_2 capture and separation from feed gases of varying CO_2 concentrations using CFCMS. The effect of varying the property of the CFCMS, characterized by the percent of the material that was burned-off during its activation, on the capture and separation of CO_2 was investigated. Because of the high thermal and electrical conductivity of the CFCMS, a new process named "electrical swing adsorption" (ESA) was developed. In the ESA process, a large amount of the adsorbed CO_2 can be desorbed by the application of a low voltage across the adsorbent. Several regeneration processes were examined in order to demonstrate and understand the ESA process.

PROCEDURE

Cylindrical billets of CFCMS, ~4.5-inches in diameter by lengths varying form 7.5 to 10 inches depending how much material was formed and on the percentage of it that was burnt-off, were processed. The burn-off amount varied from 19.0 to 42.9% resulting in different void fractions, capacities and other properties. Each cell was prepared by machining the CFCMS billet down to a diameter of 4.25 inches so that electrodes can be attached to it to power the cell during regeneration. The design is such that the feed gas has a mixing chamber both at the entrance to and exit from the cylindrical cell. The electrodes and other required mountings were shrink-wrapped onto the cell to form an airtight system. The sketch of the CFCMS cell is shown in Fig. 1. The cell was then mounted into the modified gas flow loop shown in Fig. 2. Flow through the cell can be reversed. There is a by-pass that carries the feed gas directly to the sampling system, which consists of a real-time mass spectrometer, residual gas analyxer, and a real-time CO_2 analyzer.

The feed gas is passed through the cell and then to the sampling system. The flow rate in and out of the cell and the pressure drop across it are measured. The inlet gas temperature, the temperature, one inch into either end of the cell, and the temperature on the outside of the cell can all be recorded. The inlet gas pressure is usually set at 10 psig at the compressed cylinder and the gas was carried in 0.375-inch (9.5 mm) stainless steel piping about 20 feet (~6.1 m) to the entrance of the CFCMS cell. All the experiments were run at ambient temperature unless otherwise stated.

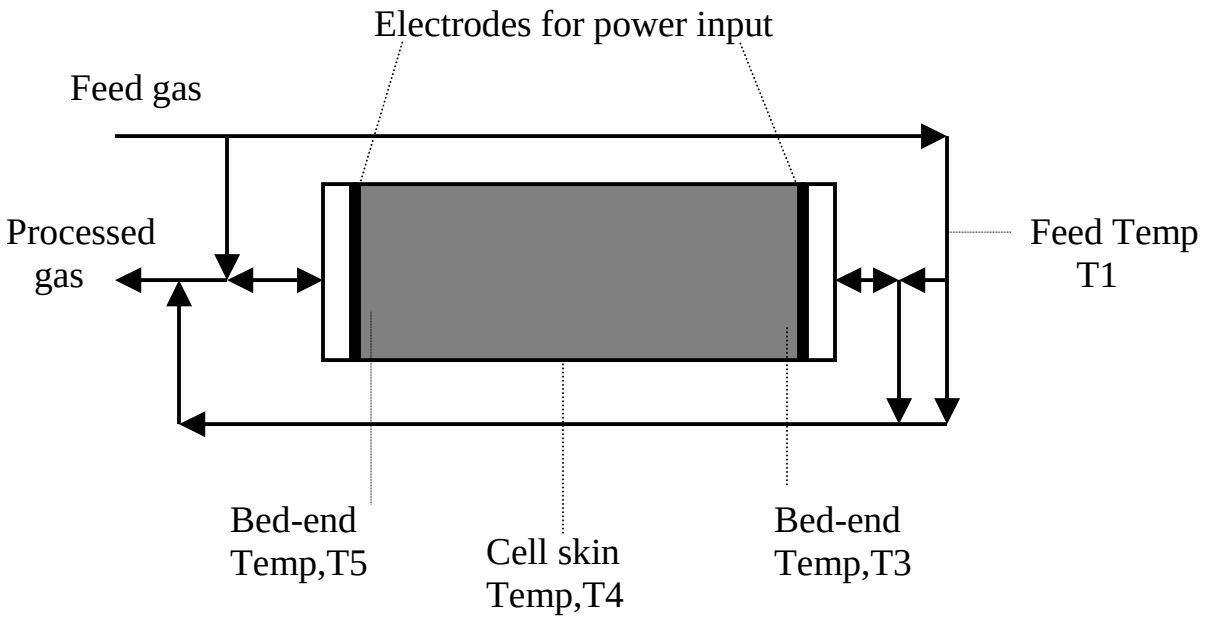

Fig. 1. The schematic of the CFCMS cell set-up.

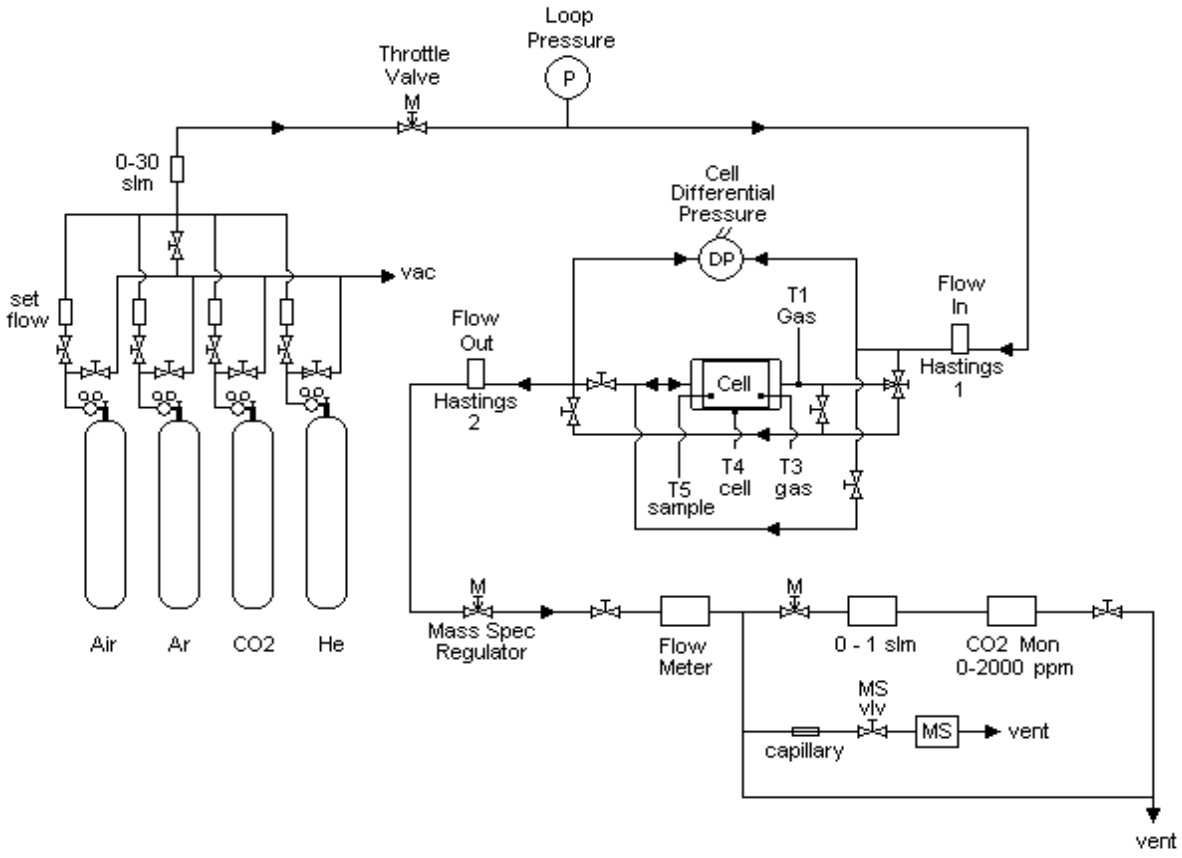

Fig. 2. The modified gas flow loop.

Two methods of attaching the electrode to the cell have been investigated. Their design is illustrated in Fig. 3(a) and 3(b), showing only an end of the cell. The first electrode was made of copper and the second was made of steel wire mesh.

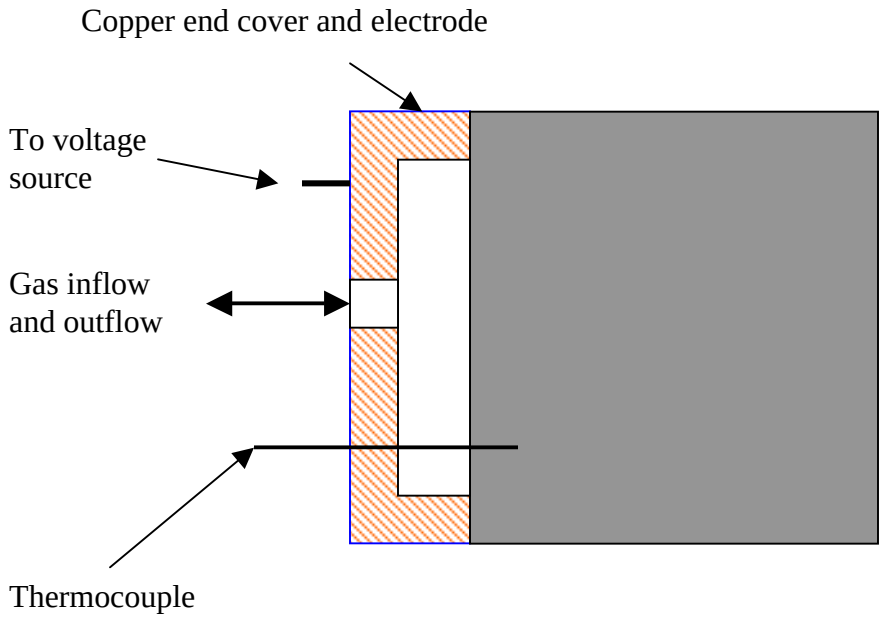

(a)

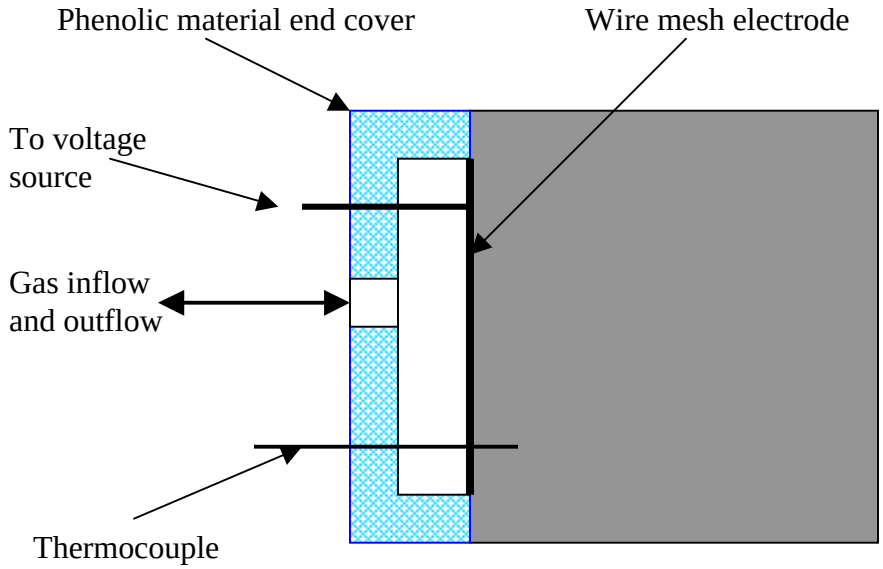

(b)

Fig. 3, (a) Schematic of a cell end showing copper end cover as an electrode. (b) Schematic of a cell end showing phenolic end cover and wire mesh electrode.

To make the copper electrode, a piece of copper disc was machined as the end cover for the CFCMS billet and to provide for gas mixing at the entrance and exit of the cell. The edge of the copper forms a ring pressing on the CFCMS and this becomes the electrode through which power is supplied to the cell. This is shown in Fig. 3(a). The end cover is then shrink-wrapped over the CFCMS billet to form the cell.

Figure 3(b) shows the schematic for the wire mesh electrode. The end cover here is fabricated from a non-conducting phenolic material. The electrode is a disc cut from a stainless steel wire mesh. The mesh sits on the CFCMS material and is held on by the end cover. The end cover is shrink-wrapped over the CFCMS cell to form the cell. The wire mesh electrode design is preferred and is now used in all the experiments

Three parameters were set during each experiment: the feed composition, the feed flow rate, and the CFCMS percent burn-off. The CO_2 composition in the feed varied from ~400 ppm in compressed air to pure CO_2. The feed rates were from a fraction of a liter to 20 liters per minute (l/m) and the CFCMS burn-off varied from 19.0 to 42.9 %. CO_2 breakthrough curves were run at a set of these parameters and from them the amount of CO_2 adsorbed was calculated per gram or liter of the CFCMS adsorbent. The results of some of these experiments are reported below.

RESULTS AND DISCUSSIONS

Figures 4 and 5 show the breakthrough curves for a feed containing 10 mol% CO_2 flowing through a cell of 24.8% burn-off CFCMS at 2 l/m. Figure 4 is the breakthrough curve measured by the CO_2 monitor with a capacity limit of 20,000 ppm (2%). Figure 5 is the same breakthrough measured by the Residual Gas Analyzer and it shows all the other gases in the feed. Figure 4 indicates how the total gas scrubbed is calculated, and from this, the amount of CO_2 adsorbed is computed. Figure 4 also shows the temperature variation at the ends of the cell due to the heat of adsorption/desorption.

Similar breakthrough curves were run at 2 l/m for feed with varying compositions of CO_2: ~400 ppm (air), 3 mol %, 10 mol%, 19.5 mol% and pure CO_2 through cells with 24.8% and 37.8% burn-off CFCMS, respectively. The result is summarized in Fig. 6. The graph shows that whereas the specific adsorption of CO_2 by the CFCMS is dependent on the CO_2 feed composition, the relationship is not linear.

Breakthrough curves were run for a 10-mol% CO_2 feed at several flow rates varying from 1.0 to 20.0 l/m through cells containing CFCMS activated to four different % burn-off's. The results are summarized in Fig. 7. These results indicate that the dynamic capacity (g CO_2 adsorbed/g of CFCMS) of the CFCMS adsorbent is dependent on both the flow rate and the treatment (% burn-off) of the CFCMS. The results also indicate that optimum capacity in these runs was at feed flow rate of 10 l/m and for CFCMS activated between 25 and 35 % burn-off.

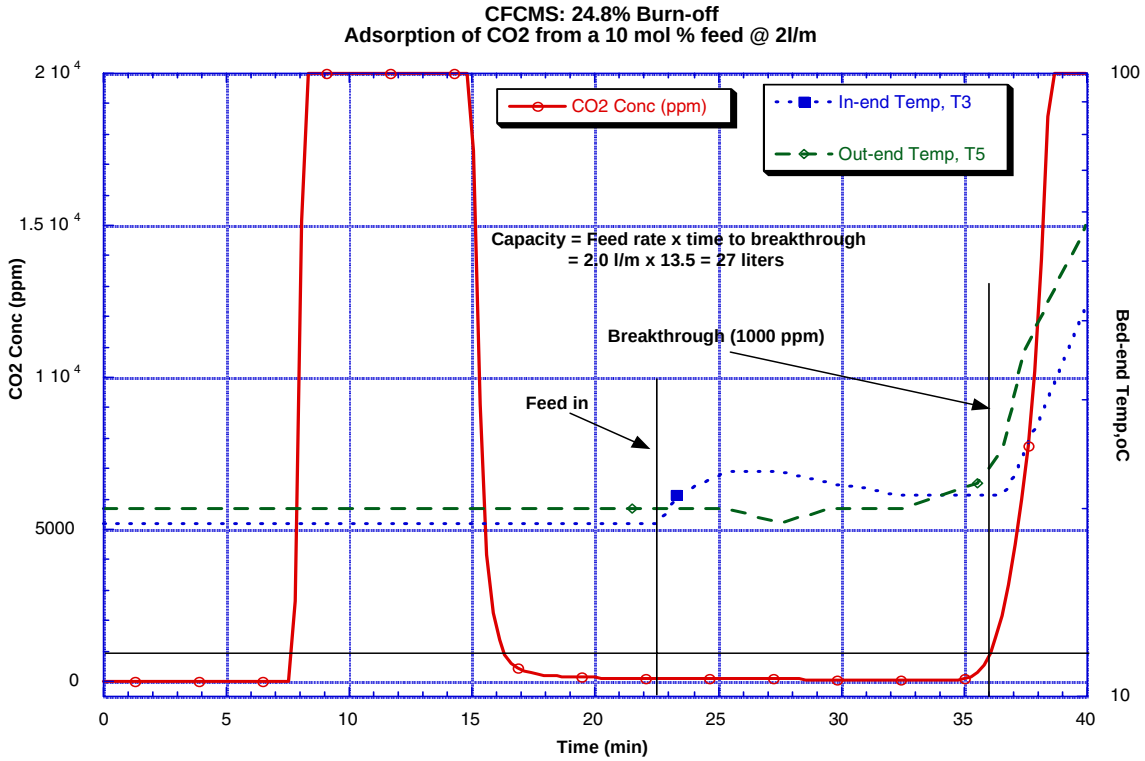

Fig. 4. Breakthrough curve on the CO_2 monitor for 10% CO_2 feed at 2 l/m.

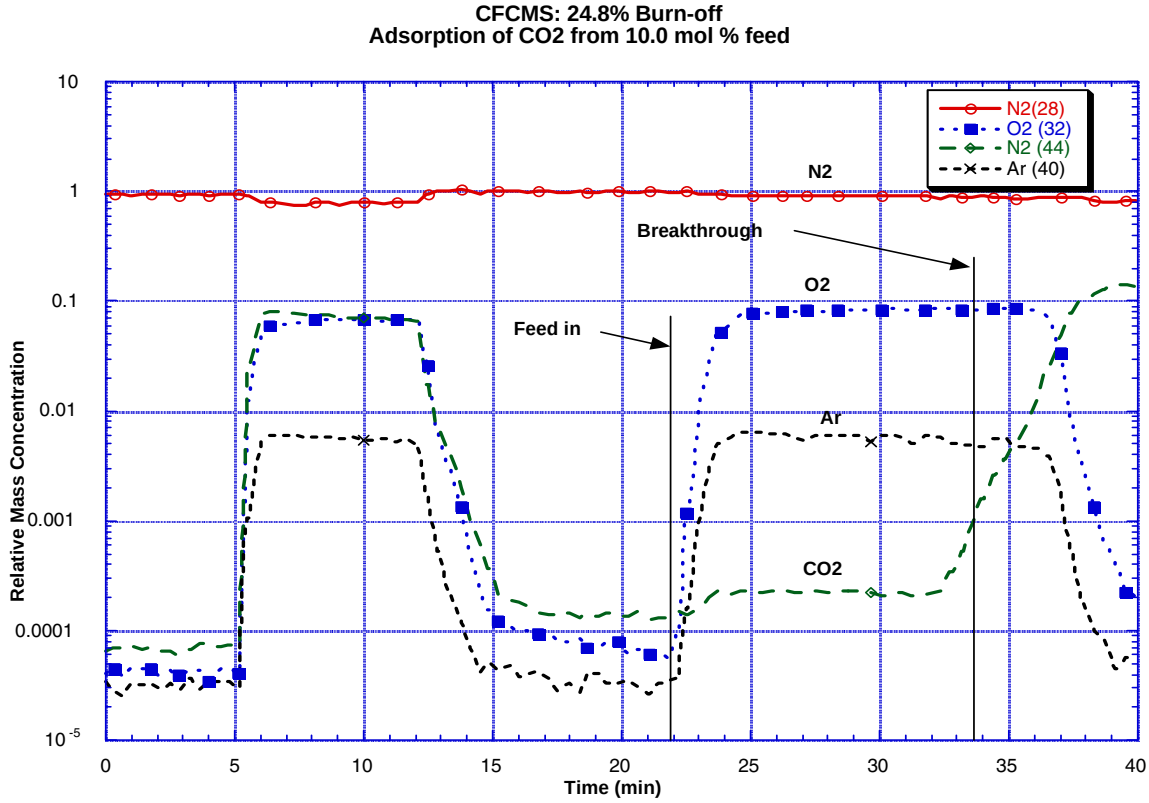

Fig. 5. Same breakthrough as in Fig. 4 but measured by the residual gas analyzer.

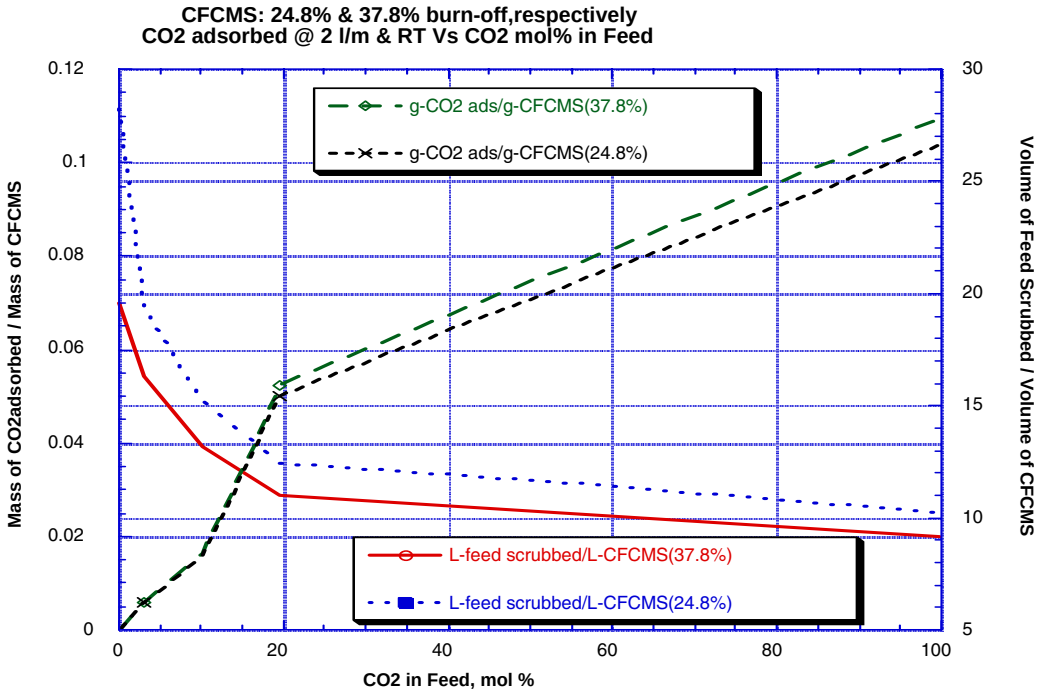

Fig. 6. Specific adsorption of CO_2 vs CO_2 mol% in the feed.

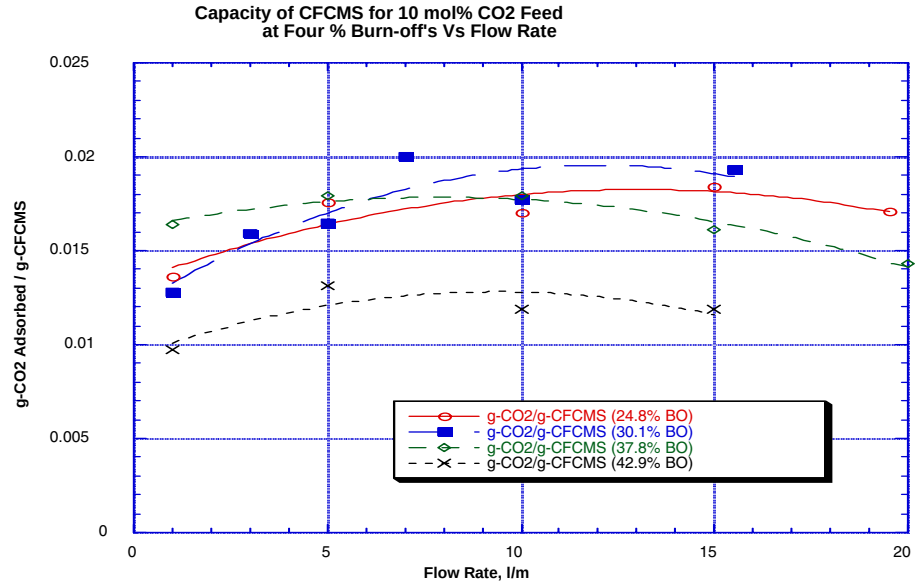

Fig. 7. Specific adsorption of CO_2 at four CFCMS treatments vs flow rate.

Pressure drop is an important parameter in determining the energy requirements for the flow through the cell. The pressure drop across the cell was measured during all the experiments. For all the four treatments (% burn-off) and flow rate 1–20 l/m, the pressure drop ranges from 0.003 to 0.02 psi/inch. The pressure drop is low because the CFCMS material is very porous with typical bulk density varying between 0.16 g/cc and 0.18 g/cc.

Regeneration is an essential step in using the CFCMS in a sorption process. Therefore, for a the CFCMS/ESA process to be viable, a well-defined regeneration step must be developed and optimized so that it consumes minimum energy and regenerant Consequently, several regeneration steps were investigated after the cell was saturated (CO_2 breakthrough at 350 ppm) at 5 l/m and feed flow stopped. N_2 flow at 1 l/m was used to complete the regeneration. The amount of N_2 required to complete the regeneration indicated the efficiency of the regeneration process.

1. **Temperature only.** Low voltage was passed through the cell until the temperature reached 70°C and was maintained there for several minutes. The flow through the cell was negligible. The N_2 needed for regeneration to complete the cycle indicated that the regeneration was very inefficient.
2. **Power only.** Low voltage was passed through the cell for 5 minutes as its temperature rose. No flow was detected. The regeneration was very inefficient.
3. **Temperature and Vacuum.** The cell temperature was raised to 70°C and maintained while the cell was put under full vacuum. There was some flow that resulted in some CO_2 removal. This process was more efficient that the first two.
4. **Vacuum only.** The cell was put under full vacuum for 5 minutes and its temperature fell. This process was more efficient than the first two but was worse than process 3.
5. **Power and Vacuum.** Low voltage was passed through the cell simultaneous with full vacuum on it. This was the most efficient regeneration process.

In all the processes, N_2 or an inert gas was needed to complete the regeneration cycle and prepare the cell for the next adsorption step. Furthermore, it seemed that only negligible pure CO_2 was produced in any of the processes. Consequently, the regeneration step requires further investigation in the CFCMS/ESA process.

CONCLUSIONS

1. Carbon fiber composite molecular sieve (CFCMS) adsorbs CO_2 completely from all feed gases until breakthrough occurs. The amount of feed gas scrubbed depends on the concentration of CO_2 in it.

2. The dynamic capacity of the CFCMS depends on both the treatment (%burn-off) of the CFCMS and the feed flow rate. The highest capacity was at feed flow rate of 10 l/m and CFCMS burn-off at 30 +/- 5%.
3. The pressure drop across the cell was very low varying between 0.003 and 0.02 psi/inch.
4. The most promising regeneration step is one that combines simultaneous power input to and vacuum on the CFCMS cell. However, further investigation is needed here to develop an efficient regeneration step that produces some pure CO_2.

REFERENCES

1. T. D. Burchell, R. R. Judkins, M. R. Rogers, and A. M. Williams, *CARBON* Vol. 35, No. 9, pp. 1279–1294 (1997).
2. T. D. Burchell, Porous Carbon Fiber-Carbon Binder Composites, Chapter 6 of *Carbon Materials for Advanced Technologies*, T. D. Burchell, Editor, pp. 169–203, Pergamon, 1999.
3. T. D. Burchell, in *Fossil Energy Program Annual Progress Report for April 1997 Through March 1998.* **ORNL-6943**, (1998), pp. 45–50.
4. T. D. Burchell, C. E. Weaver, B. R. Chilcoat, F. J. Derbyshire, and M. Jagtoyen, US Patent No. 6,030,698 *Activated Carbon Fiber Composite Materials and Method of Making*, Feb 29, 2000.
5. Roddie R. Judkins and Timothy D. Burchell, US Patent No. 5,972,077 *Gas Separation Device Based on Electrical Swing Adsorption*
6. T. D. Burchell et al., Fossil Energy Program Progress Report, 2001.

ACKNOWLEDGMENTS

Research sponsored by the U.S. Department of Energy, Office of Fossil Energy, Advanced Research Materials Program under contract DE-AC05-00OR22725 with UT-Battelle, LLC, at Oak Ridge National Laboratory.

RELIABILITY AND DURABILITY OF MATERIALS AND COMPONENTS FOR SOLID OXIDE FUEL CELLS

E. Lara-Curzio and M. Radovic
Beth Armstrong, Claudia Walls, Michael Lance, Peter Tortorelli, Shirley Waters, Larry Walker, and Amanda Murphy
Technical Contributors

1. INTRODUCTION

Fuel cells will play an important role in securing the energy future of the U.S. by providing efficient, environmentally friendly electrical energy. The Solid State Energy Conversion Alliance (SECA) is a unique alliance between government, industry, universities and National Laboratories to promote the development of solid oxide fuel cells (SOFC) as an affordable, clean and reliable source of electric power. The goal of SECA is to create solid oxide fuel cells (3–10 KW) that can be mass-produced in modular form at a target cost of $400/KW. As part of SECA's Core Technology Program, ORNL is supporting the industrial development teams to improve the durability and reliability of SOFC materials and components. In this report the results of activities related to evaluation of reliability and durability of materials and components for SOFC conducted at ORNL as part of the SECA Core Technology Program for the period of time of June 1, 2002–June 1, 2003 are presented.

2. CHANGES OF PHYSICAL AND MECHANICAL PROPERTIES DURING REDUCTION OF NIO/YSZ ANODE

One approach for the manufacture of SOFC stacks is based on the co-sintering of electrodes and electrolyte. Since these materials have different mechanical and physical properties, after sintering they will be subjected to residual stresses that could result in cracking and failure of the cell. Even if cells can be successfully co-sintered in air, subsequent processing steps (e.g., the reduction of NiO into Ni in the anode under constraints imposed by electrical interconnects and seals) may induce additional stresses that could compromise the structural and mechanical integrity of the stacks. During reduction, the physical and mechanical properties of the anode will change. Most significant is the shrinkage of the anode associated with the conversion of NiO into Ni. For the purpose of predicting the reliability and durability of SOFs, particularly during this step, it is necessary to quantify how the physical and mechanical properties of the anode change during reduction. During this reporting period a systematic study was initiated to determine and quantify how the physical and mechanical properties of anodes evolve during reduction.

2.1. KINETICS OF NiO/YSZ REDUCTION—THERMOGRAVIMETRIC ANALYSIS

A series of samples were prepared to study the evolution of the physical and mechanical properties of anodes after reduction. The samples consisted of a mixture of 75mol% NiO and the balance of 8mol%YSZ. In order to obtain a porous structure, 30vol% of organic pore former was added. Green samples were prepared by tape casting layers that were subsequently laminated into 1 mm thick specimens. Discs (nominal diameter 25.4 mm) were hot-knifed from the assembled green tapes prior to sintering at 1450°C in air. The porosity of the samples after sintering was determined to be 23.5±0.6 vol% by alcohol immersion according to ASTM standard C20-00.

The reduction of anode materials was studied using a termogravimetric unit with a detection limit of 0.1 mg at 600°C, 700°C, 750°C, and 800°C. Samples were placed on a quartz stand that was hung by a Pt suspension wire from the thermobalance. The stand with one sample was introduced in a reaction tube, which in turn was placed in a furnace. Before heating, the reaction tube was evacuated and then backfilled with argon. The sample was then heated up under a constant flow of argon up to the test temperature. After reaching thermal equilibrium, the gas was changed to a mixture of 4%H_2 and 96%Ar. A constant gas flow rate of 100 cc/min was maintained for the duration of the reduction process and the sample's weight change was recorded using an automatic data acquisition system. In addition to quantify the changes of the structural and mechanical properties as a function of the fraction of reduced NiO, a set of samples was reduced at 800^{o}C for different periods of times.

The fraction of reduced NiO is plotted as a function of time for different reduction temperatures in Fig. 2.1. These curves exhibit two stages: in the first stage the rate of NiO reduction is liner at all

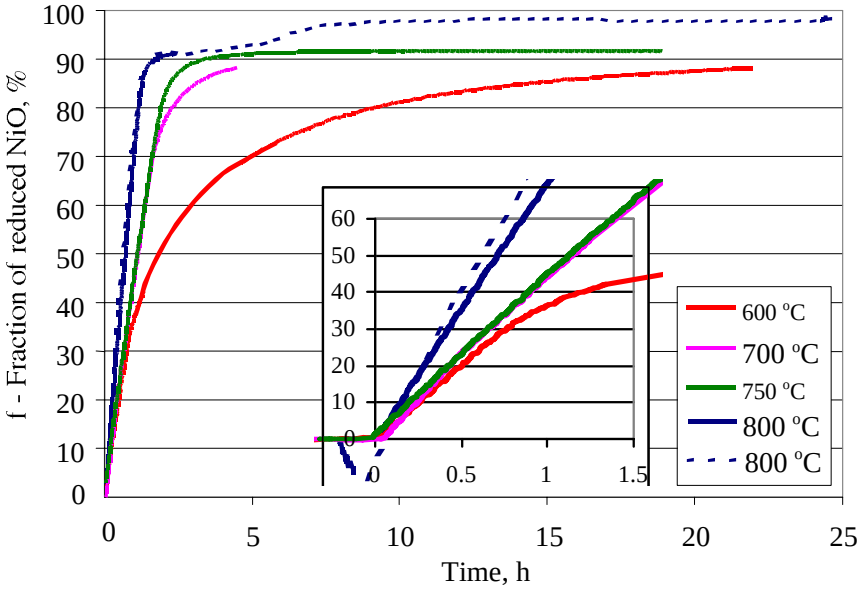

Fig. 2.1. Fraction of reduced NiO vs. time at different temperature. Insert shows magnified initial part of reduction curves.

temperatures above 600°C; in the second stage, the rate of reaction decreases continuously until the fraction of reduced NiO approaches 100%. At 600°C the rate of NiO reduction was found to decrease continuously from the start of the process. The transition from linear kinetics to semi-parabolic kinetics occurs at values of the fraction of reduced NiO that increase with temperature.

Figure 2.2 illustrates the development of the reduced layer on the surface of the anode samples during reduction in a mixture of 4%H_2-96%Ar at 800°C. The gray layers on both sides of the sample correspond to the reduced parts of the anode, while the green region in the center represents the unreduced parts of the anode. Figure 2.3. shows an SEM image, along with the WDS surface analysis of the same area, of a partially reduced NiO/YSZ anode. In this region three phases can be identified in the WDS image, namely NiO, Ni and YSZ, and thus it can be concluded that not all of NiO was reduced in the gray area. These

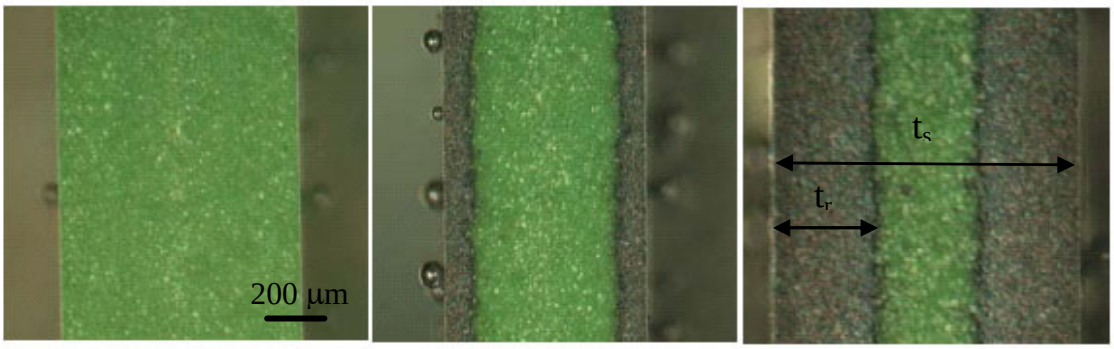

Not reduced

Reduced
at 800 °C for 0.35 h
15.1 % of reduced NiO

Reduced
at 800 °C for 1.01 h
47.3 % of reduced NiO

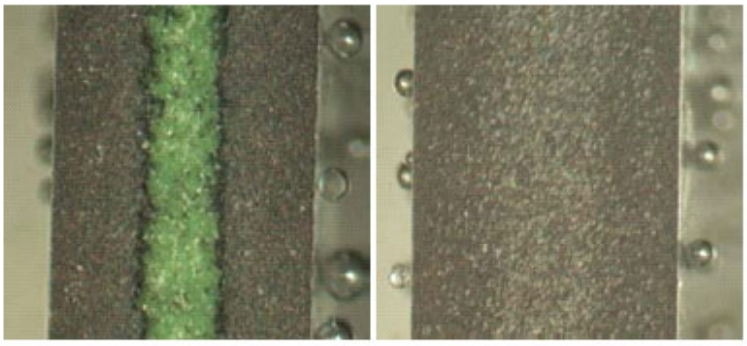

Reduced
at 800 °C for 1.32 h
71.9 % of reduced NiO

Reduced
at 800 °C for 24 h
96.5 % of reduced NiO

Fig. 2.2. Optical micrographs of polished cross-section of samples reduced in gas mixture of 4%H_2-96%Ar at 800°C for different periods of time.

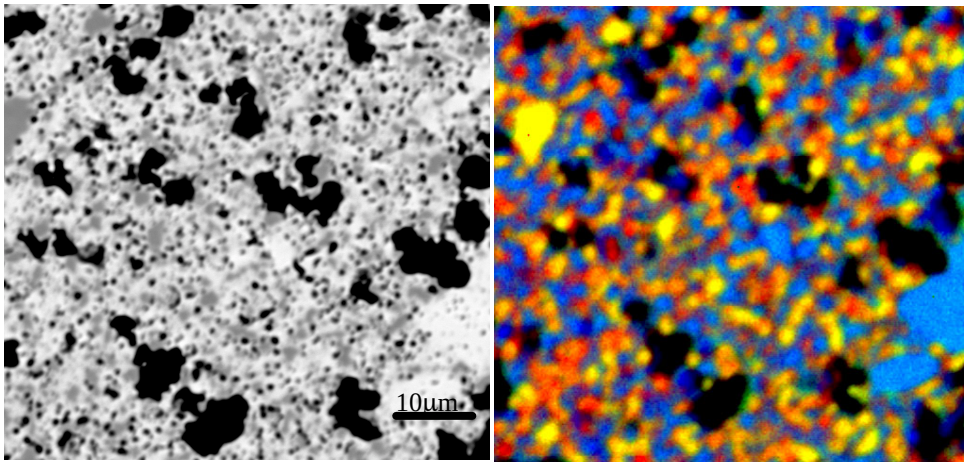

Fig. 2.3. Left: SEM secondary electron image of partially reduced NiO/YSZ anode. Right: WDS surface analysis of the same area. Blue—YSZ, red—pure Ni, yellow—NiO, black—pores. Fraction of reduced NiO in sample is 55 wt%.

results suggest that the partially reduced area grows rapidly at first (according to linear kinetics) and that further reduction of NiO grains, within the partially reduced (gray) area occurs as hydrogen reaches the interior of the sample during the second stage of the curves in Fig. 2.1. Thus, the transition point in the reduction kinetics appears to occur when the reduction fronts meet each other in the middle of the sample. Once this happens, only further reduction of the partially reduced NiO grains takes place at a much slower reduction rate.

The fraction of reduced NiO calculated after reduction for different times at 800°C is plotted in Fig. 2.4. Those data points (represented as blue diamonds) match well the continuous reduction curve obtained at 800°C for 24 hours. An Arrhenius analysis of the reduction rate, which was determined from the slop of the initial part of the ΔW_t vs. time curves showed that the activation energy associated with this process is 25.2 kJ/mol, which is comparable to published data for the reduction of pure NiO [1].

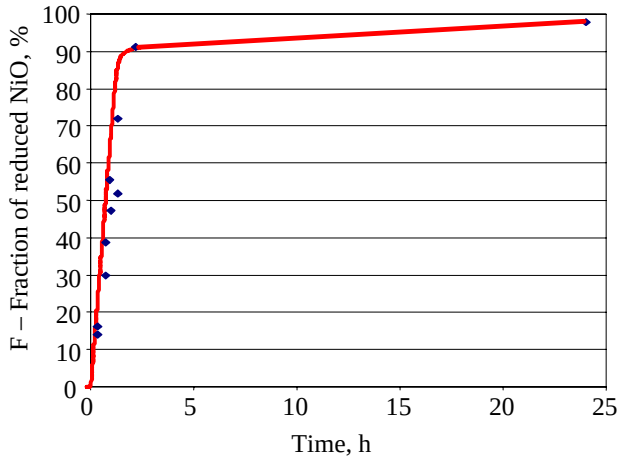

Fig. 2.4. Fraction of reduced NiO vs time at 800°C. Data points correspond to results obtained from interrupted reduction tests.

2.2. CHANGES OF POROSITY DURING THE REDUCTION OF NiO/YSZ ANODE

The porosity of samples after reduction in a gas mixture of 4%H_2-96%Ar was determined by alcohol immersion according to ASTM standard C20-00. Results are plotted in Fig. 2.5 as a function of the fraction of reduced NiO. These results demonstrate that there is a significant increase in the overall porosity of NiO/YSZ anodes as a result of reduction.

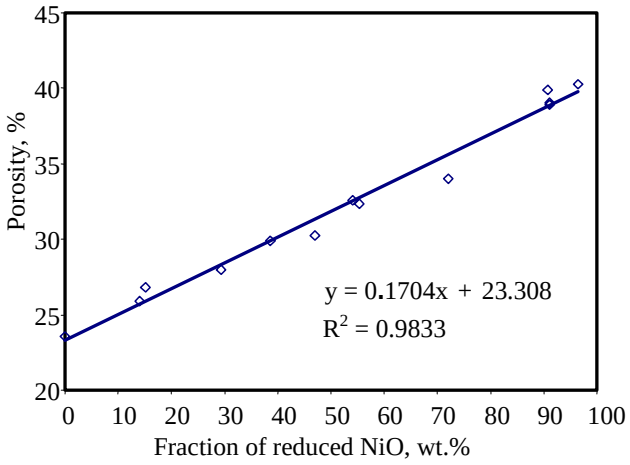

Fig 2.5. Overall porosity of the reduced NiO/YSZ samples as a function of the fraction of reduced NiO

2.3. CHANGES OF ELASTIC PROPERTIES DUE THE REDUCTION OF NiO/YSZ ANODE

The elastic properties of NiO/YSZ samples reduced for different periods of time in a gas mixture of 4%H_2-96%Ar were determined at room temperature by Impulse Excitation (IE) [2]. Young's and shear moduli values for reduced NiO/YSZ anode samples are plotted in Fig. 2.6 as a function of fraction of reduced NiO. These results show that the magnitude of Young's and Shear moduli decreases as the fraction of reduced NiO increases. After complete reduction, the magnitude of the elastic moduli are almost 50% of the values of the unreduced samples NiO/YSZ sample. Such a significant decrease of elastic moduli is a consequence of the increase in porosity and to a lesser degree to the difference in elastic modulus between NiO and Ni.

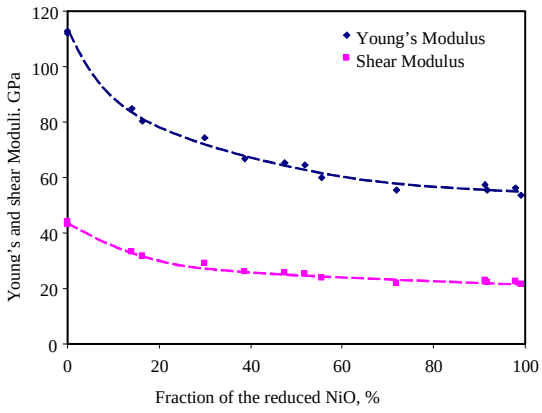

Fig. 2.6. Young's and shear moduli of reduced NiO/YSZ anode samples as a function of fraction of reduced NiO.

2.4. COEFFICIENTS OF THERMAL EXPANSION OF NiO/YSZ, Ni/YSZ, AND YSZ

The coefficients of thermal expansion (CTE) of 8mol% YSZ, 75mol%NiO/YSZ and fully reduced 75mol%NiO/YSZ (further denoted as Ni/YSZ) were determined by dilatometry. The 8mol%YSZ samples were tested in air up to 900°C at a heating rate of 2°C/min. The 75mol%NiO/YSZ sample was first heated in argon up to 800°C. Then, the gas flow was changed from pure argon to a gas mixture of 4%H_2-96%Ar. The length of the specimen was monitored for 24 hrs at 800°C and at the end of the time period the sample was cooled down at a rate of 2°C/min. Measurements of weight changes of the NiO/YSZ sample after reduction confirmed that sample was fully reduced. The coefficient of thermal expansion of 8mol%YSZ was 1.04×10^{-5} K^{-1}. The results for 75mol%NiO/YSZ before and after total reduction were found to be $1.18 \times 10^{-5}K^{-1}$ and $1.27–1.37 \times 10^{-5}K^{-1}$, respectively. These results are comparable to previously reported CTE's of 1.27 10^{-5} K^{-1} for 75mol%NiO/YSZ and 1.17 10^{-5} K^{-1} for NiO/YSZ cermets [3].

2.5. THERMAL DIFFUSIVITY OF NIO/YSZ, NI/YSZ AND YSZ

The thermal diffusivity of 8mol%YSZ and reduced and unreduced 75mol%NiO/YSZ was determined according to the laser flash method [4]. Results of thermal diffusivity measurements are presented in Fig. 2.7.

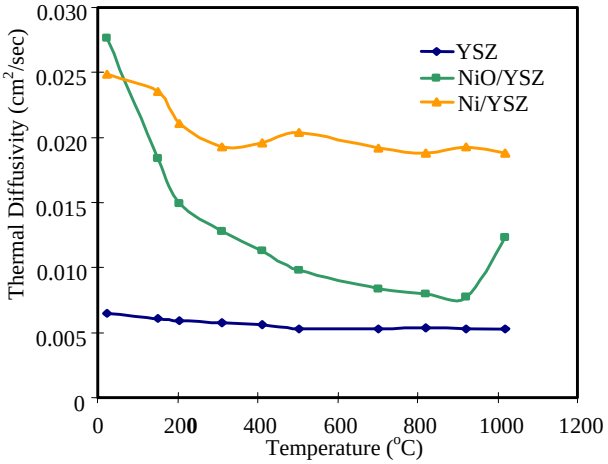

Fig. 2.7. Thermal diffusivity of YSZ, NiO/ YSZ and Ni/YSZ as a function of temperature.

2.6. MONITORING KINETICS DURING IN SITU REDUCTION OF NIO/YSZ USING RAMAN SPECTROSCOPY

Raman spectroscopy was used to monitor chemical changes in NiO/YSZ samples during *in situ* reduction. The experimental setup for in situ monitoring the reduction of NiO/YSZ anode material is schematically shown in Fig. 2.8. Raman spectra of two areas (labeled as 1 and 2 in Fig 2.9) were collected during the reduction process at 400°C. Fig. 2.9 shows optical micrographs and the corresponding Raman spectra as a function of reduction time. Raman spectra of areas 1 and 2 show characteristic peaks for NiO and cubic YSZ in both positions at room temperature and after reduction for 1 min at 400°C. After reduction at 400°C for 10 min the NiO peaks in spectra for area 1 have disappeared, while the peaks for NiO are barely detectable in position 2. After 22 min, only the characteristic peak for YSZ is present in the spectra obtained in position 1. This indicates

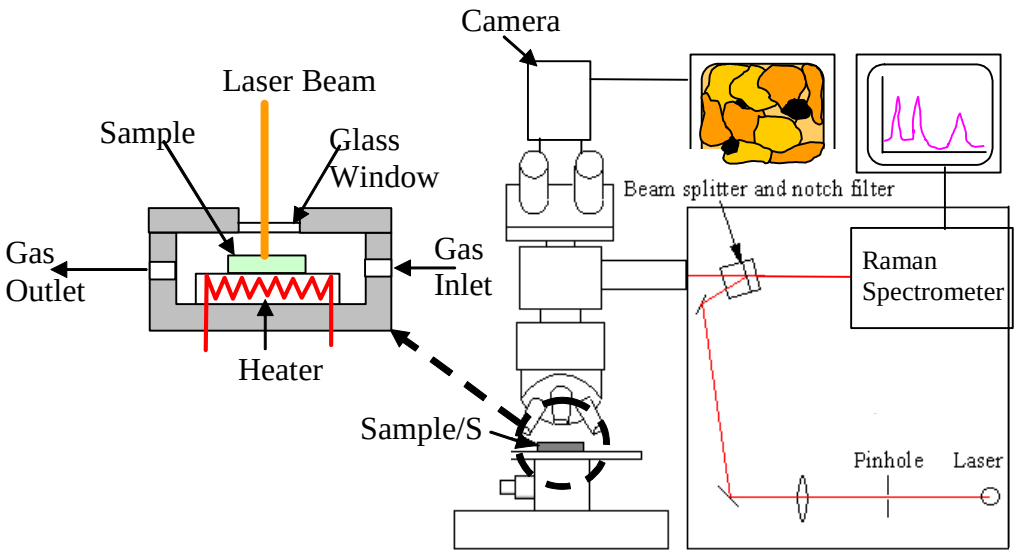

Fig. 2.8. Experimental setup for monitoring *in situ* reduction of NiO/YSZ using Raman Spectroscopy.

that position 2 was initially almost pure NiO, while position 1 was predominately YSZ. It has to be emphasized that these Raman spectra were obtained from the surface of the sample.

2.7. MONITORING STRESSES IN ELECTROLYTE DURING IN SITU REDUCTION OF NIO/YSZ USING RAMAN SPECTROSCOPY.

Attempts were made to monitor the evolution of stresses in 8%YSZ electrolytes bonded to NiO/YSZ anodes during reduction. However, the results from these experiments are still inconclusive since the position (wave number) of the cubic zirconia Raman peak as a function of temperature and stress has not been established yet. The results from these experiments will be valuable to validate predictions of internal stresses in SOFC during anode reduction

Fig. 2.9. Left: Optical micrographs of the NiO/YSZ sample after the different reduction times. Right: Corresponding Raman spectra of areas denoted as 1 (blue) and 2 (magenta) in the optical micrographs. Dashed lines in Raman spectra represent a standard position of Raman peaks for cubic YSZ. Solid vertical line in Raman spectra is a standard position of Raman peaks for NiO.

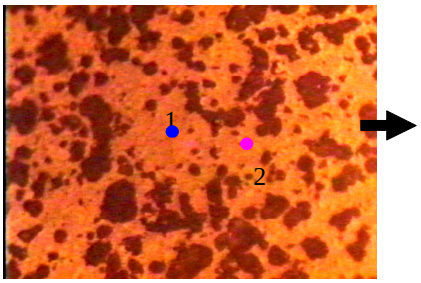

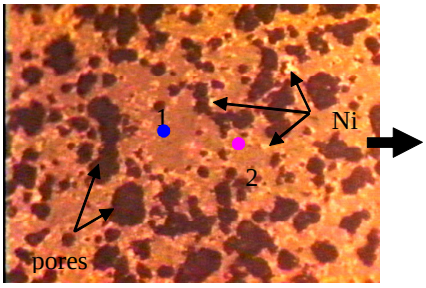

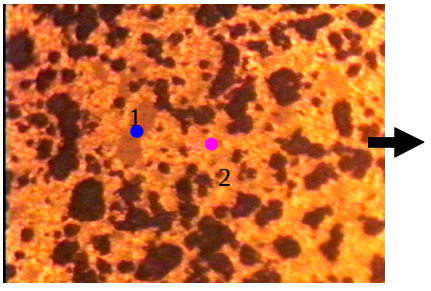

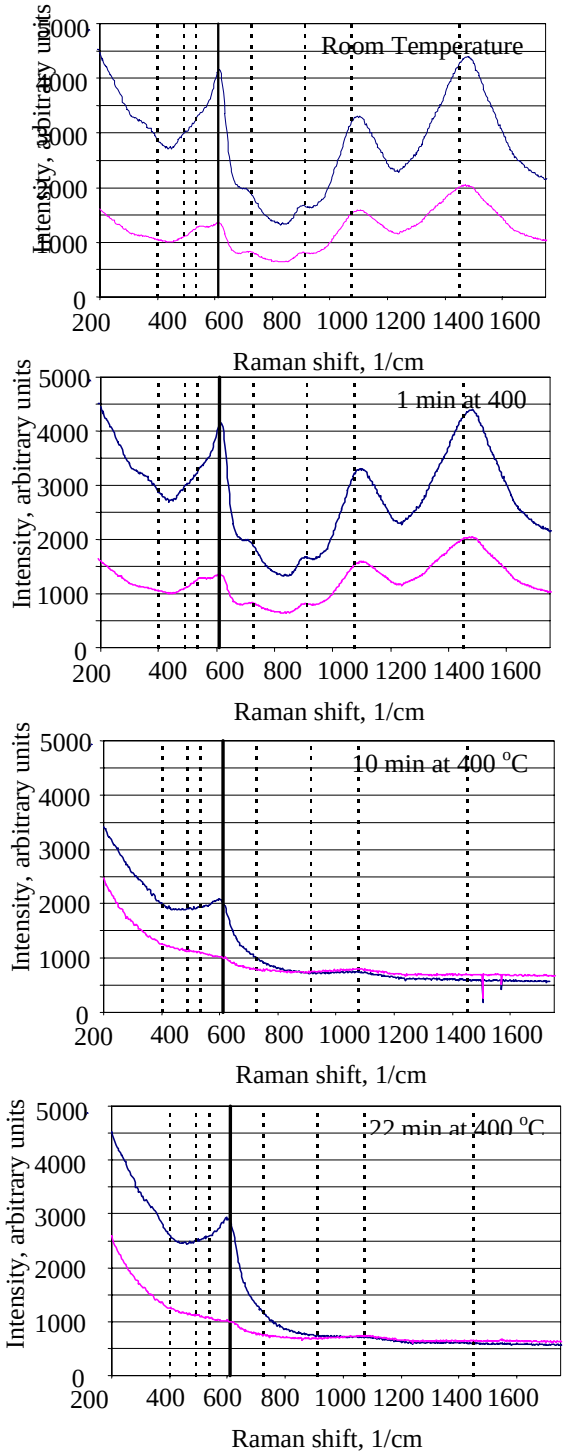

3. MECHANICAL CHARACTERIZATION OF ANODE AND ELECTROLYTE MATERIALS.

In this section the mechanical properties of electrolyte and anode materials, namely 8%YSZ, 75mol% NiO/YSZ and partially and fully reduced NiO/YSZ are presented. Young's and shear moduli, biaxial strength and fracture toughness were determined for all tested materials and the effect of testing temperature, porosity and sample's dimensions on mechanical properties were analyzed. The general characteristics of the samples evaluated in the present work are listed in Table 3.1.

Table 3.1. Characterized materials

	8YSZ			NiO/YSZ					
# of laminated layers	1	2	4	2	4	6	4	4	4
Nominal Thickness, mm	0.25	0.50	1.00	0.50	1.00	1.50	1.00	1.00	1.00
Pore former, vol%	0	0	0	30	30	30	25	20	0
Sintering conditions	1400°C for 2 h			1400°C for 2 h					
Measured porosity, %	7 ±1	7±1	6±1	–	23±1	–	20±1	17±1	7±1
Fraction of reduced NiO in fully reduced samples, %				–	98±2	–	99±1	–	–
Porosity of fully reduced NiO/YSZ samples					40±1.5	–	37±0.5	–	–
Fraction of reduced NiO in partially reduced samples, %				55±8			–	–	–

Green samples were prepared by tape casting layers that were subsequently laminated into specimens of the desired thickness. The porosity of the NiO/YSZ samples was tailored by varying the amount of organic pore former added to the tape cast formulation. Some of the NiO/YSZ samples were either partially or fully reduced in a gas mixture of 4%H_2-96%Ar.

The flexural strength of SOFC materials was determined under biaxial loading using the concentric ring-on-ring (ROR) flexural-loading configuration. Tests were carried out in air at room temperature, 600 and 800°C at a constant cross-head displacement rate of 1 mm/min. according to ASTM C1499-01.

The double torsion (DT) test was used to determine the fracture toughness, K_{IC}, of anode and electrolyte materials at ambient conditions.

3.1. ELASTIC PROPERTIES OF ANODE AND ELECTROLYTE MATERIALS FOR SOFC

The values of Young's and Shear Moduli obtained at room temperature are presented in Figs 3.1. and 3.2. as a function of porosity for 8YSZ and NiO/YSZ samples. The following two empirical relations expressing the effective modulus as a function of porosity were fitted to the experimental modulus vs. porosity data [5]:

linear [$M = M_0(1 - b_M p)$] exponential [$M = M_0 \exp(-b_M p)$]

where M is modulus (G or E), at fractional porosity p ($0<p<1$), b_M is an empirical constant and M_0 is modulus of the sample with zero porosity. Fitting results are plotted in Figs. 3.1 and 3.2 as a solid black line for linear fitting and as a dashed black line for exponential fitting. Also, published results for similar materials [5] are plotted in Figs. 3.1 and 3.2 as a solid gray line for linear fitting and as a dashed gray line for exponential fitting. The fitting constants for the linear and exponential models are listed in Table 3.2. The estimated zero-porosity moduli values obtained in this work are different from previously published data [5] by less than 8%.

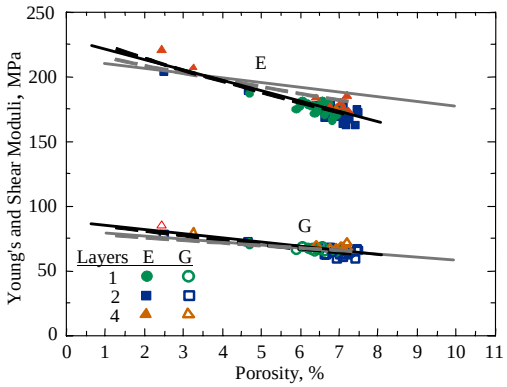

Fig. 3.1. Room temperature Young's and Shear Moduli of YSZ vs. porosity, for 1-layer, 2- and 4-layers samples.

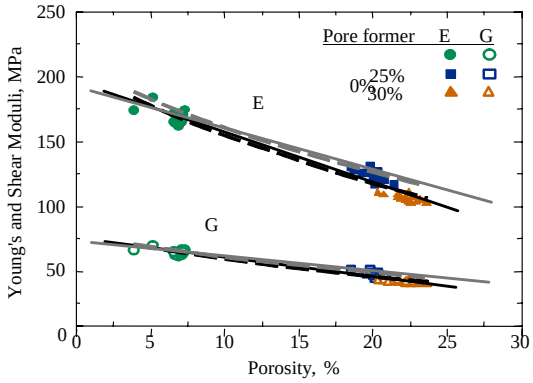

Fig. 3.2. Room temperature Young's and Shear Moduli of NiO/YSZ vs. porosity, for samples with 0, 25, and 30 % of pore former.

Table 3.2. Best fit values for zero-porosity moduli, E_0 , G_0 and porosity dependant constants (b_E and b_G) from this work and from Ref. [6]

			E_0, MPa	G_0, MPa	b_E	b_G
This work	YSZ	linear	229.8	88.2	3.8	3.7
		exponential	234.6	90.2	4.3	4.5
	NiO/YSZ	linear	195.4	75.1	2.0	1.9
		exponential	204.5	78.1	2.8	2.6
Ref. [5]	YSZ	linear	219.5	83.2	2.5	2.4
		exponential	220.3	83.5	2.7	2.6
	NiO/YSZ	linear	205.5	77.0	2.1	2.0
		exponential	207.1	78.0	2.5	2.4

3.2. WEIBULL ANALYSIS OF BIAXIAL STRENGTH OF YSZ ELECTROLYTE

The biaxial strength of YSZ samples with 1, 2 and 4 layers were determined at room temperature, 600 and 800°C. Altogether 161 samples were tested. The biaxial strengths were analyzed using Weibull statistics and values of the characteristic strength and Weibull modulus are listed in Table 3.3.

Table 3.3. Results of biaxial tests for YSZ

	T, °C	#	Characteristic Strength, MPa			Weibull modulus			Strength, MPa
			Avrg.	L.B.	U.B.	Avrg.	L.B.	U.B.	Avrg.± S.D.
4-layers	25	23	222.15	200.59	245.07	3.72	2.86	4.65	201.52±56.49
	600	21	132.81	123.69	142.12	5.65	4.24	7.26	123.14±23.50
	800	21	145.13	131.65	159.15	4.14	3.04	5.44	131.42±37.17
2-layers	25	15	176.23	159.51	193.50	4.89	3.38	6.74	161.15±39.15
	600	18	109.69	91.01	130.68	2.86	1.92	4.02	97.41±38.60
	800	12	146.15	132.39	160.25	6.86	4.15	10.39	136.40±23.78
1-layer	25	20	345.32	314.97	378.59	4.23	3.18	5.62	313.72±84.68
	600	15	140.83	133.55	148.50	8.46	6.08	11.78	133.02±18.61
	800	16	177.79	163.29	192.79	5.45	3.87	7.27	164.30±35.21

T—Temperature
Avrg.—Average value
L.B.—lower 95% Confidence bound
U.B.—Upper 95% Confidence bound
S.D.—Standard Deviation
#—number of tested samples

Weibull plots for biaxial strengths of characterized YSZ samples are shown in Figs. 3.3–3.5. These results suggest that the strength of YSZ decreases at 600°C, but increases at 800°C. However, the reasons for this dependence of the biaxial strength on temperature are not clear at this time. Also, these results indicate that the biaxial strength of multi-layered YSZ samples is lower than that of 1-layer samples, especially at room temperature. Extensive fractographic analysis of the fracture surfaces of these samples is underway with the objective of identifying the strength-limiting flaws. However, preliminary fractographic suggest that the occurrence of delaminations in multilayered samples might be associated with the observed reduction of strength.

3.3. WEIBULL ANALYSIS OF BIAXIAL STRENGTH OF NiO/YSZ PRECURSOR TO SOFC ANODE

The biaxial strength of NiO/YSZ samples was determined using samples of different porosity, namely 7, 17, 20 and 23 % at room temperature, 600 and 800°C. Also, the effect of sample thickness and number of layers were studied by evaluating samples with 2, 4 and 6 layers (Table 3.4.). Altogether 138 samples were evaluated. The biaxial strengths were analyzed using Weibull statistics and values of the

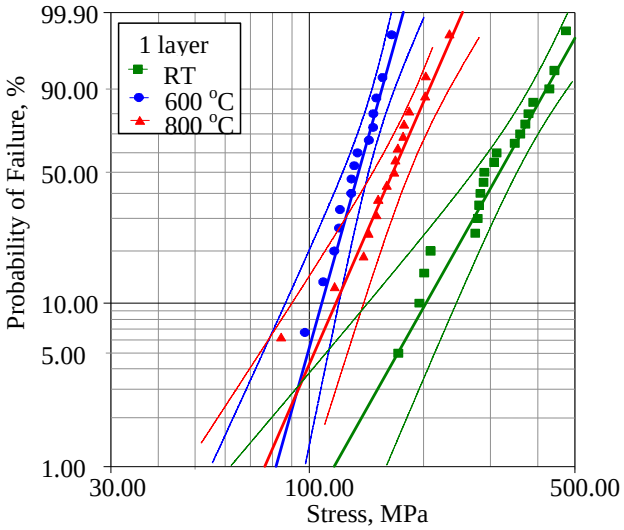

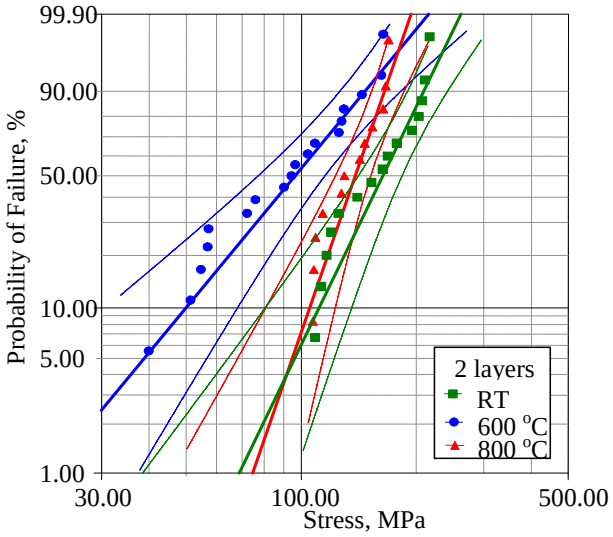

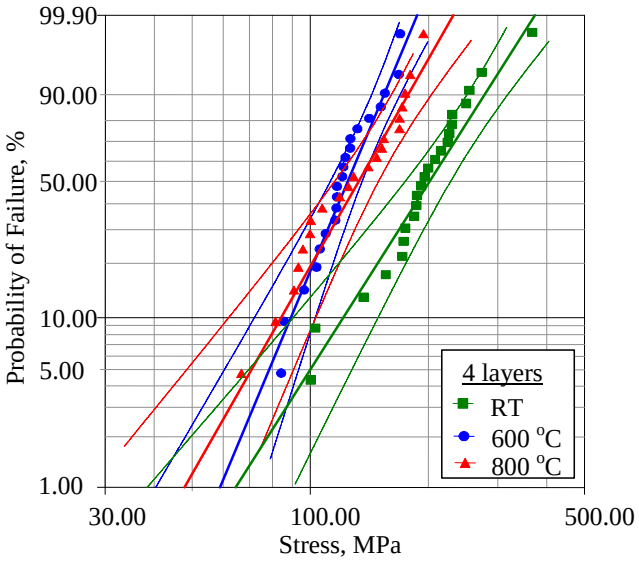

Figs. 3.3–3.5 Weibull plots for biaxial strength of YSZ samples with 1, 2 or 4 layers as a function of testing temperature. Dashed lines represent 95% confidence bounds/

characteristic strength and Weibull modulus are listed in Table 3.4. together with average strength values. Weibull plots for biaxial strengths of characterized NiO/YSZ samples are shown in Figs. 3.6–3.10.

These results suggest that the biaxial strength of NiO/YSZ has a weak temperature dependence. However, the decrease in biaxial strength with porosity is pronounced up to 17% of porosity, but the magnitude of the biaxial strength does not change considerably for higher levels of porosity. The only exception are 17% porous samples tested at 800°C. In that case, an exceptionally high characteristic strength was obtained. Also, it is worth noting that neither the number of layers nor the thickness of the samples have a significant influence on the magnitude of the biaxial strength of NiO/YSZ.

Table 3.4. Results of biaxial tests for NiO/YSZ

	T, °C	#	Characterist. Strength, MPa			Weibull modulus			Strength, MPa
			Avrg.	L.B.	U.B.	Avrg.	L.B.	U.B.	Avrg.± S.D.
4-layers 23% porous	25	14	96.26	84.55	108.69	3.91	2.63	5.54	86.69±27.26
	800	15	112.30	107.35	117.22	10.67	7.41	14.54	107.08±12.97
6-layers 23% porous	25	8	97.24	77.92	119.80	3.18	1.81	5.04	86.89±34.22
2-layers 23% porous	25	11	106.73	96.13	117.64	5.58	3.56	8.23	98.18±22.10
4-layers 20% porous	25	15	92.13	85.85	98.58	6.77	4.65	9.31	85.95±16.95
	800	15	108.57	97.76	119.86	4.61	3.27	6.19	99.42±23.25
4-layers 17% porous	25	15	99.62	90.30	109.91	4.73	3.38	6.61	91.25±21.89
	800	15	146.94	138.08	155.83	7.77	5.42	10.56	135.67±19.44
4-layers 7% porous	25	15	134.61	127.207	142.03	8.55	6.00	11.52	125.09±15.18
	800	15	145.45	132.65	158.67	5.25	3.68	7.11	130.40±26.60

T—Temperature
Avrg.—Average value
L.B.—lower 95% Confidence bound
U.B.—Upper 95% Confidence bound
S.D.—Standard Deviation
#—number of tested samples

The biaxial strength of reduced NiO/YSZ was determined at room temperature using samples with initial porosity of 23% that were subsequently reduced in a gas mixture of 4%H_2+96%Ar. Two groups of samples were tested: partially reduced with the fraction of reduced NiO of 55% and fully reduced with a fraction of reduced NiO of almost 100%. Also, the effect of the sample thickness and the number of layers on the mechanical properties were studied by evaluating samples with 2, 4 and 6 layers (Tables 3.5. and 3.6.) Altogether, 56 samples were tested. The biaxial strengths were analyzed using Weibull statistics and values of the characteristic strength and Weibull modulus are listed in Table 3.5 and 3.6 along with average strength values. Weibull plots for biaxial strengths are presented in Figs. 3.11–3.12.

3.4. WEIBULL ANALYSIS OF BIAXIAL STRENGTH OF REDUCED NIO/YSZ ANODE

As in the case of unreduced NiO/YSZ, the magnitude of the biaxial strength of fully and partially reduced NiO/YSZ does not depend significantly on the thickness of, or on number of layers in the samples. Comparing the results in Tables 3.4–3.6 and Figs. 3.11–3.12 for unreduced, partially reduced and fully reduced NiO/YSZ, it can be concluded that the magnitude of the biaxial strength of partially reduced samples with fraction of reduced NiO of 55 % is not significantly different from that of the unreduced samples. However, complete reduction of the NiO/YSZ samples leads to a decrease in the magnitude of the biaxial strength by almost 50 %.

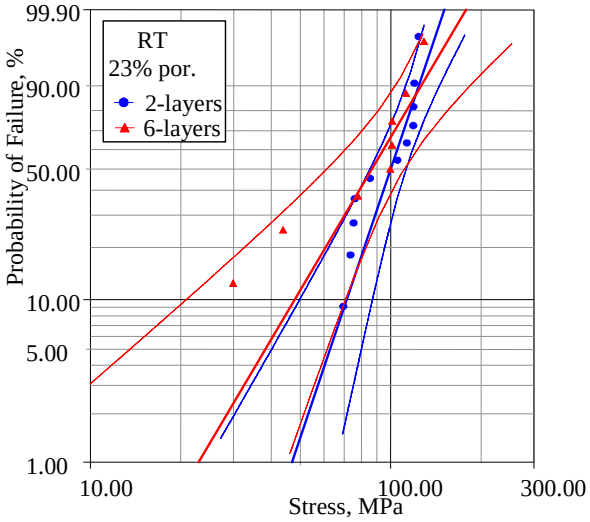

Fig. 3.6-3.10. Weibull plots for biaxial strength of NiO/YSZ samples as a function of testing temperature, porosity and number of layers. Dashed lines represent 95% confidence bounds.

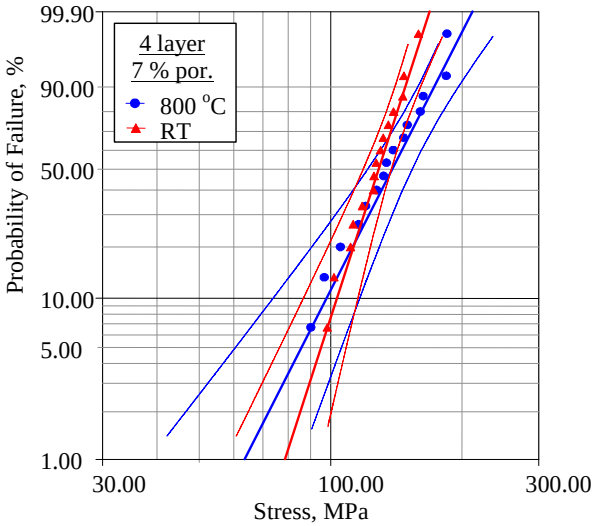

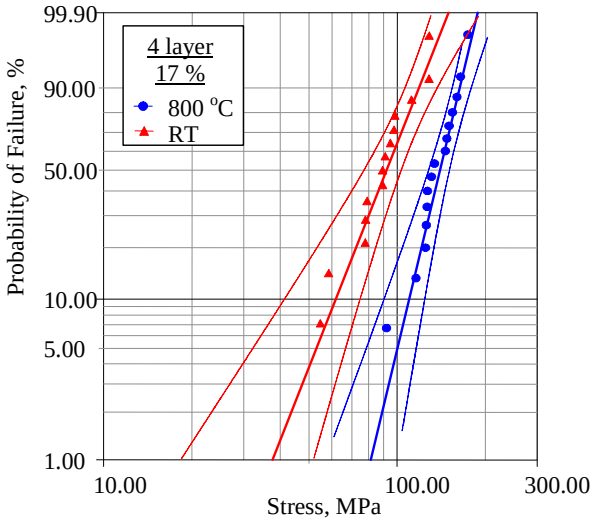

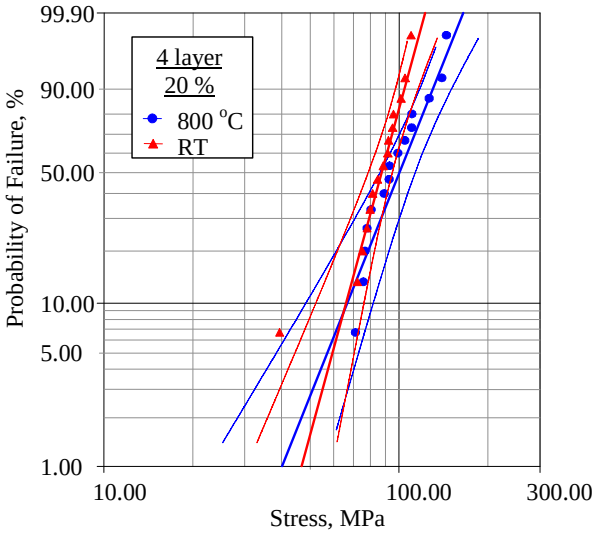

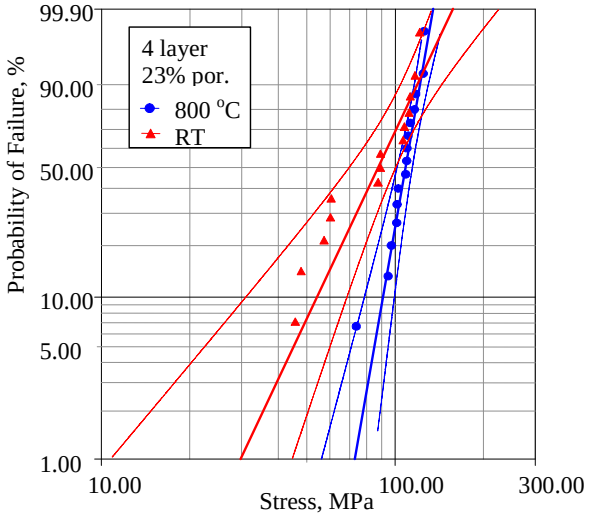

Table 3.5. Results of biaxial tests for fully reduced NiO/YSZ. Initial porosity of the samples was 23%, and porosity after reduction was measured to be 40%

	T, °C	#	Characterist. Strength, MPa			Weibull modulus			Strength, MPa
			Avrg.	L.B.	U.B.	Avrg.	L.B.	U.B.	Avrg.±S.D.
4-layers	25	14	55.32	49.68	61.62	4.33	3.14	5.98	50.52±12.42
6-layers	25	9	50.16	45.42	55.38	5.82	3.71	9.13	46.29±10.08
2-layers	25	9	76.40	69.09	83.88	6.52	3.98	9.88	71.00±13.65

T—Temperature
Avrg.—Average value
L.B.—lower 95% Confidence bound
U.B.—Upper 95% Confidence bound
S.D.—Standard Deviation
#—number of tested samples

Table 3.6. Results of biaxial tests for partial reduced NiO/YSZ. Initial porosity of the samples was 23%. Fraction of the reduced NiO was 55%

	T, °C	#	Characterist. Strength, MPa			Weibull modulus			Strength, MPa
			Avrg.	L.B.	U.B.	Avrg.	L.B.	U.B.	Avrg.±S.D.
4-layers	25	5	105.26	98.24	112.78	11.29	11.29	20.28	
6-layers	25	8	108.84	110.82	116.32	6.28	9.26	14.55	
2-layers	25	11	115.58	106.87	124.48	4.59	7.41	11.15	

T—Temperature
Avrg.—Average value
L.B.—lower 95% Confidence bound
U.B.—Upper 95% Confidence bound
S.D.—Standard Deviation
#—number of tested samples

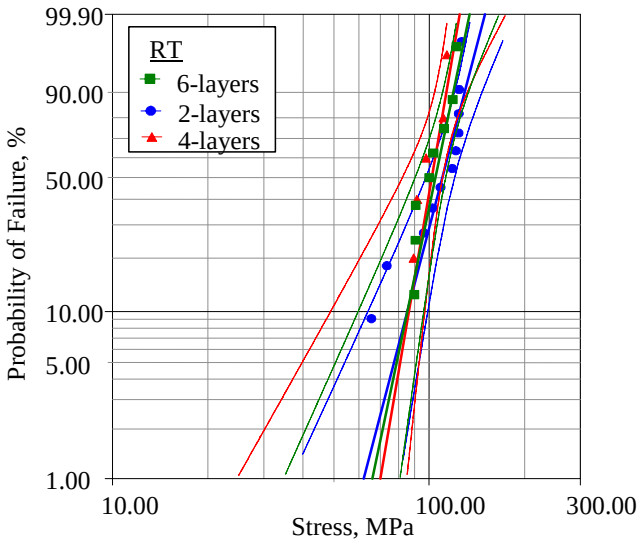

Fig. 3.11. Weibull plot for biaxial strength of 2, 4 and 4-layered partially reduced NiO/YSZ samples at room temperature. Dashed lines represent 95% confidence bounds.

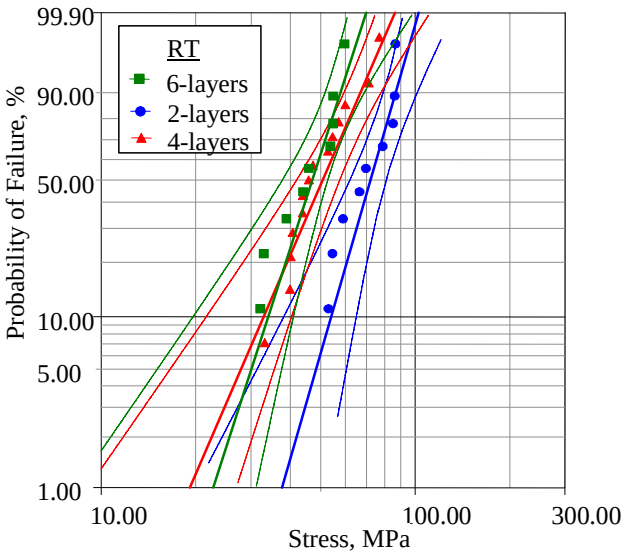

Fig. 3.12. Weibull plot for biaxial strength of 2, 4 and 4-layered completely reduced NiO/YSZ samples at room temperature. Dashed lines represent 95% confidence bounds.

3.5 FRACTURE TOUGHNESS OF ANODE AND ELECTROLYTE MATERIALS

The fracture toughness values of 4-layer 8YSZ and NiO/YSZ samples, which were determined at room temperature using Double-Torsion testing, are listed in Table 3.7. Samples were pre-cracked at a displacement rate of 0.01 mm/min and the formation of a sharp precrack was confirmed by Optical Microscopy. After precracking, all samples were tested at a constant displacement rate of 1 mm/min until failure. Results obtained for YSZ are in excellent agreement with those reported by others (1.61 MPa $m^{1/2}$) [5].

Table 3.7. K_{IC} of YSZ and NiO/YSZ at room temperature measured by Double-Torsion

	8YSZ	NiO/YSZ
K_{IC}, MPa $m^{1/2}$	1.65 ± 0.02	1.04 ± 0.13

4. SUMMARY

The kinetics of NiO reduction in a gas mixture of 4%H_2-96%Ar was investigated at temperatures between 600°C and 800°C. It was found that the initial reduction reaction followed linear kinetics at temperatures higher than 600°C until the reduction fronts reached the middle of the sample. After this point, the reaction rate decreased significantly and followed semi-parabolic kinetics. By performing interrupted reduction tests, it was possible to determine the dependence of the elastic properties and biaxial strength of NiO-YSZ anodes as a function of fraction of NiO reduction. In general, it was found that while the porosity of NiO-YSZ anodes increased with increasing fraction of NiO reduction, both the elastic modulus and biaxial strength decreased with increasing fraction of NiO reduction.

The effect of porosity and number of layers (thickness) on the biaxial strength of NiO-YSZ anodes was investigated at 20°C and 800°C and the results were analyzed using Weibull statistics. It was found that the strength of NiO-YSZ anodes decreased significantly when the porosity of the samples increased from 7% to 17%, but the strength appears to be insensitive to higher values of porosity up to 23%. It was also found that the strength of NiO-YSZ anodes is insensitive to the number of layers (2, 4 or 6) and that it has a mild temperature dependence.

The effect of number of layers was on the biaxial strength of YSZ electrolytes was investigated at temperatures between 20°C and 800°C. It was found that the strength of YSZ samples decreased significantly with increasing number of layers. Although the fractographic analysis of these test specimens has not been completed, preliminary observations indicate that delaminations might be responsible for the observed decrease in strength. It was also found that while the strength decreased from

20°C to 600°C, the strength increased at 800°C. Work is in progress to determine the mechanism(s) responsible for this behavior.

Raman spectroscopy and WDS have been used for chemical phase identification, and on-going work has been focused on using the former to determine stresses in SOFC materials.

5. REFERENCES

1. Sridhar S., Sichen D., and Seetharman S., "Investigation of the Kinetics of Reduction of Nickel Oxide and Nickel Aluminate by Hydrogen," *Z METALLKD* **85,** (1994) 616–620.
2. ASTM standard C1259-98.
3. A. C. Muller, B. Pei, A. Weber, and E. Ivers-Tiffee, HTMC IUPAC Jülich 2000, pp.1–4.
4. ASTM standard E 1461-01.
5. A. Atkinson and A. Selcuk, "Strength and Toughness of Tape-Cast Yttria-Stabilized Zirconia," *J. Am. Ceram. Soc.*, **83** (2000) p. 2029.

APPLYING ENERGY TECHNOLOGIES TO REDUCE GREENHOUSE GAS EMISSIONS

Thomas J. Wilbanks
Sherry B. Wright

INTRODUCTION

Under the auspices of its R&D Experts Working Group and its Committee on Energy Research and Technology, the International Energy Agency (IEA) is producing a major report on "Technologies for Achieving Significant Greenhouse Gas Reductions from Energy Over the Long Term." The U.S. government is supporting this effort through DOE and the National Climate Change Technology Initiative.

SUMMARY

At IEA's request and with DOE/FE's support, ORNL has provided leadership in drafting Chapters 9–13 of the report, along with providing comments on a number of other sections of the report. ORNL's responsibilities are:

Chapter 9. Linking Basic Research and Applied R&D
Section 4. What Is Needed Beyond Technology Development?
Chapter 10. The Role of Technology Deployment
Chapter 11. Engaging Industry in Stimulating Innovation and Adoption
Chapter 12. Long-Term Goals, Near-Term Actions, and Cost-Effectiveness
Chapter 13. Opportunities for International Collaboration

Figure 1 illustrates some of the content of the chapters. In the past year, ORNL has produced two drafts of these chapters, on time and within budget. Further work awaits IEA comments on the drafts.

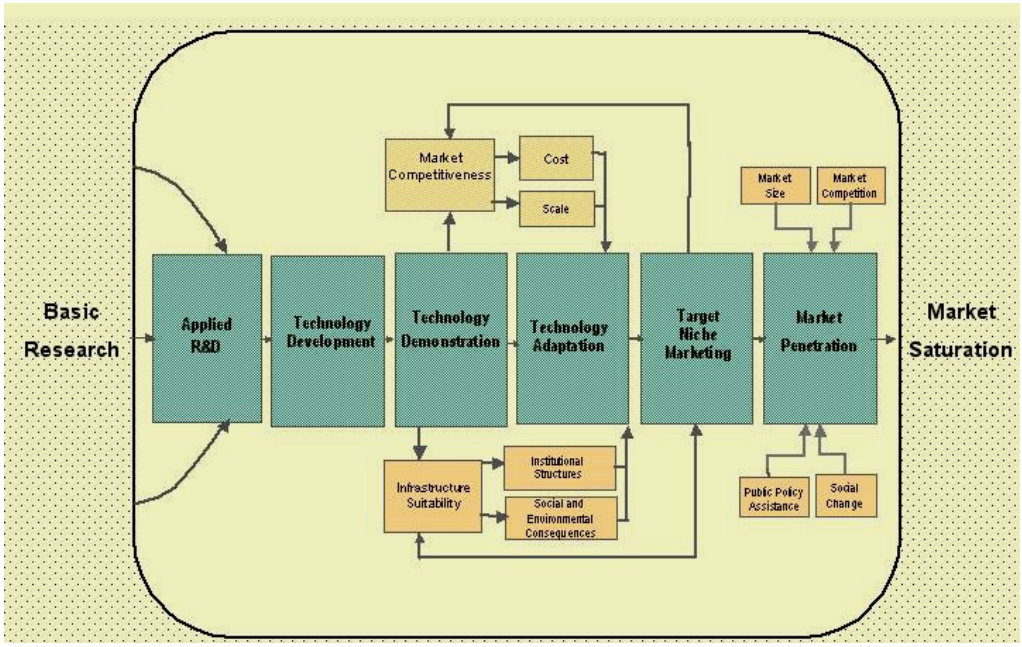

Fig. 1. Technology Deployment Process (Schematic).

COMPUTATIONAL FLUID DYNAMICS FOR MULTIPHASE FLOW

S. Pannala and E. D'Azevedo

INTRODUCTION

Fluidized bed reactors are widely used in the chemical industry and are essential to the production of key commodity and specialty chemicals such as petroleum, polymers, and pigments. Fluidized beds are also going to be widely used in the next generation power plants in aiding conversion of coal to clean gas. However, in spite of their ubiquitous application, understanding of the complex multi-phase flows involved is still very limited. In particular, existing computer simulations are not sufficiently accurate/fast to serve as a primary approach to the design, optimization, and control of industrial-scale fluidized bed reactors. Availability of more sophisticated computer models is expected to result in greatly increased performance and reduced costs associated with fluidized bed implementation and operation. Such improved performance would positively affect U.S. chemical/energy industry competitiveness and increase energy efficiency.

To improve fluidization simulation capabilities, two different projects are undertaken at ORNL with the specific objective of developing improved fluidization computer models. On one hand, a very detailed multiphase computer model (MFIX) is being employed. On the other hand a low-order bubble model (LBM) is being further developed at ORNL with the eventual aim of real time diagnosis and control of industrial scale fluidized beds.

MFIX (Multiphase Flow with Interphase eXchanges) is a general-purpose computer code developed at the National Energy Technology Laboratory (NETL) for describing the hydrodynamics, heat transfer and chemical reactions in fluid-solids systems. It has been used for describing bubbling and circulating fluidized beds, spouted beds and gasifiers. MFIX calculations give transient data on the three-dimensional distribution of pressure, velocity, temperature, and species mass fractions. MFIX code is based on a generally accepted set of multiphase flow equations. However, in order to apply MFIX in an industrial context, key additional improvements are necessary. These key improvements correspond to the two ORNL efforts: (1) To develop an effective computational tool through development of a fast, parallel MFIX code and (2) Develop infrastructure for easy collaborative development of the MFIX code and exchange of information between the developers and users.

The details of the MFIX code and parallelization are given in recent papers [1,2] while the results are described in this report.

RESULTS AND DISCUSSION

As a benchmark problem we used the simulation of a circulating fluidized bed with a square cross-section, corresponding to experiments conducted by Zhou et al. [3,4]. The bed has a square cross-section, 14.6 cm wide, and is 9.14 m in height. The schematic of this setup is shown in Fig. 1a. The solids inlet and outlet are of circular cross-section in the experiments but for geometric simplicity, we have represented them by square cross-section. The area of the square openings and the mass flow rate corresponds to that of the experiments. At a gas velocity of 55 cm/s the drag force on the particles is large enough to blow the particles to the top of the bed and make the bed flow like a fluid or fluidized bed. The particles strike the top wall and some of them exit through the outlet while the rest fall down to encounter the upcoming stream of solids and gases.

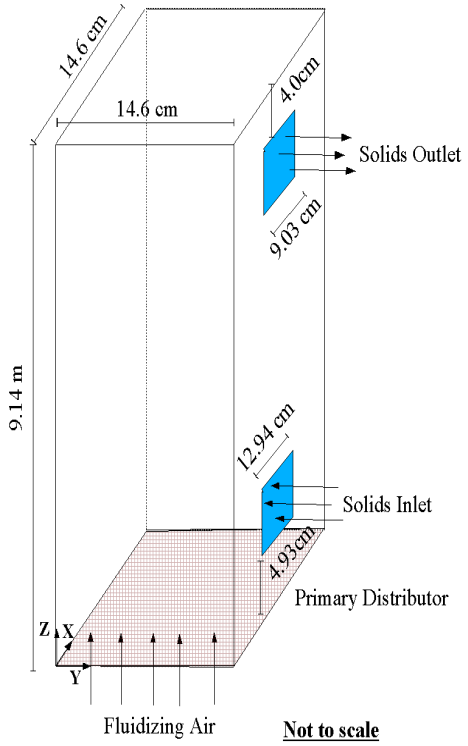

Fig. 1. Schematic of the simulated CFB.

In the benchmark problem a three-dimensional Cartesian coordinates system was used. The spanwise directions were discretized into 60 cells (0.24 cm, I & K-dimensions) and the axial, streamwise direction into 400 cells (2.29 cm, J-dimension). The total number of computational cells is around 1.6 million, including the ghost cells; the dynamic memory required is around 1.6 GB. Three-dimensional domain decomposition was performed depending on the number of processors for the DMP run. A low-resolution simulation was also carried out with half the resolution in each of the three directions for comparison.

In all of the numerical benchmarks reported here for the high-resolution case, two-different preconditioners were used with BICGSTAB linear solver. In one case, red-black coloring in the I-K plane and line-relaxation along J direction was used. With red-black coloring, the number of BICGSTAB iterations is quite insensitive to the number of subdomains used. In the other case, no preconditioner was used. The benchmarks reported here were carried out on one 32-way node of the machine Cheetah at the center for Computational Sciences, Oak Ridge National Laboratory. Cheetah is a 27-node IBM pSeries System, each node with sixteen Power4 chips, a chip consisting of two 1.3 GHz Power4 processors. Each processor has a Level 1 instruction cache of 64 KB and data cache of 32 KB. A Level 2 cache of 1.5 MB on the chip is shared by the two processors, and a Level 3 cache of 32 MB is off-chip. Cheetah's estimated computational power is 4.5 TeraFLOP/s in the compute partition.

NUMERICAL RESULTS

Figure 2 compares the axial-profiles of the time-averaged voidage with the experiments. The voidage is defined as the volume fraction of the gas in any given cell; a voidage of 1 corresponds to pure gas and a voidage of 0 corresponds to pure solid (although this is physically and numerically impossible as the solids go to random close packing with voidage around 0.4, depending on the particle size). The results at three different lateral locations match very well downstream of the inlet region but are not as accurate in the inlet region (although there is some ambiguity in the precise inlet geometry from the limited information in the literature [3,4]). The higher resolution results seem to agree with experiments better than lower resolution ones near the inlet; even higher resolution might be required to resolve the relevant scales in this section. The voidage across the bed (Fig. 3) is predicted well in the upper quarter of the bed. The solids velocity (Fig. 4) is in much better agreement in the near-wall regions of the bed while it is over predicted near the centerline for higher sections in the bed.

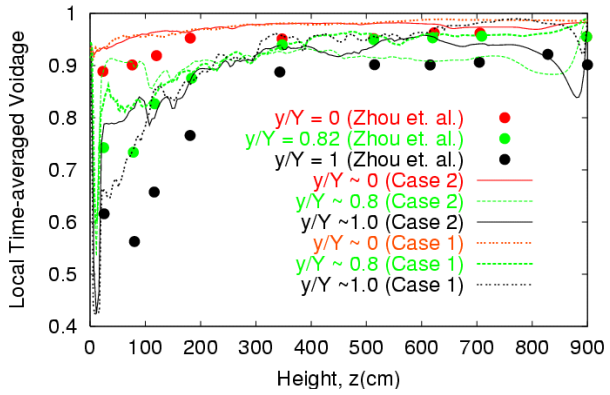

Fig. 2. Axial profiles of time-averaged voidage fraction.

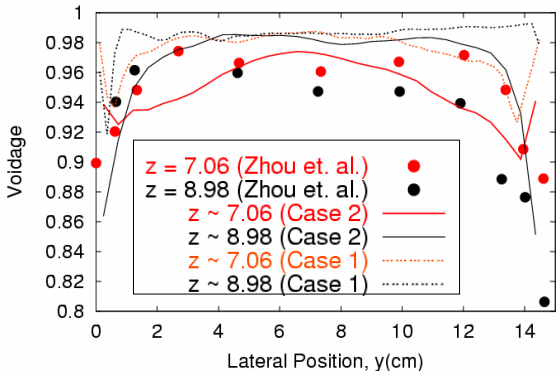

Fig. 3. Lateral profiles of time-averaged voidage fraction.

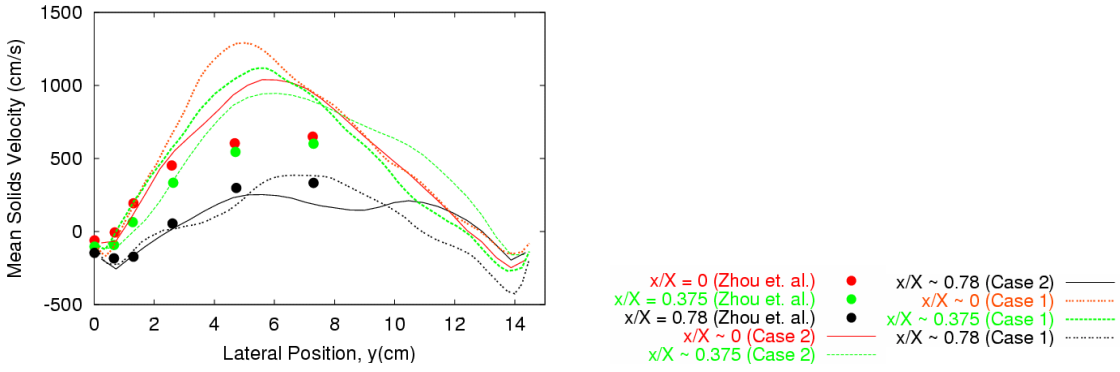

Fig. 4. Axial profiles of time-averaged solids velocity at a height of 5.13 m.

Figure 5 shows instantaneous void fraction snapshots which show recirculation of solids in the vessel. The solids are injected at the base and the high velocity inlet gas carries them to the top (Fig. 5a). The solids accumulate at the bottom. There is also a slight build-up of solids near the top, due to exit effects. Most recirculation of solids is in a narrow band close to the walls (Fig. 5b). The solids accumulated on the top fall down and encounter the upflow at the centerline of bed and tend to move towards the walls (Fig. 5c). Finally in Fig. 5d, the falling solids are mixed with the upcoming solids so as to be recirculated to the top. These figures are shown here as an illustration of the physics that can be captured using numerical simulations; a more detailed analysis of this data will be published in another journal.

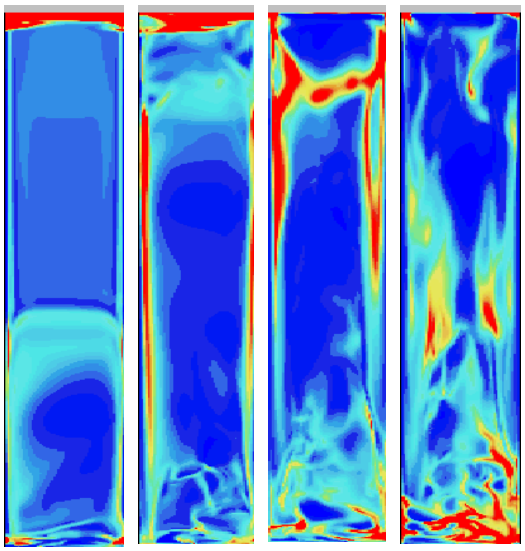

Fig. 5. Snapshots of voidage fraction in the Y-Z plane at X = 1.2 cm for different times: (a) 1.12 s, (b) 2.0 s, (c) 2.82 s, and (d) 3.42 s. Here red represents low voidage (0.6) and blue represents high voidage (1.0). Regions of red (low voidage) have higher concentrations of solids and blue corresponds to higher concentrations of air.

PARALLEL RESULTS

Table 1 shows the execution times of the code on one node of the IBM SP Cheetah, for ten time steps of the test problem using line relaxation as the preconditioner. An entry in the table gives the running time in seconds on P processors, where P is the product of the number of MPI tasks and the number of threads per task. In all the runs, message passing was through the internal shared memory and not over the network. The runtime on a single processor is not included in the table due to the large problem size which resulted in an extremely long execution time. The runs were carried out several times and the best times are recorded here. The execution times for 8 tasks or 8 threads are not reported here as the run times varied drastically from one run to another run and this behavior could not be explained. Further analysis is required to ascertain the reasons.

Table 1 indicates that for a fixed number of processors, the execution time of the code is affected by the mix of the number of MPI tasks and the number of threads per task. For the test problem on 32 processors, 32 one-thread or 16 two-thread MPI tasks give the best combination. In general, the simple rule of “one thread per MPI task, one MPI task per processor” gives the best performance. This general observation is consistent with previous hybrid parallelization efforts on somewhat similar architectures [5,6]. One of the reasons might be the fact that thread creation/destruction is very expensive on the IBM

Table 1. Runtimes (in seconds) for 10 iterations for the case using line relaxation as the preconditioner.

MPI Tasks	SMP Threads					
	1	2	4	8	16	32
1		3188	2012	1125	605	445
2	3105	1666	1025	489	350	
4	1709	1121	683	282		
8	1041	554	788			
16	449	233				
32	235					

SPs. Replacing the loop-level SMP model with a program-level SMP model, where the data is decomposed among threads at the beginning of the program, may incur less overhead.

Figure 6 compares the SMP and DMP parallel performance. It clearly shows that the DMP performance is far better than that of SMP in the extreme case of hybrid parallelization. Figure 7 captures the essence of the data given in Table 2. It is very evident that DMP parallelization, for this problem on this architecture, is desirable.

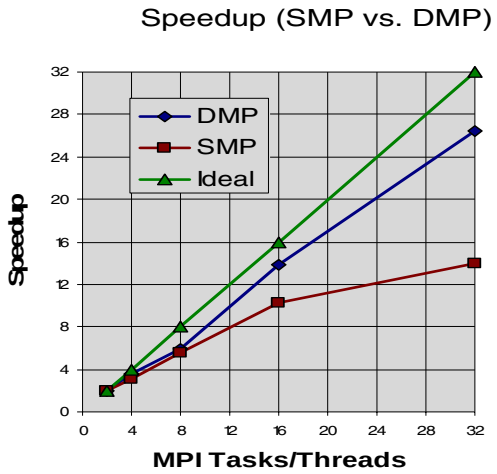

Fig. 6. SMP/DMP Speedup Comparison.

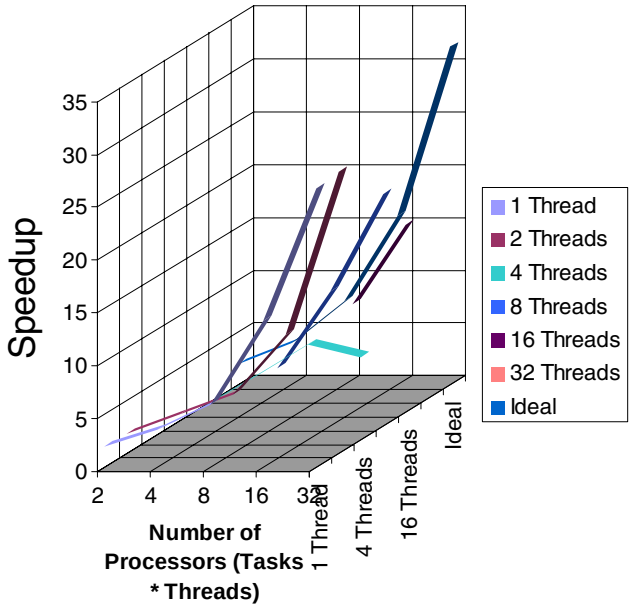

Fig. 7. Parallel performance for all the cases (Table 1) with line relaxation as the preconditioner

Table 2 gives the runtimes of the code for the test problem without the use of preconditioner. This required 124 nonlinear iterations for ten time steps compared to the 107 iterations when using the line relaxation preconditioning. However, the code was 20% faster without preconditioning; this may be

Table 2. Runtimes (in seconds) for 10 iterations for the case with no preconditioner.

MPI Tasks ↓	SMP Threads →					
	1	2	4	8	16	32
1		2273	1253	768	653	440
2	2295	1290	665	480	299	
4	1151	644	369	245		
8	689	473	443			
16	340	191				
32	186					

attributed to the considerably lower cost of an iteration without preconditioning. The speedups are graphically depicted in Figs. 8 and 9. On close observation of speedup data, it can be noted that the shared memory efficiency has dropped further, presumably because the code must take more iterations to converge than with line relaxation. This would increase the number of threads created/destroyed per time-step and explains the poorer performance of the SMP code.

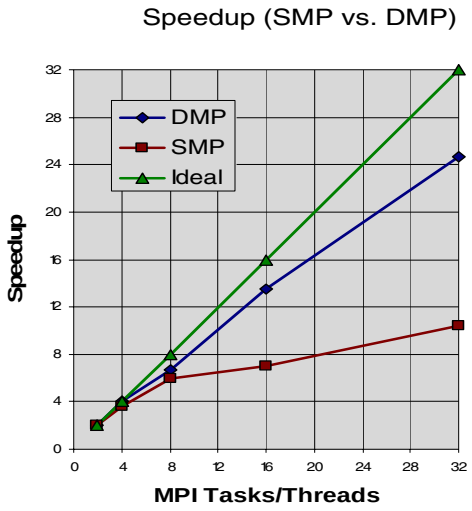

Fig. 8. SMP/DMP Speedup Comparison.

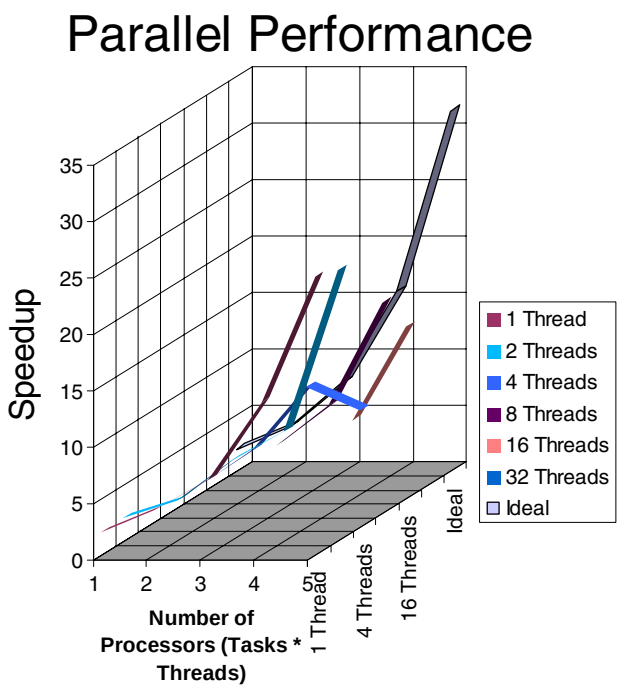

Fig. 9. Parallel performance for all the cases (Table 4) with no preconditioner.

The code has to be profiled extensively for a range of problems and also for different architectures before any general conclusions can be made regarding the advantages of DMP code versus a hybrid code. In the present case, MPI communication is memory-to-memory copy as all the processors belong to the same node. Some of the conclusions might change using node-to-node communication.

The above efforts will be continued into next year. In addition, implementation of various non-linear coupled solvers for faster convergence would be explored. The documentation, technical reports related to MFIX, and the latest version of MFIX source code are all available from http://www.mfix.org.

REFERENCES

1. D'Azevedo, E., Pannala, S., Syamlal, M., Gel, A., Prinkey, M., and O'Brien, T., "Parallelization of MFIX: A Multiphase CFD Code for Modeling Fluidized Beds," Session CP15, *Tenth SIAM Conference on Parallel Processing for Scientific Community*, Portsmouth, Virginia, March 12–14, 2001.
2. Pannala, S., E. D'Azevedo, T. O'Brien, and M. Syamlal, "Hybrid (mixed SMP/DMP) parallelization of MFIX: A Multiphase CFD code for modeling fluidized beds," *Proceedings of ACM Symposium on Applied Computing*, Melbourne, Florida, 9–12 March, 2003.
3. J. Zhou, J. R. Grace, S. Qin, C. M. H. Brereton, C. J. Lim, and J. Zhu, Voidage profiles in a circulating fluidized bed of square cross-section, Chem. Engg. Science, 49 (1994), pp. 3217–3226.
4. J. Zhou, J. R. Grace, S. Qin, C. J. Lim, and C. M. H. Brereton, Particle velocity profiles in a circulating fluidized bed riser of square cross-section, Chem. Engg. Science, 49 (1994), pp. 3217–3226.
5. F. Mathey, P. Blaise, and P. Kloos, OpenMP optimization of a parallel MPI CFD code, Second European Workshop on OpenMP, Murrayfield Conference Centre, Edinburgh, Scotland, U.K., September 14–15, 2000.
6. D. A. Mey and S. Schmidt, From a vector computer to an SMP-Cluster hybrid parallelization of the CFD code PANTA, Second European Workshop on OpenMP, Murrayfield Conference Centre, Edinburgh, Scotland, U.K., September 14–15, 2000.

REAL-TIME BUBBLE SIMULATIONS FOR FLUIDIZED BEDS

S. Pannala, C. S. Daw, and W. A. Shelton

INTRODUCTION

Fluidized bed reactors are widely used in the chemical industry and are essential to the production of key commodity and specialty chemicals such as petroleum, polymers, and pigments. Fluidized beds are also going to be widely used in the next generation power plants in aiding conversion of coal to clean gas. However, in spite of their ubiquitous application, understanding of the complex multi-phase flows involved is still very limited. In particular, existing computer simulations are not sufficiently accurate/fast to serve as a primary approach to the design, optimization, and control of industrial-scale fluidized bed reactors. Availability of more sophisticated computer models is expected to result in greatly increased performance and reduced costs associated with fluidized bed implementation and operation. Such improved performance would positively affect U.S. chemical/energy industry competitiveness and increase energy efficiency.

To improve fluidization simulation capabilities, two different projects are undertaken at ORNL with the specific objective of developing improved fluidization computer models. On one hand, a very detailed multiphase computer model (MFIX) is being employed. On the other hand the Dynamic Interacting Bubble Simulation (DIBS) is being further developed at ORNL with the eventual aim of real time diagnosis and control of industrial scale fluidized beds.

The details of the DIBS model are reported in recent papers/presentations [1–5]. Here only the salient results are reported.

RESULTS AND DISCUSSION

For understanding and evaluating the predictions of our model, we compare it to experimental measurements of ozone decomposition in a bubbling bed made by Fryer and Potter [6]. The bed schematic is shown in Fig. 1. Because the observations of Fryer and Potter were time-averaged, we compute corresponding averages from our model output. Later, we discuss the dynamical features in our model output that were not measured by Fryer and Potter.

The first comparison we make with experiment focuses on the time-average bed hydrodynamics; specifically, bubble size and bed expansion. Next we consider time-average chemical conversion.

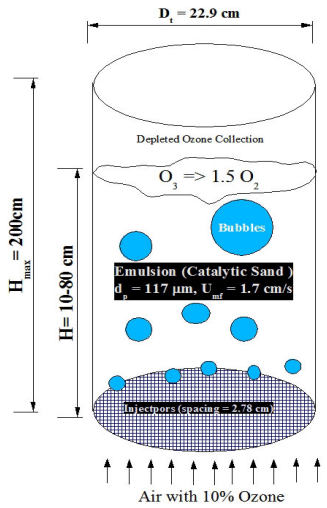

Fig. 1. Configuration of the ozone decomposition experiment—time-average comparisons.

BUBBLE SIZE

The performance of fluidized beds is usually dominated by the bed hydrodynamics. Traditionally, the time-average hydrodynamic features of greatest interest have been the axial variation of bubble size and overall the bed expansion as functions of gas flow. Figure 2 compares our predictions of bubble size versus bed height at one flow with the observations of Fryer and Potter and the widely used correlations of Darton et al. [7] and Werther [8]. In their experiments, Fryer and Potter measured bubble diameter at different heights by physically changing the amount of bed material and observing the bubble eruptions at the surface. In doing this, they assumed that such measurements were equivalent to the bubble sizes at corresponding locations in a deep bed. We note that the sizes predicted by the correlations consistently fall below those reported by Fryer and Potter.

Also plotted on the figure are the results from the model. The bubble diameter at the injectors is prescribed based on the experimental correlation as a function of excess superficial velocity as obtained by Fryer and Potter. The red line (with symbol ‘x’) is the variation of the bubble size (number mean) with axial distance for a bed of height 80 cm. The initial part of the variation (up to 40 cm) matches quite well with the experiments. The bubble diameter in the later part is under predicted. In order to address the assumption mentioned above, we simulated the experimental procedure with varying bed heights and observed the eruption diameter. From the plot it is apparent that the actual bubble diameter and the eruption diameter are in agreement for shallow beds but are different as we traverse taller beds. The eruption diameter as predicted by the model is closer to the experiments than the actual bubble diameter

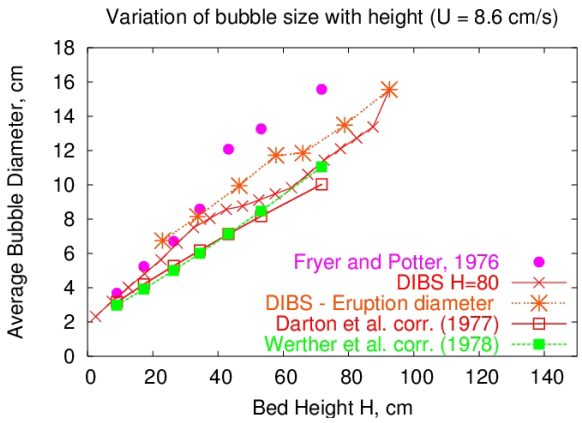

Fig. 2. Bubble-size variation with axial distance and bed height.

in a deep bed. Considering the simplicity of the model, this is very good agreement. In the next section, we point out considerable differences between various measures of the bubble size. This ambiguity points to the need to carefully evaluate the potential weighting (i.e., biasing effects) of the experimental measurement approach.

In Fig. 3, bed expansion is plotted as a function of the inlet gas velocity. As gas velocity increases, the volume of the bubbles increases and leads to greater bed expansion. Again our bubble model appears to predict the expansion with reasonable accuracy. This gives us some confidence that at least the time average aspects of our model are not too far from reality.

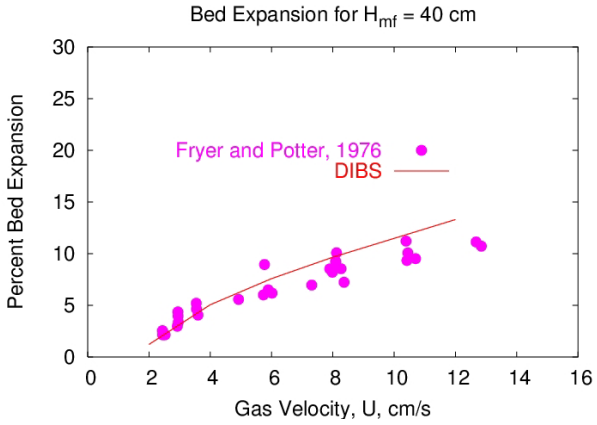

Fig. 3. Bed expansion versus gas velocity.

Other important time-average quantities that were not available here were the bubble velocities and the bubble-size distributions. Perhaps measurement of these quantities should be a future experimental goal for ozone reactors. The bubble-size distributions predicted by our model (Fig. 4) have a non-

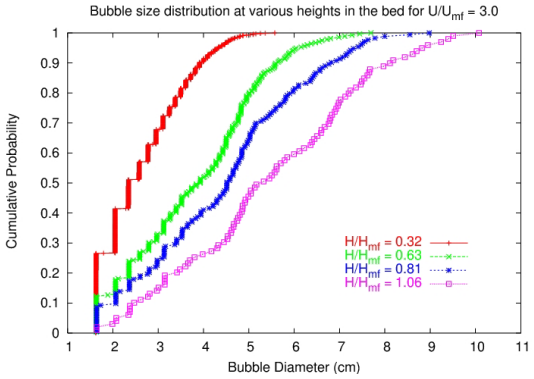

Fig. 4. Variation of bubble size distribution along the axis of the bed—ozone conversion.

Gaussian power law form that appears to scale in a self-similar fashion as one moves upward in the bed. Such scaling may be useful for diagnostics and correlations and may have some general implications for modeling. Some of these ideas have already been suggested by Gheorghiu et al. [9]. We plan to investigate these size-distribution effects further with our model in the future.

The ozone concentration at the exit is plotted for different catalyst activity (different intrinsic reaction rates) and for different gas velocities in Fig. 5. Conversion becomes reaction-rate limited at the lower reaction rates, while it becomes mass-transfer limited at higher reaction rates. The results shown here are using the model with a constant mass-transfer correction factor of 2.0 for all the cases. The model output for all the cases is in reasonably good agreement with the experiments for all the cases. Slight over prediction of ozone concentration for $k = 7.75 s^{-1}$ for high gas velocities where it is mass-transfer limited is not very surprising considering all the assumptions made in the simulations. In the current model, we do not account for reactions in the wake of the bubble, and that can easily accommodated using known correlations. In addition, the emulsion-phase circulation is not currently modeled, and thus effects of solids back-mixing are not captured. The recirculation of the solids can increase the effective emulsion-gas residence time and thus increase conversion. Fryer and Potter suggested the minimum they observed in axial ozone concentration might be due to this effect. In the future, we plan to introduce both internal bubble reactions and emulsion-phase circulation to the model.

In the above discussion, we compare time-averaged statistics of the model with those of the experiments. The temporal patterns are lost in such comparisons, so we now consider the dynamical predictions of our model.

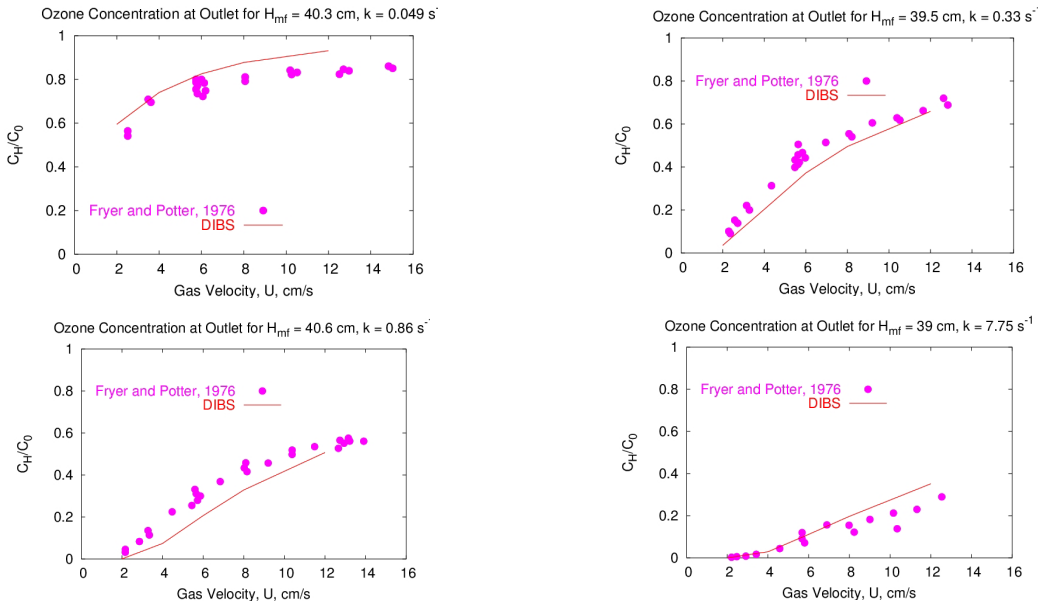

Fig. 5. Ozone conversion for various reaction rates and inlet gas velocities—temporal predictions.

FORMATION OF CHANNELS (GAS BYPASS)

A characteristic feature of our model and experimental bubbling beds is a tendency for the bubbles to collect into a persistent central channel. In the model, this channeling behavior is a natural consequence of the bubble interaction rules and the geometric boundary conditions. Specifically, given an initially uniform dispersion of bubbles at the distributor, it is always more likely that a trailing bubble will be caught in the influence of a leading bubble closer to the bed center than one further from the center. Once coalescences begin, the bias towards the center becomes further skewed because the coalesced bubbles are already displaced in that direction. The global effect of these sequential coalescences is to create an avalanche of inward moving bubble gas. Thus it is not necessary for there to be some external lateral force introduced near the walls (e.g., associated with downward moving solids) to achieve channeling. One could argue that the observed downward solids circulation near the walls is a natural result of the concentration of bubbles near the center. The avalanche of coalescences is also responsible for the overall pulsation in gas flow.

Figure 6 illustrates a simulation that resulted in the formation of a central bubble channel in a 3-D bed. The figure shows snapshots of the bubbles at different times of the simulation. This case corresponds to gas velocity of 8.6 cm/s with k = 7.75 s^{-1} in Fig. 5. The snapshots give indication of bubble size distribution and also the ozone conversion as indicated by the color. Blue corresponds to the inlet concentration of ozone, while red corresponds to almost full conversion. There are several things that can be noted from these pictures. First there is period of rapid convergence where big bubbles are formed and bubble gas passes rapidly through the middle of the bed. This is followed by period in which there are

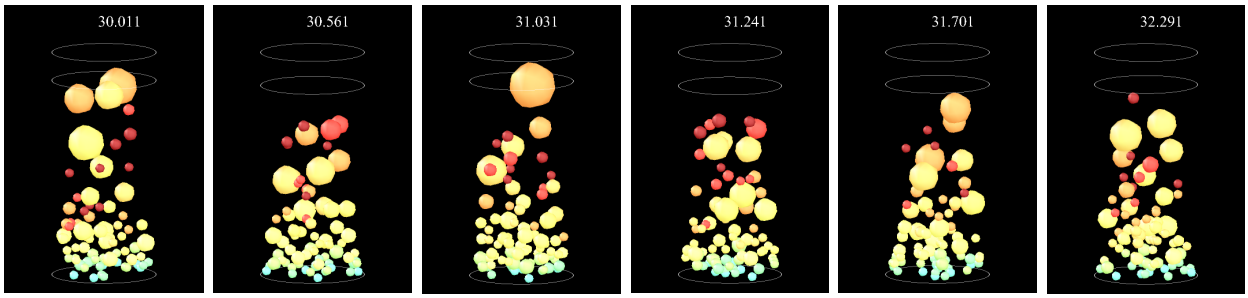

Fig. 6. Channel Formation in a Bubbling Bed .

many smaller bubbles moving upward more slowly. As the smaller bubbles become more and more numerous, a critical 'avalanche' condition is reached that triggers another round of rapid coalescence. The net result of these alternating processes is that the bubble gas pulses through a central channel that is continually reforming. This phenomenon is more pronounced in deeper beds (Halow et al., 1998; Pannala et al., 2001, 2003) where H_{mf}/D_t is larger than 5.

The pulsing flow also affects conversion. The injected bubbles have high concentrations of ozone and if the bubble size remains small, there is a good surface-to-volume ratio to ensure proper mass transfer between the bubbles and emulsion and thus resulting in higher conversion of ozone. The coalescence of the bubbles leads to bigger, faster moving bubbles with lower surface-to-volume ratio and thus exhibit poor conversion. Understanding these temporal oscillations might make it possible to perturb the bed in ways that counteract a direction to minimize the coalescence of the smaller bubbles into bigger bubbles and thus improve the conversion.

BED DYNAMICS

Figure 7 shows the number of bubbles with time for the above simulation. The simulations are run for 90 seconds, and the statistics are collected over the last 60 seconds of the simulation. Here we plot a 20 second window to illustrate the complex temporal variations. Figure 8 plots the time trace of the bed height for the same 20-second period. Bed height also behaves similarly to bubble number. For the two-phase model, one expects bed height to be directly proportional to the volume of gas in the bubble phase. From the plot it is apparent that there is are characteristic oscillations with periods of around 1 and 4 seconds.

Figure 9 illustrates the effect of the type of bubbles-size averaging on the observed trends. Average bubble diameters are computed based on number, area, volume and volume-to-surface ratio (Sauter mean or SMD). The number mean seems to be the smoothest and SMD seems to have the maximum variations. These differences indicate that the type of measurements made (i.e., the type of weighting involved in sampling) can affect the visibility of the dynamics. For evaluating gas bypassing through the bubbles, it

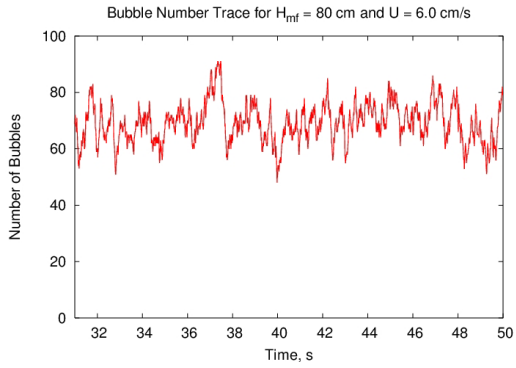

Fig. 7. Time trace for number of bubbles.

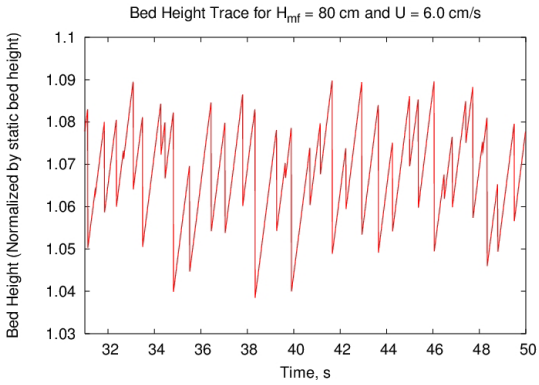

Fig. 8. The bed-height variation exhibits chaotic behavior.

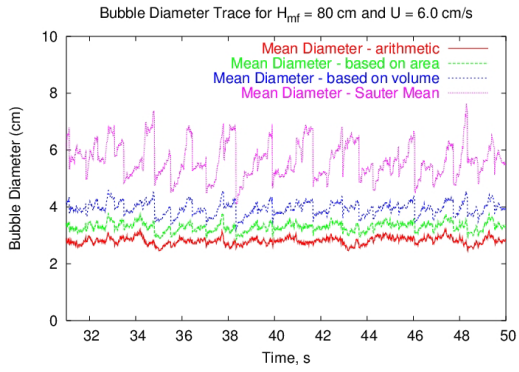

Fig. 9. Time trace of bubble size [diameter based on number mean, area, volume and Sauter mean diameter (3,2)].

would appear that SMD is more sensitive to the bubble dynamics. One also expects that the SMD bubble size would correlate most directly with conversion. Figure 10 illustrates this in terms of the average ozone concentration (normalized by the inlet concentration) in the bed overall and in the bubble phase as functions of time. Note that as the catalytic activity is increased, the relative variations in ozone

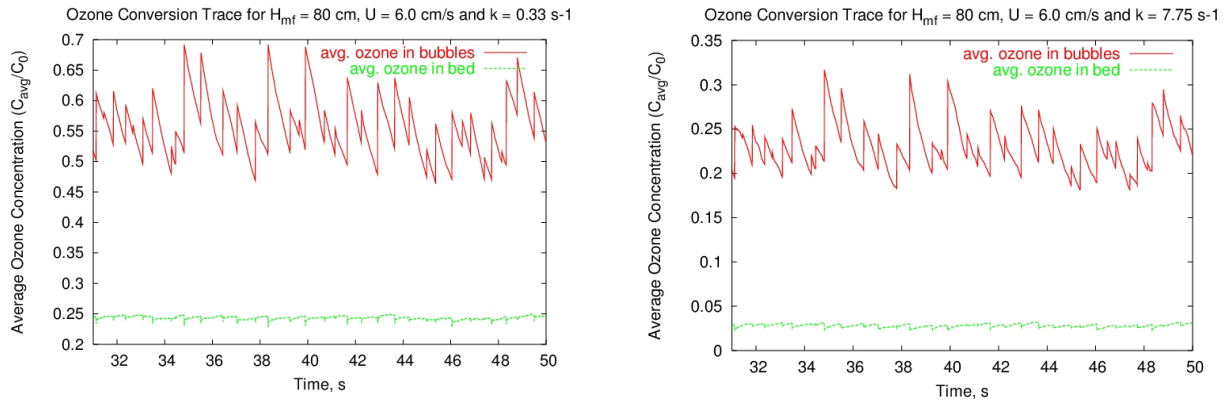

Fig. 10. Variation of Ozone concentration with time.

concentration become even more pronounced, and the ozone concentration is much lower in both measures.

In order to better quantify the temporal patterns, we computed auto-correlations, cross-correlations and power spectral density for some of the computed quantities. Figure 11(a) is a plot of the auto-correlation function for bed-averaged ozone concentration, bed height, bubble number, and SMD. Here we observe strong oscillations in all these quantities over time scales of a few seconds to tens of seconds. Figure 11(b) is a plot of cross correlations between bed-average ozone concentration and bed height, number mean bubble diameter and SMD. It is clear that ozone concentration in the bubble phase is strongly correlated with SMD. As expected, the cross correlation at zero time lag between ozone concentration in the bubbles and SMD is strongly negative, reflecting the impact of bubble size on mass transfer. The effect of bed pulsation is evident at longer time scales where bubble ozone concentration and bubble size become positively correlated. On the contrary, the overall average ozone concentration in the bed has a positive correlation with bubble size at small times that is out of phase with the bubble gas. We speculate that this difference in phase is due to the time delay associated with mass transfer and might potentially be used as a way to indirectly measure mass transfer. At further time delays, the cross correlations between gas phase and bubble phase ozone and bubble size appear to continue to shift in and out of phase. Figure 11(c) illustrates the cross-correlation between bed height with the number of bubbles and volume average bubble diameter. It is evident from this plot that bed height and volume average bubble diameter are strongly correlated, but there is an unexpected anti-correlation with the number of bubbles.

Fourier power spectra are useful for further resolving some of the oscillation time scales. As shown in Fig. 11(d–e), the power spectral densities of the bed ozone concentration, bed height, number of bubbles, and SMD reveal strong oscillations below 1 Hz. The latter three quantities have similar periods, but the ozone concentration is definitely varying at a lower frequency (about half) compared to the others.

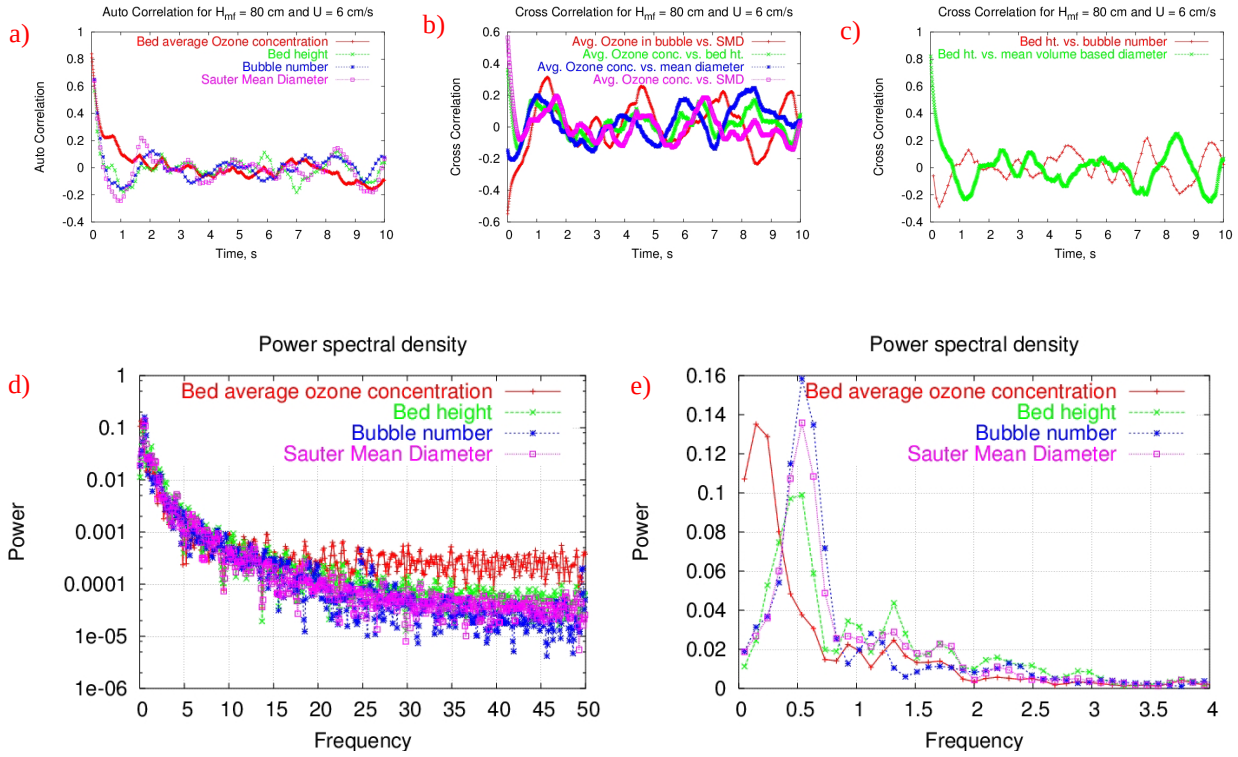

Fig. 11. Time series analysis of the model output: (a) Auto-correlation, (b) Cross-correlation for ozone concentration (c) Cross-correlation for bed height, and (d–e) Power spectral density.

LONG TIME SCALE FEATURES

In the above discussion, we observe that many dynamical features occur over time scales of seconds to tens of seconds. We observe from our model, however, that there are some global features that occur over even longer time scales. Because our model runs so fast, it is possible to explore these features in relatively great detail. Long time scale dynamics are reported in Daw et al. (2003).

SUMMARY

We find that a simple model of bubble dynamics combined with appropriate mass transfer and chemistry can simulate many key features of bubbling bed reactors. In addition, such a model predicts important spatial and temporal variations in conversion and performance that need to be further investigated. Specifically, we observe large variations in the degree of gas bypassing that might be altered by making appropriately timed external perturbations. These large variations occur as the result of the formation of bubble chains that grow and then catastrophically coalesce. We conjecture that simple models such as ours may provide a practical way for implementing model-based control of these global processes.

REFERENCES

1. Daw C. S., S. Pannala S., and J. S. Halow, "Simulations of Reacting Fluidized Beds Using an Agent Based Bubble Model," *To appear in the proceedings of Chemical Reaction Engineering IX; Chemical Reactor Engineering—Meeting The Challenges For New Technology*, Quebec City, Quebec, Canada, June 29–July 4, 2003.
2. Pannala S., C. S. Daw, and J. S. Halow, "Agent-Based Model for Bubbling Fluidized Beds," *2003 SIAM Conference on Computational Science and Engineering*, San Diego, February 10–13, 2003.
3. Pannala S., C. S. Daw, and J. S. Halow, "Low-Order Bubble Dynamics Model for Gas-Fluidized Beds—A Case Study of Ozone Decomposition," *7th Experimental Chaos Conference*, San Diego, August 25–29, 2002, Poster.
4. Pannala S., C. S. Daw, and J. S. Halow, "Near Real-Time Simulations of Fluidized Bed Reactors Using a Low-Order Bubble Model," *GRC conference on Granular & Granular-Fluid Flow*, Holderness School, Plymouth, NH, June 30–July 5, 2002, Poster.
5. Pannala S., C. S. Daw, and J. S. Halow, "Near Real-time Simulations of Large Fluidized Beds with a Low Order Bubble Model," Session 199b, *AIChE Annual Meeting*, Reno, Nevada, November 4–9, 2001.
6. Fryer, C., and O.E. Potter, "Experimental Investigation of Models for Fluidized Bed Catalytic Reactors," *AIChE Journal*, **22**, 38–47 (1976).
7. Darton, R.C., R. D. La Nauze, J. F. Davidson, and D. Harrison, "Bubble growth due to coalescence in fluidised beds," *Trans I Chem E*, **55**, 274, (1977).
8. Werther, J., "Influence of the distributor design on bubble characteristics in large diameter gas fluidized beds," *Fluidization—Proceedings of the 2nd Engineering Foundation Conference* [J. F. Davidson, D. L. Keairns (Eds.)], Cambridge University Press, Cambridge 1978, pp. 7–12, (1978).
9. Gheorghiu, S., J. R. van Ommen, and M.-O. Coppens, "Power-law Distribution of Pressure Fluctuations in Multiphase Flow," To appear in *Physical Review E*, (2003).

DEVELOPMENT OF A CENTRIFUGAL DOWNHOLE SEPARATOR

J. F. Birdwell

INTRODUCTION

Significant volumes of produced water–a mixture of formation and injection process water containing oil, salts, chemicals, solids, and trace metals–are generated in the production of crude oil and natural gas. In 1991, Louisiana generated over 1 billion barrels and Texas generated 7.5 billion barrels of produced water as a result of oil and gas operations. More than 250 million barrels of produced water are discharged each year to surface waters in these two states alone.

Because of the tremendous volume of water generated and the specific constituents typically present, discharge of produced water from oil and gas production operations has come under increased scrutiny by regulatory agencies. The maximum concentrations of contaminants in produced water that can be discharged are limited by the latest Environmental Protection Agency (EPA) regulations under the Clean Water Act. Future regulations are likely to be more restrictive and may include zero-discharge standards.

Compliance with water discharge standards is particularly onerous for small, independent oil producers. This category of producers maintains a significant percentage of technically recoverable but unproven reserves in the form of depleted reservoirs. In many instances, these deposits have been abandoned by larger producers due to low profitability. It is estimated that over 100 billion barrels of domestic oil reserves are in depleted reservoirs, with over half of these reserves maintained by independent producers. Because of low production rates and relatively high volumes of water produced in mining these reserves, the fraction of production cost attributable to water treatment and disposal is high.

Two primary alternatives exist for reducing produced water costs: (1) improved technologies for treatment of produced water prior disposal and (2) reduction of water production by performing oil/water separation in situ with water reinjection. Available water treatment technologies include reverse osmosis, membrane filtration, gas flotation, carbon adsorption, bioreactors, chemical oxidation, stripping/extraction, and UV oxidation. All of these processes are complicated and expensive, and systems consisting of multiple, discrete processes are required to reduce pollutant concentrations to discharge limits.

In-well oil/water separation with water recycle has the potential to be a less-expensive, less-complicated approach for minimization of produced water handling costs. Successful use of reinjection has increased in the last several years. The suitability of produced water for reinjection is determined by the recovery process, water quality, and rock formation properties. Options for in-well separations have been evaluated but no technology has reached maturity.

The objective of the subject project was evaluation and demonstration of a centrifugal separator suitable for downhole installation and operation to perform in situ removal of water from recovered oil. The separator evolved from centrifugal solvent extraction contactors that were developed at the U.S. Department of Energy's Savannah River Site, Argonne National Laboratory, and Oak Ridge National Laboratory for use in selective extraction of metals. Centrifugal extractors of various sizes (from 2- to 25-cm rotor diameter) have been built and operated over the last three decades in a variety of applications.

Several characteristics of the centrifugal extractor make a modified but conceptually similar device attractive for use as an in situ oil/water separator. These characteristics include (a) excellent phase separation; (b) reliability in remote applications with >20,000 hours of operation prior to maintenance; and (c) the ability to handle relatively high volumetric throughput with a very low residence time.

Several modifications required for conversion of the extractor into an apparatus suitable for use as a centrifugal downhole separator (CDHS) have been evaluated. The primary need that has been addressed is increasing the throughput of the device while remaining within inherent space constraints. As an extraction device, throughput increases are normally achieved by increasing the diameter of the rotor in order to increase residence time and centrifugal separation force. In the downhole application, it is necessary to achieve throughput increases by increasing the rotor length, or by otherwise reducing the amount of residence time required in the separator.

Additional issues pertinent to the downhole application that have been addressed include issues associated with the introduction of solids into the separator and reconfiguration of solution inlets and outlets to accommodate downhole operation.

MATERIALS AND METHODS

Several model V-2 centrifugal separators (having 2-inch rotors) were obtained from a commercial vendor (CINC, Inc., Carson City, NV). A Petroleum Environmental Research Forum (PERF) industrial partner supplied two crude oils for use in separations testing. One is a Gulf of Mexico light crude with an API gravity of 34.06°, specific gravity of 0.8547 at 60°F, and a viscosity of 9.0 cP at 77°F. The other is a heavy North Sea crude with an API gravity of 19.3°, specific gravity of 0.948 at 60°F, and a viscosity of 400 cP at 77°F. Substitute ocean water for use in testing has been formulated according to ASTM Standard Specification D1141-90. Most of the testing performed to-date has used the lighter oil, based on recommendations from industrial partners, who have indicated that addition of water to heavy oils is generally needed to facilitate pumping to the surface.

Typically, the water and oil inventories were kept in separate feed vessels and were mixed just prior to delivery into the separator. Discharge solutions were continuously recycled to the feed tanks, permitting testing for extended periods. In some instances, samples of discharge solutions were collected

in API centrifuge tubes, were acidified with 0.125 mL of 1 N HCl, and were centrifuged for 10 minutes at 4500 rpm. Water contamination of the oil discharge stream was measured by direct reading using the graduations on the centrifuge tubes. Oil contamination of the water stream was determined by dissolving the oil from the water samples in two 1-mL aliquots of hexane, evaporating the hexane, and weighing the oil residue. In other instances, direct visual observation of phase carryover was made after processing effluent stream samples in a batch-type laboratory centrifuge.

All tests were performed in a laboratory setting and at limited flow rates. No testing has been performed in a well-type configuration with integration of the separator and typical ancillary equipment (feed and product pumps, and interconnecting piping). A schematic of the separator is shown in Fig. 1.

The project strove to achieve functional criteria that were developed with input from the Department of Energy and representatives from the PERF. These functional criteria were listed in preceding years' progress reports, and have been updated to reflect work performed in the current reporting year (Table 1).

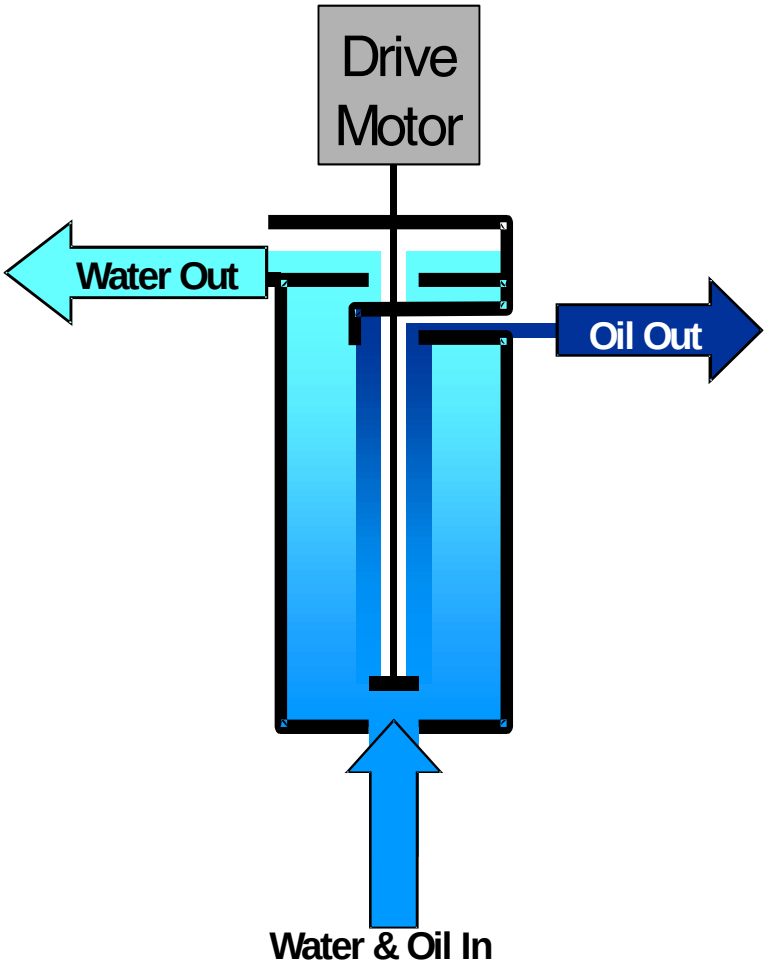

Fig. 1. Schematic drawing of the centrifugal separator rotor.

Table 1. Functional criteria for development of the CDHS

Industry-supplied criteria	Achieved to-date	Comments
Flow rate: 2,000 to 10,000 bbl/d	15 bbl/d	Results indicate that industry criteria cannot be met within the physical constraints imposed by well bore
Diameter: 6 inches maximum for 7-inch diameter well	2-inch dia. by 4-in. rotor 2-inch dia. by 6-in. rotor	An extended length rotor has been fabricated. A design modification has been proposed that will provide the mechanical stability required for longer rotors.
Temperature: 100 to 180°F	75–150°F	Increasing operating temperature was found to improve separations using heavy North Sea crude
Water-to-oil ratio: 1:10 to 10:1	1:19 to 10:1	The bench-scale separator has been operated over the stated criteria range without loss of separating efficiency
Is gas processing feasible?	Yes	Tests have been performed at gas levels up to 21% (v/v) without loss of performance
Solids: 0–3% (sand to clay)	3% sand Feed modification made to reduce solids uptake	3% sand was processed through a hydroclone as a pretreatment step. The recent modification of the feed mechanism reduces solids uptake
Product quality: <2000 ppm cross-phase contamination	Achieved in tests to-date	Separation efficiency can be increased by dimensional adjustments and speed increase
Reliability: 18 months between failure	27 months or greater time between failure	Mean time to failure has been determined from prior DOE tasks. Units currently in use as extraction equipment have greatly exceeded 27 months in chemically harsh environment.

RESULTS

Tests were conducted using the Gulf of Mexico crude at volume ratios ranging from 10:1 to 1:19 (water-to-oil). The water concentration in the oil discharge was typically <0.2% (vol) up to throughputs of approximately 0.4 gpm. The oil concentration in the water discharge in all tests ranged from 0.002 to 0.3 g oil/100mL discharge water. Typical separation results are presented in Figs. 2 and 3. Results from limited testing using heavy crude demonstrate the range of oils that can successfully treated using the centrifugal separator.

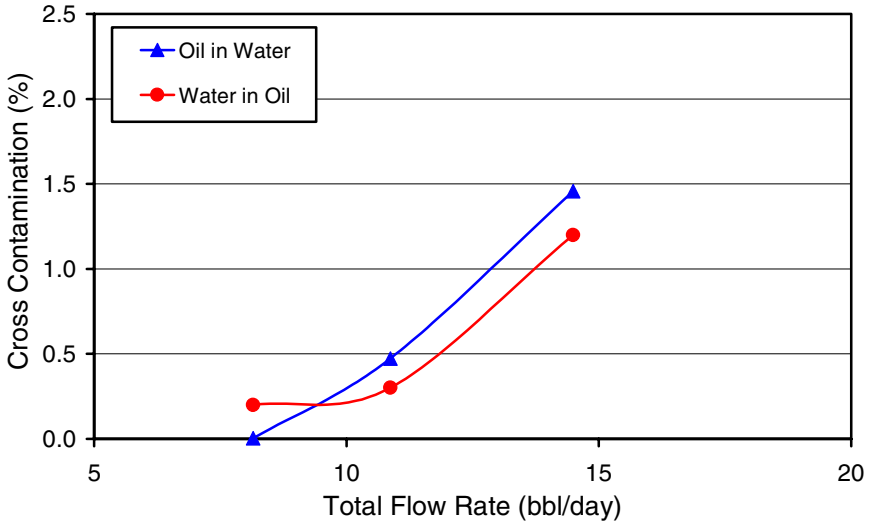

Fig. 2. Performance of separator using Gulf of Mexico light crude, 1:1 water-to-oil feed ratio, 2500 rpm rotor speed.

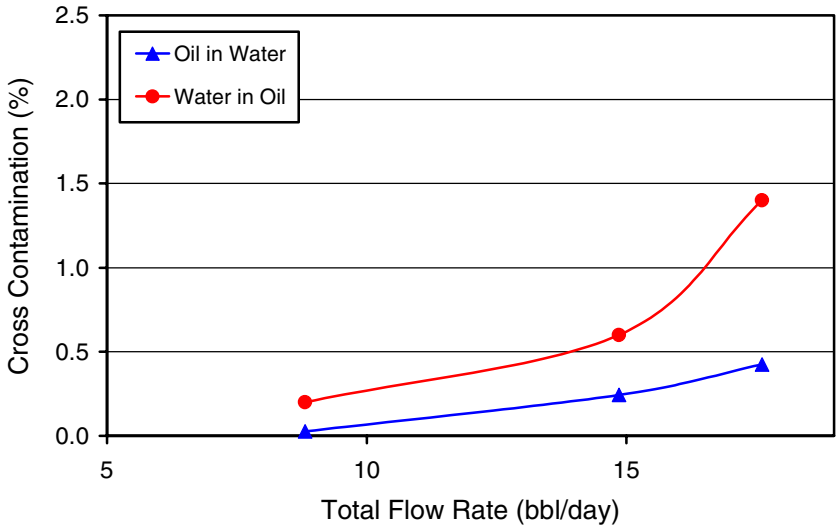

Fig. 3. Oil-water separation from a stream consisting of Gulf of Mexico light crude, 10:1 water-to-oil feed ratio, 2500 rpm rotor speed.

Most recently, oil/water separation tests have been performed in bench-scale modified centrifugal contactors. The modifications have been directed toward eliminating the mixing characteristic of the contactor that is required for efficient extraction performance but is unnecessary and undesirable in applications requiring only phase separation. In addition, the feed, withdrawal, and internal component configurations have been designed to conform to the physical confines of small-diameter well casings.

Results reported previously indicate that separation performance is improved at elevated (above ambient) temperatures, and that addition of gas to the inlet stream did not affect phase separation. The

latter finding is attributable to the presence of a liquid-free column along the center axis of the rotor during operation. As a result, the light-phase flow path is not obstructed through the rotor, allowing for two-phase (gas/liquid) flow.

Activities in the reporting year have been focused toward design and testing of modifications to increase the throughput of the unit. Using a mathematical model of separator hydraulics, the effect of length increases on throughput has been evaluated and an extended-length device has been fabricated by modifying one of the commercially available units. Testing of this unit has been completed.

Of perhaps greater significance, a modified feed configuration has been devised and tested. In general, the modification reduces the mixing effect which the rotor has on entering fluids. Consequently, the liquid material entering the rotor is not a dispersion of the feed phases, as is the case in the prior state of the art. Because the feed stream is not dispersed, the residence time required within the rotor to achieve separation is greatly reduced. Based on preliminary observations and hydraulic calculations, it is estimated that the throughput of the device can be increased by at least a factor of ten without any increase in rotor length or rotational speed.

Modification of the separator hydraulic model has confirmed an anticipated result; outside a finite range of flow conditions, the pressure drop through the internal passages of the separator and the inability of the separator to overcome this pressure drop becomes the throughput-limiting factor. In this circumstance, increasing the residence time of fluids within the separator by increasing the length is not an effective means of increasing throughput. Additional physical modifications of the separator should expand the envelope of acceptable flow conditions, but will not result in a separator that will achieve the throughput objectives listed in Table 1. However, performance (separation and throughput performance) are applicable to lower-yield wells. Consequently, a proposal has been submitted by ORNL and the University of Tennessee Department of Chemical Engineering in response to a call by the DOE Fossil Energy for technologies benefiting independent oil producers.

SUMMARY

Modifications have been made to optimize a centrifugal device originally designed as a liquid-liquid extractor for use as an oil/water separator. The modifications were intended to accommodate the constraints imposed by the physical dimensions of well bores and to minimize incidental mixing of feed solutions entering the device. Preliminary testing using a commercial device with few modifications confirmed acceptable phase separation performance on light and heavy crude oils. Testing at elevated temperatures and with introduced gas has indicated no loss of separation performance. Pretreatment of the inlet stream to remove solids has been demonstrated.

Recently, a novel feed configuration intended to reduce the extent to which the feed streams are mixed by rotor-generated shear forces was devised and tested. Preliminary analysis of results confirms the effectiveness of the modification.

Results of a modification of the hydraulic model of the separator confirm the expectation that, beyond a limiting boundary, separator throughput is limited by pressure drop through the flow channels, and not by the residence time of fluids in the separator. Beyond this limit, increasing the length of the separator to increase residence time is of not benefit in terms of increased separator capacity.

BIOPROCESSING OF FOSSIL FUELS

Abhijeet Borole
Life Sciences Division

The overall objective of this research program is to develop novel technologies for processing fossil fuels using biocatalysis and bioprocessing concepts. As compared to current thermochemical technologies, the bio-based technologies operate at lower temperature and pressure and have the potential to be more energy-efficient. Processes based on oxidative as well as reductive reactions are being investigated for bioupgrading applications. One project is focused on sulfur removal and a second one on developing thermophillic enzymes for breakdown of polyaromatic molecules in an oil environment.

BIODESULFURIZATION OF PETROLEUM FEEDSTOCKS

The objective of this project is to develop improved enzymes for biodesulfurization of petroleum feedstocks. The goal was to improve the activity and broaden the selectivity of desulfurization enzymes using directed evolution as a tool as well as to explore the impact of ring-opening on biological desulfurization. This was the second year of the project and included work on genetic engineering of the desulfurization enzymes (particularly the desulfinase enzyme, which breaks the carbon-sulfur bonds in organosulfur compounds), investigation of the specificity of the desulfurization enzymes for removing diffeent organosulfur molecules from diesel, and a study of synergistic biodesulfurization-biocracking process. The project partners included ExxonMobil, ChevronTexaco, and University of Tennessee, Knoxville (UTK). ChevronTexaco was the lead in developing the biocracking catalysts and ExxonMobil assisted in the genetic engineering of the desulfinase enzyme. The first generation of mutagenesis of the desulfinase enzyme (cloned into an E. coli) produced about 800 colonies. A mutant with four-fold activity was isolated from this experiment. The specificity experiments were conducted with three different organisms and two different diesel fuels. The organisms studied were Rhodococcus sp. IGTS8, Pseudomonas putida, and E. coli. The IGTS8 was the parent strain (not genetically engineered) from which the desulfurization genes (dszABC) were cloned into the other organisms. The results indicated that the IGTS8 strain was able to achieve maximum desulfurization of the diesel fuels. The synergistic experiments with biocracking (ring-opening) catalysts conducted so far have not yielded any conclusive results and more research needs to be done to understand the effect of the synergistic process.

BIOLOGICAL HYDROGENATION OF ORGANOSULFUR COMPOUNDS

This project is aimed at investigating the potential of enzymatic and biomimetic catalysts for hydrogenation and hydrodesulfurization of oil compounds with the goal of upgrading crudes via sulfur removal and improving downstream processing. This was the second year of the project. During this year,

the enzyme hydrogenase was studied to determine the hydrogenation of dibenzothiophene. In its native state, it was unable to catalyse the reaction, although it was found to be able to perform the hydrogen activation even in 10% acetonitrile or 10% ethanol—water system. The need to bring the substrate near the active site (which has the active hydrogen bound to it) was realized and further work was conducted in isolating the enzyme active site. This was done by digestion of the enzyme followed by separation via size exclusion and ion exchange chromatography. An invention disclosure was submitted on this subject matter. The isolated active center was still able to activate hydrogen gas, however, the yield of the active center from the enzyme was very low, due to which large quantities could not be isolated. The active center potential seems to have potential to hydrogenate/reduce organosulfur compounds and these tests are in progress.

BIOUPGRADING OF HEAVY CRUDES USING THERMOPHILLIC ENZYMES

Heavy oils consist of a significant portion of asphaltenes, which are condensed polyaromatics that increase viscosity and melting point of the crudes. Enzymes which can degrade polyaromatic hydrocarbons can potentially be used to degrade the molecules via ring-opening. Cytochrome P450 enzymes are capable of introducing the first oxygen molecule into the PAHs. This project is focused on developing biocatalysts, which will be capable of ring-opening and operation at slightly higher temperatures in the oil phase. The cytochrome P450 class of enzyme also consist of some enzymes which have thermostability up to 90°C. We have initiated protein engineering of cytochrome P450 to produce hybrid enzymes which will be capable of PAH oxidation as well as operation at higher temperatures. Further optimization of these enzymes is planned using directed evolution and other genetic engineering techniques.

PUBLICATIONS AND PATENTS

Borole A. P., Eric N. Kaufman, M. J. Grossman, V. Minak-Bernero, R. Bare, and M. K. Lee, *Emulsion formation and breakage characteristics of Rhodococcus erythropolis and Echereshia coli hosting biodesulfurization genes*, Biotechnology Progress, 2002, 18, No. 1, 88–93.

Borole, A. P., and Hamilton, C. Y., *Enzyme specificity and host effect during biodesulfurization of petroleum feedstocks*, a poster presented at the 24th Symposium on Biotechnology for Fuels and Chemicals, Gatlinburg, TN, May 2002.

Borole, A. P., *Potential for Biocatalysis in Petroleum and Petrochemical Industry: Related Issues and Challenges*, a poster presented at the Gordon Research conference, Meriden, NH, July 2002.

Invention disclosure: Borole, Abhijeet P., and S. R. Kulkarni, Development of Ni-Fe hydrogenation catalyst from *D. gigas* hydrogenase, submitted August 2002, approved for Patent application: November 2002.

IMPROVING TOOLS AND METHODS FOR ECOLOGICAL RISK ASSESSMENT AT PETROLEUM-CONTAMINATED SITES

R. A. Efroymson, D. S. Jones, and W. W. Hargrove

INTRODUCTION

This project, FEAC319, began in May of 2000 with support from the U.S. Department of Energy (Fossil Energy Program, National Petroleum Technology Office, Tulsa, OK; Nancy Comstock and Kathy Stirling, Project Managers). The project is intended to provide risk assessment tools and methods to the Petroleum Environmental Research Forum (PERF) project 99-13, "Expanding the Science Basis of Risk." Although the kickoff meeting for this project was planned for 1999, it did not occur until February of 2001. ChevronTexaco, ExxonMobil, BP, Unocal, and the Canadian Association of Petroleum Producers have contracts in place with PERF, in addition to Proprietary Agreements with Lawrence Berkeley National Laboratory and Oak Ridge National Laboratory. FEAC319 has four ongoing tasks: (1) to develop a framework for Net Environmental Benefit Analysis, (2) to develop plant uptake models for chemical contaminants that are found at downstream sites, (3) to develop or to evaluate spatial analysis models and tools for risk assessment of vegetation and wildlife, and (4) to finalize a review of soil ecotoxicity values for petroleum mixtures in soil.

The justification for this work is that remedial activities at refinery or other downstream locations may be more expensive than necessary for at lease three reasons. First, models for estimating ecological exposure are not readily available, so excessively conservative estimates of exposure and risk are sometimes made. Second, certain remedial actions such as soil removal and the associated destruction of habitat may result in greater risk to ecological populations or processes than the continued presence of the original, aged contamination. Third, certain ecological functions may be replaced by on-site or off-site restoration.

Net Environmental Benefit Analysis (NEBA). NEBA attempts to answer the question: what type and scope of remediation, restoration, or natural attenuation of chemicals in environmental media would cause the least damage or most benefit to the value of habitat, local populations, and valued ecological functions? NEBA involves calculating a net environmental benefit of remediation or ecological restoration, compared to natural attenuation (no action) or another regulatory baseline. Remedial alternatives include traditional methods such as excavation, and less invasive options, such as microbial bioremediation (nutrient additions and tilling), phytoremediation, natural attenuation, wetland enhancement, and planting of native species. The recolonization of areas damaged by contamination, excavation or tilling may depend on the extent of fragmentation of a landscape.

The term “NEBA” was probably coined by agencies and industries evaluating options for marine oil spills. A report was published by the National Oceanographic and Atmospheric Administration (NOAA) in 1990 entitled *Excavation and rock washing treatment technology: net environmental benefit analysis.* In that study a group of scientists and engineers comprised of Exxon, NOAA, and State of Alaska scientists evaluated the environmental tradeoffs associated with excavating and washing hydrocarbon-contaminated sediments that were deeply buried along parts of the Alaskan shoreline affected by the Exxon Valdez oil spill. Several precedents for NEBA exist, but they provide little, specific methodological guidance for the assessment of contaminated sites. These range from federal and state government examples (e.g., Texas Commission on Environmental Quality) to industry examples. A framework for Net Environmental Benefit Analysis, analogous to the EPA framework for ecological risk assessment, has not been developed prior to the effort under this project.

Plant uptake models. A primary gap in any ecological risk assessment for terrestrial wildlife is in the quantification of chemical concentrations in wildlife foods. It is advisable to measure these concentrations at a site of concern. However, because funding or seasonal constraints may limit the number and type of measurements that may be made at a site, it is useful to have models available to estimate contaminant concentrations in plant materials and invertebrates, based on concentrations in soil, soil characteristics, and taxonomic characteristics. Elements and compounds of concern at downstream petroleum sites include: polycyclic aromatic hydrocarbons, lead, nickel, selenium, mercury, and vanadium. Published soil-plant uptake factors tend to overestimate bioaccumulation and risk when concentrations of elements in soil are high and to underestimate uptake at lower concentrations. In addition, soil and/or plant characteristics have not previously been incorporated into uptake models.

Spatial modeling. The exposure of ecological receptors to chemical contaminants has spatial dimensions. Wildlife exposure models include dietary uptake but rarely the habitat and movement preferences that also determine exposure. Refineries, landfarms, or pipelines may be located at the center of a single habitat type (e.g., grassland), in which case the sizes of the habitat patches are important, or between remnant patches habitat. Pertinent questions are: (1) what is the role of wildlife movement and preferential uses of different habitat in determining exposure; (2) what is the role of the fragmentation of habitat in determining exposure; and/or (3) how do habitat loss and contamination interact to determine risk to wildlife? Moreover, the most efficient corridors for establishing connectivity between habitat remnants is unknown, and if these could be established, optimal restoration plans could be developed. Spatial modeling adds to the realism of estimates of ecological exposure, so that fewer conservative assumptions may be used in risk assessments.

Ecotoxicity values. Ecotoxicity benchmarks for petroleum mixtures (i.e., concentrations in soil that are associated with a particular level of ecological effect) can be used to help determine which impacted

sites might require an ecological risk assessment. Several studies of the ecotoxicity of petroleum in soils have been conducted in the past decade, including toxicity tests of plants, soil invertebrates, and other organisms in field-contaminated and laboratory-contaminated soils. This information has not previously been assembled. Such a review is a necessary precursor to determining research gaps and ultimately selecting concentrations of petroleum hydrocarbons that may be used as screening levels for ecological risk assessments at petroleum exploration and production sites, refinery sites, pipeline locations, or other petroleum-mixture-contaminated locations.

It is assumed that improved methods for ecological risk assessment should lower costs of remediation by decreasing the need for conservative assumptions in estimates of ecological exposure.

DISCUSSION OF CURRENT ACTIVITIES

Net Environmental Benefit Analysis. Net Environmental Benefit Analysis (NEBA) provides a methodology for revealing and comparing benefits and risks of alternative management options. NEBA of chemically contaminated sites has been defined as the comparison of risks and benefits associated with any pair of three principal alternatives, as well as combinations of these: (1) leaving contamination in place; (2) physically, chemically, or biologically remediating the environment through traditional means; and (3) improving ecological value through on-site and off-site restoration alternatives that do not directly focus on removal of chemical contamination. The focus of this task has been on the development of a framework for NEBA; petroleum industry representatives indicated that such a framework would provide a useful product. We completed a report in January 2003, Efroymson, R. A., J. P. Nicolette, and G. W. Suter II. 2003a. *A Framework for Net Environmental Benefit Analysis for Remediation or Restoration of Petroleum-contaminated Sites*. ORNL/TM-2003/17. Oak Ridge National Laboratory, Oak Ridge, TN. In December of 2002, we submitted a manuscript to the peer-reviewed journal *Environmental Management*: Efroymson, R. A., J. P. Nicolette, and G. W. Suter II. 2003. *A framework for Net Environmental Benefit Analysis for remediation or restoration of contaminated sites.* This paper is in review at the time of this writing.

We have chosen to adopt risk assessment terminology to describe the NEBA framework to facilitate the use of NEBA by risk assessors. The NEBA framework described here has a single problem formulation stage to define the management goals of the assessment, the assessment endpoint entities, the stressors of interest, temporal and spatial scales of analysis, and the plan for comparison between alternatives, including proposed, comparative metrics for ecological states. Parallel characterizations of exposure for each alternative include chemical concentration dynamics (e.g., estimates of rate, extent, and metabolites of biodegradation) and changes in bioavailability. Parallel characterizations of effects (benefits and risks) for the alternatives include the dynamics of ecological recovery, as well as direct

restoration dynamics. NEBA, by definition, includes a final step of comparing ecological states among alternatives. The high-level framework for NEBA is depicted in the flow chart in Fig. 1. Additional flow charts for NEBAs of individual alternatives (natural attenuation, remediation, ecological restoration) are depicted in the report on NEBA cited above.

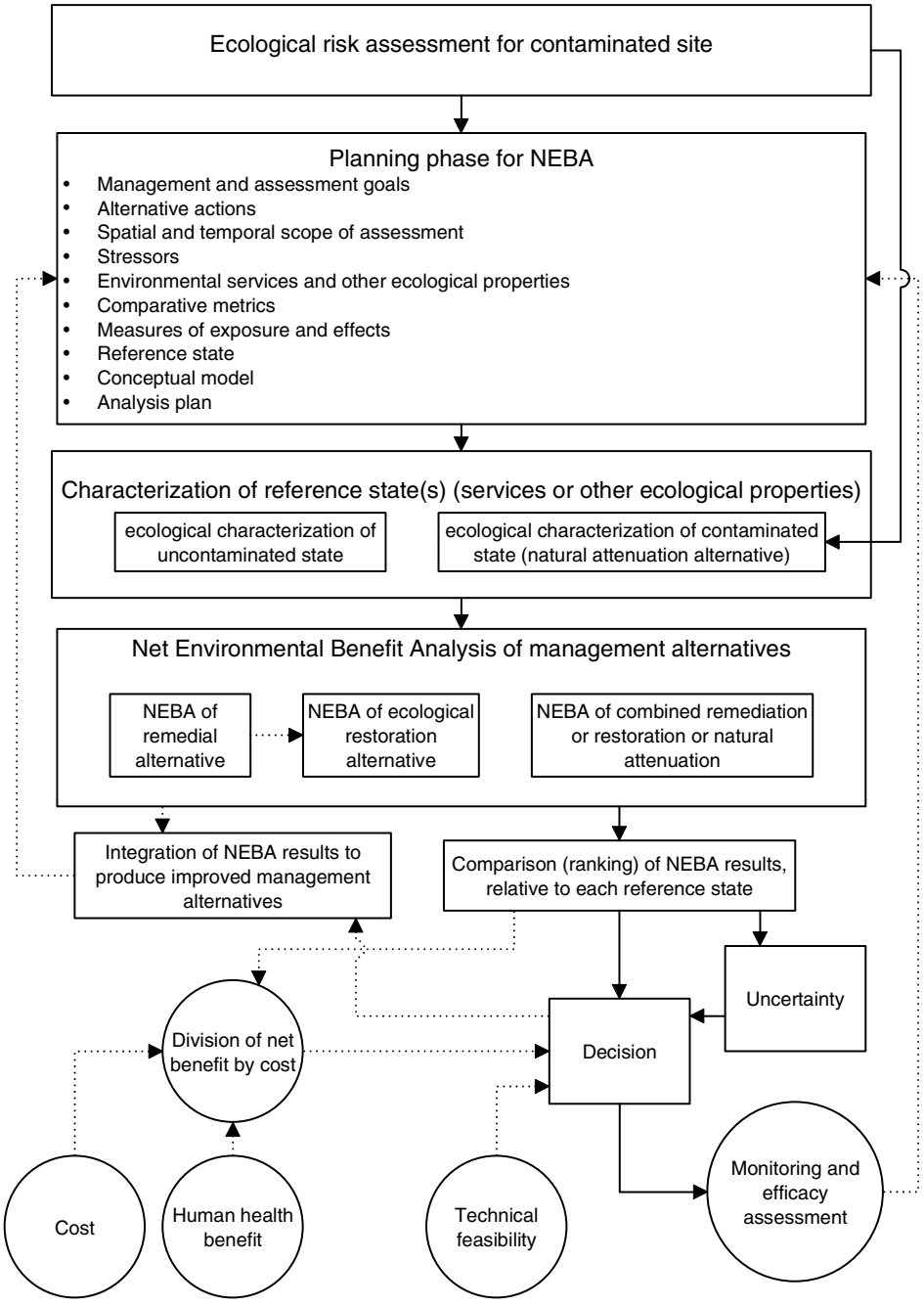

Fig. 1. Framework for Net Environmental Benefit Analysis for contaminated sites. Dashed lines indicate optional processes; circles indicates processes outside of NEBA framework.

Plant uptake models. To evaluate the relationship between the contaminant concentration in soil and plants, single-variable and multiple regressions were performed using SPSS 11.5 (SPSS 2002). Earlier in this project, regression models were developed for (1) vanadium in soil and soil pH; (2) lead in soil, one common co-contaminant (cadmium), and three soil characteristics (i.e., pH, percent organic matter, and cation exchange capacity); and (3) selenium in soil and three soil characteristics (i.e., pH, percent organic matter, and cation exchange capacity). The current reporting period includes efforts to refine the vanadium models through the incorporation of additional soil characteristics into the uptake model and to compare the regression models derived for various types of plants. This report focuses on the former effort.

A two-variable regression model for vanadium and soil pH was developed previously using funds from FEAC319. Multiple regression analyses were conducted for vanadium in soil and two soil characteristics (i.e., pH and percent organic matter). Soil cation exchange capacity data also was collected, but insufficient data were available to perform statistically rigorous analyses. Preliminary results of a log-log regression analysis of soil and plant vanadium concentrations suggest that this model may be only marginally useful for predicting plant concentrations of vanadium. The single-variable regression based on all 120 data points in the data set was statistically significant ($p < 0.001$) but explained relatively little of the observed variance in plant vanadium concentrations ($r^2 = 0.220$).

Including soil pH and percent organic matter ($n = 106$) resulted in a statistically significant ($p < 0.001$) multiple regression model that explained more of the variance in plant vanadium concentrations ($r^2 = 0.630$) than did the single-variable model. However, a "backward removal multiple regression analysis" failed to retain soil vanadium concentration as an explanatory variable (i.e., the Probability of F-to-remove was ≥ 0.100). The Condition Number for the multiple regression model containing all three explanatory variables was 26.86. This suggests that the three-variable model may be somewhat unstable due to collinearity among one or more of the explanatory variables. Further review of the collinearity diagnostics suggested that soil pH was the primary source of the observed collinearity (i.e., the variance proportion was 0.99).

Therefore, a two-variable regression model for soil vanadium and percent organic matter was developed. This new model was also statistically significant ($p < 0.001$) and it explained almost as much of the variance in plant vanadium concentrations ($r^2 = 0.622$) as did the three-variable model. However, the Condition Number for this new model was only 3.868. Based on these results, this two-variable regression model that included percent organic matter and soil vanadium concentrations was the best of the models tested above.

Spatial analysis tools and models. The Pathway Analysis Through Habitat (PATH) tool was developed to identify and map corridors of animal movement across maps of land cover categories (e.g.,

roads, grass, industry, etc.) or more specific features (e.g., structures or land farms). Applications of the tool to the petroleum industry lie in the identification of key areas for ecological restoration; spill remediation; wildlife barrier construction; or avoidance areas for road, pipeline or refinery facility development. Corridors are the "roadways" most commonly used by animals as they travel through an area. Corridors represent frequent movement paths among discrete patches of suitable habitat in a diverse matrix of land cover categories. Despite its importance, the idea of landscape corridors remains largely conceptual. No analytical tool has existed which could examine a real-world map, quantify landscape connectance, and identify wildlife corridors. The tool simulates virtual animals, termed "walkers," which are imbued with the movement characteristics and habitat preferences of particular animal species.

Three types of results are generated for each analyzed map: (1) the collective "footprints" of all walkers successfully dispersing, summed to map corridors; (2) a matrix of pair-wise rates of transfer from each patch to each other patch in the map; and (3) a set of importance values for each patch in the landscape, in terms of the addition that patch makes to overall connectivity across the map. The absence of corridors may represent barriers to movement, and absolute barriers are explicitly included in the modeling process. The transfer matrix indicates whether particular patches of habitat are population “sources” or “sinks,” which indicates the overall effect of this patch on the demography of the animal population.

The patch importance values are an important potential result of the tool. We calculate a connectivity index for the map with the patch present, then conceptually remove the patch and recalculate map-wide connectivity to compute an importance value for each patch in the map. Patches with high importance could be protected or preferentially remediated; patches with low importance would be more favorable for industrial growth and development. In the case of an invasive species, the sense of the importance values would reverse. Patches important for connecting movements of a weedy species could be made inhospitable for the invader. In addition, the tool could lead to mitigation measures, such as the identification of key areas for habitat restoration or barrier construction.

The code is written in parallel to allow the analysis of very large maps or maps with large numbers of habitat patches. The tool has been tested with several artificial maps; that is, corridors are predicted where they would be expected. The tool has also been used to identify corridors in three realistic landscapes. An example is depicted in Fig. 2. The corridor analysis tool, PATH, is summarized in a manuscript that was submitted to an American Society for Testing and Materials publication. Hargrove, W. W., Hoffman, F. M., and Efroymson, R. A. 2004. A Practical Map-Analysis Tool for Detecting Dispersal Corridors, *In Landscape Ecology and Wildlife Habitat Evaluation: Critical Information for Ecological Risk*

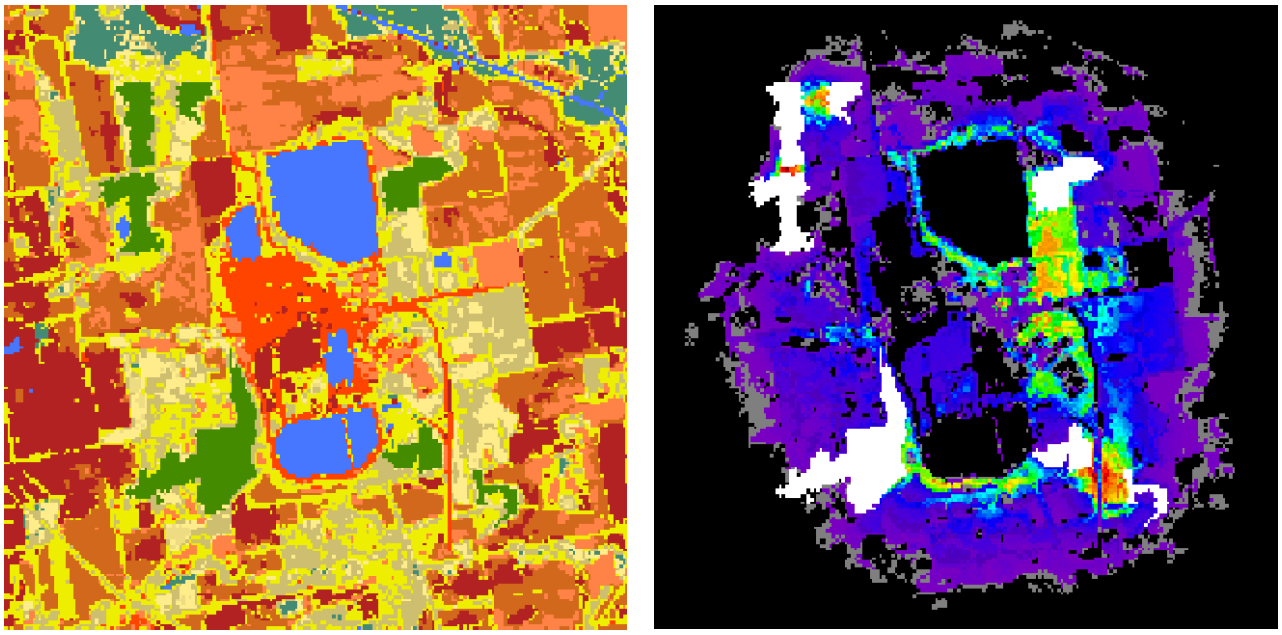

Fig. 2. (left) Patches of habitat at a gravel pit operations site, with forest remnants depicted in green-black, and ponds in blue. (right) Output of PATH showing the forest remnants in white, strong corridors in red, moderate corridors in green or yellow, and poor corridors in blue.

Assessment, Land-Use Management Activities, and Biodiversity Enhancement Practices, ASTM STP 1458, L. Kapustka, H. Galbraith, M. Luxon, and G. R. Biddinger, Eds. American Society for Testing and Materials, West Conshohocken, PA.

Ecotoxicity benchmarks. Project funds were used to revise a journal article on ecotoxicity benchmarks for plants and soil invertebrates that was originally written under FEAC303 "Biological quality of soils containing hydrocarbons and efficacy of ecological risk reduction by bioremediation alternatives." The article was accepted by *Environ. Toxicol. Chem.* but withdrawn after results were presented at a PERF 99-01 meeting in October 2000 and received substantial review comments from petroleum industry representatives. The article was revised in June of 2001 and again in November of 2001 and November of 2002, based on additional petroleum industry comments. The paper has become a review of existing ecotoxicity values and guidance to regulatory agencies and others regarding recommended considerations in the derivation of soil ecotoxicity benchmarks. The new version of the paper was submitted in February 2003 to the peer-reviewed journal *Human and Ecological Risk Assessment* with five related papers on ecological impacts of petroleum contamination: Efroymson, R. A., B. E. Sample, and M. J. Peterson. Ecotoxicity test data for total petroleum hydrocarbons in soil: plants and soil-dwelling invertebrates.

Data on the toxicity of total petroleum hydrocarbons (TPH) to plants and soil invertebrates were reviewed for possible application to benchmark development. Toxicity data included Lowest Observed

Adverse Effects Concentrations (LOAECs); estimated 25th percentile effective concentrations (EC25s), EC20s, and median lethal concentrations (LC50s); effective concentrations that caused greater than a 20% level of effect; and No Observed Adverse Effects Concentrations (NOAECs). The variabilities in petroleum material, chemical analytical methodology, age of hydrocarbon-soil contact, nutrient amendment, and measured effects levels did not permit much aggregation of the data. Tenth, twenty-fifth, and fiftieth percentiles of toxicity and no-effects data were presented for unaggregated results. Some toxicity values for plants exposed to various refined petroleum mixtures in soil were below the 10000 mg/kg TPH level that is sometimes recommended as a protective criterion for plants exposed to crude oil waste. Toxicity to invertebrates often occurred at concentrations of TPH lower than those associated with toxicity to plants. Lighter mixtures generally were associated with lower ranges of effects concentrations than heavier mixtures such as heavy crude oil. Existing toxicity data were not sufficient to establish broadly applicable TPH ecotoxicity screening values with much confidence, even for specific mixtures.

The following guidance was suggested for regulatory entities or other interested parties that are considering establishing screening benchmarks for ecotoxicity:

1. A party with interest in developing screening benchmarks must consider what entities to protect.
2. A user of the toxicity data should have two levels of protection in mind: (1) an approximate response level and (2) a percentile that represents the acceptable percentile of the community that may exhibit the response.
3. A decision should be made about which analytical data to use. Considerations include the accuracy and availability of data obtained using various methodologies.
4. The regulatory agency or other interested party should decide whether toxicity data for TPH or petroleum fractions are most useful (and available) for estimating toxicity of aged mixtures in soil.
5. Screening benchmarks should be established with detection limits in mind.
6. Regulatory agencies and other interested stakeholders should strongly consider collecting new ecotoxicity data for petroleum hydrocarbons in soil.
7. Given the paucity of existing ecotoxicity data for TPH, a well-conducted field survey may currently be a more useful screening tool than a benchmark comparison.

REFERENCES

BJC (Bechtel Jacobs Company). 1998. Empirical models for the uptake of chemicals from soil by plants. ES/ER/TM-198. Oak Ridge National Laboratory, Oak Ridge, TN, USA.

Efroymson, R. A., B. E. Sample, and G. W. Suter II. 2001. Bioaccumulation of inorganic chemicals from soil by plants: regressions of field data. *Environ. Toxicol. Chem.* 20:2561–2571. SPSS 2002. SPSS 11.5: Brief Guide. SPSS Inc., Chicago, IL.

DEVELOPING AN ECOLOGICAL FRAMEWORK TO EVALUATE THE IMPACTS OF RELEASES AT UPSTREAM EXPLORATION AND PRODUCTION SITES: THE EFFECT OF SIZE AND DISTRIBUTION

R. A. Efroymson, H. I. Jager, T. L. Ashwood, E. A. Carr, W. W. Hargrove, and R. A. Washington-Allen

INTRODUCTION

This project, FEAB321, began in July of 2000 with support from the U.S. Department of Energy (Fossil Energy Program, National Petroleum Technology Office, Tulsa, OK; Nancy Comstock, Project Manager). The framework and ecological modeling are collaborative research between Lawrence Livermore National Laboratory (Tina Carlsen, Principal Investigator) and Oak Ridge National Laboratory. The project has several long-term goals: (1) to quantify the effects of habitat removal and fragmentation from petroleum exploration and production (E&P) activities on population densities and extinction probabilities of vertebrates, (2) to develop an ecological framework for evaluating impacts of brine and/or oil spills at E&P sites, utilizing population models based on patchiness of landscapes and/or trophic transfer; and (3) to develop early exit criteria from the ecological risk assessment process (if possible), based on size and distribution of spills in the context of potentially patchy habitat. The primary tasks of the past year have been (1) to develop a spatially-explicit, individual-based model for American badger *(Taxidea taxus*) at the Tallgrass Prairie Preserve (TPP) near Pawhuska, Oklahoma, (2) to modify the code for an artificial spill generator for use in testing hypotheses about population responses to decreases in available habitat area and fragmentation; and (3) to develop a preliminary ecological framework. Essentially, this project is intended to inject ecology into ecological risk assessment, a field that has been dominated by conservative assumptions about exposure and toxic responses. The project will contribute to Petroleum Environmental Research Forum (PERF) project 99-01, “Ecological Evaluations for Upstream Site Remediation Programs.” Improved methods for ecological risk assessment should lower costs of remediation by decreasing the need for conservative assumptions in estimates of ecological exposure.

BACKGROUND

The exposure of ecological receptors to chemical contaminants has a spatial context. Wildlife exposure models include dietary uptake but rarely the habitat preferences that also determine exposure. The premise of this project is that organisms experience the environment spatially, as a patchwork. Patches may be beneficial, as in the case of suitable habitat for the animal, or patches may be detrimental, as in the case of some hydrocarbon or brine spills. In addition, background processes, such as controlled burns and grazing by bison, can contribute to patchiness of habitat. Areas denuded of vegetation are non-

habitat for most vertebrates. The integrated effect of the patchwork landscape on a particular species will depend on the spatial arrangement of those patches of varying quality.

DISCUSSION OF CURRENT ACTIVITIES

Case study site. The subject of the case study for this project is the Tallgrass Prairie Preserve (TPP) in Pawhuska, OK. The TPP is approximately 37,000 acres of mostly intact prairie grassland with approximately 600 historic wells (about 120 in current production) and isolated spills of hydrocarbons and brine. The Nature Conservancy, which owns the site, has attempted to restore ecosystem function through controlled burns and grazing by introduced bison. Tallgrass prairie vegetation forms comprise about seven percent of oil and gas well locations in the U.S., and prairie generally comprises 32 percent (Fig. 1). Thus, our case study site is representative of about one out of three upstream oil and gas locations.

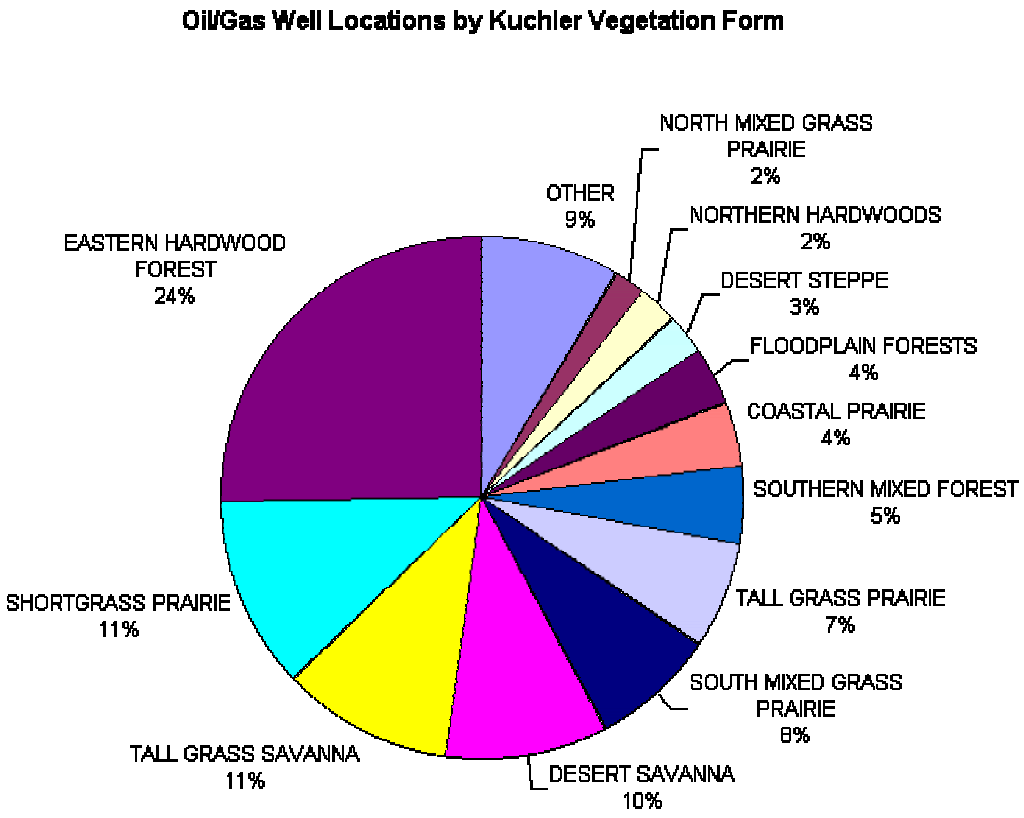

Fig. 1. Predominant vegetation forms in ¼ mile by ¼ mile cells in which productive and unproductive oil and gas wells in the U.S. are located. Data on well locations in USGS (1995) were obtained from David Ferderer at USGS.

Geographic Information System (GIS). A web-based interface for the GIS, that includes map layers provided by ORNL, was released by Lawrence Livermore National Laboratory (LLNL). The web site, entitled "Managing Ecological Impacts at Exploration and Production Sites" is accessible at http://gis.llnl.gov/mei/ to project team members, DOE sponsors, and PERF 99-01 partners. The GIS includes the following types of data, described more fully in the 2001 *Fossil Energy Program Annual Progress Report*: (1) soil survey, (2) vegetation type, (3) digital ortho quarter quadrangle photos, (4) Landsat Multispectral Scanner data (North American Landscape Characterization data from USGS/EPA/NASA), (5) Normalized Difference Vegetation Index for six years, (6) prescribed burn history (annual 1991-1999), (7) management usage and years of bison grazing, (8) bison pastures with dates opened, and (8) land ownership. Most of these layers are available on the web site. Airborne Visible/Infrared Imaging Spectrometer (AVIRIS) hyperspectral data have been obtained from the USGS, and these have been radiometrically corrected by USGS and georectified.

Spill Generator. The TPP case study relied on artificial maps of disturbance features. Artificial spills are necessary to identify potential spill area or fragmentation thresholds that result in population-level effects. Maps with different spill patterns also aid in understanding causes of declines. Two spill generators were developed, one theoretical, and one more realistic and dependent on pipeline distribution. The theoretical model generates point patterns of spills and assumes that oil well placement is random across a two-dimensional space. A random walk algorithm simulates diffusion to neighboring cells until the specified spill area is disturbed. The well-complex model simulates spills in locations of well complexes that are assumed to be rectangular grids (based on many of the well arrangements at the TPP) of gather lines and tank batteries. The user specifies the number and dimensions of well complexes. The model assumes that the likelihood of encountering a spill along any segment of pipe of a specified length is constant, so that the likelihood of a spill within a cell increases with the length of pipe located within its boundaries. A manuscript summarizing these tools has been submitted for petroleum industry review prior to submission to a peer-reviewed journal (Jager et al. 2003a).

Ecological Modeling. The presence of oil or brine spills may affect population density and persistence of animal populations through several mechanisms. Patches of spills may impact animal movement, food availability, shelter availability and availability of refuge from predators. Habitat loss may lead to local extinction at low population densities ("Allee effect") because of the inability to find mates or breeding territories.

The structure of the object-oriented model template for ORNL and LLNL models is described in Fig. 2. The cell, as well as its immediate surroundings, is conceived as the source of food resources and shelter for individual animals. The model will simulate population changes over time in response to disturbances by brine spills.

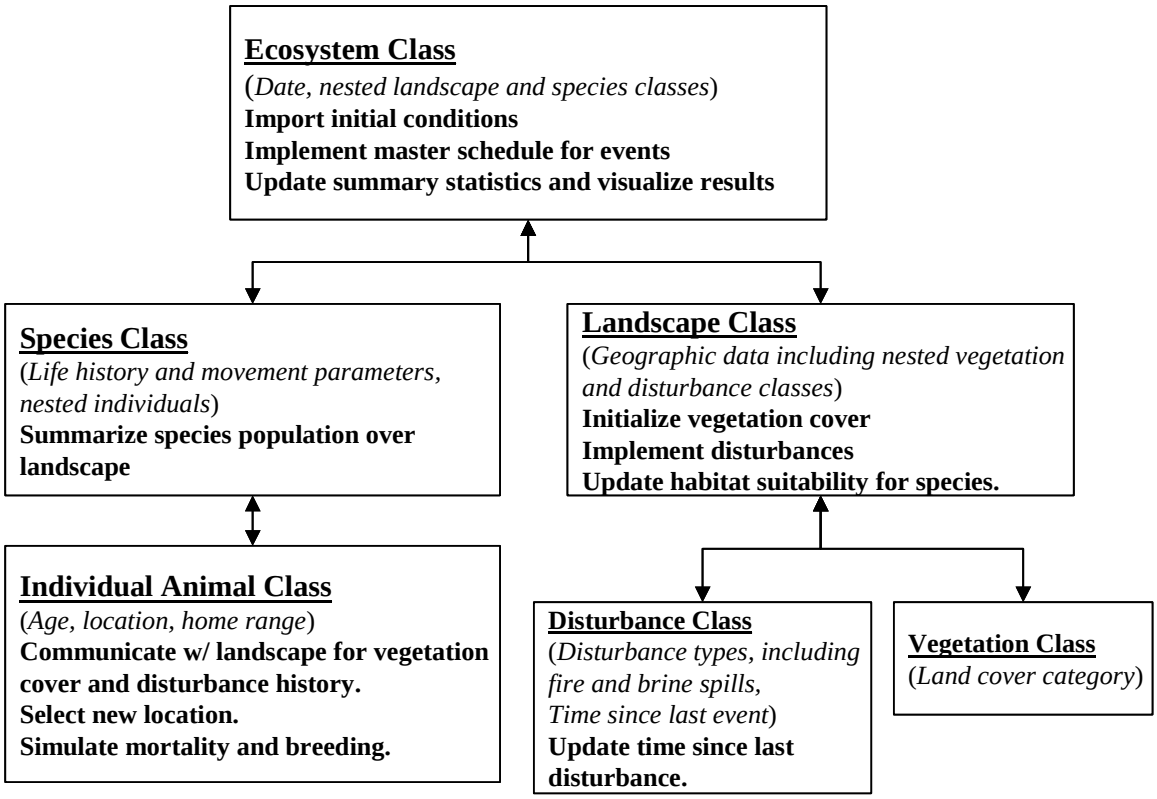

Fig. 2. Diagram of the proposed model template. Objects in the model are defined by classes that include data members (*italics*) and member functions (**bold**). Each class is represented by a box in the diagram.

Trophic interactions (e.g., vegetation growth and reduction due to grazing, herbivory, and bioenergetics) are a focus of the model in development by LLNL. The prairie vole (*Microtus ochrogaster*), a monogamous herbivore, feeds on grassland vegetation and is preyed upon by predators such as owls and badgers.

Habitat individual-based models are well suited for studying the differential susceptibility of species with different life histories and habitat requirements to habitat loss from brine spills. We implemented a habitat-based model for the American badger (*Taxidea taxus*), a voracious, solitary predator with low tolerance for other individuals. We assigned habitat suitability indices to various vegetation categories at the TPP based on known compatibilities with the presence of small, fossorial mammals or burrowing requirements (Jager et al. 2003b). Brine spills, structures, and streams are designated as unsuitable habitat. Habitat quality of cells influences reproduction simulations through acquisition of territory used for breeding and survival via movement costs and habitat-related mortality. This model does not explicitly represent foraging or predation.

Individuals pass through five periods of pre-breeding, mating, post-mating, birthing, and rearing of young (Jager et al. 2003b). They establish a permanent home range, equivalent to the breeding territory.

Following dispersal and territory establishment, within-range movement is simulated. Movement, which is described in Jager et al. (2003b), depends on seasonal and gender-based parameters. Mating is assumed to occur for any mature female with a home range overlapping the home range of at least one mature male. Reproduction timing and survival of young are also described in Jager et al. (2003b). Sources of mortality include: baseline, age-related mortality; habitat-related mortality; mortality based on movement; and emigration from the study area. Sensitivity analyses are in progress. We conducted a simulation experiment to investigate the effects of loss of habitat area and fragmentation (represented here by increasing numbers of spills). We used the Poisson-gamma statistical model described above and in Jager et al. (2003b) to generate spill landscapes with a specified target percentage of area covered by spills (1%, 10%, 20%, 30% or 50%), and a specified number of spills (100 or 1000). Six of these maps are depicted in Fig. 3. Effects of spills on final average population sizes and the proportion of potential breeding females that successfully mated were compared. In addition, Allee effects were noted.

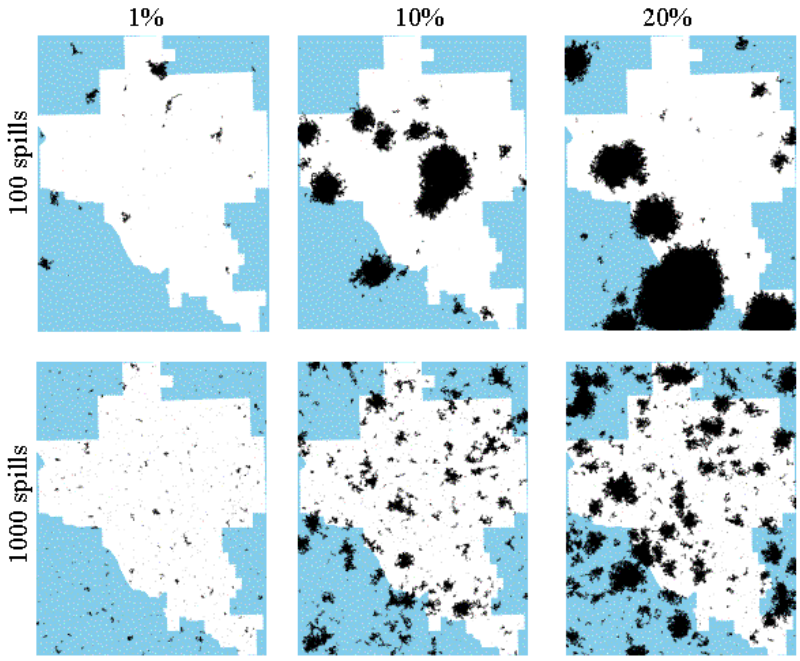

Fig. 3. Example landscapes generated by the Poisson-gamma model, with different numbers of spills and spill areas.

Results showed a decrease in the average, simulated badger population size with increasing area of habitat loss, and a similar decline in the proportion of replicate populations that persisted (Fig. 4). Population persistence declined to 80% (100 spills) or 40% (1000 spills) when 10% of land area was covered by spills. Thus, extreme landscape fragmentation led to increased effects on population densities. Similarly, the fraction of populations persisting decreased with the area of disturbance, but the threshold

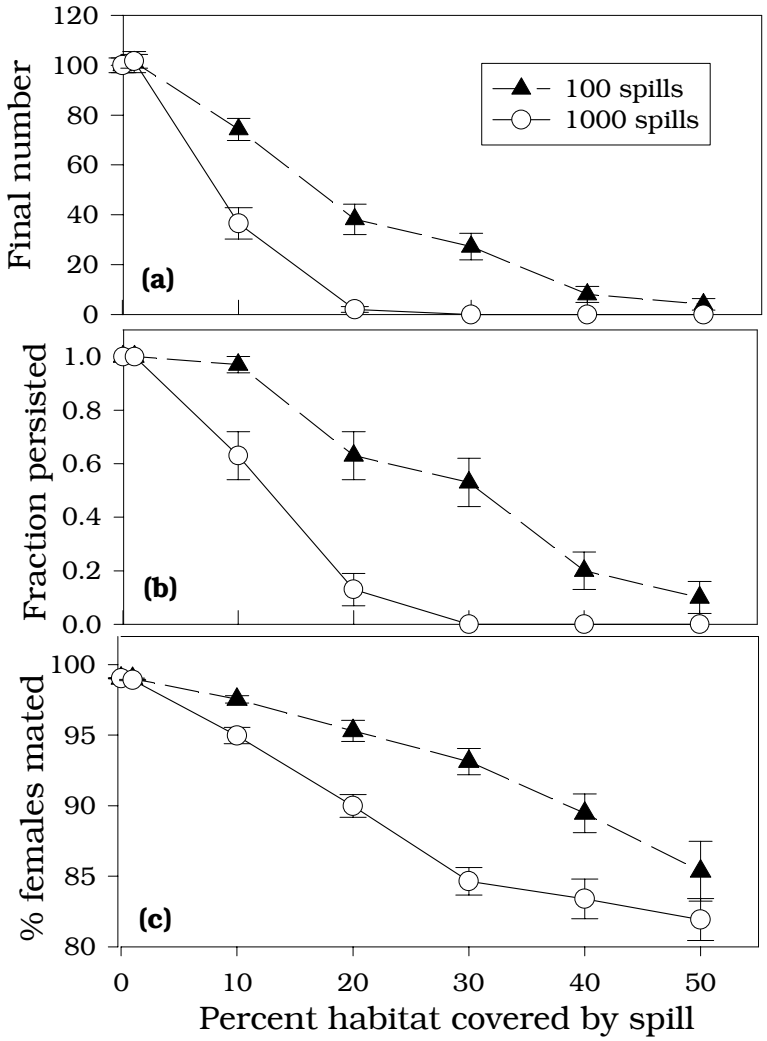

Fig. 4. Response of simulated (a) final population size and (b) fraction of replicate populations that persist, and (c) fraction of females eligible to breed that find mates to habitat loss. Error bars show 1 standard error surrounding the mean of 30 replicate simulations for landscapes with 100 and 1,000 spills.

for this effect was apparently higher than 10% disturbance. These declines were accompanied by declines in the proportion of females mating. The area thresholds are higher than the 0.1% of the TPP covered with brine scars and the less than 1% of the TPP that is directly disturbed by wells, roads or spills.

Model results will contribute to generalizations about the effect of the size and distribution of brine and oil spills on the demographics of wildlife populations. Exclusion criteria and/or mitigation measures for E&P sites may be recommended, based on results of population modeling.

Ecological framework. A preliminary ecological framework for evaluating terrestrial vertebrate populations at E&P sites is presented in Fig. 5. Assessment endpoint populations are chosen using a site

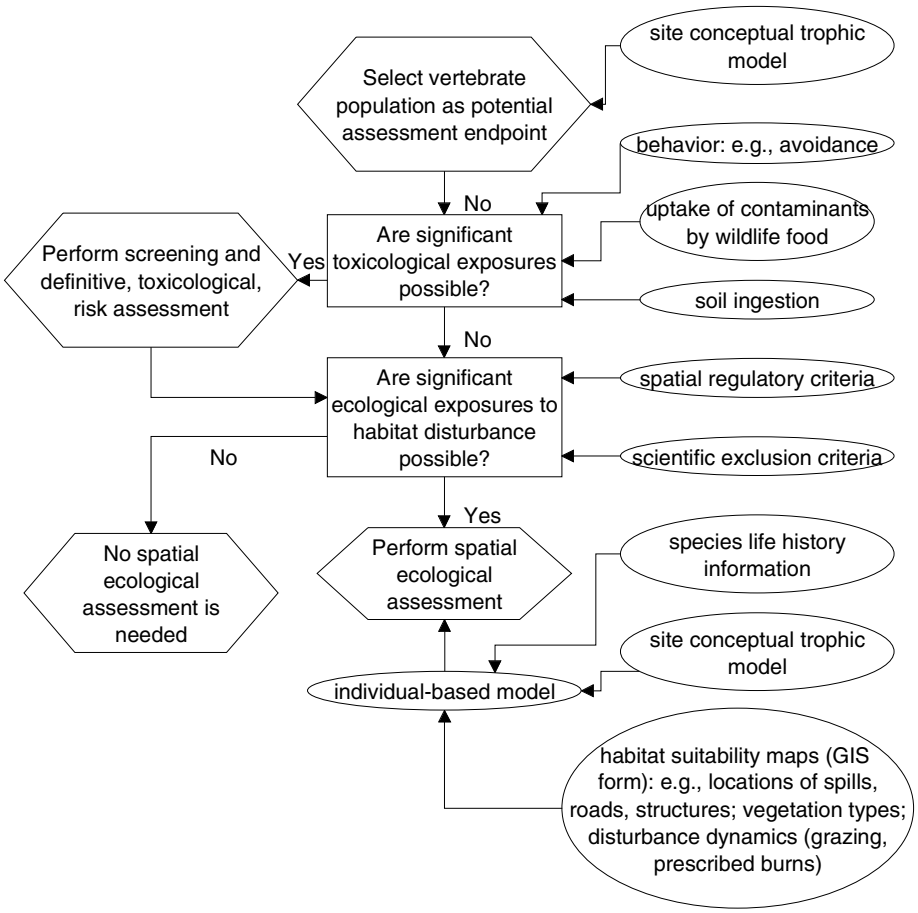

Fig. 5. A preliminary ecological framework for evaluating terrestrial vertebrate populations at E&P sites.

conceptual trophic model and other management criteria. The potential for exposure to contaminants is determined by contaminant bioavailability and animal behavior. The threshold for conducting a toxicological risk assessment may be lower for threatened and endangered populations than for other populations. The spatial regulatory criteria (contaminated area thresholds) and scientific exclusion criteria that determine whether an exposure to habitat disturbance may be significant and may require a spatial ecological assessment are described below. Species life history information, trophic relationships, and habitat suitability may be explicitly or implicitly modeled in an IBM.

Presentation and manuscripts. This project was presented at an American Society for Testing and Materials conference on "Landscape Ecology and Wildlife Habitat Evaluation: Critical Information for Ecological Risk Assessment, Land-Use Management Activities, and Biodiversity Enhancement Practices" in Kansas City, MO, in April 2003. This conference represented a forum for discussion of the integration of landscape ecology and ecological risk assessment. A book chapter was written to summarize this project and to serve as a final report for the project, and this manuscript is in peer review (Efroymson

et al. 2003). Two manuscripts (Jager et al. 2003a, 2003b) are in review by petroleum industry representatives prior to journal submission.

REFERENCES

Efroymson, R. A., T. M. Carlsen, H. I. Jager, T. Kostova, E. A. Carr, W. W. Hargrove, J. Kercher, and T. L. Ashwood. 2003 Submitted. Toward a Framework for assessing risk to vertebrate populations from brine and petroleum spills at exploration and production sites, In *Landscape Ecology and Wildlife Habitat Evaluation: Critical Information for Ecological Risk Assessment, Land-Use Management Activities, and Biodiversity Enhancement Practices, ASTM STP 1458*, L. Kapustka, H. Galbraith, M. Luxon, and G. R. Biddinger (eds.), ASTM International, West Conshohocken, PA, 2004.

Jager, H. I., Carr, E. A., and R. A. Efroymson. 2003b manuscript. A simulation study to evaluate the effects of habitat loss and fragmentation on the American badger (*Taxidea taxus*). *Conservation Biology*.

Jager, H. I., Efroymson, R. A., Sublette, K., Carr, E. A., and T. L. Ashwood. 2003a manuscript. Unnatural landscapes in ecology: Generating the spatial distribution of oil spills.

MODELING OF WATER SOLUBLE ORGANIC CONTENT IN PRODUCED WATER

J. McFarlane

INTRODUCTION

Produced water remediation to National Pollution Discharge Elimination System (NPDES) target levels can represent a significant cost for oil production in the Gulf of Mexico. Off-shore analysis and remediation of produced water is expensive, and the relatively high polar content of Gulf of Mexico crude oil also means a higher solubility of organic components in the aqueous phase. In addition, neither are the identities of the water-soluble components well known, nor are their concentrations in the produced water brines. These concentrations will be affected by physical variables such as pH and temperature, but also by the depth of the formation and the age of the well. The objective of this project was to address part of the gap in the knowledge base, building upon earlier work of the characterization of simulated produced water contacted with actual crude oil samples undertaken at ORNL, through the modeling of the produced water/crude oil system using chemical thermodynamics. Because of the focus on semi-volatile components, the chemical system was modeled as a liquid-liquid equilibrium with activity coefficients based on a UNIFAC functional group analysis. A random sampling method was introduced to allow uncertainties in the input data to be reflected in the results of the computation. The model has successfully reproduced parametric studies carried out at Oak Ridge National Laboratory, allowing explanation of changes in solubility observed with variations in pH and temperature.

DISCUSSION OF ACTIVITIES

BACKGROUND

Soluble organics in produced water and refinery effluents are treatment problems for the petroleum industry. Production facilities and refineries have to meet regulatory discharge requirements for dissolved organics. This is expected to become more difficult as environmental regulations become stricter and production from deep-water operations increases. Deep-water crude oil has a large polar constituent, which increases the amount of dissolved hydrocarbons in produced water and refinery effluents. Published work focused on North Sea crude oil suggests that the high polar content is mainly comprised of short-chain organic acids (Røe Utivk 1999). The oxidized organic material is formed from the redox-controlled decomposition of source rock or of organic precursors in the petroleum (Borgund and Barth 1994). Although the chemistry of formation water has been carefully studied (e.g., Barth and Riis 1991, Helgeson et al. 1993, Barth et al. 1996), further questions remain concerning the identity, chemistry, and toxicity of water-soluble organics in produced water after borehole separation, particularly for crude oil from the Gulf of Mexico. For instance, the concentration of carboxylic acids appears to be related to the

air exposure and age of the oil, as the acids can arise from biological breakdown of hydrocarbons in the separator (Barth 1987). There appears to be no direct correlation; however, between oxygen content and organic acid concentration (Borglund and Barth 1994) or pressure, temperature, or depth (Barth and Riis 1991). Hence, several petroleum companies, including Shell, ChevronTexaco, Phillips, and Statoil, developed a collaborative Petroleum and Environmental Research Forum (PERF) project to characterize and evaluate water solubles from Gulf of Mexico crude oil, to better understand the production of these contaminants.

Quantitative characterization data are needed as the first step in understanding the dissolution of water-soluble organic (WSO) compounds in produced water. Hence, between 1999 and 2002, Oak Ridge National Laboratory (ORNL) completed a study of the characterization of crude oils and water-soluble compounds in produced water under a variety of experimental conditions (Bostick et al. 2002, McFarlane et al. 2002). Industrial partners provided ORNL with two separate samples of crude oil from Gulf of Mexico deep-water wells. The oil samples had been stripped of their volatile components and little produced water was directly associated with the samples. Because of this, the study focused on the solubility behavior of semi-volatile organic compounds in simulated brine solutions, which were prepared to contain the principal inorganic components normally found in Gulf of Mexico seawater. Contact experiments between the crude oil and the brine were carried out under equilibrium conditions, to study the effects of brine pH, salinity, temperature, pressure and crude oil source on the transfer of organic compounds from the hydrocarbon to the aqueous phase. Of the six variables tested, the factor that most controlled the total WSO in produced water was that of aqueous phase pH. Trends in temperature were also observed. The overall concentrations of water-soluble organics derived from two different samples of crude oil were not substantially different; however, the water-soluble organics were almost exclusively polar from one of the crude oil samples, and were split between aromatic and polar from the other crude oil sample. The effects of water cut, pressure, and salinity on organic solubility were found to be very slight or not significant within the uncertainties of the experimental measurements. Hence, the modeling effort focused on deriving an explanation for the effect of pH and temperature on organic solubility rather than on the effect of these other physical variables.

CURRENT STATUS

The objective of the project is to develop a model of crude-oil derived organic solubility in produced water, ultimately to be used as a predictive tool. Aqueous-hydrocarbon systems can be modeled in a variety of ways. The option of using an empirical approach was considered, but ultimately it was decided that a model based on equilibrium thermodynamics was the most appropriate to the task. The advantage of a thermodynamic equilibrium model is that physical variables, such as temperature and salinity, can be

incorporated into the expressions for the activity coefficients (Huron and Vidal 1979). Volatile components and the dependence of solubility on pressure can be introduced with an additional gaseous phase, described by an equation of state. This approach has been successfully implemented to describe hydrocarbon-aqueous systems representative of those found in crude oil production, with solubility predicted by non-random two liquid (NRTL) activity coefficients in the aqueous and hydrocarbon phases (Pedersen et al. 1996).

The main difficulty of formulating the thermodynamic model is in the selection of which components will represent the system, comprising over 1000 different components. It was hoped that the compositional characterization of the crude oil would allow derivation of lumped parameter properties for different classes and sizes of soluble compounds; however, this approach was precluded by the large uncertainties in the data. In the current study, an activity coefficient model was used for both the hydrocarbon and aqueous phases, based on the UNIFAC group contribution formulation (e.g., Fredenslund and Sørensen 1993). In particular, UNIFAC parameters for liquid-liquid equilibrium were used in the model (Magnussen et al. 1981). Such an approach is often used to model aqueous and non-aqueous solubilities of environmentally important chemicals, for instance alkanes, alkyl benzenes, polyaromatic hydrocarbons and phenols (e.g., Kan and Tomson 1996). Limitations of the model have been documented in regards to systems involving solids (Gracin et al. 2002) and some interaction parameters are not available for selected functional groups, particularly for liquid-liquid equilibrium (Hansen et al. 1991). Hence, it is important to compare calculations to experimental measurements to validate the model.

Because the concentrations of the components were not individually determined, representative molecules were selected for the computational analysis, in particular hydrocarbons of various sizes, cyclohexane (a representative napthene or cyclic saturated hydrocarbon), aromatic compounds, organic acids, a ketone (acetophenone), and because these crudes contain 1–2% sulfur, a thiophene. These compounds were selected based on published descriptions of the composition of crude oil (Speight 1991, British Petroleum 2003). Large non-soluble compounds such as asphaltenes and resins were not included in the model, as they were assumed to have little impact on the solubility of other organic compounds. The quantities of each compound were also estimated, based on the results of the analyses of crude oil done at ORNL. The experimental uncertainties were used to derive distributions in feedstock concentrations, which were randomly sampled to provide input into the thermodynamic calculation. The thermodynamic model was run 100 times for each set of physical conditions, to give an output distribution in water-soluble organic concentration in produced water. The water-hydrocarbon ratios determined by the calculation were compared to the experimental results using a Welch 2 sample t-test, an analysis that gave the probability that the means of the two populations were the same. This statistical

test was required to assess the validity of the calculation. If agreement was good, then the compounds included in the calculation could include, or be similar in functionality to, the compounds that were actually present in the produced water.

The stochastic thermodynamic calculations were programmed in Maple 7 and were run on a personal computer. Besides the crude oil composition, inputs to the calculation included pressure, temperature, and brine. Salinity was incorporated as ionic strength in a Debye-Hückel correlation. Results of the calculation are presented in the table below, showing representative compounds and mean output water-hydrocarbon ratios and standard deviations. It was found that, with the exception of the phenols, the concentration of the compound in the crude oil had little effect on the distribution ratio between the oil and the brine. The distribution coefficients for selected hydrocarbons and aromatic compounds agreed very well with those measured in the experiment, with the probability for a particular component derived from the t-test shown in the table. A comparison was not done for the longer chain aliphatic compounds because the amounts measured in the produced water were so low. The calculated distribution coefficients for the polar components were very diverse, ranging from being fairly insoluble (dibenzothiophene) to miscible (formic acid), and so did not lend themselves to an overall comparison as done with the aliphatic and aromatic hydrocarbons. A cyclic aliphatic acid; however, was found to best match the measured distribution coefficient for the polar water-soluble fraction.

Results of Liquid-Liquid Equilibrium Calculations

Compound	Calculated water/hydrocarbon distribution coefficient pH7, 300 K, 1 bar, 65000 mg·L^{-1} Cl^-	Produced water analysis, Welch 2-sample t test probability	pKa values at 298K (Smith and March 2001, IUPAC 1979)
*n*hexane	5×10^{-5}		51
cyclohexane	8×10^{-5}		46
*n*octane	5×10^{-6}	Aliphatic C_6–C_{10} 4×10^{-6}, P = 0.59	51
*n*decane	4×10^{-7}		51
*n*eicosane	3×10^{-12}		51
$C_{28}H_{58}$	2×10^{-16}		51
benzene	3×10^{-4}		43
toluene	8×10^{-5}		43
napthalene	8×10^{-6}		43
methylnapthalene	2×10^{-6}	Aromatic 7×10^{-6}, P = 0.72	40
phenanthrene	2×10^{-7}		43
methanol	2		15.2
phenol	0.2		9.994
omethylphenol	0.03		10.02
formic acid	1×10^{4}		3.751

acetic acid	90		4.756
propanoic acid	20		4.874
nbutanoic acid	7		4.81
benzoic acid	5		4.205
naphthalene acetic acid	0.04		4.23
napthenic acid $(C_{13}H_{21})COOH$	2×10^{-4}	Polar 1×10^{-4}, P = 0.59	5
acetophenone	2×10^{-4}		19.2
dibenzothiophene	2×0^{-5}		43

The model was successfully used to fit the pH-dependence data that were generated in a crude-oil/simulated brine system, presented in Fig. 1. This model incorporated the acidity of the polar components (Khan et al. 1995). As can be seen in Fig. 1, the methylene-chloride extractable material (particularly in the C_{10}–C_{20} range) became more soluble as the brine became basic, pH > 7, as shown by the apparent inflection point in the data at ~pH7. This corresponded to the behavior calculated for naphthalene acetic acid. The pH behavior for the second crude oil sample, with monotonically increasing solubility as a function of pH, was more typical of the combination of naphthalene acetic acid and a cyclic carboxylic acid (or napthenic acid). Highly water-soluble acids, such as acetic acid, give a distribution coefficient between the organic and aqueous phases of one very close to their pKa values. Even though the degree of dissociation increases dramatically for less soluble acids at pH = pKa, the solubility doesn't trace the titration curve, because much of the acid remains in the organic phase even at higher pH values. Bases, such as quinoline, are present in their dissociated form at low pH, and hence exhibit the opposite trend in solubility behavior to that of an acid (Standal et al. 1999). It is probable that such weak bases were present in the crude oil samples, and would have transferred to the produced water simulant. They were not observed in the GC-MS analysis; however, a not unexpected result as nitrogen-containing species are expected to be present in much lower concentration that sulfur and oxygen containing species in the crude oil (Speight 1991), the latter dominating overall solubility behavior.

Testing of the model over a range of temperatures indicated that the solubility of many hydrocarbons did not change much over the temperature range of 300 to 350 K. For instance, no change in solubility was predicted for the short chain fatty acids, such as acetic acid, being already highly soluble in the aqueous phase at pH7. A slight increase in solubility was predicted for the bulky carboxylic acids, acetophenone and dibenzothiophene, Fig. 2, in agreement with characterization of the simulated produced water. Temperature effects have been measured (Cai et al. 2001) and predicted (Kojima and Ogawa 2001) for organic acids in aqueous systems, but these can be mainly attributed to dimerization equilibria which occur at higher concentrations than observed in produced water. At temperatures above

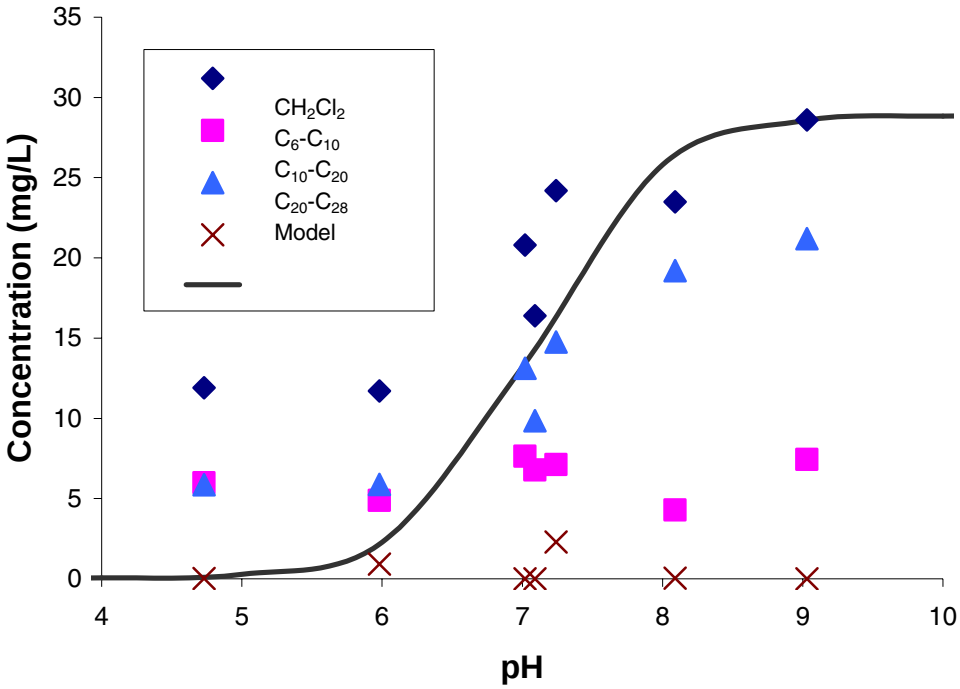

Fig. 1. Plot of water-soluble organic concentration for different carbon sizes as a function of pH. Superimposed on the plot are results of liquid-liquid equilibrium calculations for naphthalene acetic acid, salinity = 65,000 mg·L^{-1}.

320K, breakdown of organic acids via decarboxylation is a competing mechanism (Borglund and Barth 1994).

Equilibrium calculations on the hydrocarbon-brine system were run with salinity ranging from 40 to 115 g·L^{-1}, with results showing little apparent effect on solubility, in agreement with the experimental data. There was no evidence for the "salting" effect observed by Bennet and Larter (1997) for the substituted cresols that exhibited a greater partitioning into the hydrocarbon phase as the ionic strength of the aqueous phase increased. The phenomenon has been described as arising from the neutralization of charge about the molecule, increasing its absorption into the hydrocarbon layer. It is possible that many of the polar molecules in the produced water studied here behaved more like phenol than cresol, which demonstrated only a slight dependence on salinity in Bennet and Larter's studies. Khan and co-workers (1995) found that an increase in salinity caused an increase in the activity coefficient of the undissociated 2-oxopropanoic (pyruvic) acid in aqueous solution, yielding a decrease in solubility. However, the effect was not demonstrated with the shorter chain organic acids, which dissociate in aqueous solution.

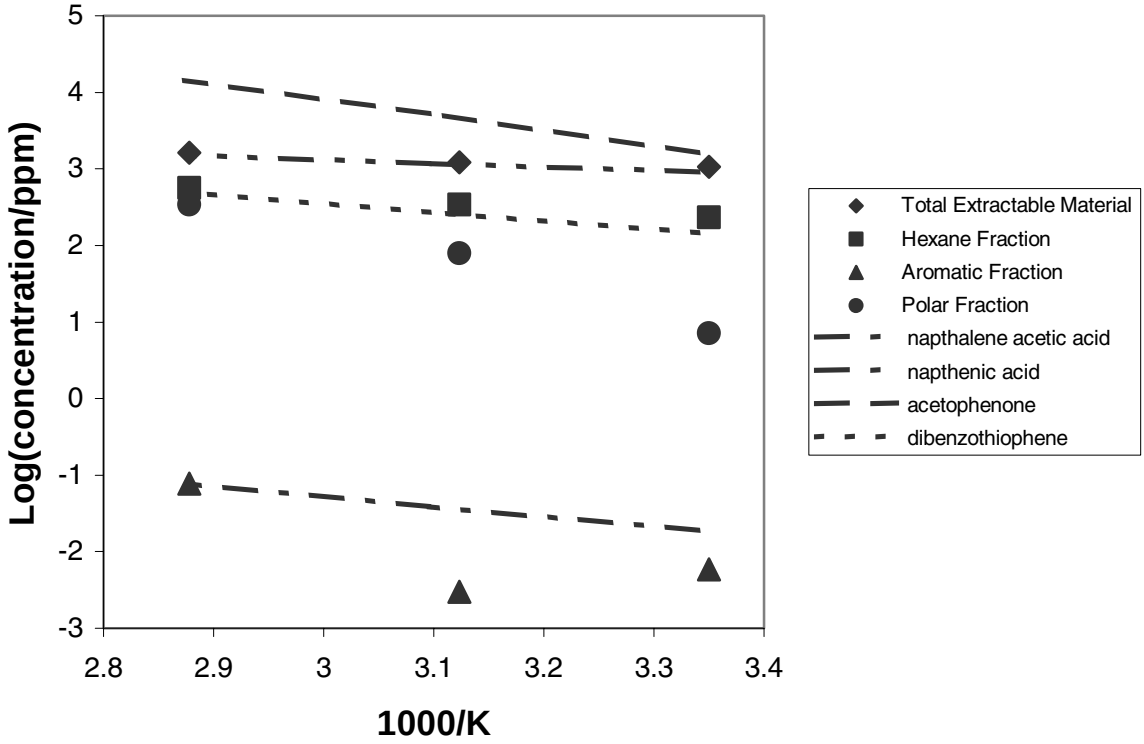

Fig. 2. Plot of water-soluble organic concentration as a function of inverse temperature for water contacted with crude #1. Superimposed on the plot are calculated concentrations of selected polar hydrocarbon compounds under reference conditions, and initial concentrations of 0.05 g·L^{-1} for each of the acids, 5.5 g·L^{-1} for acetophenone, and 29 g·L^{-1} for benzothiophene to make up the requisite polar fraction in the oil.

FUTURE PROGRESS

Future study will investigate cross-correlations between the variables that control solubility, such as water-soluble polar content, sulfur in the crude, and depth or location of formation, temperature and pH or carbonate concentration (Barth and Riis 1991) in the produced water. In addition, actual produced water may contain a colloidal precipitate after bulk separation from the crude oil. Under such conditions, the partitioning of molecules between the organic and aqueous phases will be affected by the droplet size and carbon chain length (Lang et al. 1992). Modeling such an effect will require consideration of mass transfer and the thermodynamic properties of the disperse phase (Gracin et al. 2002), and will be considered along with other variables related to the physical state of the oil during production and separation from the produced water.

Being able to fit laboratory data is the first step in demonstrating our ability to understand solubility of contaminants in produced water. It is expected that this knowledge will lead to the development of a predictive model for use in the design of new oil production facilities. The prediction of the effect of

changing production conditions on water soluble organic content will assist the petroleum industry to target produced water cleanup to best protect the environment.

REFERENCES

Barth, T. 1987. Quantitative determination of volatile carboxylic acids in formation waters by isotachophoresis, Analytical Chemistry 59, 2232–2237.

Barth, T., and Riis, M. 1991. Interactions between organic acid anions in formation waters and resevoir mineral phases, Advances in Organic Geochemistry 19, 455–482.

Barth, T., Andresen, B., Iden, K., and Johansen, H. 1996. Modelling source rock production potentials for short-chain organic acids and CO_2—a multivariate approach. Organic Geochemistry 25, 427–438.

Bennet, B., and Larter, S. R. 1997. Partition behavior of alkylphenols in crude oil/brine systems under subsurface conditions. Geochimica et Cosmochimica Acta 61, 4393–4402.

Borgund, A. E., and Barth, T. 1994. Generation of short-chain organic acids from crude oil by hydrous pyrolosis, Organic Geochemistry 21, 943–952.

Bostick, D. T., Luo, H., and Hindmarsh, B. 2002. Characterization of soluble organics in produced water, Oak Ridge National Laboratory Technical Memorandum, ORNL/TM-2001/78.

British Petroleum. 2003. BP assays field in Gulf of Mexico, Oil and Gas Journal, 54–55.

Cai, Weibin, Zhu, Shenlin, and Piao, Xianglan. 2001. Extraction equilibria of formic and acetic acids from aqueous solution by phosphate-containing extractants, J. Chem. Eng. 46, 1472–1475.

Fredenslund, A., and Sørensen, J. M. 1993. Group contribution estimation methods, in Models for Thermodynamic and Phase Equilibria Calculations, S. I. Sandler editor, Marcel Dekker, 287–361.

Gracin, S., Brinck, T., and Rasmuson, A. C. 2002. Prediction of solubility of solid organic compounds in solvents by UNIFAC, Ind. Eng. Chem. Res. 41, 5114–5124.

Hansen, H. K., Rasmussen, P., and Fredenslund, A. 1991. Vapor-liquid equilibria by UNIFAC group contribution. 5. Revision and extension, Ind. Eng. Chem. Res. 30, 2352–2355.

Helgeson, H. C., Knox, A. M., Owens, C. E., and Shock, E. L. 1993. Petroleum, oil field waters, and authigenic mineral assemblages: Are they in metastable equilibrium in hydrocarbon reservoirs? Geochimica et Cosmochimica Acta 57, 3295–3339.

Huron, M.-J., and Vidal, J. 1979. New Mixing Rules in Simple Equations of State for Representing Vapor-Liquid Equilibria of Strongly Non-Ideal Mixtures, Fluid Phase Equilibria 3, 255–271.

IUPAC. 1979. Ionization constants of organic acids in aqueous solution. Serjeant, E. P. and Dempsey, B. Editors, Pergammon Press, Oxford.

Kan, A. T., and Tomson, M. B. 1996. UNIFAC prediction of aqueous and nonaqueous solubilities of chemical with environmental interest, Environmental Science and Technology 30, 1369–1376.

Khan, I., Brimblecombe, P., and Clegg. S. L. 1995. Solubilities of Pyruvic Acid and the Lower (C1-C6) Carboxylic Acids. Experimental determination of equilibrium vapor pressures above pure aqueous and salt solutions, J. Atmospheric Chemistry 22, 285–302.

Kojima, I., and Ogawa, M. 2001. Thermodynamics of the distribution of some carboxylic acids, between organic solvents and a perchlorate solution, Analytical Sciences 17, 417–420.

Lang, J., Lalem, N., and Zana, R. 1992. Quaternary water-in-oil microemulsions. 2. Effect of carboxylic acid chain length on droplet size and exchange of material between droplets, J. Physical Chemistry 96, 4667–4671.

Magnussen, T., Rasmussen, R., and Fredenslund, A. 1981. UNIFAC parameter table for prediction of liquid-liquid equilibria, IEC Proc. Des. Dev. 20, 331–339.

McFarlane, J., Bostick, D. T., and Luo, H. 2002. Characterization and modeling of produced water. In Proceedings of the Groundwater Protection Council Produced Water Conference, Colorado Springs, Oct 15–17, 2002. http://www.gwpc.org/Meetings/PW2002/Papers-Abstracts.htm.

Pedersen, K. S., Michelsen, M. L., and Fredheim., A. O. 1996. Phase Equilibrium Calculations for Unprocessed Well Streams Containing Hydrate Inhibitors, Fluid Phase Equilibria 126, 13–28.

Røe Utvik, T. I. 1999. Chemical characterization of produced water from four offshore oil production platforms in the North Sea, Chemosphere 39, 2593–2606.

Smith, M. B., and March, J. 2001. March's advanced organic chemistry. 5th Ed. Wiley-Interscience, NY.

Speight, J. G. 1991. The chemistry and technology of petroleum. M. Dekker, NY.

Standal, S. H., Blokhus, A. M., Haavik, J., Skauge, A., and Barth, T. 1999. Partition coefficients and interfacial activity for polar components in oil/water model systems, J. Colloid and Interface Science 212, 33–41.

PETROLEUM RISK INFORMATION DECISION EVALUATION SYSTEM

C. W. McGinn and M. E. Langston
Oak Ridge National Laboratory

L. D. Galloway and D. J. Thomas
University of Tennessee

INTRODUCTION

The petroleum industry has a need for an expert system to provide information and models necessary to conduct assessments of risk to workers, public, and the environment. Risk assessment is a critical component to the decision processes, ensuring that significant problems are addressed in a cost effective manner. Consequently, such assessments are conducted by the petroleum industry at upstream and downstream sites on an international scale. Currently, there is no centralized resource for industry guidance, information, or tools in support of risk assessment and management activities. Individual companies and contractors responsible for risk assessments must “reinvent the wheel” with every evaluation. This results in duplication of effort and the inconsistent use of data. More importantly, because the best science is not readily available, assessment results may be inaccurate and lead to unsuitable and costly actions. A centralized risk system specific to the petroleum industry is needed to ensure consistency in approach, data quality and cost effectiveness while providing information essential to the protection of human health and the environment. To meet this need the National Petroleum Technology Office (NPTO) and the Petroleum Environmental Research Form (PERF) have teamed with ORNL to create the Petroleum Risk Information Decision Evaluation System (PRIDES)

PRIDES is a public, service-oriented, web-based instructional system in support of the application of human health and ecological risk assessment by the petroleum industry. PRIDES reduces assessment costs by providing the latest peer reviewed risk tools and information to an international audience in an effort to encourage the use of risk assessment in the decision process. PRIDES is a platform-independent web-based system with an easy-to-use interface as well as many visual tools that aid in understanding the risk assessment process.

This system provides tools essential for performing basic risk assessment activities. In addition, this system provides the latest risk guidance and directs the user to specific guidance necessary for performing risk assessment activities. PRIDES and its associated guidance will streamline the risk assessment process and eliminate the need for costly duplication of effort.

DISCUSSION OF CURRENT ACTIVITIES

The strategy for site development has near and long term considerations. In the near term (FY 2003) site framework and infrastructure will be the focus. The objective is to make upstream approaches, tools, and data currently in use readily available. In the following years the site will be developed to include more leading edge methods and tools to improve the assessment process based on needs assessment provided by NTPO and PERF. The near term scope is comprised of planning, development and maintenance activities.

System Planning and Documentation. Several planning activities have been conducted to define objectives, ensure quality, and support deployment. The majority of these efforts have been undertaken simultaneously with system development.

The *Petroleum Risk Information and Decision Evaluation System Configuration Control Plan* was submitted and an overview was presented to the members of PERF 99-13 subcommittee in September, 2002. The primary objective of the Configuration Control Plan is to ensure system integrity with data entry formats, audit trails, and user training as well as to enable documented, quality-controlled enhancements. In addition this plan details how routine updates, sponsor/user requests, and regulatory changes will be consistently controlled, documented, tracked, and distributed to users. Based on comments and suggestions the plan has been revised and “finalized”; however, the plan will be updated, as necessary, to meet the changing needs of the project.

The concepts of system objectives and design, the basis for the PRIDES Development Plan, were presented at the September PERF 99-13 meeting. Based on feedback at this meeting the first draft has been completed and posted on the PERF 99-13 web site for review. To ensure that expectations and goals are met the Development Plan provides an outline of system objectives. This plan is based on the needs identified by the petroleum industry representatives to PERF and NPTO. The Development Plan is expected to be dynamic enabling the system to respond to the needs of the petroleum industry. To ensure that the system adapts to industry requirements, objectives will be reviewed and specific tasks identified annually.

System Development and Maintenance. The following tasks comprise the nucleus of the proposed system. Web Site Construction includes the creation of web pages and links incorporating modules addressing industry-specific risk assessment guidance and information. These modules will provide data that is searchable and downloadable for assessment on the user’s PC. The first Draft of PRIDES home page and links to introductory pages for What's New, FAQ, What is Risk Assessment, Tutorial, Contacts, Regulatory Guidance, Risk Tools, and Affiliated Organizations has been created in the development area. The operational site should be up and running for review in the development area by May. Depending on

comments from NPTO and PERF, the site will go into production and available to the public by June. Table 1 lists specific information to be incorporated in PRIDES by the end of the FY.

As part of the management of this system an on-line user support service will be available to ensure that the system is accessible and user friendly for all users regardless of risk assessment expertise. This e-mail based service will provide information on use of the system and suggested solutions to specific risk problems. In addition to addressing specific user issues, this service provides a conduit for user feedback, which will aid in the identification of risk issues affecting the petroleum industry on a broad scale. Management of the system will also include the tracking of access by user group and area of interest.

Table 1. Information tasks to be completed in FY 2003

Activity	Description
Introductory materials	• What is risk assessment, how it should be used in the decision process • Objective of website and how information should be employed, online tutorial • Illustration of RA process linked to online tools and data • Links to API website
Guideline Documents	• TPHCWG TPH Fraction method • Analytical recommendations, test kits • COC lists for E&P sites • Technical background (e.g., *Risk-Based Decision-Making for Assessment Petroleum Impacts at E & P Sites*) • Links to API reports
Tools	• Link to API spreadsheet • Specific tools identified through PERF (e.g., ecological exclusion criteria, international exposure factors database)
User Support	Response to user questions, tracking of FAQs
System Deployment	E-mail announcement, link to petroleum industry sites (API, etc), link to risk sites

REMOTE SENSING FOR ENVIRONMENTAL BASELINING AND MONITORING

David Reister, Robert Washington-Allen, and Art Stewart

INTRODUCTION

Hyperspectral remote sensing is an emerging technology with the potential to identify plant species, map vegetation, characterize soil properties, identify contamination, classify ecological units and habitat characteristics, and differentiate causes of vegetation stress. The main benefit of this project, both to the DOE Fossil Energy Program and to our petroleum industry partners, will be an improved ability to provide detailed environmental data for a region, rapidly, at low cost. Increasingly, environmental data are needed to assess present conditions of lands owned, leased or managed by petroleum companies, and to characterize and quantify changes in the environmental conditions of these lands through time. Present methods of assessing large areas depend extensively on field surveys, which can take weeks or months to complete. Such methods are inconvenient and can be expensive. Further, some areas that are inaccessible or very large are difficult or virtually impossible to monitor accurately using field-survey techniques only.

Investigators from ChevronTexaco, the University of California at Davis (UCD), the Carnegie Institution of Washington at Stanford University (CIW), the U.S. Geological Survey (USGS), the U.S. Department of Agriculture's Agricultural Research Service (ARS), and the Oak Ridge National Laboratory (ORNL) are collaborating to develop remote (airborne or satellite) hyperspectral sensor techniques specifically to characterize conditions at exploration and production (E&P) sites, where vegetation and soil may be impacted by oil or gas production. Project objectives include: (1) identifying hyperspectral signatures of plant responses to hydrocarbons, toxic metals and other stressors; (2) developing advanced analytical methods for evaluating hyperspectral data, so as to more clearly reveal environmental impacts from spectrally "noisy backgrounds;" and (3) demonstrating techniques for revealing environmental impacts by analysis of hyperspectral data. These techniques are not currently available. This report will discuss three topics: (1) Analysis of remote hyperspectral data at the Jornada Experimental Range near Las Cruces, NM (Jornada), (2) Analysis of field hyperspectral data from Jornada, and (3) Plans to collect airborne high spatial resolution hyperspectral imagery in Osage County , OK, analyze the data set to identify distinct groups of similar spectra, and perform field validation.

REMOTE HYPERSPECTRAL ANALYSIS

An ideal (but costly) experiment for this project would be to apply petroleum hydrocarbons on a plot, and obtain hyperspectral images of the plants on the plot before and after the spill, to characterize changes in vegetative condition through time. In June 2000, a near-ideal "natural" experiment occurred when a road grader accidentally cut an oil pipeline, allowing oil to spray over a two-hectare site at Jornada (see

Fig.1). Jornada has been operated as a research park by the Agricultural Research Service (ARS) since 1912 (see http://usda-ars.nmsu.edu/). Thus, the oil-spill accident at this park was a particularly fortuitous event for our project. In 1981, the National Science Foundation selected Jornada as a Long-Term Ecological Research (LTER) site. The Jornada Experiment (JORNEX) was begun in 1995 to collect remotely sensed data from ground, airborne, and satellite platforms. In May 1997, an 11-day field sampling campaign occurred at Jornada. This sampling campaign was designed to collect ground and airborne hyperspectral data to validate satellite images. During the campaign, the Airborne Visible/Infrared Imaging Spectrometer (AVIRIS) sensor was used to collect data at Jornada. Subsequently, this sensor has been used to collect data at Jornada at least twice a year. AVIRIS is an imaging hyperspectral sensor with 224 bands; it is carried aboard a NASA ER-2 airplane (a modified U2 plane) at an elevation of ~20 km. An AVIRIS flight over the Jornada site occurred on June 10, 2000, just ten days after the oil-spill. Unfortunately, the AVIRIS image missed the oil spill site. Subsequent AVIRIS flights occurred in September 2000 and June 2001. The Jornada site also was imaged with the AVIRIS sensor before the spill (September 1999), and hyperspectral data on vegetation and soils at the site have been obtained during site-characterization projects by ARS investigators. Thus, Jornada has a rich set of before-and-after hyperspectral data, both from ground and airborne platforms.

Fig. 1. Oil spill at Jornada.

The Jornada oil spill site has a plant canopy dominated by creosote bush (Larrea tridentata (Sesse & Moc. Ex DC.) Coville) shrub land that is one of the five major plant community types in the Jornada basin. Qualitative field inspection in early February 2001 indicated that upper plant canopy contact with the diesel fuel was manifest as: (1) etiolation (lack of photosynthetic activity) and probable chlorosis (loss of chlorophyll) that resulted in a grey to white color of the upper canopy and a white to slight reddening of the lower canopy graminoids and litter, (2) partial and complete defoliation of shrubs, (3) apparent high mortality of much of the above ground phytomass, including grasses, cactoids, and biological crusts, and (4) darkening of the orange-red alluvial soil (see Fig. 1). It was also evident that the spill boundary could be delineated on the basis of smell, as diesel was still volatizing from the soil. These features were still evident one year after the release. It must be noted that the canopy dominant, creosote bush, is expected to recover from the diesel spill because it resprouts after injury. This aspect of plant physiology is significant for studies of resilience in desert ecosystems.

The AVIRIS sensor was used to collect data at Jornada at least twice annually, including prior to and after the diesel spill. Consequently, three scenes from September 1999 and 2000, and June 2001 are available for the diesel spill site. Time series analysis of hyperspectral data is rare, only one other study prior to this has been conducted and that was by Dr. Susan Ustin and one her students at UCD. Consequently, this is an opportunity for us to study the response and recovery of a desert plant community to a diesel spill using indicators derived from hyperspectral imagery. Past studies have shown that plant stress is usually detected between 400 to 735 nm and hydrocarbons near 1700 and 2200 nm. The three AVIRIS scenes were acquired from Dr. Greg Asner at CIW. Analysis has been completed for the two September scenes and indicated separation between the before and during spectral responses, with the “during” response showing plant response in the 400 to 735 nm and evidence of absorption in the 1700 nm region. The June 2001 “after” scene is currently being processed by both ORNL and UCD for comparison to the 1999 and 2000 scenes. A manuscript of these results is in preparation and will be submitted to the Journal: Ecological Applications.

FIELD HYPERSPECTRAL ANALYSIS

In April 2002, we received data for the 665 field measurements that were made at the Jornada Experimental Range by ARS investigators in September 2000. Using the field data, our goal was to explore the resolution limits for pixel unmixing and plant species identification. We have completed an analysis of 211 measurements that were made at the grass site. Each measurement consists of 2151 numbers that are the reflectance values at wavelengths ranging from 350 nm to 2500 nm. Each measurement is described with one or two of the following 12 labels: “Bare,” “Litter,” “Aristada,” “Capa,” “Datu,” “Forb,” “Grass,” “Mesquite,” “Senna,” “Snakeweed,” “Tila,” and “Yucca.” Here, “Bare”

represents bare soil, “Litter” represents plant litter, and the other 10 labels designate plant species. This data set can be used to test whether or not each of the 12 labels has a distinct hyperspectral signature. We have completed a paper: Endmembers, Pixel Unmixing, and Clustering. and submitted it to the IEEE Transactions on Geoscience and Remote Sensing. The three authors are: David B. Reister (ORNL), Jerry C. Ritchie (ARS), and Albert Rango (ARS). This section will provide a short summary of the paper.

Endmembers have been used to analyze multispectral and hyperspectral images since the paper by Adams, et al. [1] that analyzed an image of Mars using four image endmembers, that included a shade endmember. The three nonshade image endmembers were identified by comparison with a library of laboratory reflectance spectra. The measured spectrum (ρ_i) of a pixel in the image is the weighted average of the spectra of the endmembers (a_{ij}) and the weights (p_j) are the fraction of the total area of the image that is occupied by each subcomponent:

$$\rho_i = \sum_j a_{ij} p_j \quad , \tag{1}$$

where the weights are nonnegative numbers that sum to one.

Gillespie, et al. [2] analyzed hyperspectral AVIRIS (Airborne Visible/Infrared Imaging Spectrometer) data using image endmembers. The number of endmembers is one more than the numerical rank (K) of the measurements, which can be determined by using Principal Component Analysis (PCA) to find the number of dimensions required to explain the data variance. However, PCA does not identify the endmembers, which are extreme pixels in data clusters. Boardman and Goetz [3] estimated an illumination factor at each pixel and constrained the weights to be nonnegative and to sum to one or less. Boardman [4] uses the framework of the geometry of convex sets to identify the K+1 end members as the vertices of the smallest simplex that bounds the measured data. Roberts, et al. [5] have developed multiple endmember spectral mixture analysis, in which they evaluated 889 two-endmember models and used the evaluation results to generate 276 three-endmember models. The best 24 two-endmember and 12 three-endmember models were chosen to generate vegetation maps.

Boardman and Roberts are using endmembers in quite different ways. Boardman generates a single set of endmembers and calculates the weights for each pixel to determine the fractional abundance patterns in the region. Roberts has a large library of laboratory and field measurements and evaluates many two-endmember models. Since a two-member model has one free parameter, he finds which model provides the best fit for each pixel. However, the results are not unique and one or more of the models may provide a good fit for a pixel.

Our objective is the same as Boardman and Roberts: to group hyperspectral measurements into as many distinct classes as possible. Richards and Jia [6] draw the distinction between information classes

and spectral classes, where information classes are human classifications and spectral classes are groups or clusters of measurements made by a computer.

We will consider (1) to be a general linear mixing model and allow the spectra and weighs to be any real number. The spectra are columns of the matrix $\boldsymbol{A}$. All linear combinations of the spectra form a subspace (the range space of $\boldsymbol{A}$) that has a numerical rank (K) and can have many sets of basis vectors. The null space of $\boldsymbol{A}^{\mathrm{T}}$ is all vectors that are orthogonal to $\boldsymbol{A}^{\mathrm{T}}$.

We distinguish between two problems: forward and inverse. For the forward problem, we are given the spectra of the subcomponents and the weights, and we calculate the measured spectra. For the inverse problem, we are given the spectra of the subcomponents and the measured spectra, and we calculate the weights. While the forward problem always has a unique solution, the inverse problem usually does not have a unique solution. Given a solution to the inverse problem, another solution can be found by adding any vector from the null space of $\boldsymbol{A}^{\mathrm{T}}$.

Since pixel unmixing is an inverse problem, there should be many solutions to the pixel unmixing problem. The basic problem is that the measured spectra are not linearly independent, but are highly correlated. Singular value decomposition (SVD) [7] can be used to create an uncorrelated orthonormal basis for the spectra, that will provide a solution to the inverse problem. The solution for the inverse problem could also be expressed as a linear combination of any K linearly independent members of the original spectral library. However, this form of pixel unmixing is neither unique nor informative.

The second section of the paper describes a method for partitioning hyperspectral measurements into distinct classes. When we began our research, we expected that the distinct classes would be a basis for the measurements. As the research has progressed, we realized that the basis vectors are not classes. Instead, the classes are groups (clusters) of distinct measurements. There can be many more classes than there are basis vectors. A familiar example is the population distribution on the Earth's surface. We know that there are many distinct towns and cities on the 2D surface of the Earth.

The third section discusses the methods used to collect a hyperspectral field data set at the Jornada Experimental Range near Las Cruces, NM. In the fourth section, we use our clustering method to partition the field measurements into distinct groups and compare the clusters (spectral classes) with the labels (information classes) that were given to each of the field measurements at the time of data collection.

Our objective is to group hyperspectral measurements into as many distinct classes as possible. A new clustering algorithm for unsupervised classification has been developed. The algorithm has been applied to a hyperspectral field data set (with information classes). Using SVD, we calculated an orthonormal basis for the 211 measurements. When we define the numerical rank (K) as the number of basis vectors required to explain 99% of the variance in the data, we find that K = 4 for this data set.

In our clustering algorithm, we vary the cluster radius to find the maximum number of clusters. For this data set, the maximum number of clusters is 20. Each cluster consists of the neighbors of a root measurement vector that has a label. In all 20 cases, the label of the root measurement in the cluster is consistent with the cluster membership. All of the 12 labels are at the root of at least one of the clusters.

Using the first five vectors in the SVD basis for the measurements, we have plotted the location of the 20 root vectors on 2D "slices" through a 5D space. While axis 1 is not useful for distinguishing distinct groups in the central clusters (the 12 root vectors that have more than a 0.95 correlation with axis 1), it is quite useful for separating the central clusters from the outlier clusters (the 8 root vectors that have lower correlations with axis 1). The slices reveal that each of the 12 root vectors for the central clusters has a distinct location in the 5D space.

ENVI has two clustering algorithms for unsupervised classification: Isodata and K-means. For our data set, the clusters found by both Isodata and K-means were significantly different than our clusters. We found that the most of the cluster radii were much larger than our radius and the largest radius was more than a factor of 10 larger. When a cluster has a large radius, many members of other clusters can be inside the ball defined by the radius. Further analysis found that both Isodata and K-means placed more than half of the measurements in the wrong cluster. Since our algorithm does not require iterations, it requires less computation for large data sets than Isodata and K-means. Thus, our new algorithm appears to advance the state-of-the-art.

REMOTE DATA for OSAGE COUNTY

Osage County, OK is the Osage Indian Reservation and has been a major oil producing area (38,500 oil wells) since 1896. The county is large (2,260 square miles) and 1,480 square miles are within a quarter mile of an oil well. The mineral rights are owned by the Osage Nation and there are 500 independent operators in the county. Many areas in the county have brine scars or weathered oil pits (The USGS has sample photographs: http://ok.water.usgs.gov/skiatook/Skiatook.Photo.html). Figure 2 is a wintertime photo of an Osage County salt scar area. The maximum depth of erosion is about 2 meters. The original soil profile is preserved in the pedestal in the upper right. Saline water in the middle drops below the surface toward the foreground.

Hyperspectral remote data will be collected in selected regions in Osage County and analyzed to detect brine scars, oil pits, and plant stress associated with brine and oil. The imagery will be collected by the HyVista Corporation (http://www.hyvista.com/). The hyperspectral imagery has 126 spectral bands and 3.2 m spatial resolution. Our new data analysis techniques will identify clusters (distinct groups of similar spectra). Limited fieldwork will be required to identify the geological and botanical characteristics of the members of each cluster.

Fig. 2. Osage County salt scar.

REFERENCES

1. J. B. Adams, M. O. Smith, and P. E. Johnson, “Spectral mixture modeling: A new analysis of rock and soil types at the Viking Lander 1 site,” *J. Geophys. Res.*, vol. 91, no. B8, pp. 8098–8112, 1986.
2. A. R. Gillespie, M. O. Smith, J. B. Adams, S. C. Willis, A. F. Fischer III, and D. E. Sabol, “Interpretation of residual images: Spectral mixture analysis of AVIRIS images, Owens Valley, California,” *AVIRIS Workshop Proc.*, JPL Publication 90-54, Jet Propulsion Laboratory, Pasadena, CA, pp. 243–270, 1990.
3. J. W. Boardman and A. F. H. Goetz, “Sedimentary facies analysis using AVIRIS data: A geophysical inverse problem,” *AVIRIS Workshop Proc.*, JPL Publication 91-28, Jet Propulsion Laboratory, Pasadena, CA, pp. 4–13, 1991.
4. J. W. Boardman, “Automated spectral unmixing of AVIRIS data using convex geometry concepts,” *AVIRIS Workshop Proc.*, JPL Publication 93-26, Jet Propulsion Laboratory, Pasadena, CA, pp.11–14 (1993).

5. D. A. Roberts, M. Gardner, R. Church, S. Ustin, G. Scheer, and R. O. Green, “Mapping chaparral in the Santa Monica mountains Using multiple endmember spectral mixture models,” *Remote Sens. Environ.*, vol. 65, no. 3, pp. 267–279, 1998.
6. J. A. Richards and X. Jia, “Remote Sensing Digital Image Analysis,” Third Edition, Springer-Verlag, Berlin (1999).
7. G. H. Golub and C. F. Van Loan, “Matrix Computations,”3rd ed., Baltimore, MD, The Johns Hopkins University Press, 1996.

FUNDAMENTAL CHEMISTRY OF HEAVY OIL

W. V. Steele

INTRODUCTION

Catalytic hydroprocessing continues to be the core method for upgrading of feedstocks with high aromatic content. European environmental organizations have already established standards in this area and the U.S. is expected to follow in the near future. The reduction of aromatics in heavy petroleum upgrading will require careful management of hydrogen during hydroprocessing. Effective hydrogen management requires an understanding of the relationship between the distribution of the hydrogenated products in the process streams and the conditions of their formation, i.e., temperature and pressure.

To counteract the adverse effects of carbon rejection methods, refiners have the option of hydrogen-addition (hydroprocessing) methods. However, hydroprocessing consumes large quantities of hydrogen. As refineries reconfigure to produce the new "clean fuels" ("reformulated fuels," i.e., those with oxygenates present), hydrogen shortages are occurring, and new sources of supply are required. The addition of oxygenates to gasoline means that less octane is required from the reformer, lowering the severity of the operation and the amount of hydrogen formed. Also, the mandated reduction of aromatics content by the U.S. government in the 1990 Clean Air Act Amendments has resulted in a further reduction of reformer operating severity, hence, severely reducing hydrogen production. Other contributions to the problem in managing hydrogen result from mandated lower gasoline temperature endpoints and reduced sulfur levels. Hence, the use of hydrogen exactly where it will "do the most good" is paramount. Over-hydrogenation will have to be minimized.

The purpose of the cooperative work between the Design Institute of Physical Property Data (DIPPR)® and the Thermophysical Property Group within the Separations and Materials Research Group at ORNL is to develop thermodynamic and thermophysical property data for use in leading edge chemical technology. The property measurements are directed by the DIPPR Project Steering Committees responsible for Project 821-Pure Component Liquid-Phase Vapor Pressure Measurements and Project 871-Pure Component Ideal-Gas Enthalpies of Formation. The objective of Project 821 is to obtain precise and accurate liquid-phase vapor pressure data for selected pure components. The objective of Project 871 is to measure the enthalpies of combustion and derive the enthalpies of formation in both the condensed and the idea-gas phases of "key" compounds that have been chosen to elucidate the enthalpy of particular atomic groupings. These group contributions can then be used to estimate data on large families of related compounds each containing that particular atomic arrangement.

DIPPR, now in its 24th year of funded research, is the oldest of the American Institute of Chemical Engineers' (AIChE) active Industry Technology Alliances. In 2003, DIPPR has 30 sponsors from industry and government bodies. Its purpose is to make possible, through joint sponsorship,

thermophysical property data measurement, correlation, and dissemination. The objective of the Design Institute for Physical Property Data (DIPPR)® is to develop the world's best set of critically evaluated thermophysical and environmental property data to satisfy industry needs. Data developed in DIPPR projects have become the data of choice for leading chemical process simulators and are used throughout the world.

DISCUSSION OF CURRENT ACTIVITIES

BACKGROUND

Worldwide demand for petroleum products continues to expand as the nations develop. However, if the demand is analyzed in terms of the three major classes of petroleum cuts: light products such as gasolines; petrochemical feedstocks, middle distillates such as jet fuels and diesels; and heavy products such as fuel-oils and lubricants; then there has been a drastic shift in emphasis toward the light end. Whereas in 1972, both the light products and the middle distillates accounted for approximately 30% of the market. By the turn of the century the light products are 38%, the middle distillates 40%, leaving only 22% for the 1973 major component the heavy-ends.

Whether it is an East Coast refinery importing crude oil from Nigeria, or a U.S. Gulf Coast refinery importing crude oil from Saudi Arabia, or even a U.S. West Coast refinery operating on Alaskan North Slope crude, over the last decade or more for which records are available (1986–96), the quality of the crude oil processed by refineries has declined. If the decline in the quality of crude processed in U.S. refineries is denoted in terms of the API gravity, the gravity has decreased by an average of 0.15° per year in the decade 1986–95.[1] Furthermore, the decline appears to have accelerated back to the rate applicable in the early 1990's. Measured as a five-year average (1989–93), the API gravity had declined by 0.22° per year. After leveling at 31.3° for the next four years, in 1996 it was back on the line pointing to a value of 30.5° for the API gravity in the year 2000. As the API gravity of crude oil falls, the aromatic content (carbon content) increases and the correlations derived for the light crudes begins to break down. The failure of the correlations is well documented in the literature. New or revised correlations are necessary for continued high thermal efficiency in the refining of present and future crudes.

Within the petroleum industry, catalytic hydroprocessing continues to be the core method for upgrading of feedstocks with high aromatic content, as well as for heteroatom removal through HDS and HDN. Meetings such as the 3-day symposium, "Recent Advances in Heteroatom Removal," presented at the Division of Petroleum Chemistry meeting as part of the ACS biannual meeting held in Dallas, March 1998, demonstrate the extensive interest by the petroleum and catalysis industries in this area. In a review of fuel-quality specification for transportation fuels, Touvelle et al. of Exxon Research and Engineering discussed trends in the regulation of aromatics in fuels. Although benzene content is carefully scrutinized, the total aromatics content is not regulated specifically in the U.S. In contrast, European environmental

organizations have already established standards in this area and the U.S. is expected to follow in the near future.

The reduction of aromatics in petroleum and particularly in heavy petroleum will require careful management of hydrogen during hydroprocessing. Effective hydrogen management requires an understanding of the relationship between the distribution of the hydrogenated products in the process streams and the conditions of their formation, i.e., temperature and pressure. To meet this need, a dual-track approach involving both state-of-the-art property measurement and advanced Ab Initio computations is proposed.

The property measurement program previously funded by DOE Fossil Energy in Oklahoma has accumulated extensive results for partially hydrogenated two, three and four-ring aromatics. The majority of these results have not been published; particularly those which allow calculation of hydroaromatic distributions under processing conditions. Ab Initio computational coding is in its infancy in this area. Accurate atomistic modeling of hydroaromatic systems will use the codes and techniques we have developed for parallel molecular simulations on the ORNL Paragons and other parallel supercomputers. Using our simulation capabilities, we believe we can substantially surpass the best prior efforts in realism and quantitative, predictive accuracy. These simulations will build on existing ORNL world-class efforts on simulating high temperature liquid and supercritical aqueous systems.

The experimental database and the fundamental understanding from the simulations will be brought together to develop useful models for correlating data and predicting stability under hydroprocessing conditions. The two fundamental questions to be addressed in this research are: (1) What are the “ideal condition” for meeting low aromatics levels and still meet sulfur levels, smoke point, etc., (2) How does the model react to changes in the complex heterogeneous and multi-component systems (i.e., addition of a new crude oil from, say, Nigeria to the refinery)?

Results from this research will allow the industrial participants to lead the field in catalyst development and process condition controls in processing particularly middle distillates. It can be anticipated that severe operating conditions such as high temperatures, low space velocities, and high pressures can be mediated as the result of insights developed with the program. For example, at low temperatures and high space velocities, the amount of monoaromatics in the product can be higher than in the original feed. This is not unexpected since every mole of triaromatic compound that is saturated would add a mole to the diaromatics, each diaromatic compound hydrogenated would add a mole to the monoaromatic category, and as the number of rings decrease, the rate of saturation should also decrease. Interaction between the various options can be simulated in the model and options such as increased catalytic activity balanced again two- or even three-stage process designs.

The project has been set up in the CRADA form with an initial lifetime of three years. Subcommittees comprised of DIPPR Project supporters, DOE Fossil Energy Staff, and ORNL staff will decide at the

annual AIChE/DIPPR meeting in November a list of compounds for study in the following year in each of the two project areas. Compounds will be chosen to represent whole families containing the necessary functionalities and to facilitate extension of available data bases, rather than to fulfill the specific needs of any single member company.

PROGRESS

Work is in progress on a number of fronts within this project. An initial literature search is being performed to ascertain the relative importance of various aromatic compounds and sulfur-containing compounds in the range of heavy petroleum being imported to refineries in the U.S. Emphasis will be placed on finding the degrees of condensation and substitution of the compound types. The results of the study will be used to define the scope of the experimental work and the reaction schemes to be studied. Available literature data are being collected and process conditions defined where applicable. Properties for the majority of the species have not been published in the open literature, particularly those that allow calculation of hydroaromatic distributions under processing conditions. Hydroaromatic distributions will be derived where possible and a list of gaps in the database highlighted. This work will conclude with the reporting of sets of compounds to be studied to widen the applicability of the derived correlations.

Work is also in progress to ascertain the practicality of using the range of heavy petroleum being imported to refineries in the U.S. to produce both 5 ppm sulfur gasoline and a “clean diesel” with the following specifications: 50 ppm sulfur with lower density, lower PAH (polyaromatic hydrocarbons), lower boiling point, and higher cetane number than the “best diesel being produced for the California market. Preliminary results of calculations of the conditions necessary to obtain various sulfur levels in diesel using hydrodesulfurization are given in Table 1. In the table the baseline is assumed to be the conditions (temperature/pressure/catalyst activity) required to produce 500 ppm sulfur diesel.

Table 1. Conditions necessary to produce certain sulfur ppm levels in diesel

Sulfur content	Catalyst activity	Temperature F	Hydrogen pressure
Baseline 500 ppm	100%	Baseline	Baseline
350 ppm	130%	+15F	120%
200 ppm	190%	+30F	170%
100 ppm	300%	+55F	300%
50 ppm	450%	+70F	600%

To obtain the required sulfur level, only one of the listed options would be required. Obviously, the hydrogen pressure increase option is not realistic. Note also that the increase in temperature would mean that the amount of aromatics would increase, requiring even greater hydrogen pressure to premeditate the effect.

Another option other than hydrodesulfurization to meet the sulfur level is alkylation of the sulfur-containing molecules raising the boiling point of sulfur-containing fraction and removing the sulfur in the resid. Or, in yet a further option, the sulfur-containing compounds can be removed by selective adsorption using a catalyst containing a zero-valent transition metal. Presently, both methods of sulfur removal are being presented by refiners as new technology options. Results from this research project will aid in both research areas (property measurements will give examples of boiling point of substituted benzothiophenes with both degree of substitution and actual position of substitution). Initial calculations point to several metals being particularly capable of reversible adsorption of benzothiophenes and dibenzothiophenes under very moderate reaction conditions. Further computational chemical calculation during FY 2001 will expand on these initial ideas.

Finally, work is also in progress on what the PI of this project calls “The 2015 Refinery” where all processes within the bounds of the refinery are as environmentally sound as possible. The 2015 refinery would for example not have any alkylation units with the associated problems of HF^{-} or H_2SO_4. Fuels would be manufactured via olefin formation and upgrading. Possibilities then increase of producing “zero sulfur” gasoline and even cleaner-burning naphthenic fuels.

In the reporting period, DIPPR)® project committees met during the AIChE meeting in November 2002. Lists of possible compounds for measurements were tentatively drawn up at those meetings and finalized after subsequent literature surveys were conducted to ensure the quantity and quality of any available data. Samples of each of the chemicals chosen for study were obtained and purification via spinning-band distillation or (in case of solid samples) zone-refining are in progress. The property measurements are due to commence in early May 2003.

Results from earlier work completed at Bartlesville, Oklahoma, have cleared full committee review and were published in the *Journal of Chemical & Engineering Data* in May 2002. The titles of the 6 papers are:

Steele, W. V., R. D. Chirico, S. E. Knipmeyer, and A. Nguyen. Vapor pressure, heat capacity, and density along the saturation line: Measurements for benzenamine, butylbenzene, sec-butylbenzene, tert-butylbenzene, 2,2-dimethylbutanoic acid, tridecafluoroheptanoic acid, 2-butyl-2-ethyl-1,3-propanediol, 2,2,4-trimethyl-1,3-pentanediol, and 1-chloro-2-propanol. J. Chem. Eng. Data v. 47, 2002, 648–666.

Steele, W. V, R. D. Chirico, A. B. Cowell, S. E. Knipmeyer, and A. Nguyen. Thermodynamic properties and ideal-gas enthalpies of formation for methyl benzoate, ethyl benzoate, (R)-(+)-limonene, tert-amyl methyl ether, trans-crotonaldehyde, and diethylene glycol. J. Chem. Eng. Data v. 47, 2002, 667–688.

Steele, W. V., R. D. Chirico, S. E. Knipmeyer, and A. Nguyen Vapor pressure, heat capacity, and density along the saturation line measurements for ε-caprolactam, pyrazine, 1,2-propanediol, triethylene glycol, phenyl acetylene and diphenyl acetylene. J. Chem. Eng. Data v. 47, 2002, 689–699.

Steele, W. V., R. D. Chirico, A. B. Cowell, R. D. Chirico, S. E. Knipmeyer, and A. Nguyen Thermodynamic properties and ideal-gas enthalpies of formation for trans-methyl cinnamate, α−methyl cinnamaldehyde, methyl methacrylate, 1-nonyne, trimethylacetic acid, trimethylacetic anhydride, and ethyl trimethylacetate. J. Chem. Eng. Data v. 47, 2002, 700–714.

Steele, W. V., R. D. Chirico, S. E. Knipmeyer, and A. Nguyen Vapor pressure, heat capacity, and density along the saturation line measurements for cyclopropane carboxylic acid, N,N'-diethyl-ethanolamine, 2,3-dihydrofuran, 5-hexen-2-one, perfluorobutanoic acid, and 2-phenylpropionaldehyde. J. Chem. Eng. Data v. 47, 2002, 715–724.

Steele, W. V., R. D. Chirico, A. B. Cowell, S. E. Knipmeyer, and A. Nguyen Thermodynamic properties and ideal-gas enthalpies of formation for 1,4-diisopropylbenzene, 1,2,4,5-tetraisopropylbenzene, cyclohexanone oxime, dimethyl malonate, glutaric acid, and pimelic acid. J. Chem. Eng. Data v. 47, 2002, 725–739.

In addition a bibliography of the publications of the Bartlesville Thermodynamics Group from its inception in 1943 through the present was given in the *Journal of Chemical & Engineering Data* May 2002 issue. In all, the papers and bibliography took up **over 100 pages** of the issue.

In addition, during this reporting period, two papers on the thermodynamic properties of naphthalene and benzophenone respectively, were published in the *Journal of Chemical Thermodynamics* and a further paper on the properties of dihydrobenzo[b]thiophene was accepted for publication:

Chirico, R. D., S. E. Knipmeyer, and W. V. Steele. Heat capacities, enthalpy increments, and derived thermodynamic functions for naphthalene between the temperatures of 5 K and 440 K. J. Chem. Thermodynamics v. 34, 2002, 1873–1874.

Chirico, R. D., S. E. Knipmeyer, and W. V. Steele. Heat capacities, enthalpy increments, and derived thermodynamic functions for benzophenone between the temperatures of 5 K and 440 K. J. Chem. Thermodynamics v. 34, 2002, 1885–1895.

Steele, W. V., R. D. Chirico, A. B. Cowell, A. Nguyen, S. E. Knipmeyer, J. W. Reynolds, and A. P. Rau. Possible precursors and products of deep hydrodesulfurization of gasoline and distillate fuels. II. The thermodynamic properties of 2,3-dihydrobenzo[b]thiophene. Accepted for publication in Journal of Chemical Thermodynamics, November 2002.

REFERENCE

1. S. W. Benson, *Thermochemical Kinetics*, 2nd Edition; Wiley: New York, 1976.

APPLICATION OF BARRIER MEMBRANE TECHNOLOGY TO CATALYTIC CRACKER RECYCLE GAS HYDROGEN SEPARATIONS

L. D. Trowbridge

INTRODUCTION

In FY 2000, ORNL's Chemical Technology Division constructed a test bed for lab-scale evaluation of inorganic membranes designed to separate hydrogen from hydrogen/hydrocarbon gas streams. In FY 2001, a 6-month extension of this activity was funded under the Ultra-Clean Fuels program and further funding in FY 2002 was received from DOE's National Petroleum Technology Office to continue this work. The inorganic membranes tested were prototypes developed under a different portion of the Fossil Energy Program by the Inorganic Membrane Technology Laboratory (IMTL) located at East Tennessee Technology Park (ETTP) in Oak Ridge, TN. ORNL's experimental role is to test IMTL's membranes using flammable gas mixtures, initially using surrogate binary gas mixtures (e.g., $H_2 + CH_4$ or $H_2 + C_2H_6$), later (funding permitting) using gas mixtures generated by a lab-scale catalytic cracker.

The gas membranes to be tested take the form of tubes. The test bed is intended to hold one short section of such a tube. Full scale application will involve many longer, parallel tubes. The goal of this work is to determine the capability of specialized inorganic membranes for separating hydrogen from hydrocarbon streams. Realistic gas separation measurements will yield separation factors that incorporate a number of inherent inefficiencies that can be fairly well characterized and predicted from gas transport measurements. To be able to predict performance under conditions other than the specific ones examined experimentally, it is necessary to make the appropriate measurements allowing one to factor out these known, predictable inefficiencies so as to reveal the inherent ideal separation efficiency of the membrane.

Gas separation efficiency is generally interpreted by the equation:

$$.(- 1) = E_p\, E_m\, E_c\, E_b.(* - 1)$$

In this equation, is the measured separation factor, a function of the concentrations of the components in the two product streams:

$$. = [\ Y / (1 - Y)\ ] / [\ X / (1 - X)\ ]$$

where Y is the mole fraction of the desired component flowing out the enriched stream and X is the mole fraction of that component flowing out the depleted stream. E_p is the back pressure correction factor (the ratio of the pressure drop across the membrane to the high-side pressure). E_m is the mixing efficiency, a function of the flow and composition-dependent gas transport parameters, such as the diffusivity and viscosity of the gases. E_c is the cut correction factor, a function of the fraction of the gas which transits

the membrane. These factors can be calculated from measurable experimental parameters following the formulations presented in Ebel (1972) and Hogland (1979).

Two variables in the above equation which have not been mentioned are E_b, the membrane (i.e., barrier) efficiency, anḍ *, the ideal separation factor. Separation relying purely on the relative velocity of gas molecules, so-called Knudsen flow (from whence the term "Knudsen membrane" derives), has aṇ * equal to the ratio of the average molecular velocities. A design variation on this is the "molecular sieve" membrane, which hash pores sufficiently small that it relies on both the molecular velocities plus the effect of different molecular sizes to improve separation of light, small molecules over larger, heavy ones. If the pore size distribution is known, the ideal separation factor for this type membrane can also be estimated. For these two membrane designs, * can be readily calculated, leaving E_b as the ultimate parameter to be determined from the experiment. A third design strategy, the "surface flow" membrane, involves transport via surface condensation, surface diffusion, and re-evaporation of the more condensable component. Its ideal separation factor is not as well defined, and the experimental parameters to be determined are the combined factor "$E_b.(* - 1)$." In the data presented below, * will be taken as the Knudsen ideal separation factor, and all effects unaccounted for by E_c, E_m, etc. will be subsumed into E_b.

The IMTL-designed and manufactured membranes, though by no means identical to those used in the gaseous diffusion uranium enrichment plants, are descended from those types of membranes. As such, these membranes are at present considered classified materials, so the work is done in a secure laboratory utilizing security-cleared personnel. It should be said that though each particular inorganic membrane design and application is initially considered classified, when there is sufficient interest for commercialization, a review can be undertaken to determine if the application can be considered unclassified. This has been successfully done for over a dozen applications. The process is, however, sufficiently time-consuming that it is not appropriate to do it during the R&D stage of application development.

EXPERIMENTAL APPARATUS

The experimental system, largely constructed in FY 2000, was completed, tested, and utilized for separation measurements on an IMTL Knudsen membrane in FY 2001. A simplified schematic of the experimental system is shown in Fig. 1.

The system utilizes pre-mixed binary gas mixtures for the gas inlet supply. The gases are separated in a single pass through the membrane. Figure 2 shows a photograph of a membrane holder mounted in its temperature-controlled oven.

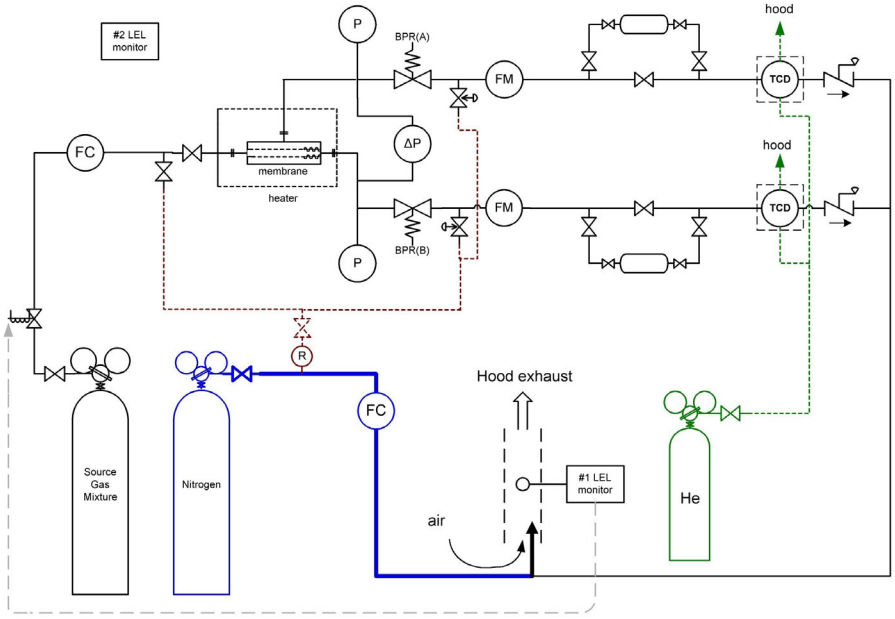

Fig. 1. Schematic of membrane test apparatus showing major operational elements only.

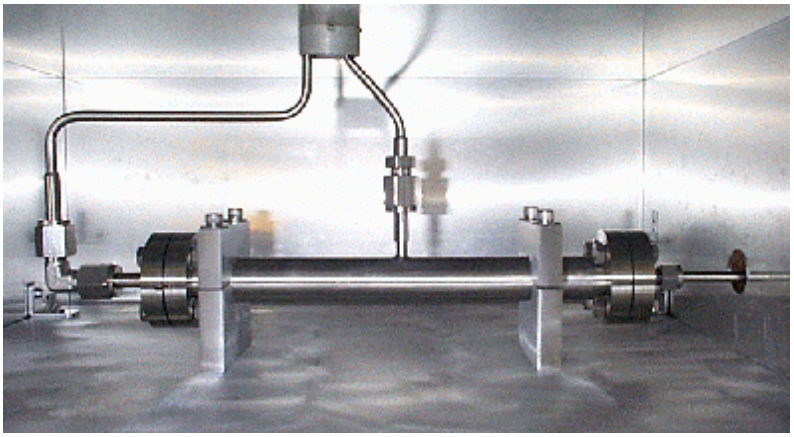

Fig. 2. Membrane holder mounted in oven.

Pressure is monitored in each stream (P) as is the pressure difference between the two separated stream (P). Pressure is controlled in each stream by back-pressure regulators (BPR). The total flow in the system is controlled upstream of the membrane by a flow controller (FC) and measured downstream in each stream by flow meters (FM). Each stream (or a side-stream thereof) passes through a thermal conductivity detector (TCD) to determine composition. Downstream of the TCDs, the two streams are mixed and then diluted below the lower flammability limit with a controlled flow of nitrogen. The mix is then exhausted to the laboratory hood. Flows, pressures, temperatures and concentrations are measured

and recorded by an on-line data acquisition system. As a more definitive back-up to the composition measurements made by the TCDs, samples can also be taken for analysis by gas chromatography.

The primary control on the flammability of the gases is the dilution of the exhaust stream to below its flammability limit. Control on the degree of dilution is set by the flow controllers (FC) on the source gas stream and the nitrogen diluent stream. To verify that the gas is indeed below the flammability limit, an LEL (lower explosion limit) device monitors the exhaust stream continuously. A second LEL device monitors the general atmosphere in the vicinity of the apparatus.

A typical experiment consists of the following steps:

a. The temperature the membrane holder is brought to the desired temperature.
b. The TCDs are calibrated using two or three calibrated gas mixtures.
c. A flow of diluent N_2 is established which will keep the system effluent below the LEL for the mixture at the maximum mixture flow contemplated.
d. An open path is set up from the inlet through the membrane and through the two TCDs.
e. Target conditions are selected (inlet mixture flow, low-side P, high-side P); the appropriate control elements (inlet flow-controller and the two back-pressure regulators) are set to achieve these conditions.
f. TCD outputs are tracked on the data acquisition system computer. When the concentrations in both the high- and low-pressure sides of the membrane have stabilized, the outcome of the experiment is recorded.

At this point, new target conditions can be selected and the process iterates through (e) and (f). Data for all measured parameters (temperatures, pressures, flows, LEL indication in exhaust, TCD output) is continuously recorded by the data acquisition computer; this data is post-processed to calculate separation factors and separation efficiency.

Last year's annual report discussed results of testing on a single inorganic membrane tube (designated 1226678-1-1) provided by IMTL. That was a relatively large-pore membrane (average pore diameter 4.5 nm). It can be termed a Knudsen membrane since, at that pore size, the separative flow should be dominated by Knudsen flow (also termed effusive or molecular flow). During 2002, two additional membranes were made available for testing. These had a similar base structure, but were treated with TEOS (tetraethylorthosilicate) and TMA (trimethyl aluminum). Average pore diameters were closer to molecular dimensions (0.8 and 0.6 nm). These characteristics are summarized in Table 1.

Table 1. Characteristics of membranes tested.

Membrane ID	Support layer	Separative layer	Additional treatment	Average pore dia (nm)
1226678-1-1	Ni	Al_2O_3	—	4.5
1230530-89	Ni	Al_2O_3	TEOS/TMA	0.8
1230530-108	Ni	Al_2O_3	TEOS/TMA	0.6

PROGRESS

The Knudsen membrane previously mentioned was tested during FY 2001, and results were reported in last year's annual report. Similar testing on the two additional membranes was conducted in FY 2002 and the early months of FY 2003. In general the same sorts of tests were conducted on all three membranes. After preliminary single-gas permeability tests confirmed that the membrane and its seals were intact after transport from IMTL and installation into the separation apparatus, separation tests were conducted using five gas mixtures (He/Ar, He/CO_2, H_2/CH_4, H_2/C_2H_6, and H_2/C_3H_8). In all cases the gases consisted of 75 mole % of the light component (He or H_2) and 25% of the heavy component.

Experiments spanned the pressure and flow ranges accessible to the instrumentation. Due to significant permeance differences in the three membranes, this led to some differences in the parameter-space explored between the membranes. For the Knudsen membrane (1226678-1-1), flow limitations restricted some experiments (i.e., to a lower ΔP than the instruments would nominally allow), while the smaller-pore membranes, the maximum ΔP restricted the range of experiments. For the smallest pore diameter membrane (1230530-108), the *minimum* flow readings were a limitation. For each gas, experiments were run at three or four temperatures between room temperature and about 200°C. A given series of experiments would yield up to several dozen separation points at average pressures (defined as the average of the high- and low-side membrane pressure) ranging from just over 1 bar to about 9 bar absolute. The cut (the fraction of gas transiting the membrane) ranged from a low of ~0% to a high of ~90% (when possible).

Accessible temperatures were limited by two factors. One was the heating system (easily modified if necessary), but the other was the seals. The membrane must be sealed so that leakage from the high to low pressure side is insignificant compared to the permeating gas flow, but must also withstand thermal expansion differences as the temperature changes. The sealing system used on these membranes handled these conditions satisfactorily to above 150°C, but in the 200°C range, proved to have a limited life before leaking. For the first membrane, the seal functioned in the 200°C range, but leaked on later cooldown. For the other two membranes, the seal began leaking within a day of two of reaching the 200 to 220°C range, limiting the number of high temperature measurements that were obtained.

Separation factors were calculated from the concentrations observed by the two TCDs. These were then corrected for the known effects previously alluded to (cut, back pressure and mixing) and a

membrane efficiency was calculated. In effect, this membrane efficiency (E_b) represents the efficiency of the membrane relative to that expected of an ideal Knudsen flow membrane. E_b collects all behavior nor readily explained by known gas dynamic effects. Typical observed values of the membrane efficiency for the various gas mixtures and temperatures are tabulated in Table 2.

Table 2. Experimental average separation membrane efficiency E_b, expressed in percent
<P> is the average of the membrane high- and low-side pressures

	1226678-1-1			**1230530-89**			**1230530-108**		
		Low<P> ~1.5 bar	**High<P>** ~7 bar		**Low<P>** ~1.5 bar	**High<P>** ~8 bar		**Low<P>** ~4 bar	**High<P>** ~8 bar
	T / °C	**E_b**	**E_b**	**T / °C**	**E_b**	**E_b**	**T / °C**	**E_b**	**E_b**
He/Ar	**23**	85	70	**23**	64–75	55	**22**	39	35
	93	85	70	**84**	80–96	75	**90**	57	55
	130	—	—	**150**	85–103	75	**150**	85	81
	196	85	70	—	—	—	**220**	110–130	—
He/CO_2	**24**	80	57	**22**	17	8	**22**	30	26
	93	85	67	**88**	39–46	34	**90**	46	42
	130	—	—	**145**	53–64	48	**150**	64	62
	196	83	70	—	—	—	**210**	93	—
H_2/CH_4	**23**	78	63	**19**	50–58	43	**22**	30	28
	93	85	70	**89**	63–71	56	**92**	40	35
	130	85	70	**150**	72–82	65	**150**	51	48
	183	85	70	—	—	—	**210**	88	—
H_2/C_2H_6	**24**	75	55	**23**	24	13	**22**	22	17
	88	75	57	**88**	41–46	35	**90**	28	23
	133	75	60	**140**	51–57	43	**150**	37	—
	196	75	55	—	—	—	**210**	63	—
H_2/C_3H_8	**24**	52	40	**23**	31	***–15***	**22**	12	—
	90	60	50	**88**	29	18	**90**	21	—
	133	63	52	**140**	39–46	34	**150**	33	—
	190	65	52	**210**	45	**	**202**	53	—

The general and trend in separation efficiencies common to all three membranes is as follows:

1. At lower average pressure, the efficiency is typically higher that at higher average pressure (where one would expect a greater fraction of the flow to be in the non-separative viscous flow regime). Surface flow effects would also be greater at higher pressures.
2. Higher temperatures tend to lead to higher separation efficiencies. This effect is markedly different for the three membranes studied. In the Knudsen membrane the effect was evident but not large.

3. Mixtures containing more condensable gases (e.g., CO_2 and C_3H_8) tend to have lower efficiencies and exhibit more of a temperature effect. This is likely a surface adsorption/flow effect.

There is a suggestion that higher temperature may lead to better separation efficiency, but experimental scatter do not make this conclusion a firm one for this system.

Table 2 summarizes the separation efficiencies for the systems and temperatures examined at lower and higher average pressures and for several temperatures. Differences between the membranes can readily be seen. The Knudsen membrane (1226678-1-1) shows a moderate effect that we may attribute to surface-enhanced flow (i.e., lower separation factors for more condensable gases at lower temperatures). The effect, however, is very evident the data for the smaller pore diameter membranes. Membrane 1230530-89, at room temperature and in the higher pressure range actually showed a reversal of the separation for the propane-hydrogen mixture—that is, the heavier propane preferentially separated through the membrane to the low pressure side, contrary to normal Knudsen flow expectations. This effect diminished strongly with increasing temperature. The effect was also evident in other pressure regimes and with other gas mixtures, though to a lesser degree for the less condensable gases. A similar effect is seen for membrane 1230530-108. Due to its lower permeance, the accessible experimental conditions did not allow measurements at the same high-pressure, low temperature conditions where separation reversal was observed.

Very small pore diameter membranes can in principle enhance separation by molecular sieving or screening. As the experimental data are being presented here, this should lead to separation efficiencies greater than 100%. A modest (but reproducible) enhancement above the ideal Knudsen separation factor was seen for He-Ar separations at higher temperatures for the two smaller-pore membranes. It was not observed for the hydrogen-hydrocarbon mixtures. Given the strong (apparent) surface effects, the simplest explanation is that, though molecular screening effects should be present, they are overshadowed by surface effects at the conditions examined. At higher temperatures and lower pressures, surface effects will diminish, and screening effects should become more evident.

Absolute separation varies strongly with cut, but this is accounted for by a cut correction factor (E_c). After making that correction, separation in the Knudsen membrane (1226678-1-1) showed no further correlation with cut. Membrane 1230530-89, however, showed a significant further cut-related effect: separation efficiencies at low cut were systematically lower than at high cuts. This effect was stronger at lower average pressures. The range of separation efficiencies shown in Table 2 for this membrane is not scatter: the lower efficiency value is for lower cuts (typically 25%) while the higher value is for high cuts (typically 75%). Due to membrane permeance and apparatus limitations, high-cut experiments were not practical on membrane 1230530-108, so it is not known if this occurs in that membrane.

CONCLUSIONS

Separation efficiency for hydrogen/light hydrocarbon mixtures has been examined for three IMTL-manufactured inorganic membranes. One was a (relatively) large pore-diameter Knudsen membrane and the other two had much smaller pore sizes. In these last two membranes, separation efficiency was typically lower than Knudsen separation, but strongly dependent on temperature, pressure, and gas mixture, the most condensable gases showing the strongest effect. This suggests that the separation is strongly affected by surface effects (adsorption, diffusion) which enhance the transport of the heavier and more condensable component and possibly also physically occlude the lighter component. In one series of experiments, separation reversal was observed (the heavier component preferentially separating to the low pressure side of the membrane). This could be taken advantage of by judicious selection of temperatures and pressures, but the optimum conditions would be specific to the particular compounds and concentrations, so a multi-component separation would be complex.

Molecular sieving effects should enhance the permeation of smaller molecules relative to larger molecules. Separation efficiencies in excess 100% (ideal Knudsen flow) were observed only for Ar-He separations. On a molecular size basis, this was the least favorable gas mix in which to see this phenomenon, but the most favorable from a surface effect standpoint. For all the other gas mixtures, however, factors we attribute to surface effects were stronger and apparently overshadow molecular sieving effects. Surface effects diminish with increasing temperature, but temperatures were not attained in which molecular sieving could be seen for the hydrogen/hydrocarbon mixtures examined.

One overall implication of these experiments is that higher temperatures need to be explored. This would allow further elucidation of surface effects (e.g., at what temperature do they become insignificant for a given gas and membrane?), demonstrate the degree to which molecular sieving enhances separation, and also explore the upper limits of operation from a hydrocarbon thermal decomposition standpoint. Follow on work in this realm, should it be done, would require addressing the question of improved high temperature seals and related questions of membrane and holder differential thermal expansion.

This report has given an overview of work that will be covered in detail in a topical report, currently in preparation.

REFERENCES

R. A. Ebel and L. P. Pasquier, “Design of a Gaseous Diffusion Stage,” NUCLEAR ENGINEERING—PART XXIII, AIChE Symposium Series, 123(68) p. 107 (1972).

R. L. Hoglund, J. Schacter, and E. von Halle, “Diffusion Separation Methods,” ENCYCLOPEDIA OF CHEMICAL TECHNOLOGY, vol 7, 3rd Edition, J. C. Wiley and Sons, (1979).

ENVIRONMENTAL COMPLIANCE ASSISTANCE SYSTEM (ECAS) FOR THE NATIONAL PETROLEUM TECHNOLOGY OFFICE

A. B. Walker

INTRODUCTION

The Environmental Compliance Assistance System (ECAS) is a website provided through the National Petroleum Technology Office (NPTO). The ECAS is an information resource targeted at the independently owned and operated, oil and gas exploration and production (E&P) industry. In general, these E&P facilities are small, family-owned operations, and therefore do not have the capital to support the personnel needed to research and maintain information regarding environmental compliance issues concerned with their industry. The website was developed to provide consolidated environmental compliance information in a concise, easy to use format. As such, the ECAS serves as a tool to assist these and other interested parties with regulatory information on the E&P industry; local, state, and federal contacts; waste handling/treatment/disposal options; and to direct them to other related web sites. A link to the ECAS can be found on the NPTO home page (http://www.npto.doe.gov/) or the site may be found directly at http://www.npto.doe.gov/ecas/index.html.

ANNUAL REPORT, 2003

This NPTO funded project is tasked with updating the ECAS system that is currently on the web.

Work on creating the web site began in January 1999. The website was completed in late 2000, and has been publicly accessible since early 2001. The site is updated monthly with information and links concerning new and pending environmental regulations, issues, and related pertinent information in the petroleum extraction industry. The remainder of the site includes links to federal and state regulatory contacts as well as guidance on waste management plans, records management, emergency response, and remediation methods applicable to soil and groundwater impacted by crude oil and brine. Information summaries and links for federal statutes and regulations are also provided. These areas of the site are reviewed, reworked, and updated as necessary. In addition to monthly updates of current events and

periodic maintenance of the rest of the website, an Ongoing Issues section was developed during 2002. The Ongoing Issues section provides a tracking mechanism for proposed rules during the usually lengthy rulemaking process. Historical accounts of continuing issues are also reported in the Ongoing Issues section. Tracking of website access has shown it regularly receives in excess of 10,000 hits per month. More than 2,000 unique visitors used the site during the October-December 2002 timeframe. The information requests came through a wide variety of channels and linked to virtually all areas of the site.

EFFECTS OF TEMPERATURE AND GAS MIXING ON FORMATION PRESSURE, CO_2 SEQUESTRATION AND METHANE PRODUCTION IN UNDERGROUND COALBEDS

J. G. Blencoe
Oak Ridge National Laboratory

INTRODUCTION

Evidence is mounting that rising levels of atmospheric CO_2, caused primarily by combustion of fossil fuels, will lead to rapid global warming. To address this problem, numerous nations are developing plans for lowering CO_2 emissions to the atmosphere. The principal approaches under consideration are: improving energy efficiency; making greater use of alternative sources of energy; and creating economically viable technologies for capture, separation, and long-term storage of CO_2. The latter strategy, which keeps large masses of CO_2 separate from the Earth's atmosphere for hundreds to thousands of years (a concept commonly known as "CO_2 sequestration"), is receiving increasing attention because it permits continued use of high-carbon fossil fuels to generate electrical power while ensuring that CO_2 releases to the atmosphere are reduced.

A potentially attractive means for terrestrial CO_2 sequestration is injection of gaseous CO_2 into underground reservoirs. The primary candidate sites are active or depleted oil and gas fields, deep brine formations, and unmineable, underground coalbeds. To date, studies to determine the feasibility of geologic CO_2 sequestration have focused on oil and gas fields, and deep brine formations. However, four characteristics of deep, unmineable coalbeds make them extremely attractive for wide-scale CO_2 sequestration. (1) Like deep brine formations, unmineable subsurface coalseams are widely distributed across the U.S. (2) When CO_2 is injected into a coalbed, it efficiently displaces adsorbed methane (Fig. 1). Therefore, CO_2 sequestration and coalbed methane (CBM) production are synergistic technologies, the additional natural gas produced by CO_2 sequestration serving to offset the costs of CO_2 injection. (3) CO_2 is twice as adsorbing on coal as CH_4, and remains tightly bound to coal surfaces after

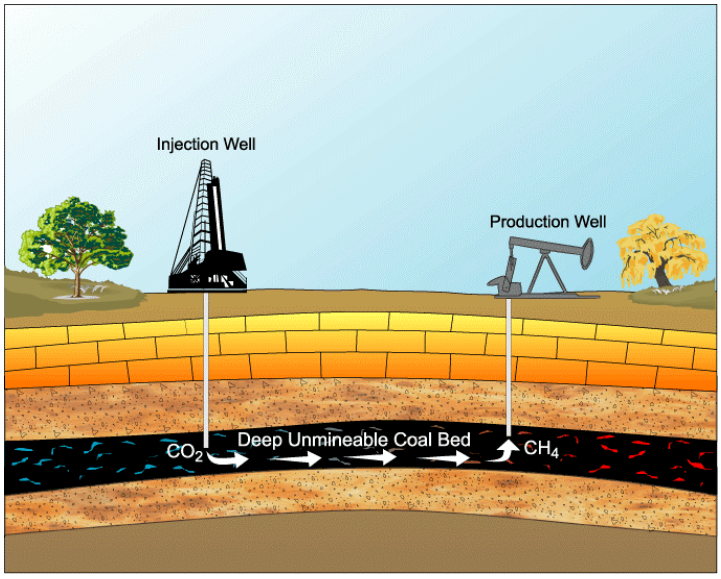

Fig. 1. A schematic diagram of CO_2-enhanced coalbed methane (CBM) production.

CH_4 is displaced. Therefore, after being injected into an underground coalbed, there is little risk that sequestered CO_2 will leak to overlying strata, or to the surface. *This is an enormous advantage over CO_2 storage in deep saline formations, where escape of gas through caprock is a serious problem.* (4) Many unmineable coalseams are located near coal-fired power plants, which are large point sources of CO_2. Thus, minimal pipeline transport of CO_2 would be required to deliver it to a suitable site for subsurface injection. In contrast, oil and gas fields, and particularly deep saline formations, are often far removed from fossil fuel-fired power plants.

CBM recovery, accomplished principally by pumping formation water out of a subterranean coalbed, is a mature technology. In contrast, *CO_2-enhanced CBM recovery* is a recent concept, which has been demonstrated only in pilot tests. Consequently, opportunities abound in fundamental and applied research aimed toward advancing this rapidly emerging technology.

PURPOSE

The central purpose of the research is to acquire critically important technical information for assessing the feasibility of sequestering CO_2 in deep unmineable coalbeds. This carbon management technology is currently in its embryonic stages; therefore, vigorous fundamental and applied research programs are needed to fill major knowledge gaps. A particularly important line of scientific inquiry arises from the observations that underground coalbeds are often rich in methane (CH_4), and that CO_2 injected into those formations will adsorb on coal surfaces, causing CH_4 to desorb. Thus, it has been proposed that CO_2 sequestration can be combined with coalbed methane recovery operations to enhance natural gas production. Brought to full fruition, this synergistic coupling could greatly reduce the costs of CO_2 sequestration. However, to enable reliable numerical modeling of CO_2-enhanced natural gas production, the effects of temperature and CO_2(±nitrogen, N_2)-CH_4 mixing on gas pressures, gas viscosities, gas sorption-desorption reactions, and gas sorption/desorption-induced coal swelling and shrinkage, must be known quantitatively. <u>These effects cannot be predicted accurately by modern methods of process modeling and simulation; consequently, experiments must be performed to obtain the required information</u>. Accordingly, this project is focused on data analysis and equation development designed to quantitatively characterize the effects of temperature and CO_2-CH_4 mixing on coal/gas interactions that influence the efficiency and cost-effectiveness of sequestering CO_2 in CH_4-rich underground coalseams.

APPROACH

The equilibrium densities and viscosities of CO_2-CH_4 mixtures will be determined experimentally at 30–70°C, 10–200 bars, using a custom-designed autoclave apparatus with a 1.2 liter internal volume

(Fig. 2). The following procedure will be applied to make the measurements: (1) The autoclave is heated to a predetermined temperature in an infrared, forced-air convection oven (Fig. 3), then evacuated to a pressure <10 torr with a vacuum pump; (2) The autoclave is then filled with pure CH_4 to a predetermined pressure, and a precalculated mass of (denser) CO_2 injected into the upper section of the autoclave. The CO_2 will sink toward the bottom of the vessel, mixing with CH_4 as it descends. (3) After the partially mixed gas has settled to the bottom of the vessel, the autoclave is inverted to induce gravity settling of any remaining, unmixed CO_2. (4) Step 3 is repeated until complete gas mixing is achieved. Rates of CO_2-CH_4 mixing will be monitored by continuously recording changes in pressure. Because mixed CO_2-CH_4 gases have large positive excess molar volumes at *P-T* conditions near the critical point of CO_2, mingling of the two species is reflected by increases in gas pressure. When a plateau value is reached, complete homogenization of the mixed gas is indicated. (5) After the gas mixture has been completely homogenized: (i) a final pressure reading is taken to determine the equilibrium density of the gas, and (ii) a viscosity measurement is made using a rolling-ball apparatus. Densities and viscosities measured in

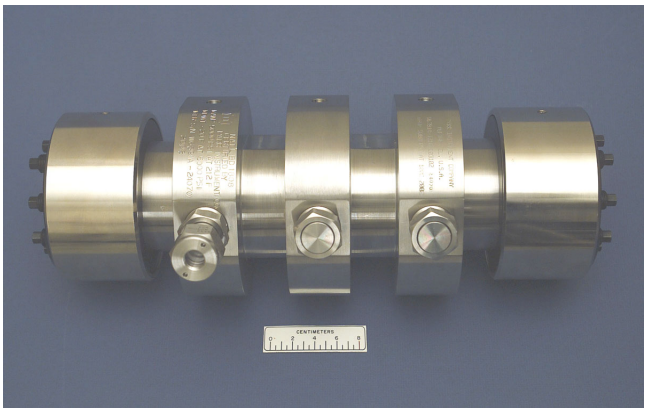

Fig. 2. Photograph of the rocking autoclave.

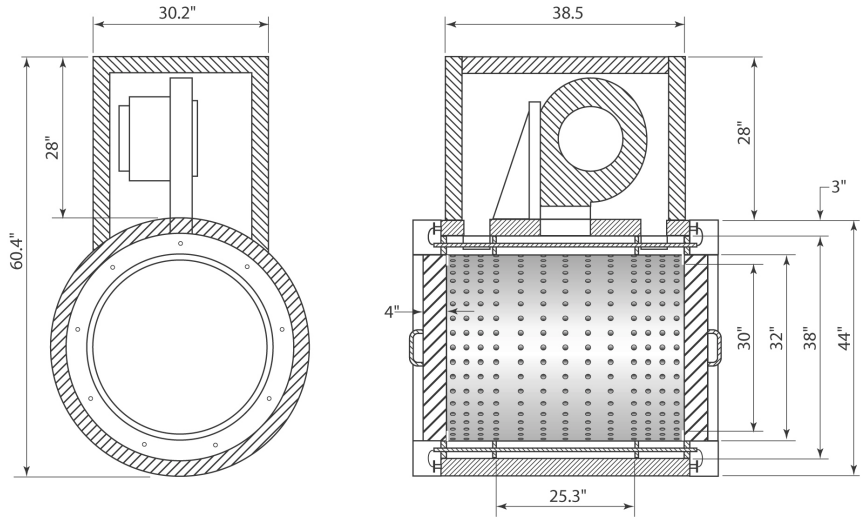

Fig. 3. Front and side engineering drawings of the infrared, forced-air convection oven that was built to heat the rocking autoclave to temperatures as high as 100°C.

this way for wide ranges of temperature, gas pressure, and gas composition can be used to develop mathematical expressions for predicting the fluctuations in gas pressure and viscosity that will occur when CO_2 mixes with CH_4—either during mixed-gas/coal adsorption-desorption experiments, or in field tests when CO_2 is injected into a methane-saturated subsurface coalbed.

STATUS OF THE PROJECT

Construction of the special autoclave facility is nearly complete, and data collection is scheduled to start in late June, 2003. Initial experiments will be performed at closely spaced temperature intervals between 30 and 40°C, and at a series of pressures between 10 and 200 bars for numerous intermediate gas compositions, to determine the effects of temperature and total gas pressure on the volumetric properties and viscosities of CO_2-CH_4 gases. The array of data produced by the experiments will indicate the changes in formation pressure and gas viscosity that will occur when CO_2 is injected into a CH_4-saturated, subterranean coalbed. The results are likely to show that the *P-V-T* properties and viscosities of CO_2-CH_4 mixtures are highly dependent on proximity to the critical point of CO_2 (located at approximately 31°C and 74 bars). Due partly to the highly nonideal mixing of CO_2-CH_4 gases at 30–40°C, 50–100 bars, large increases in pressure and gas viscosity will occur as CO_2 mixes with CH_4. The magnitudes of these pressure increases and viscosity variations, as a function of temperature, total gas pressure, and gas composition—presently unknown—must be determined precisely and accurately to enable reliable numerical modeling of CO_2 sequestration in CH_4-rich underground coalbeds.

Research conducted for this project in out years will build on the results obtained in FYs 2003 and 2004. Experiments will be performed to quantify the equilibrium densities and viscosities of CO_2-CH_4 gases at 40–50°C, 10–200 bars. In addition, the density data obtained in FYs 2003 and 2004 will be used to interpret the results of mixed-gas/coal adsorption-desorption experiments performed at other laboratories. The rates and extents of CO_2 adsorption on—and CH_4 desorption from—coal surfaces will depend on temperature, total gas pressure, coal rank and composition, and initial mixed-gas composition. The net effects of these variables cannot be predicted accurately before experiments are performed; however, it seems likely that results will indicate that gas adsorption/desorption varies systematically with the thermodynamic mixing properties of the gas from which CO_2 is being extracted, and into which CH_4 is being released. If so, it would then be possible to develop numerical expressions that relate the thermodynamic mixing properties of CO_2-CH_4 gases with the adsorption/desorption that occurs when mixed CO_2-CH_4 gas comes into contact with buried coal. This would be an exciting and highly significant outcome of our research, as numerical expressions of that kind are badly needed to further develop computer codes for predicting the nature and extent of CO_2 capture and retention during and after injection into an underground coalseam.

FUTURE WORK

The research performed for this project will lead naturally to subsequent laboratory work aimed at elucidating the effects of injecting CO_2-N_2 mixtures into subsurface coalbeds. This future research direction stems partly from ongoing efforts to gauge the feasibility of injecting processed (deoxygenated) flue gas, rather than pure CO_2, into deep-seated coal layers. Evaluations of this potential CO_2-sequestration technology are prompted by economics. It is expensive to separate CO_2 from flue gas prior to subsurface sequestration. It is much less expensive to strip oxygen from flue gas and inject the remaining gases (mostly CO_2 and N_2) directly into a coalseam. Significantly, it has already been demonstrated in field tests performed in the San Juan Basin (New Mexico/Colorado) that injecting pure N_2 into a coal layer can greatly enhance flow of CH_4 toward a production well. Therefore, the idea behind injecting mixed CO_2-N_2 gas into a coalseam is that four positive results would accrue: the CO_2 in the injectate would adsorb on coal surfaces, causing CH_4 to desorb; the N_2 in the injectate would lower the partial pressure of CH_4 in the coalseam, inducing additional release of CH_4; the CO_2 adsorbed on coal surfaces would remain tightly bound in the seam after injection (CO_2 sequestration); and finally, the three foregoing processes would—in combination—constitute a coupled CO_2 sequestration/CBM technology that is not only economically viable, but also highly effective in reducing CO_2 emissions to the Earth's atmosphere.

Clearly, to realize the great promise of CO_2+N_2-enhanced CBM recovery, it is necessary to develop a better understanding of CO_2-CH_4-N_2 gas mixing at *P*-*T* conditions achieved in subterranean coalbeds. This mingling will affect not only formation pressure and mixed-gas/coal adsorption-desorption reactions, but also coal expansion and contraction as gas species adsorb onto, and desorb from, coal surfaces. In this regard, it is noteworthy that our new autoclave facility is well-suited to measurements of coal swelling and shrinkage at temperatures and gas pressures representative of those found in deep, unmineable coalbeds. Therefore, a long-term goal of our research is to determine the effects of temperature, gas pressure, and $CO_2(\pm N_2)$-CH_4 mixing on the dimensionality of small, coherant fragments of coal. Coal expansion and contraction will be measured using miniature strain gauges mounted on the surfaces of coal samples. Whenever feasible, 2–3 strain gauges will be attached to a coal fragment in orientations that facilitate determination of expansion and contraction in directions parallel and perpendicular to original bedding. This will indicate the anisotropy in coal swelling/shrinkage that develops due partly to layering of organic and mineral matter in the sample.

ACKNOWLEDGMENTS

The research described in this report is being sponsored by the Office of Fossil Energy, U.S. Department of Energy, National Energy Technology Laboratory, under contract number DE-AC05-00OR22725 with UT-Battelle, LLC.

APPLICATION OF NATURAL AND INTRODUCED TRACERS FOR OPTIMIZING VALUE-ADDED SEQUESTRATION TECHNOLOGIES

D.R. Cole and T. J. Phelps
(Collaborators: S. Fisher, J. G. Blencoe, J. Horita, J. C. Parker, A. V. Palumbo, and G. R. Moline)

INTRODUCTION

This project is one element (Task B.3) of an interdisciplinary public-private partnership, GEO-SEQ, that was established to develop and deliver the enabling technology and information needed to accelerate application of safe and cost-effective methods for geologic sequestration of carbon dioxide. Team members include researchers from LBNL, LLNL, Stanford University, the Texas Bureau of Economic Geology and the Alberta Research Council. The overall goal of the ORNL effort is to provide methods to interrogate the subsurface that will allow direct improvement of CO_2 sequestration during EOR, ECBM, EGR, or use of brine formations. This will be accomplished by utilizing the power of natural (isotopic) and applied gas tracers to decipher the fate and transport of CO_2 injected into the subsurface as well as other relevant processes. These methods have the potential to provide near-real-time information on process optimization. The resulting data will be used also to calibrate and validate the predictive models used for (a) estimating CO_2 residence time, reservoir storage capacity, and storage mechanisms, (b) testing injection scenarios for process optimization, and (c) assessing the potential leakage of CO_2 from the reservoir. This activity is being conducted in concert with the geophysical and inverse-modeling methods described in Tasks B.1 and B.2 and will provide a means for calibrating the transport model and as an aid to interpreting the time-series geophysical data. This work directly addresses a key objective of the overall GEO-SEQ project: to increase confidence in and the safety of geologic sequestration by identifying and demonstrating cost effective and innovative monitoring technologies to track migration of carbon dioxide and its reaction products in geologic formations.

RESULTS: APPLIED GAS TRACERS

Tracer studies have become an important technique for *in situ* subsurface characterization, allowing detailed interrogation of complex systems, which have components moving, mixing, and reacting. Simultaneous injection of multiple tracers at different concentrations and frequencies can lead to a maximum retrieval of information on subsurface conditions relevant to the fate and transport of CO_2. This approach has been used successfully to isolate and in many cases quantify specific processes affecting transport, including: diffusion into low permeability materials, sorption, partitioning into non-aqueous phase liquids, partitioning into trapped gas phases, and biodegradation.

COMPLETION OF FLOW SYSTEM

Pressure testing and construction of the flow-through system has been completed. Components of the system can be broken down into five main areas: injection, column, tracers, fluids, and data collection (Table 1, Fig. 1).

Table 1. Overview of flow-through system capabilities and design.

Injection
Multiple gas homogenization reservoirs (95 ml, 150 ml, 300 ml) allow for continuous sampling
Metered flow rates from 0.01 ml/min to 10 ml/min
Column
Constructed of corrosion resistant Monel (brine injection areas) and 2507 stainless steel with Swagelock valves and tubing
Working pressure range up to 344 bar (~5000 psi)
Working temperature up to 100°C
Temperature measurements by type T thermocouples
Pressure measurements using piezoelectric transducers (0–6000 psi)
Helium used to measure of substrate porosity
Tracers
Conservative tracers include stable isotopes, noble gases, nonreactive salts, and perfluorocarbons
Fluids
Ability to add hydrocarbons and/or brine conditions to column
System can operate with CO_2 as a gas, liquid, or supercritical fluid
Data Collection
System can be remotely operated via internet connection
Valco sample valve inject gaseous effluent directly into HP gas chromatograph with an electron capture detector
Data continuously monitored using Labview

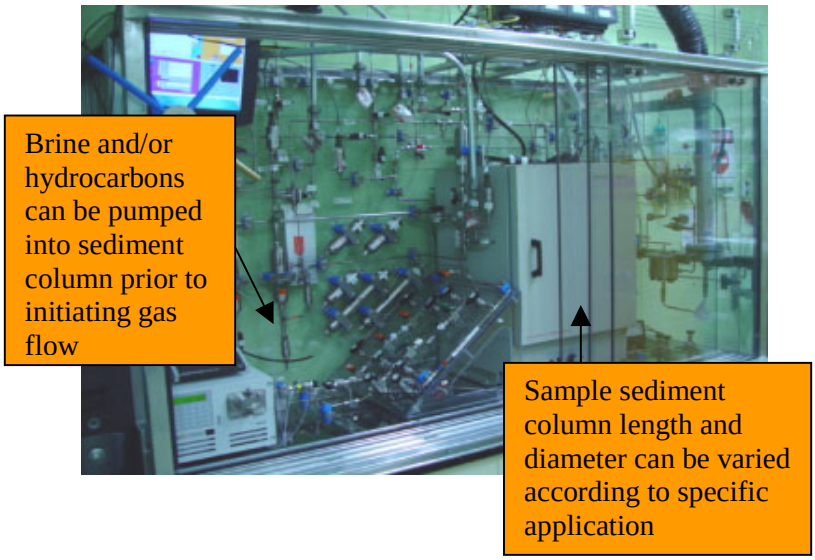

Fig. 1. Flow-through column apparatus.

The experimental plan for the laboratory flow-through column was designed to progress from simple to more complex systems: single phase (solid), dual phase (solid, brine), dual phase (solid, hydrocarbon), three phases (solid, brine, and hydrocarbon), and Frio core materials. Columns will be filled with solid material (clean quartz sand, carbonate, clay, and mixed reservoir solids) and each will be used for a succession of injections. Initial helium porosimetry measurements will be taken to obtain precise values for porosity. Brine and hydrocarbon saturations will be determined by repeating the He porosimetry after saturation and subtracting from the original pore volume. At every addition of some phase to the column, porosity will be re-determined. Thus, saturations will be known to great accuracy without having to disassemble the column to measure weight differences.

PERFLUOROCARBON TRACER METHOD DEVELOPMENT

The development of a PFT calibration standard dilution scheme was conducted. Because the PFT standards will exist in an aqueous and gaseous phase, calculations were done incorporating the density of the perfluorocarbons while taking into account the fact that PFTs are mostly insoluble in water. Therefore, methanol was incorporated into the scheme to aid in the solubility. Currently the perfluorocarbon standard curve ranges from 1.5 picograms to 5 nanograms conducted under injection volumes of 50 μL while the instrument detection limit had been determined at 1.5×10^{-14} g. Figure 2 shows the standard curve for all perfluorocarbons injected. Standard errors for injection replicates on the gas chromatograph have been >5%.

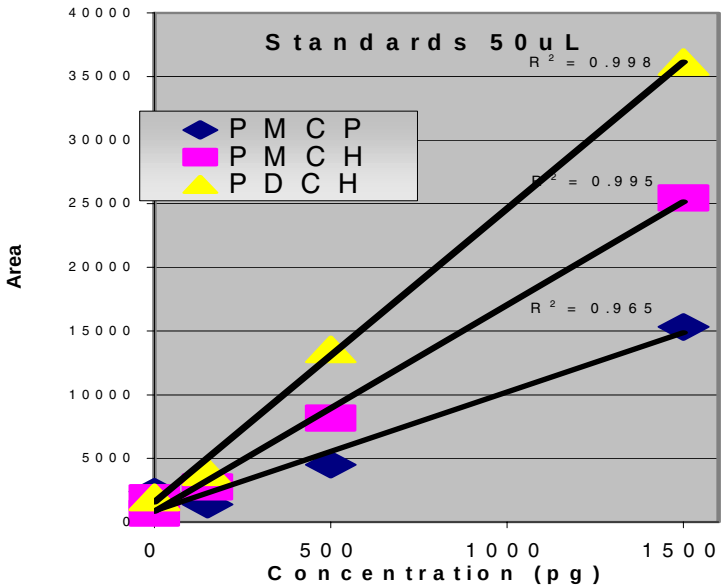

Fig. 2. Standard calibration curves (pg) for determination of PFTs.

PRELIMINARY GAS TRACER ANALYSES

Preliminary testing of single PFTs and evaluation of the dynamic flow system were conducted. Perfluoromethyl cyclopentane (PMCP) was chosen as the initial tracer for preliminary injection testing. 1mL of the 0.1 μg standard was injected through a 70°C-heated gas-tight syringe and allowed to homogenize overnight. System evaluation indicated a source of potential tracer dilution through the condensation trap located on the system, therefore the system was modified. Additional proceeding tests were conducted using perfluorodimethyl cyclohexane (PDCH) because of its distinct isomeric peak signatures that are distinct from nitrogen peaks. A 10-ml headspace sample of the 0.1 μg PDCH standard was drawn using a gas-tight syringe that was heated to 70°C and injected under vacuum into the simulator for homogenization in gas homogenization reservoir (GHR). The system was then pressurized to the selected experimental pressure of 700 psi with an ambient temperature of 19°C. Samples were allowed to homogenize overnight to ensure though mixing with the nitrogen carrier gas. An equal pressure gradient was maintained both upstream and downstream of the sediment flow-column. Upstream pressure was maintained by the use of an HPLC pump (Varian Instruments) with a built-in pressure transducer, while downstream pressures were regulated the use of a backpressure regulator. An experimental flow rate of 3ml/min was established using the HPLC to direct tracers from the GHRs into the sediment flow-column through a series of valves.

A Hewlett-Packard 5890 gas chromatograph (Agilent Technologies, Wilmington, DE) was used to quantify peak separation of PDCH. GC parameters included the use of an $ALOH_2$ column (50 m length, 0.53 mm ID), 51 ml/min split vent, 2.6 ml/min septum purge, 11.5 ml/min column flow, 250°C detector temperature, and injector temperature of 90°C. Oven parameters followed a temperature ramp program by setting the initial temperature to 120°C and raised 50°C (per 40 seconds) to reach a final temperature of 170°C. Samples were retrieved 7 minutes through a 10-inlet valco gas-sampling valve containing a 250 μL sample loop. Sample times were based upon retention times of perfluorocarbon standard curves.

RESULTS

The initial injection of PDCH into one of the 300mL GHRs was 2ng, thus 7pg/mL of PFT was allowed to homogenize within the GHR. Upon exiting the flow through column filled with Ottawa sand, PFT sample concentrations were determined based upon the standard curve to be 0.1pg (Fig. 3), corresponding to our predictions. The resulting concentration approached the instrument detection limit, but was approximately 10 above the baseline.

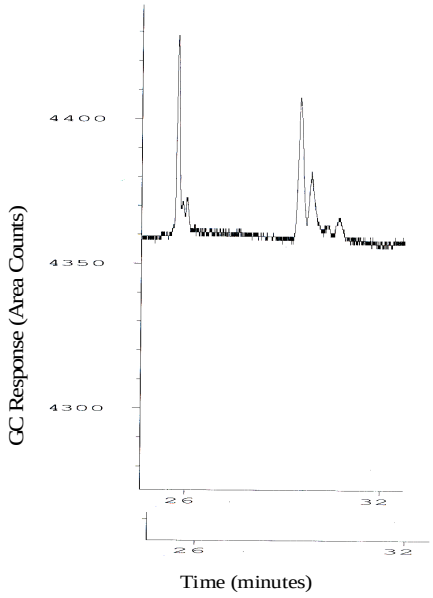

Fig. 3. GC Response for PDCH determined from preliminary PFT injections on flow-through system sampled from gas sample valve.

Results from our preliminary experiments on the Geo-Sequestration Simulator have demonstrated a working system that is reproducible, sensitive to low levels of detection, and is capable of distinguishing physical and geochemical parameters effecting long-term sequestration of CO_2.

RESULTS: NATURAL ISOTOPE TRACERS

Naturally-occurring elements, such as the stable isotopes of the light elements (O, H, C, S, N), noble gases and their isotopes (He, Ne, Ar, Kr, Xe), and radioactive isotopes (e.g., tritium, ^{14}C, ^{36}Cl, ^{125}I, ^{129}I, ^{131}I), have been used extensively to determine the sources of fluid and gas species and their mechanisms of migration, assess the extent of fluid/rock interactions, and quantify the residence times of fluids in the subsurface. These naturally occurring constituents and their isotopic compositions have the advantage of being readily available in most systems. In particular, by accounting for how $^{13}C/^{12}C$ and $^{18}O/^{16}O$ ratios in CO_2 vary during the injection process, we can (a) understand complex natural geochemical processes involving CO_2 in the subsurface, and (b) assess and monitor quantitatively both short- and long-term consequences of subsurface CO_2 injection and sequestration, and possible leakage from the system.

ISOTOPE AND GAS CHEMISTRY AT THE LOST HILLS, CA CO_2 INJECTION SITE

We have now completed gas and isotope (carbon; oxygen) analyses of samples obtained from the Chevron Lost Hills, CA CO_2 injection test. Samples were taken this past year on 2/14/02, 6/12/02 and 10/8/02. The gas chemistries from these samples are plotted together with results we had obtained previously from earlier samplings on CO_2–CH_4–ΣC_2-C_6 ternaries show in Fig. 4. By way of review, gases sampled prior to injection were dominated by CH_4 (~60%) with lesser amounts of CO_2 (~30%) and subordinate amounts of C_2-C_6 (~10%). The $\delta^{13}C$ (PDB) values for CH_4 in pre-injection and all return gases were very similar, ranging from –36 to –42%, with an average of –40.4% (±1.5% 1 σ). The initial injection CO_2 had a $\delta^{13}C$ (PDB) value of about –31% and $\delta^{18}O$ (VSMOW) values of between –1 and –2 %. The brine has a $\delta^{18}O$ value of about –1% VSMOW. The most extensive CO_2 injection was conducted at the end of 2002, with lesser magnitude injections occurring during the end of 2001 and the

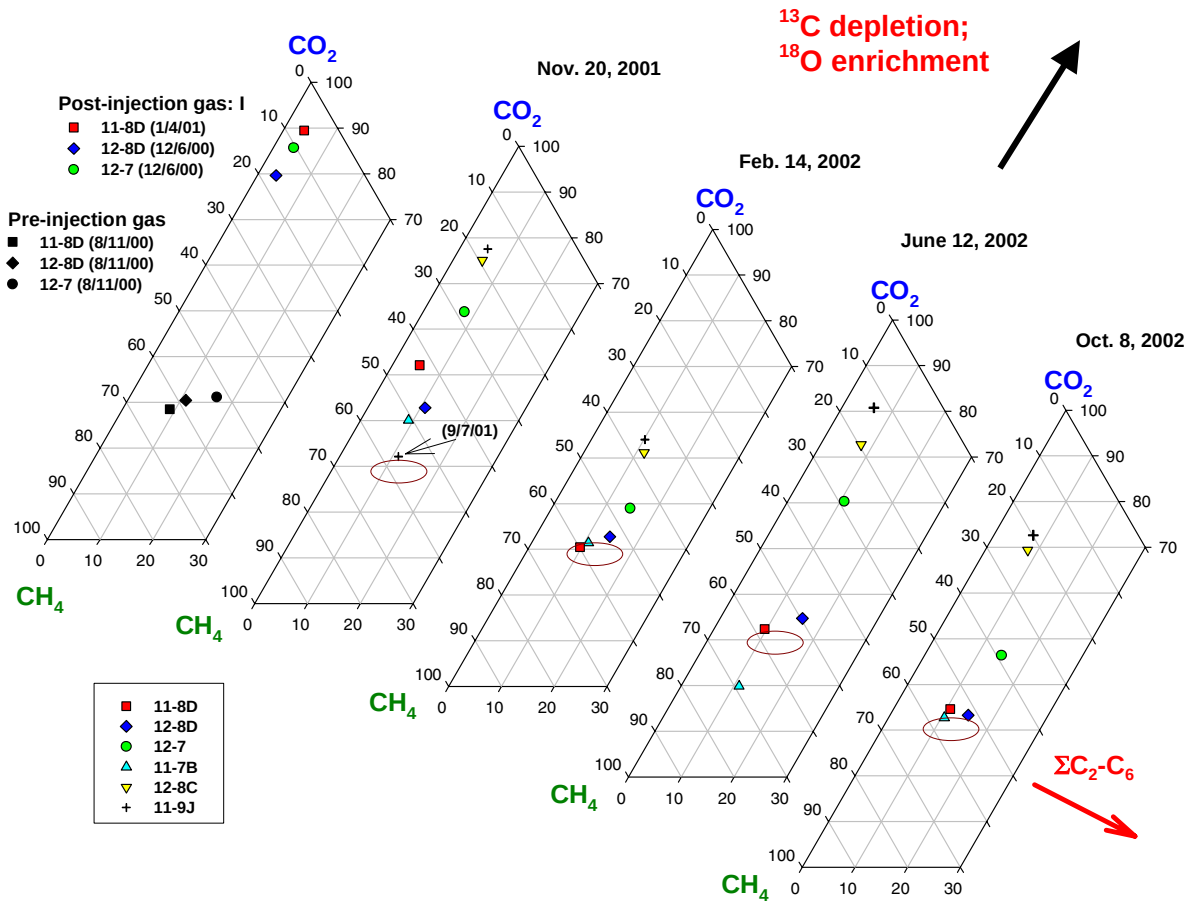

Fig. 4 Lost Hills gas chemistry plotted in CO_2-CH_4-ΣC_2-C_6 ternary space as a function of sample date.

summer of 2002 (June–August). A major water flood was conducted prior to CO_2 injection (Jan. 2000–August 2000) and also in early 2002.

Based on data presented in Fig.4, it is clear that the contribution by injectate CO_2 becomes far less pronounced with an increase in time starting from our earliest post-injection samplings (12/6/00; 1/4/01). In fact, after the 11/20/01 sampling time, three of the wells, 11-8D, 12-8D and 11-7B, exhibit gas compositions very similar to those for wells sampled prior to the initiation of the CO_2 injection test (9/19/00) which we presume represents the "baseline" reservoir chemistry. The caveat here, however, is that this part of the Lost Hills reservoir had been undergoing water injection as far back as 1/7/00, some 8 months prior to the CO_2 test. Thus, the gas and isotope chemistry of reservoir gas will never be known for this area because of the long history of perturbation.

Samples obtained from Lost Hills, CA on Feb. 14, 2002 coincide with an extensive period of water injection that started in mid-November of 2001. The contribution of injectate CO_2 appears to be considerably less than the previous sample time of 2/14/02 as well as subsequent samplings (6/12/02 and

10/8/02). These latter two sample times occurred during periods of modest CO_2 injection. The contribution by injectate CO_2 became somewhat less pronounced with an increase in time since the June 12th sampling for some wells (11-9J, 11-7B, 12-7). Gas chemistries for wells 11-8D, 12-8D and 11-7B sampled in October, 2002 plot very close to the gas compositions determined for wells sampled prior to the initiation of the CO_2 injection test (9/19/00), i.e. the "reservoir" signature. The gas chemistry for well 11-7B plots within the range of compositions thought to represent the indigenous reservoir system, but with considerably more CO_2 than it exhibited in the more CH_4-rich June sample. The reason for this shift to more CO_2 is not immediately apparent since the CO_2 injection activity ended on Sept. 15, 2002. Despite the fact that CO_2 injection had been stopped roughly three weeks prior to the Oct. sampling, there is still a significant contribution of injectate to three of the six wells sampled. Interestingly, these three wells are located at approximately opposite corners of the four 2.5 acre pattern—i.e., wells 11-9J and 12-8C are in the SW quadrant, and well 12-7 is located in the NE corner. The implication of this observation is being assessed in the context of both the nature of the injection (i.e. which injection wells were used and for how long), and the known fault structure in the area.

The carbon isotope compositions of CO_2 are plotted as a function of time in Fig. 5. The $\delta^{13}C$ (PDB) values for pre-injection CO_2 ranged from 15.6 to 18.5% whereas the return CO_2 gases from the first sampling effort (12/6/00 and 1/4/01) exhibited a narrow range of values, –27.5 to –29.9%, very similar to the injectate value of –31%. Chemically, return gases from this first sampling effort were very rich in CO_2 and clearly have carbon isotope values very close to the injection CO_2. Carbon isotope values determined for samples obtained during intervals of CO_2 injection are more depleted in ^{13}C compared to samples obtained during or just after water injection. This is consistent with an increased contribution of injectate CO_2, which has a very negative carbon isotope signal (~ –31%) compared to the "reservoir" CO_2. For example, CO_2 obtained June 12th had much lower $\delta^{13}C$ values for wells 11-9J and 12-7 compared to the Feb. 14 sampling, but a somewhat modest shift to a more depleted value for well 12-8C. In fact, the carbon isotope compositions of these three wells mimic those observed from the Nov. 20, 2001 sampling which also was conducted during a period of CO_2 injection. At no time, however, have the gas chemistries ever exhibited as rich a CO_2 content, nor as negative a carbon isotope value as were observed in the very first samples obtained at the end of the first (and most major) CO_2 injection period (9/00–12/00). Because 12-7 and 11-9J/12-8C are located at opposite corners of the four 2.5 acre well pattern, separated by major faults, it is clear that increase in CO_2 concentration (along with more negative carbon isotopes) is probably a consequence of communication with the closest injector wells, 12-7W and 11-8WA, respectively. Tracking the changes in chemistry and stable isotopes are complicated by the fact that the durations and capacities of separate injections of water and CO_2 have been varied through time, as was which set of the wells was used during a particular injection test.

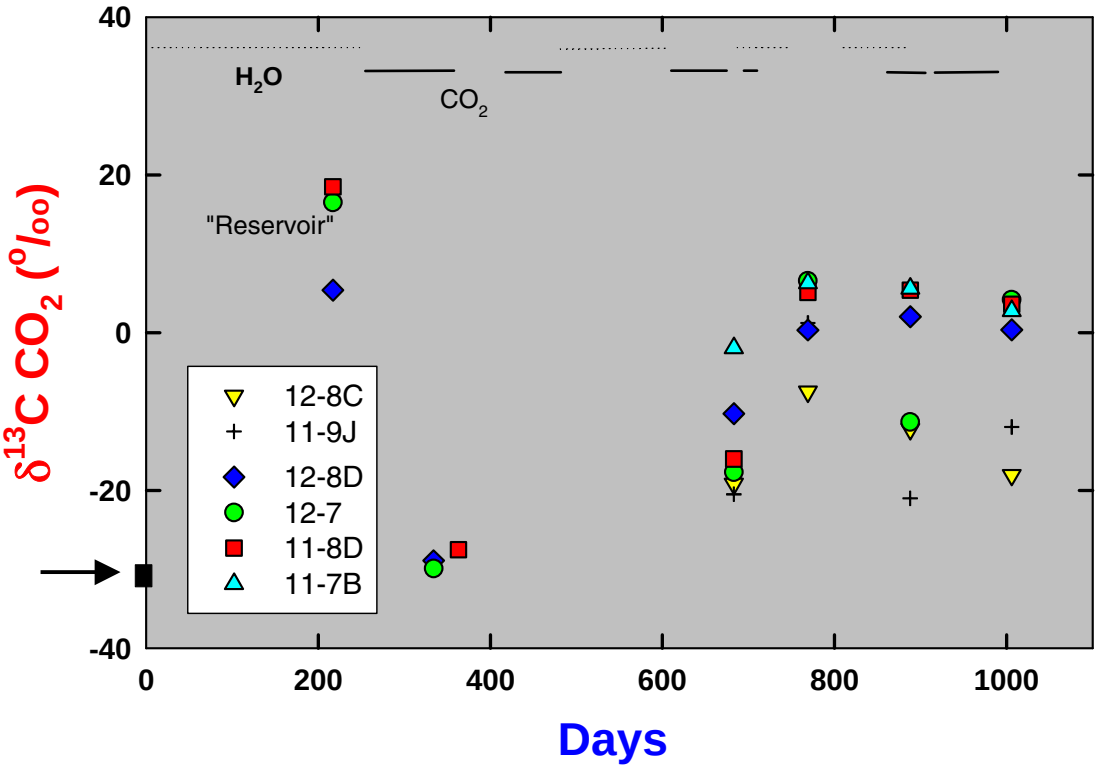

Fig. 5 Carbon isotope compositions of CO_2 plotted against time for the Lost Hills system. The injectate CO_2 has a $\delta^{13}C$ value of roughly –31%.

The $\delta^{18}O$ compositions of the pre-injection CO_2 ranged from about 16 to 24% (average ~20.9%), whereas the return CO_2 gases from the first sampling effort were somewhat more enriched, ranging from approximately 29 to 34%. Since these samples are dominated by injectate CO_2 (78–90%), this constitutes nearly a ~30% increase in $\delta^{18}O$ from the injection value of –1.1%. Subsequent CO_2 samples exhibit $\delta^{18}O$ values that have remained relatively constant over time, varying between 36 and 40%. Simple mixing of an isotopically light injectate and the heavy "reservoir" CO_2 cannot explain the even heavier $\delta^{18}O$ values measured in the three return wells. It is likely that the enrichment in ^{18}O is due to kinetically fast exchange of CO_2 with water encountered during migration. The values we observe (36 to 40%) would be expected if the CO_2 equilibrated with reservoir brines (–1%) at temperatures between ~40 and 60°C.

SUMMARY

(1) Gas and isotope chemistry of the CO_2 clearly demonstrates that increases in CO_2 and more depleted ^{13}C values correlate with periods of CO_2 injection.

(2) During water flood events, the CO_2 gas contents decrease and the ^{13}C values in CO_2 return to more "reservoir-like" in magnitude.

(3) Certain wells communicate with the injection wells far more readily than others, which may be controlled, in part, by faults that strike NE-SW.

(4) Oxygen isotope values in CO_2 demonstrate that the gas has equilibrated with reservoir brine in the temperature range of ~40 to 60°C.

REFERENCES

Hayduk, W., and H. Laudie, 1974. Prediction of diffusion coefficients or non-electrolysis in dilute aqueous solutions. AIChE J. 20:611–615.

Sanford, W. E., R. G. Shropshire, and D. K. Solomon, 1996. Dissolved gas tracers in ground water: Simplified injection, sampling, and analysis. Water Resour. Res. 32:1635–1642.

Wilke, C. R., and C. Y. Lee, 1955. Estimation of diffusion coefficients for gases and vapors. Ind. Eng. Chem. 47:1253–1257.

PRESENTATIONS AND PUBLICATIONS

L. S. Fisher, D. R. Cole, J. G. Blencoe, G. R. Moline, J. C. Parker, and T. J. Phelps (2003). High-pressure flow-through column for assessing subsurface carbon sequestartion. 2nd Annual Conference on Carbon Sequestration.

D. R. Cole, J. Horita, M. C. van Soest, B. M. Kennedy, and M. F. Morea (2003). Gas chemistry and isotope monitoring during the Lost Hills, CA CO2 injection test. 2nd Annual Conference on Carbon Sequestration.

ESTIMATION OF CARBON CREDITS IN CARBON DIOXIDE SEQUESTRATION ACTIVITIES

K. T. Klasson and B. H. Davison
Oak Ridge National Laboratory

INTRODUCTION

The approach for the activity, Estimation of Carbon Credits in Carbon Dioxide Sequestration Activities, will be based on the proposed approaches for forest systems. The desired result is a general methodology for evaluation of other sequestration options, which may result in temporary or permanent carbon fixation. The scope will be to develop the model in a series of small focus group meetings.

A process that involves sequestration of carbon, either from the atmospheric carbon dioxide (or other carbon-based greenhouse gas) or from the stack gases of a plant, should be evaluated on the same basis so that it can be compared to other sequestration options. As an example, we are providing the following discussion of some of the variables that may be evaluated:

1. ***Net Mass of Carbon Sequestered:*** It is important to have accurate estimates for the mass of carbon sequestered. For example, if a pond is used for heavy algae growth on atmospheric carbon dioxide, it is necessary to estimate any amount of methane that may be formed and emitted from the pond during anaerobic digestion in the sediments. Also, if substantial amount of lime is used to control the pH, it may be appropriate to assign a carbon equivalent corresponding to the amount of carbon dioxide (or other carbon) emitted during the production of the lime. To address these issues it is important to draw distinct boundaries and account for all the carbon flows.

2. ***Duration of Carbon Sequestration:*** It is intuitive that a long sequestration period is advantageous. However should it be expected that any sequestration activity should pass a threshold duration (e.g., 100 years) before being considered? Or, should the carbon sequestration activity receive full credit the year it is effective, and later receive a debit when possibly the carbon is released? The latter approach corresponds to some of the accounting strategies that are discussed in support of the Kyoto protocol. However, it does not allow for a priori comparison when two alternative activities are considered for the sequestration. If the time factor is important, several approaches may be taken—the threshold method is one, a linear relationship between the credit assigned and the duration sequestered is a second method. A third and fourth method may be to consider progressive approaches to bring incentives for longer- or shorter-term sequestration activities. It is possible that a threshold sequestration time (e.g., 100 years) is common among all methods after which full credit is

given. When discussing time it is also important to realize that the sequestration and the emissions may be spread out over time and that a life-cycle approach for the activity is used. For example, if the algae pond is used for several decades before it is harvested and the algae converted into bio-fuels, the activity has sequestered a net amount of carbon each year, but it is being released all at once. It is probably appropriate to take into account that some of the carbon was sequestered for a long time, but other portions were not. An attractive method to approach the time factor may be to define the Time Value of Carbon (analogous to the time value of money) and to use present-value-type calculations to bring all carbon flows to a single time.

3. ***Energy Use for Carbon Sequestration:*** The use of easily distributed energy (e.g., electricity) during the sequestration or maintenance of the stored carbon may be important to consider. This is energy that most likely resulted in carbon dioxide emissions during its generation. Thus, the energy can be converted into carbon equivalence and taken into account in the same fashion that other carbon flows are considered with respect of time. The use of waste energy that cannot be distributed (e.g., geothermal heat or process plant waste heat) should be considered "carbon neutral."

4. ***Land Use for Carbon Sequestration:*** If the sequestration activity will occupy a significant amount of land and if that land is a sink for carbon this has to be taken into account.

5. ***Others:*** Cost, regulatory issues, environmental impact, and social impact fall into this category. These are items very important for any undertaking and should be considered. However, it is in some cases very subjective and they should be kept separate from the carbon metrics evaluation. They each have strong merit and should be addressed but it may be appropriate to abstain from assigning any value to these factors. Cost represents a separate factor that can be evaluated through standard cost estimation methods. Costs will be part of this work if data are available. For example, if the cost for an algae pond has been estimated, it will be noted, but it will not be part of the carbon metrics.

In order to investigate if the above factors are appropriate to consider when a carbon sequestration activity is being evaluated, several focus group meetings will be held with others who are working on carbon credit trading and carbon credits for Land Use Change and Forestry. Both ORNL internal and external focus group meetings will be held. This will make sure that the initial approach taken gains support and understanding.

PRESENTATIONS AND PUBLICATIONS

1. Klasson, K. T., and B. H. Davison, "A General Methodology for Evaluation of Carbon Dioxide Sequestration Activities," Nineteenth Annual International Pittsburgh Coal Conference Proceedings, Pittsburgh Coal Conference, Pittsburgh, PA, 2002.
2. Klasson, K. T., and B. H. Davison, "A General Methodology for Evaluation of Carbon Sequestration Activities and Carbon Credits," Oak Ridge National Laboratory, ORNL/TM-2002/235, November 2002.
3. Klasson, K. T., and B. H. Davison, "A General Methodology for Evaluation of Carbon Dioxide Sequestration Activities," presented at the Nineteenth Annual International Pittsburgh Coal Conference, Pittsburgh, PA, 2002.
4. Klasson, K. T., R. M. Counce, and B. H. Davison, "Development of a General Methodology for Evaluation of Carbon Sequestration Activities," in meeting proceedings from the 223rd American Chemical Society National Meeting in Orlando, FL, 2002.
5. Klasson, K. T., R. M. Counce, and B. H. Davison, "Evaluation of a Carbon Dioxide Separation Activity Based on Absorption from Flue Gas Streams: A White Paper," Oak Ridge National Laboratory, Oak Ridge, TN 37831, 2002.
6. Klasson, K. T., R. M. Counce, and B. H. Davison, "Development of a General Methodology for Evaluation of Carbon Sequestration Activities," presented at the 223rd American Chemical Society National Meeting in Orlando, FL, 2002.
7. Klasson, K. T., and B. H. Davison, "Full-Cycle Carbon Emissions (FCCE) Factors from Resource Use in Carbon Sequestration Activities: A White Paper," Oak Ridge National Laboratory, Oak Ridge, TN 37831, 2001.
8. Klasson, K. T., and B. H. Davison, "Evaluation of a Carbon Dioxide Sequestration Activity Based on Production of Carbon-rich Fertilizers: A White Paper," Oak Ridge National Laboratory, Oak Ridge, TN 37831, 2001.
9. Klasson, K. T., and B. H. Davison, "A General Methodology for Evaluation of Carbon Dioxide Sequestration Activities," presented at the Twelfth Symposium on Separation Science and Technology for Energy Applications, Gatlinburg, TN, 2001.
10. Klasson, K. T., and B. H. Davison, "Estimation of Carbon Credits in Carbon Dioxide Sequestration Activities," presented at the First National Conference on Carbon Sequestration, Washington, DC, 2001.
11. Klasson, K. T., and B. H. Davison, "A General Methodology for Evaluation of Carbon Dioxide Sequestration Activities," presented at the 23rd Symposium on Biotechnology for Fuels and Chemicals, Breckenridge, CO, 2001.

12. Klasson, K. T., and B. H. Davison, “Chemical Engineering and Carbon Dioxide Sequestration Strategies,” presented to Knoxville-Oak Ridge Section of American Institute of Chemical Engineers, Knoxville, TN, 2001.
13. Klasson, K. T., “A General Methodology for Evaluation of Carbon Dioxide Sequestration Activities,” presented at University of Arkansas, Fayetteville, AR, 2001.
14. Klasson, K. T., and B. H. Davison, “Estimation of Carbon Credits in Carbon Dioxide Sequestration Activities: A White Paper,” Oak Ridge National Laboratory, Oak Ridge, TN 37831, 2000.
15. Klasson, K. T., and B. H. Davison, “Estimation of Carbon Credits in CO2 Sequestration Activities,” presented at the 22nd Symposium on Biotechnology for Fuels and Chemicals, Gatlinburg, TN, 2000.
16. Klasson, K. T., and B. H. Davison, “Estimation of Carbon Credits in CO2 Sequestration Activities,” presented to a forum at National Energy Technology Laboratory, Morgantown, WV, 2000.
17. Klasson, K. T., and B. H. Davison, “Estimation of Carbon Credits in CO2 Sequestration Activities,” presented as a technical seminar at Oak Ridge National Laboratory, Oak Ridge TN, 2000.

COAL MODIFICATION TO REDUCE MERCURY EMISSIONS

K. Thomas Klasson
Oak Ridge National Laboratory

INTRODUCTION

Mercury emissions from coal burning or reforming will be an issue in the future. The objective of this project is to address this issue utilizing biological coal modification, removing a large fraction of the mercury trapped in the coal prior to thermal processing. Sulfur oxidizing bacteria can release sulfur an iron from coal in a process called bioleaching. We expect the majority of the mercury to be released by the same process. This is a novel approach that has a high probability of succeeding because of the following:

1. High-sulfur coal contains high mercury concentrations.
2. Mercury-sulfur compounds are likely to be the main form of mercury in coal.
3. Biological leaching of coal has been shown to remove sulfur from coal.
4. Thus, we hypothesize that mercury will fortuitously be removed with the sulfur during bioleaching.

The project focuses on:

- quantifying the amount of mercury removed by bioleaching along with the sulfur and iron;
- characterizing speciation of mercury during this process;
- in the case of native organisms, identify bacterial genus capable of performing the biomodification;
- assess if mercury, along with sulfur and iron removal, increases attractiveness of bioleaching technology through larger-scale testing and rate modeling based on earlier sulfur bioleaching; and
- demonstrating a method of mercury removal from the leachate so it can be recycled.

The project was started in the fall of 2002. During the first two quarters, work was initiated with well-defined species of bacteria and coal for proof of concept tests. In the second year, work will be performed with environmental culture samples from which indigenous bacteria will be enriched and identified. Larger-scale testing, together with mercury dissolution rate determinations and technology assessment, will progress in the third year of this project with the best performing organisms.

TECHNICAL PROGRESS

Five different coals were obtained from the Penn State Coal Bank (PSOC). The coals obtained were PSOC-275 (Ohio #6A, Lower Freeport Seam) with a reported mercury content of 0.57 mg/kg, PSOC-

1286 (Ohio #5, Lower Kittanning Seam), PSOC-1296 (Pennsylvania B, Lower Kittanning Seam), PSOC-1368P (Weir-Pittsburg/Cherokee Seam, Missouri), PSOC-1479 (Pratt Seam, Alabama) with a high pyritic sulfur content and possibly high mercury levels based on coal seam data. The pyritic, total sulfur, total mercury content of these coals are shown below. The sulfur concentrations were provided with the coals from PSOC and the mercury analysis was performed according to the procedure developed by the U.S. Geological Survey (O'Leary, R.M. in USGS Bulletin 2144).

Coal	Pyritic Sulfur (%)	Total Sulfur (%)	Total Mercury (mg/kg)
PSOC-275	1.51	2.3	0.26
PSOC-1286	8.38	10.4	0.37
PSOC-1296	4.87	6.2	0.22
PSOC-1368P	8.83	12.5	0.27
PSOC-1470	2.37	3.15	0.29

Microorganisms (*At. ferrooxidans*, *L. ferrooxidans*, *At. thiooxidans*, and *A. caldus*) were obtained from American Type Culture Collection and are grown in the recommended media.

ENHANCED PRACTICAL PHOTOSYNTHESIS CARBON DIOXIDE MITIGATION

J. D. Muhs

ORNL has continued development of the solar lighting system for a engineered photobioreactor being developed by Ohio University to sequester carbon at power plants. Ohio University has prepared a comprehensive annual report detailing the project. A prototype solar collector was installed at Ohio University by ORNL in June 2002 and was fully-operational for the remainder of 2002.

The collector is being updated and refurbished, in preparation for a 6-month test that will begin in June 2003 at Ohio University.

In addition to developing the collector, ORNL has also developed the illumination system within the bioreactor, using illumination sheets containing side-emitting optical fibers sandwiched between algae growth membranes. The system was installed in June 2002 along with the solar collector. Refinements to the illumination system are continuing in FY 2003.

ENHANCING CARBON SEQUESTRATION AND RECLAMATION OF DEGRADED LANDS WITH FOSSIL-FUEL COMBUSTION BYPRODUCTS

Anthony V. Palumbo, J. Zhou, Madhavi Martin, and L. Suzanne Fisher
Oak Ridge National Laboratory

James E. Amonette and F. Blaine Mettting
Pacific Northwest National Laboratory

W. Lee Daniels and Kathryn Haering
Virginia Tech

Jana Tarver and Susan M. Pfiffner
The University of Tennessee

INTRODUCTION

This joint ORNL and PNNL project examines the potential use of lands that have been disturbed by mining, highway construction, or poor management practices for terrestrial carbon sequestration. The approach includes examination of the effects of amendments with solid byproducts from fossil-fuel combustion, paper production, and biological waste-treatment facilities for enhancing carbon sequestration. The primary goal is to identify and quantify the key factors leading to successful C sequestration and reclamation of degraded lands and to communicate this information to the community. A scientific evaluation of existing field sites where amendments have been applied provides the basis for the guidelines. Results from the available literature are combined with additional new measurements of properties at these sites including (1) the extent and nature of the sequestered C, (2) microbial communities and their influence on greenhouse-gas emissions, and (3) redox, alkalinity, toxic metals, and key soil physical properties. Specific tasks focus on the accumulation of carbon in soil over time (including carbon sequestered in deep soil horizons) and the impact of environmental conditions on the rate of accumulation, assaying for populations of denitrifying bacteria that can effect emissions of greenhouse gases, assessing potential environmental health impacts (accomplished through a series of column leaching and toxicity experiments), comparing the results to DOE/CSiTE measurements, and evaluating management practices to optimize this sequestration strategy. Technology transfer workshops, presentations at academic and industrial meetings, and publications are employed to engage industry and create working partnerships. Project results will be summarized in a set of optimum site-management practices and practical guidelines, which include policy and technical considerations.

BACKGROUND

The concern for the potential global change consequences of increasing atmospheric CO_2 has necessitated the development of mechanisms to reduce or stabilize atmospheric CO_2. During the next several decades, a program focused on terrestrial sequestration processes can make a significant contribution to abating the increase, and easing the transition to other renewable energy sources. Within this context, the restoration of degraded soils represents an opportunity to couple carbon sequestration with the utilization of fossil fuel and energy byproducts and other waste material (e.g., industrial sludges, municipal biosolids, mulch) while achieving ecological and aesthetic benefits for society in improved soil quality, biodiversity, and ecosystem services.

The goal of this project is to study the use of fossil fuel byproducts to foster carbon sequestration in degraded lands. This has the triple benefits of carbon storage, byproduct utilization and land reclamation. This research will be conducted in conjunction with the DOE Center for Research on Enhancing Carbon Sequestration in Terrestrial Ecosystems (CSiTE), which will allow DOE to leverage existing CSiTE activities by expanding its research and partnerships to degraded lands and the use of fossil energy byproducts to stimulate carbon sequestration in those terrestrial ecosystems.

The potential of energy byproducts such as fly ash as soil amendments to enhance C sequestration in degraded lands can be most fully realized if these inorganic byproducts are applied in conjunction with organic amendments, including both mulch from biomass productivity, as well as process waste materials such as biosolids, and pulp and sludge from paper production. These organic amendments can have beneficial effects that complement and extend those of the inorganic fly ash material, including:

- Improving soil structure and moisture retention capacity of soil
- Releasing nutrient elements within the organic structure, adding pH buffering capacity, and acting as a metal-ion buffer in soil to make micronutrients available to plants.
- Stabilizing toxic metals in soil, thereby reducing their migration to groundwater and reducing their uptake and toxic effects in plants.

GOALS AND TECHNICAL APPROACH

The **goals of this project** encompass both scientific and technology transfer components:

Scientific Goal: Identify optimal selection and delivery strategies to maximize the contribution of amendments to carbon sequestration.

Technology Transfer Goal: Foster interactions between the scientific and user communities to maximize the application of new knowledge and approaches for enhancing terrestrial C sequestration through optimal utilization of fossil energy byproducts and management of degraded lands.

Our **research strategy** to achieve the Scientific Goal of optimizing C sequestration has three parts.

1. *Evaluate Existing Experimental Sites:* Because of the diversity and extent of previous amendment studies and the long times needed to determine success or failure from a C-sequestration perspective, we are evaluating a number of existing sites where fly ash and biosolids amendments have already been applied. These experimental sites were selected to represent different levels of amendments, different types of fly ash (alkaline and acid), and different ages since treatment. Data obtained from these experimental manipulations includes parameters such as the depth distribution and amounts and types of organic and inorganic C present, emission of greenhouse gases, and changes in nitrogen cycling microbial communities. This new information is being correlated with amendment treatment parameters and other soil properties to identify the most favorable (and detrimental) combinations of soils, fossil-fuel combustion byproducts, and management practices
2. *Conduct Laboratory Experiments to Identify Key Amendment Types and Potential Management Strategies:* A set of laboratory experiments to assess the relative impacts of different environmental conditions such as wetting and drying cycles, oxidizing and reducing conditions, and specific amendments that enhance the accumulation of C by soils are being conducted at PNNL. In addition, we are examining the potential for release of other greenhouse gases because of the amendments in greenhouse scale studies. This work will focus on nitrous oxide emissions as a result of nitrogen input via the amendments. The results of these bench-scale experiments will guide the design of field-scale experiments and help ensure their success.
3. *Conduct Laboratory Experiments to Assess the Environmental Implications of Coal Combustion Byproducts and Biosolid Amendment Utilization:* A series of experiments designed to address public concern over the release of toxic metals from fly ash and biosolid amendments will be accomplished through laboratory column leaching procedures. Results taken from this simulated weathering or leaching will be examined using a standard biosensor-based measurement technique for toxicity testing of water and soil.

Our current efforts to achieve the *Technology Transfer* goal are focused on communication but the focus will be expanding to include policy studies

1. *Communication*: The Regional Partnerships in Terrestrial Carbon Sequestration Workshop conference was sponsored by the U.S. Department of Energy and National Energy Technology Laboratory (NETL) and The DOE Consortium for Research on Enhancing Carbon Sequestration in Terrestrial Ecosystems (CSiTE) in November, 2001 in Lexington, KY. Presentations from the meeting and summaries of the breakout sessions can be found at: http://www.netl.doe.gov/publications/ proceedings/01/carbon seq terr/cseq-terr01.html. Recent presentations include, “Evaluation of

Microbial Communities in Soil Using a Mixed Functional and Phylogenic Array," by A. V. Palumbo, Z. Yang, S. M. Tiquia, L. Wu, R. A. Hurt, J. R. Tarver, L. S. Fisher, C. C. Brandt, and J.-Z. Zhou; and "Carbon Accumulation and Microbial Community Structure in Reclaimed Mine Soils," by S. M. Pfiffner, A. V. Palumbo, J. R. Tarver, L. S. Fisher, J. Cantu, and C. C. Brandt at the AGU Fall Meeting on December 6–10, 2002. "Development of Measurement Techniques for Carbon and Microbial Communities in Mine Soils," by A. V. Palumbo, M. Martin, Z. Yang, J. Tarver, S. Fisher, and S. Wullschleger was presented at the USDA Carbon Symposium on Natural Resource Management to Offset Greenhouse Gas Emissions in November, 2002. In addition, we plan on presenting the following presentations in 2003: "Issues with the Use of Fly Ash for Carbon Sequestration," by A. V. Palumbo, L. S. Fisher, J. R. Tarver, W. L. Daniels, Z. Yang, S. M. Tiquia, L. Wu, J.-Z. Zhou, and J. Amonette; and "Fly Ash Amendments Catalyze Soil Carbon Sequestration," by J. E. Amonette, J.-B. Kim, C. K. Russell, A. V. Palumbo, and W. L. Daniels at the 2nd Annual Conference on Carbon Sequestration sponsored by the Department of Energy and the National Energy Technology Laboratory (NETL) to be held May, 2003; "Microbial Communities, Carbon, and Nitrogen in Mine Soils Reclaimed with Fly Ash and Biosolid Amendments," by A. V. Palumbo, L. S. Fisher, J. R. Tarver, W. L. Daniels, Z. Yang, S. M. Tiquia, L. Wu, J.-Z. Zhou, and J. Amonette at the 2003 Annual ASM meeting on May 18–22; "Metals in Leachates of Soil, Biosolids, and Fly Ash," by A. V. Palumbo, L. S. Fisher, J. R. Tarver, J. E. Amonette, and W. L. Daniels, and "Enhancement of Soil Carbon Sequestration by Amendment with Fly Ash," by J. E. Amonette, J.-B. Kim, C. K. Russell, A. V. Palumbo, and W. L. Daniels at the 2003 Fly Ash Utilization Conference to be held October 20–23, 2003; and "Metal Leaching and Toxicity Measurements: Fly Ash Implications for Land Application," by S. Fisher, A. V. Palumbo, J. R. Tarver, J. E. Amonette, W. L. Daniels, and Y. Roh at the American Society of Agronomy Annual Meeting to be held on November 2–6, 2003. In addition, we have papers published (Martin et al. 2003), in press, and submitted.

2 *Policy Studies:* The potential effectiveness and efficacy of combining carbon sequestration and mine land reclamation has yet to be assessed from ecological, economic, social, and institutional perspectives. This approach seeks to undertake a portion of this assessment, by focusing on economic, social, and institutional issues that must be addressed for the technical information to be effectively applied. We envision a three-fold approach: (a) assessing the current situation in light of existing regulations and the values, goals, and positions taken by parties typically engaged in mine reclamation policy and decision making; (b) developing realistic scenarios to analyze the potential for carbon sequestration on reclaimed land; and (c) proposing realistic mechanisms for promoting carbon

sequestration on reclaimed land in ways that are likely to comply with regulations and have the potential to be acceptable (or, not highly objectionable) to involved constituency groups.

TECHNICAL PROGRESS

SOIL CARBON IN RECLAIMED MINE SOILS

Samples were taken from sites in the eastern United States, including West Virginia and Virginia (Lee Daniels) and from sites in the Midwest including several sites in Ohio (Rattan Lal). Samples were analyzed at Va. Tech, Ohio State, and ORNL. Results from this series of experiments were presented in the Fossil Energy 2001 Annual Report. In summary, mine soil C levels in samples taken from the Powell River Biosolids Project (PRS) PL experimental plots did not show a long-term effect of biosolid treatment on C levels in the surface soils (A horizon); however, deeper soil layers (AC horizon) do appear to be higher in organic C. While soil organic matter levels in the Controlled Placement mine soils showed a clear effect of the 1982 treatment, applications of biosolids and sawdust did not appear to differ in soil C levels from the untreated controls. Fly ash treatment also appeared to consistently increase soil C in the reclaimed mine soils.

MICROBIAL ANALYSIS

We examined the carbon content of reclaimed mine soils treated with soil amendments (e.g., fly ash and biosolids) for measures of soil diversity using terminal restriction fragment length polymorphism (TRFLP) and phospholipid fatty acid (PLFA) lipid biomarkers. We examined the diversity among fungal communities under various aspects of carbon content using TRFLP. TRFLP was run on 18S rDNA from polymerase chain reaction (PCR) amplification using primers specific for fungi. Results from the TRFLP (presented in last Annual Report) were compared to sequencing of 18S clones. Cloning and sequencing indicated that, along with the few dominant populations, there was a surprising diversity of fungal clones. Rarefraction analysis of the data indicated that although total diversity of fungal clones was greater than we were able to measure with this level of effort (Fig. 1) it appeared that we were able to effectively sample the dominant populations.

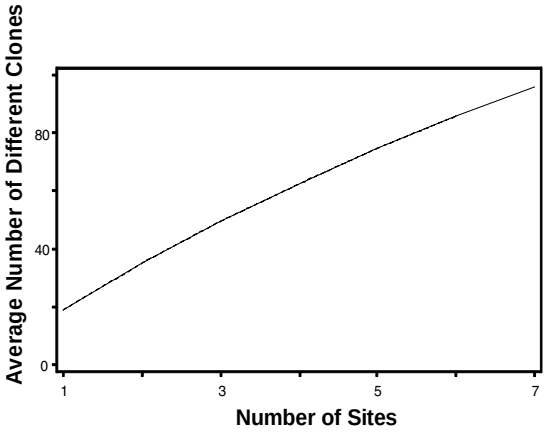

Fig. 1. Rarefraction analysis species area curve (including all sites).

The five most dominant populations (>50%) included *Mortierella verticillata*, a common acidophilous fungus in forest soils of temperate zones, *Sordaria fimicola*, a common coprophilous pyrnomycete found on fresh droppings of many herbivorous animals; *Mortierella chlamydospora*, generally found in agricultural fields and capable of decomposing chitin (Domsch et al. 1980); C*ryptococcus humicolus*, that has been isolated from acidic sandy soil supplied with benzene compounds and coke-plant wastewater (Middelhoven et al. 1992; Kwon et al. 2002); and *Cercophora septentrionalis*, which is often found on submerged wood (Domsch et al. 1980). The >50% pattern of sequences coming from only 5 clones is quite different from that observed in surface soils for bacteria where the most dominate populations account for just a few percent of the total (e.g., Zhou et al. 2002). However, Buchan et al. (2002) observed this dominance by a few cloned types for ascomycete fungi on Spartina alterniflora blades in a salt marsh.

Ordination techniques used to assess relationships among the sites in terms of fungal community structure revealed little consistency among samples from the same treatment (data not shown). One possible explanation is that, because cloning and sequencing techniques are of necessity done on only a small portion of the genetic material in the samples, the samples do not represent the community well. DNA microarrays could better assess the community (e.g., Wu et al. 2001) as these would assess 10^6 to 10^8 more genomes in each measurement than with cloning and sequencing. Thus, microarrays would sample a much larger portion of the population and could be applied to more sites.

We have used the clone data to design an array to be utilized on these sites. An array using many of the common species found in the clone libraries and a selection of relatively uncommon species was constructed and is being tested. The array also includes hundreds of sequences for bacterial functional genes. Thus, we hope to determine whether if the differences in carbon content related to the original treatments (e.g., fly ash and biosolids) are related to differences in the microbial community that can be assayed with this combined functional and phylogenetic array.

PLFA ANALYSIS

PLFA data indicated viable biomass for bacterial and fungal communities varied among amendment treatment, depth, and sites. The highest bacterial biomass was present in the Jenkins Farm A1 soil horizon containing the fly ash and sawdust amendment (Fig. 2). The total PLFA biomass ranged from 1.9 to 265 nmol/g, which corresponded to cell densities of 4.8×10^7 to 6.6×10^9 cells/g. It was also determined that biomass decreased with depth (A horizon: ≥120 noml/g, A2 horizon: 70–100 nmol/g, weak B horizon: 40–80 nmol/g).

Results from the principal component analysis (PCA) showed that low biomass samples (data from control S4 and mine soils) were influenced mostly by gram-positive-indicating PLFA biomarkers (Fig. 3).

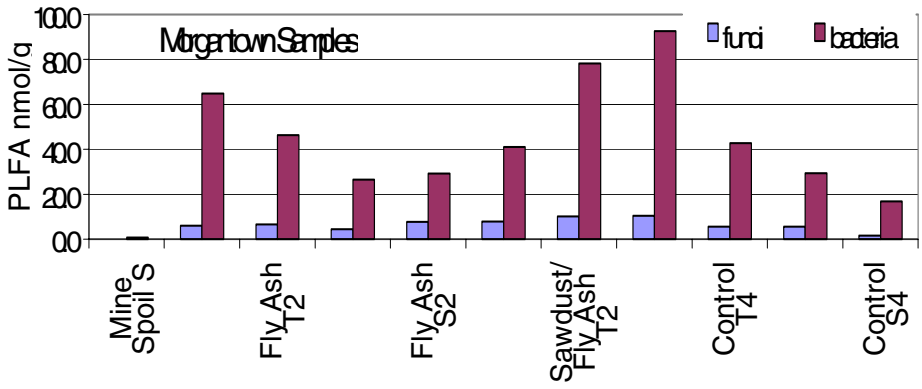

Fig. 2. PLFA biomass determined from surface mine spoils, fly ash treated plots (T2) Walls Farm 2 A1 horizon, (S2) Walls Farm 2 A1 horizon; sawdust and fly ash treated plots (T2) Jenkins Farm A1 horizon; and control sites (T4) Jenkins Farm A horizon and (S4) Jenkins Farm B horizon.

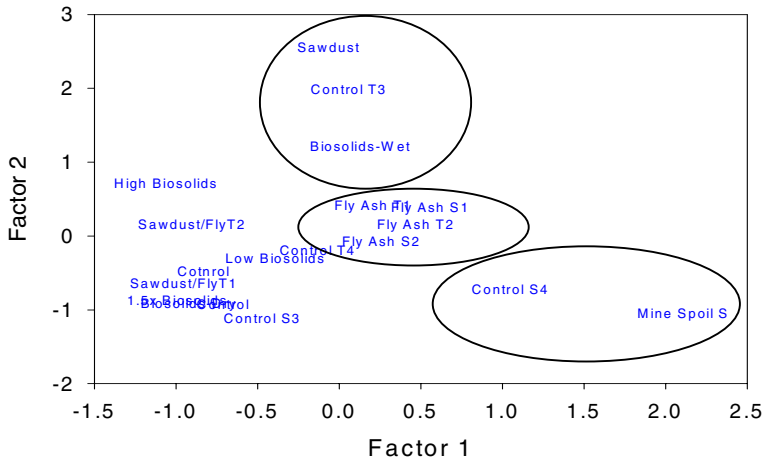

Fig. 3. Principle component analysis (PCA) performed using PLFA results from all treated plots.

Samples containing the highest amounts of carbon (fly ash treated T1, T2, S1, S2) were associated with PLFA biomarkers indicative of eukaryotes, especially those associated with plant residue (Fig. 3). These were determined to have been mostly samples taken from the plots amended with fly ash. PLFA generally indicative of gram-negative and eukaryotic microorganisms were found to influence samples collected from the plots amended with wet biosolid application and sawdust/fly ash material (Fig. 3).

FUNCTIONAL ANALYSIS

In addition to phylogenetic data, we are obtaining information about significant carbon cycling enzymes and metabolic processes. Twenty samples showed products using PCR amplification with

primers designed for lignase. We cloned the PCR products from 8 samples and have stared sequencing of the products. Additional genes will be targeted including those for tyrosinase (a fungal phenol oxidase) that is being used in other tasks on the project. Extracted DNA will also be hybridized in a microarray format to give information on the diversity and quantity of enzymes that are involved in aerobic metabolism, denitrification, iron reduction, sulfate reduction, and methanogenesis.

APPLICATION OF INNOVATIVE CARBON AND NITROGEN ANALYSIS METHODS

We have been testing the application of newer more rapid methods for carbon analysis to mine soils and have evaluated the use of laser-induced breakdown spectroscopy (LIBS) for determination of the total concentration of carbon and nitrogen in soils.

Our sampling generated a large range in soil carbon (less than 0.2 to approximately 8% in individual replicates) over which to generate and compare the LIBS technique to chemical oxidation and combustion methods (Walkley-Black and LECO). Soil carbon content measured by the LIBS technique exhibited a strong linear relationship for the previously mined soils when compared with the content measured by the LECO gas combustion technique (Fig. 4, insert) and the Walkley-Black method over the range of carbon up to approximately 6%. However, a sample at higher carbon (8.25%) did not fit the regression (Fig. 4, insert). Comparisons of the LECO technique and the Walkley-Black method appeared to have a nonlinear relationship at high amounts of carbon (Fig. 4). Apparently, there are discrepancies among the methods at high levels of carbon in soils.

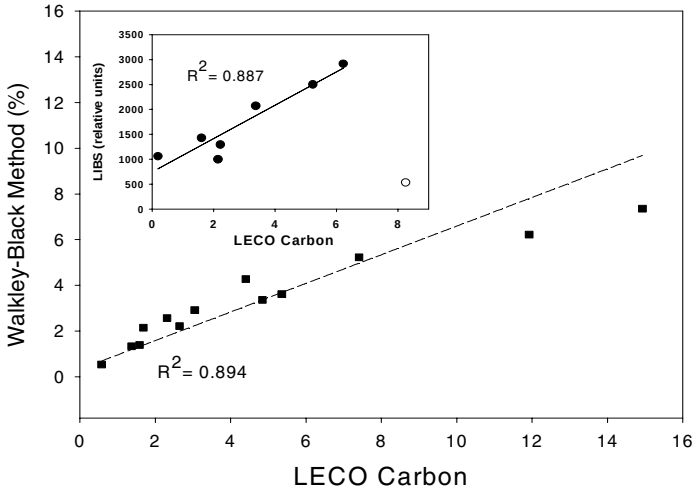

Fig. 4. Walkley-Black method compared to LECO gas combustion method for previously mined soils and LECO carbon calibration of LIBS data (insert). Discrepancies appear among the methods in these soils at above 6% carbon (as measured by LECO) where the LECO and Walkley-Black fit becomes non-linear (e.g., poor fit of regression at high carbon) and the LECO calibration fails (open circle on insert).

To achieve these results with the LIBS technique, it is advisable to make a large number of measurements. For example, although the range can be substantial, approaching 50% of the mean for some samples (e.g., Fig. 5), the standard error of the measurement is quite small (approximately 3%) when 20 measurements are made on a soil sample (Fig. 5). Thus, the major source of error is likely to be

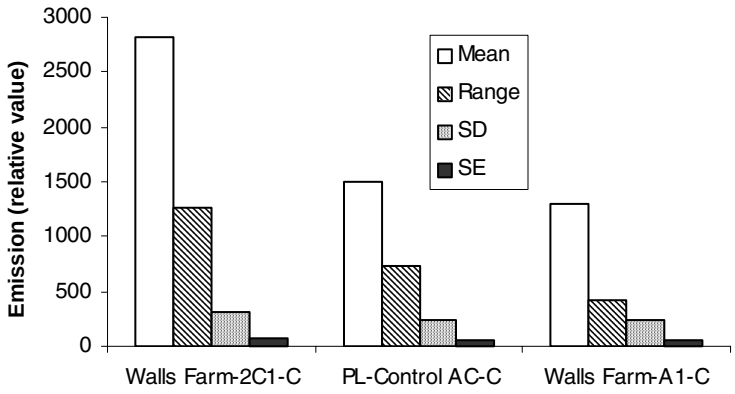

Fig. 5. LIBS measurements on twenty soil samples from previously mined soil.

sampling error, which must be addressed by taking multiple samples within a plot. A carbon assessment strategy should likely be based on application of the technique to a relatively large number of samples from a plot with a small number of subsamples (e.g., pellets).

POTENTIAL FOR LEACHING OF METALS

One significant concern in the utilization of coal combustion products is the potential for leaching of toxic metals from the fly ash. Our experiments were designed to examine the variability with regard to the source of the fly ash in leaching of metals under relatively mild extraction procedures that would be more relevant to environmental applications than standard EPA methods. We also designed experiments to determine if leaching of potentially toxic materials was influenced by mixing of the fly ash with soil and biosolids and if the biosolids could also be a concern for release of metals. We tested both type F and type C ash. Class F is produced from burning anthracite or bituminous coal and class C is produced from burning subbituminous coal and lignite. Class C also has cementitious properties and pozzolanic properties from the free lime (Stouraiti et al., 2002).

Both biosolids and fly ash appeared to contribute to leaching of some metals in the column leaching studies but for As and B only fly ash appeared to contribute to the leaching (Fig. 6). There were similar values in treatments receiving fly ash and biosolids for Mg, K, Ca, Fe, Ni, Cu, and Zn. The presence of elevated concentrations of these elements in the biosolid treatments that received fly ash indicated the contribution of the biosolids to the metals in the extracts. Elevated concentrations of Al and Na when fly ash was present with the biosolids clearly indicated the contribution of the fly ash to concentration of these elements in the effluent. As and B were found only in $CaCl_2$ extracts of samples treated with fly ash.

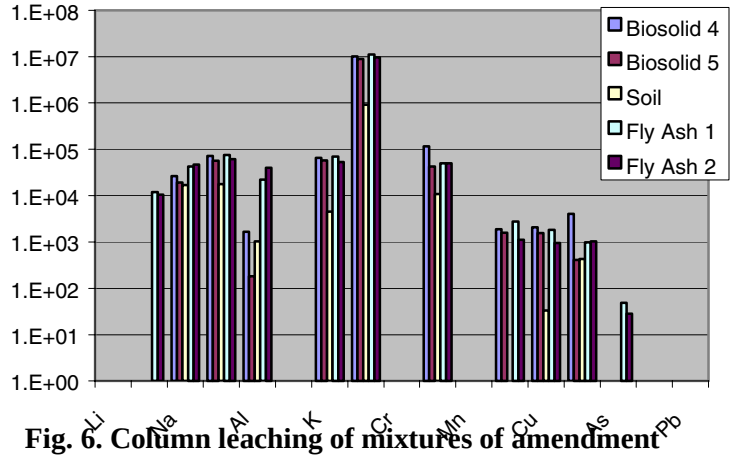

Fig. 6. Column leaching of mixtures of amendment materials. Ratios of fly ash/biosolids/soil are as follows: Biosolid 4 = 0/4/6; Biosolid 5 = 0/5/5; Soil = 0/0/10; Fly Ash 1 = 1/4/5; Fly Ash 2 = 2/3/5.

Differences in the presence and concentrations of the metals in the extracts between those from the column experiments (Fig. 6) and from the fly ash extractions (data not shown) may indicate the influence of the soil and biosolids in adsorption of specific elements. For example, Cr and Li were detectable in both hot water and acid extracts of the fly ash but was not detected in these experiments where the fly ash was combined with soil and biosolids. Although Si was detected in the hot water extracts of the fly ash it was not evident in the extracts from these experiments where the fly ash was combined with soil and biosolids. In addition, although Pb, and Cd were present in the acid extracts of the fly ash they also were not evident in the extracts from the columns with fly ash, soil, and biosolids.

Although potentially toxic metals can be leached from the fly ash using mild methods of leaching, for many of the most toxic elements leached the concentrations were very low. It was also evident from these studies that the TVA fly ash was considerably different that the western fly ash. The soil apparently reduced the leaching of several metals from the biosolids. Examination of combinations containing only soil and biosolids indicated that many of the metals detected in the analysis of the biosolids were not present in detectable amounts in the leachate of the column experiment. Although we detected As, Cr, and Cd in the biosolids none were detected in the column leaching experiment. Cu was detected in the biosolids and was leached at low levels from the biosolids treatments in the column experiments. Differences are likely due to the source of the coal, the post burning handling of the fly ash, or both. Leachates from TVA samples showed lower concentrations of some light elements and lower pHs.

Preliminary examinations of the data from measurements of toxicity using the Microtox system indicate the low levels of metals leaching do not result in detectable levels of toxicity. Experiments with a

variety of combinations of soils, fly ash, and biosolids give uniformly negative results for toxicity. Data analysis and experiments are continuing in this area.

LABORATORY ASSESSMENT OF POTENTIAL AMENDMENT TECHNOLOGIES

Research at PNNL seeks to understand the process by which organic-C is sequestered by soils (i.e., humification) and to develop practical approaches for enhancing the rate at which this sequestration occurs. Only a brief synopsis of that work is presented here. Experiments have focused on a model humification reaction involving a common phenoloxidase enzyme (tyrosinase) and organic monomers (polyphenols, hydroxybenzoic acids, and amino acids). A synergetic effect on the reaction rate when highly porous silica or manganese-oxide minerals are present in addition to the enzyme has been noted. As the porous silica bears some similarity to the cenospheres commonly found in fly ash, the effects of four alkaline fly ashes {Class C (sub-bituminous), Class F (bituminous), Class F [bituminous with flue-gas desulfurization (FGD) products], and Class F (lignitic)} on the reaction have been tested. The presence of FGD products completely halted the reaction, and the bituminous ash showed no benefit over an ash-free control. The sub-bituminous and lignitic fly ashes, however, increased the reaction rate by several-fold. In addition to their physical properties, the strong synergetic effect of these ashes may stem from their high Cu contents, as Cu activates tyrosinase, and from their alkaline pH.

REFERENCES

Buchan, A., S. Y. Newell, J. I. L. Moreta, and M. A. Moran. 2002. Analysis of internal transcribed spacer (ITS) regions of rRNA genes in fungal communities in a southeastern US salt marsh. *Microbial Ecology* 43:329–340.

Domsch, K. H., W. Gams, and T.-H. Anderson (eds). 1980. Compendium of Soil Fungi Volume 1. Academic Press, New York, NY.

Kwon, H. K., S. H. Woo, and J. M. Park. 2002. Degradation of tetracyanonickelate (II) by *Cryptococcus humicolus* MCN2. *FEMS Microbiology Letters* 214:211–216.

Martin, M. Z., S. D. Wullschleger, C. T. Garten, and A. V. Palumbo. 2003. Laser-induced breakdown spectroscopy for the environmental determination of total carbon and nitrogen in soils. Appl. Optics. 42:2072–2077.

Middelhoven, W. J., M. Koorevaar, and G. W. Schuur. 1992. Degradation of benzene compounds by yeasts in acidic soils. *Plant and Soil* 145:37–43.

Smit, E., P. Leeflang, B. Glandorf, J. D. Van Elsas, and K. Wernars. 1999. Analysis of Fungal Diversity in the Wheat Rhisosphere by Sequencing of Cloned PCR-amplified Genes Encoding 18SrRNA and Temperature Gradient Gel Electrophoresis. *Applied and Environmental Microbiology* 65:2614–2621.

Stouraiti, C., A. Xenidis, and I. Paspaliaris. 2002. Reduction of Pb, Zn, and Cd by the Application of Lignite Fly Ash. *Water, Air, and Soil Pollution* 137:247–265.

Wu, L., D. K. Thompson, G. Li, R. A. Hurt, J. M. Tiedje, and J. Zhou. 2001. Development and Evaluation of Functional Gene Arrays for Detection of Selected Genes in the Environment. *Applied and Environmental Microbiology* 67:5780–5790.

Zhou, J., B. Xia, D. S. Treves, L. Wu, T. L. Marsh, R. V. O'Neill, A. V. Palumbo, and J. M. Tiedje. 2002. Spatial and resource factors influencing high microbial diversity in soil. *Applied and Environmental Microbiology* 68:326–334.

BIOMINERALIZATION FOR CARBON SEQUESTRATION

T. J. Phelps, R. J. Lauf, and Y. Roh
Oak Ridge National Laboratory

INTRODUCTION

The purpose of this research is to develop an understanding of the mechanisms by which iron-reducing and carbonate-precipitating microorganisms sequester carbon dioxide into solid carbonate mineral phases and to use this knowledge to design biological processes to capture carbon dioxide from fossil fuel plants while stabilizing fly ash wastes. This research will develop a scenario by which fly ash is stabilized into carbonate solid conglomerates that could potentially be useful as fill materials or road construction aggregates. We envision an open system whereby ash collection ponds would be colonized with calcareous microorganisms capable of producing calcite, aragonite, and iron carbonates such as siderite. These carbonates would be formed in-situ, at depth by anaerobic carbonate producing bacteria. Results to date demonstrate that iron-reducing bacteria indeed convert CO_2 into sparingly soluble carbonate minerals such as calcite and siderite using metal containing fly ash and lime. Biological carbonate mineral formation using fly ash and lime materials indicated that bacteria may complement the capture of carbon dioxide from fossil fuel plants while potentially stabilizing fly ash wastes and bind the fly ash into solid materials. First, it would remove carbon from the atmosphere and immobilize it into a stable mineral phase. Second, it could turn waste ash into a useful product. Third, it could at the very least stabilize the ash to reduce the leaching of metals into the environment. Fourth, the process could be combined with a waste treatment strategy in which the carbonate forming microbes would use waste products from agriculture or food processing to supply energy for microbial growth. This would constitute energy plexing by combining multiple diverse waste streams into new products.

GOALS AND EXPERIMENTAL APPROACH

The objective of this research is to examine biogeochemically facilitated carbon sequestration processes using metal-rich fly ash in the presence of CO_2 atmosphere as well as in HCO_3^- buffered media. Biological conversion of CO_2 into sparingly soluble carbonate minerals such as calcite ($CaCO_3$) and siderite ($FeCO_3$) has been studied using Fe(III)-reducing bacteria in conjunction with metal containing fly ash and lime. This coal utilization research will develop a scenario by which fly ash is stabilized into carbonate solid conglomerates that could potentially be useful as fill materials or road construction aggregates.

Psychrotolerant (NV-1, W3-7-1), mesophlic (BrY), and thermophilic (TOR-39, C1) Fe(III)-reducing bacteria were used to examine biogeochemical processes such as dissolution and mineralization using fly ash in the presence of N_2, N_2-CO_2, and H_2-CO_2 headspace gases as well as in HCO_3^- buffered media (30–210 mM). In this study, we examined the microbial formation of carbonate minerals using thermophilic (*Thermoanaerobacter ethanolicus,* TOR-39), mesophilic (*Shewanella alga,* BrY), psychrotolerant (*Shewanella alga,* NV-1*; Shewanella pealeana,* W3-7-1), and alkaliphilic (CBS-011, *Alkaliphilus transvaalensis*) bacteria (Table 1).

Table 1. Microbial isolates chosen for current and ongoing investigations at ORNL

Organisms	Source	Incubation temperature	Electron donors used for growth
TOR-39	Subsurface sediments	45–75°C, Thermophile	Glucose, Lactate, Formate
C1	Subsurface sediments	45–75°C, Thermophile	Glucose, Lactate, Pyruvate, H_2, Formate
BrY	Estuary sediments	25°C, Mesophile	Lactate, H_2, Formate
W3-6-1	Oceanic sediments	0–37°C, Psychrotolerant	Lactate, H_2, Formate
NV-1	Sea water near hydrothermal vent	0–37°C, Psychrotolerant	Lactate, H_2, Formate
CBS-011	Boron-rich sites at the U.S. Borax mine in Borax, CA	High level of salt (~12% NaCl) and boric acid (2–8 g/L B) at pH 9–0, Alkaliphile	Lactate, H_2, Formate, Acetate

Table 2 shows the Fe- and Ca-rich fly ashes and lime chosen for biologically facilitated precipitation of carbonate minerals for carbon sequestration. These Fe- and Ca-rich fly ashes selected based on mineralogical and chemical characterization from several sources.

Table 2. Fly ash and lime currently investigated at ORNL

Material	pH	SiO_2	Al_2O_3	Fe_2O_3	CaO	MgO	Mineralogy
ORNL Steam Plant Ash Oak Ridge, TN	7.7	34.4	19.1	15.2	1.8	0.4	Mullite ($Al_6Si_3O_{15}$), Quartz (SiO_2)
TVA Bull Run Ash, Oak Ridge, TN	6.4	48.1	24.4	8.4	1.6	0.9	Mullite ($Al_6Si_3O_{15}$), Quartz (SiO_2)
TVA Johnsonville Ash Chattanooga, TN	8.4	44.9	20.9	24.7	2.5	1.1	Mullite ($Al_6Si_3O_{15}$), Maghemite (Fe_2O_3), Quartz (SiO_2)
Springerville Ash Joseph city, AZ	11.4	45.9	19.1	2.9	15.0	0.9	Mullite ($Al_6Si_3O_{15}$), Portlandite [$Ca(OH)_2$], Quartz (SiO_2)
ORNL Inhouse Lime	11.7	8.9	1.5	0.7	44.8	22.9	Calcite ($CaCO_3$), Quartz (SiO_2)

The Fe(III)-reducing bacteria (Table 1) and metal-rich fly ashes (Table 2) were used to examine microbially facilitated precipitation and mineral formation in the presence of N_2, N_2-CO_2 (80% N_2-20% CO_2), and H_2-CO_2 (80% H_2/20% CO_2) headspace and different bicarbonate buffer concentration (30–210 mM). Experiments were performed at 25°C for psychrotolerant cultures (W3-7-1, NV-1), the alkaliphilic culture (CBS-011) and for the mesophilic culture (BrY), and at 60–65°C for the thermophilic culture (TOR-39, C1).

TECHNICAL PROGRESS

The Fe(III)-reducing bacteria (Table 1) and metal-rich fly ash (Table 2) were used to quantify the increased microbially facilitated precipitation and mineral formation in the presence of N_2 and CO_2 (80% N_2-20% CO_2 and 80% H_2/20% CO_2) headspace and under the different bicarbonate buffer concentration (30–210 mM). Under all conditions examined in batch systems of 15 ml to 4 liters the presence of microorganisms dramatically increased carbon sequestration.

XRD analysis showed that the Fe(III)-reducing bacteria precipitated calcium carbonate and iron carbonate using metal-rich fly ash with a H_2-CO_2 atmosphere and using bicarbonate buffer (>120 mM). SEM with EDX spectra showed that calcium carbonate precipitated by bacteria using fly ash and lime. No carbonate minerals formed using fly ash and lime without bacteria. SEM and EDX analysis also showed that the Fe(III)-reducing bacteria facilitated the precipitation of calcite using Ca-rich Springerville fly ash (15% Ca) under a H_2/CO_2 atmosphere and a high bicarbonate buffer (210 mM). The Fe(III)-reducing bacteria facilitated calcite precipitation using Ca-rich fly ash or Ca-poor fly ash plus lime under a H_2-CO_2 atmosphere and a high bicarbonate buffer (210 mM):

$$Ca(OH)_2(cr) => Ca(OH)_2(aq) + CO_2(aq) => CaCO_3(cr) + H_2O$$

XRD analysis showed that increased bicarbonate buffer (210 mM HCO_3^-) facilitated biomineralization of siderite using Fe-rich Johnsonville fly ash (25% Fe_2O_3) and ORNL steam plant ash (15% Fe_2O_3) under a N_2 atmosphere at 65°C. SEM with EDX spectra showed that microbially-facilitated precipitation of iron carbonate with the Fe-rich fly ashes under a H_2-CO_2 atmosphere. In environments with high bicarbonate concentrations, the microbial production of Fe(II) from Fe-rich fly ash may stimulate siderite formation:

$$Fe^{2+} + HCO_3^- => FeCO_3 + H^+$$

This study indicates that siderite and calcite precipitation using metal-rich fly ash lime is generally associated with the bacterial metabolism of organic matter and hydrogen coupled with microbial Fe(III) reduction in the presence of reducing environments and high bicarbonate buffer or a H_2/CO_2 atmosphere.

High alkalinity and Fe(II) ions, as prompted by bacterial activity, seem important to biologically facilitated precipitation of carbonate minerals such as calcite and siderite. The microbial production of Fe(II) and lowered redox potential (Eh) also stimulates siderite precipitation.

The atmosphere and bicarbonate buffer concentration in conjunction with biomineralization processes exhibited profound influences on the types of minerals and the rate of carbonate mineral precipitation. Total carbon analysis of Ca-rich fly ash used for carbon sequestration showed that total carbon content in fly ash directly correlated with pCO_2 and $NaHCO_3$ concentration. The capacity of Fe(III)-reducing bacteria to precipitate carbonate minerals such as calcite and siderite using metal-rich fly ash creates the possibility of more effective CO_2 sequestration than would be possible with photosynthetic systems in alkaline ponds. In addition to microbially facilitated precipitation of carbonate minerals using fly ash, the microbial utilization of organic matter and hydrogen to produce sparingly soluble carbonate minerals may also contribute to direct or indirect precipitation of redox sensitive metals in fly ash ponds.

Scale-up experiments (up to 4-L scale experiment) using thermophilic metal-reducing bacteria have proved successful at sequestering carbon while using Ca and Fe-rich fly ash (Fig. 1). Biomineralization processes for carbon sequestration dramatically reduced water-soluble metals such as iron, calcium, and other metals under blankets of carbon dioxide. These upscaled experiments show potential for dramatic improvements of carbon and metal sequestration by complementing existing fly ash handling with biomineralization processes.

Fig. 1. Scale-up carbon sequestration experiment using Ca-rich fly ash and Fe(III)-reducing bacteria (TOR-35) at 60°C.

The capacity of iron-reducing bacteria to precipitate carbonate and metal containing minerals using fly ash creates the possibility of more effective CO_2 and metal sequestration than would be possible with photosynthetic systems in alkaline ponds and far greater than current technologies. In environments with high bicarbonate concentrations, the microbial production of Fe(II) from Fe-rich fly ash may stimulate siderite formation. Ca-rich fly ash or lime facilitated the calcium carbonate crystallization by the organisms altering local Eh, pH, and nucleation conditions. Biological carbonate mineral formation using

fly ash and lime materials indicated that bacteria may complement the capture of carbon dioxide from fossil fuel plants while potentially stabilizing fly ash wastes and solving red water problem in leachate from fly ash ponds. Interestingly, the results also suggest that many fly ash streams are less than saturated with respect to carbon dioxide. While biologically facilitated mineralization resulted in dramatic impacts, a significant portion of the total sequestration (30–60%) could be accomplished by saturating the fly ash waters with carbon dioxide. Future efforts will include discussions for the potential utility of engineered upscaling of both biotic and abiotic mechanisms of increased carbon and metal sequestration in fly ash streams.

Solution chemistry data showed pH decreased from 8.0 to 6.5 and Eh decreased from ~40 mV to –550 mV during the growth of the Fe(III)-reducing bacteria. Microbial processes with lactate and fly ash under a higher bicarbonate buffer (140–210 mM) resulted in lower Eh values than microbial process with a lower bicarbonate buffer (30–70 mM) (Fig. 2), suggesting greater microbial reduction of Fe(III) in association with the increased bicarbonate buffering capacity. Similarly, the microbial utilization of hydrogen under a H_2-CO_2 atmosphere resulted in significantly lower Eh values (< –450 mV) than lactate utilization under a N_2 (~200 mV) and a N_2-CO_2 (~300 mV) atmosphere, suggesting greater microbial reduction of Fe(III) in association with H_2 oxidation. The observation of microbial siderite and calcite formation using metal-rich fly ash in a higher bicarbonate buffer (210 mM) and under a H_2-CO_2 atmosphere was consistent with the Eh measurement. The presence of a H_2-CO_2 atmosphere and the high bicarbonate buffer (210 mM) provided more reducing conditions and significant buffering capacity allowing the complete reduction of Fe(III) in metal-rich fly ash than did the N_2/N_2-CO_2 atmosphere and low bicarbonate buffer

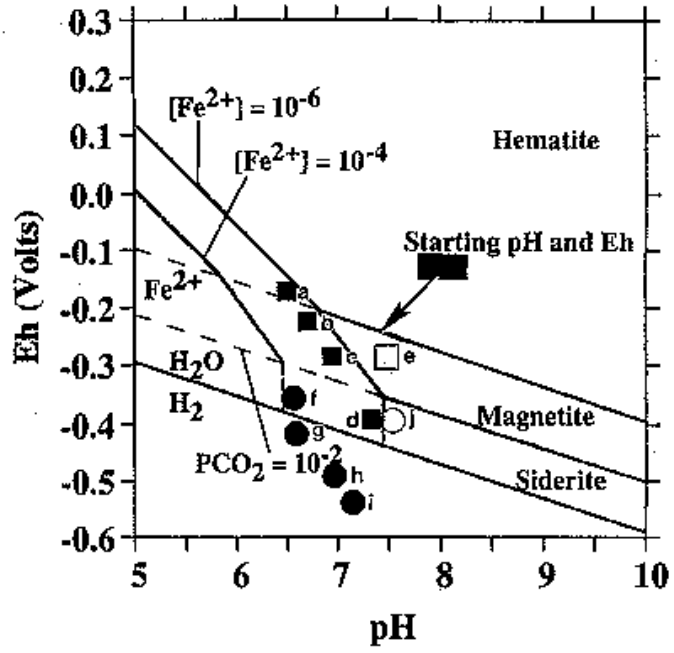

Fig. 2. Eh-pH stability fields for hematite, magnetite, and siderite in the water-iron-CO_2 system at 25°C and 1 atm total pressure (modified from Zhang et al., 1997). (a) 30 mM HCO_3^-, TOR-39; (b) 70 mM HCO_3^-, TOR-39; (c) 140 mM HCO_3^-, TOR-39; (d) 210 mM HCO_3^-, TOR-39; (e) control; (f) 30 mM HCO_3^-,C1; (g) 70 mM HCO_3^-,C1; (h) 140 mM HCO_3, C1; (i) 210 mM HCO_3^-, C1; (j) control.

(30–140 mM). Thus, the Eh-pH diagram shows that carbonate minerals including calcite and siderite precipitation is likely facilitated by the microbial alternation of Eh conditions, pH conditions, or both and creating conditions of potentially localized supersaturation with respect to a mineral phase.

Chemical analysis of water-soluble metals in the culture media after incubation revealed that the leaching of Li, Si, K, Ca, Fe, Ti, Co, Se, Br, Rb, Sr, Mo, Ba, Cd, and Cs from fly ash was significantly reduced in the presence of a CO_2 atmosphere (Fig. 3) and in HCO_3^- buffered media (>140 mM) (data not shown). This effect was likely a consequence of microbial metal reduction and the precipitation of carbonate minerals in the presence of appropriate electron donors such as hydrogen, lactate, and glucose. Water-soluble metals were expected sequestered into carbonate mineral during the mineralization of carbonate minerals.

APPLICATION

The capacity of iron-reducing bacteria to precipitate carbonate and metal containing minerals using fly ash creates the possibility of more effective CO_2 and metal sequestration than would be possible with photosynthetic systems in alkaline ponds and far greater than current technologies.

In environments with high bicarbonate concentrations, the microbial production of Fe(II) from Fe-rich fly ash may stimulate siderite formation. Ca-rich fly ash or lime facilitated the calcium carbonate crystallization by the organisms altering local Eh, pH, and nucleation conditions. Biological carbonate mineral formation using fly ash and lime materials indicated that bacteria may complement the capture of carbon dioxide from fossil fuel plants while potentially stabilizing fly ash wastes and solving red water problem in leachate from fly ash ponds. Interestingly, the results also suggest that many fly ash streams are less than saturated with respect to carbon dioxide. While biologically facilitated mineralization resulted in dramatic impacts, a significant portion of the total sequestration (30–60%) could be accomplished by saturating the fly ash waters with carbon dioxide. Future efforts will include discussions with TVA and the Paradise plant as to the potential utility of engineered upscaling of both biotic and abiotic mechanisms of increased carbon and metal sequestration in fly ash streams.

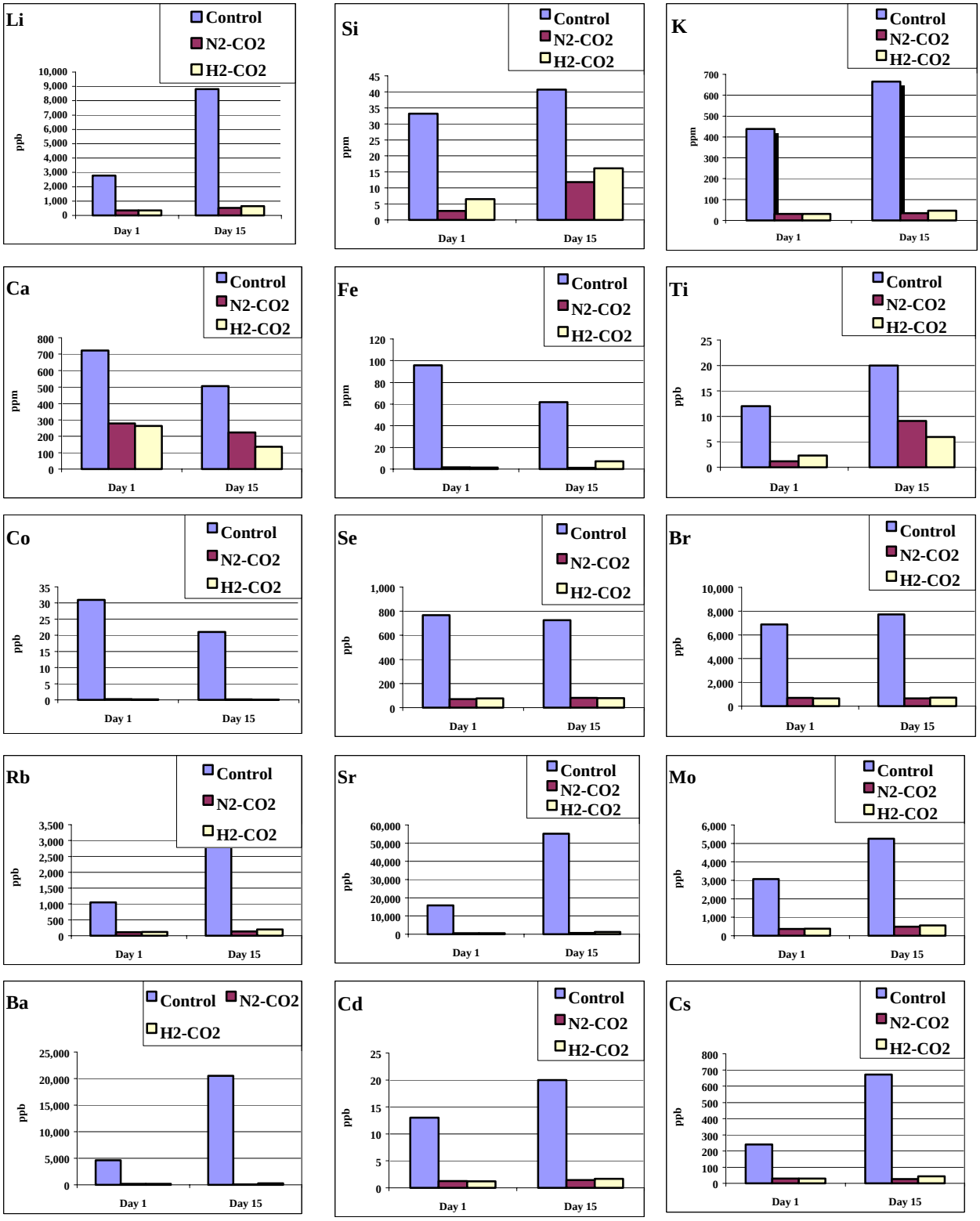

Fig. 3. Water soluble metals after Ca-rich Springerville fly ash used for carbon sequestration (20% CO_2).

PUBLICATIONS

Zhang C., J. Horita, D. R. Cole, J. Zhou, D. R. Lovley, and T. J. Phelps. 2001. Temperature-dependent oxygen and carbon isotope fractionations of biogenic siderite . Geochim. Cosmochim. Acta. 65:2257–2271.

Roh, Y., T. J. Phelps, A. D. McMillan, C. Zhang, C. J. Rawn, R. J. Lauf, and J. Bai. 2001. Microbial Synthesis and the Characterization of Metal-Substituted Magnetites. Solid State Communications. 110:529–534.

Roh, Y., T. J. Phelps, A. D. McMillan, and R. J. Lauf. 2001. Utilization of Biomineralization Processes with Fly Ash for Carbon Sequestration. 1st Nat. Conference on Carbon Sequestration. http//www.netl.doe.gov/events/01conferences/carbseq/carbseq01.html.

Zhou, J. Z., S. Liu, B. C. Xia, C. L. Zhang, A. V. Palumbo, and T. J. Phelps. 2001. Molecular characterization of thermophilic iron reducing enrichment cultures from deep subsurface environments. J. Appl. Microbiol. 90:96–105.

Hazen, T., and T. J. Phelps. 2002. Reducing Boron toxicity by microbial sequestration. DOE's Journal of Undergraduate Research. Vol II:40–47.

Roh, Y., S. Liu, G. Li, H. Huang, T. J. Phelps, and J. Zhou. 2002. Isolation and characterization of metal-reducing *Thermoanaerobacter* strains from deep subsurface environments. Applied and Environmental Microbiology. 68(12):6013–6020.

Roh, Y., C.-L. Zhang, H. Vali, R. J. Lauf, J. Zhou, and T. J. Phelps. 2003. Biogeochemical and environmental factors on iron biomineralization: magnetite and siderite formation. Clays and Clay Minerals. 51(1): 83–95.

Roh, Y., R. D. Stapleton, C. Zhang, A. V. Palumbo, T. J. Phelps, M. Fields, J. Zhou. 2003. Iron Reduction by Extremophiles: Geochemical and biotechnological implications. Book Chapter for: The Biogeochemicatry of Iron Cycling in the Environments. J. D. Coates and C. Zhang eds. Kluwer Academic Press (In Press).

Romanek, C. S., C. Zhang, Y. Li, J. Horita, H. Vali, D. Cole, and T. J. Phelps. 2003. Effects of reaction pathways on fractionation of carbon and hydrogen isotopes by dissimilatory Fe(III)-reducing bacteria. Chem. Geol. (In Press).

Phelps, T. J., Y. Roh, and R. J. Lauf. 2003. Biogeochemical processes utilizing fly ash for carbon sequestration. 2nd National Conference on Carbon Sequestration.

Roh, Y., and T. J. Phelps. 200_. Microbial Formation of Fe Minerals and Metal-Substituted Magnetite Nanoparticles by Iron Reducing Bacteria. In preparation for Geochemical Transactions. (Invited for Paper Preparation).

Roh, Y., R. D. Stapleton, H. Vali, T. J. Phelps, and J. Zhou. 200_. Anaerobic Fe(III) reduction with concomitant magnetite/siderite formation by psychrotrophic Fe(III)-reducing bacteria. In Preparation for Geochimica et Cosmochimica Acta. (Invited for Paper Preparation).

Roh, Y., Q. Ye, J. Zhou, C. Zhang, T. J. Phelps, and M.W. Fields. 200_. Metal reduction and mineral formation by an alkaliphilic Fe(III)-reducing bacterium isolated from an alkaline leachate pond. In Preparation for Geochimica et Cosmochimica Acta. (Invited for Paper Preparation).

ABSTRACTED PRESENTATIONS

Roh, Y., C. Zhang, R. J. Lauf, C. J. Rawn, S. M. Pfiffner, A. V. Palumbo, and T. J. Phelps. 2003. Microbially Mediated Synthesis of Metal-Substituted Magnetic Nanoparticles. ASM Conference on Bio-, Micro-, and Nanosystems. In collaboration with the Engineering in Medicine and Biology Society (IEEE-EMBS). July 7–10, 2003, New York, New York.

Roh, Y., S. Lee, I. Lee, and T. J. Phelps. 2003. The Influence of Manganese Ion on Iron Biomineralization by *Shewanella Alga* at 25°C and *Thermoanaerobacter ethanolicus at* 60°C. A Joint Meeting of Clay Mineral Society and Mineralogical Society of America. June 7–12, 2003. Athens, GA.

Roh, Y., R. J. Lauf, and T. J. Phelps. 2003. Biogeochemical Processes Utilizing Fly Ash for Carbon Sequestration. 2nd Annual Conference on Carbon Sequestration. May 5–8, 2003. Alexandria, Virginia.

Roh, Y., and T. J. Phelps. 2003. Microbial Formation of Fe Minerals and Metal-Substituted Magnetite Nanoparticles by Iron Reducing Bacteria. The Impact of Nanoparticle Growth and Transformation Processes on Contaminant Geochemical Cycling Sponsored by the Division of Geochemistry. 225th ACS National Meeting, March 23–27, New Orleans, LA.

Roh, Y., H. Vali, R. D. Stapleton, M. W. Fields, T. J. Phelps, and J. Zhou. 2002. Metal reduction and mineral formation by a psychrotolerant Fe(III)-reducing bacterium isolated from iron-rich waters near a hydrothermal vent. American Geophysical Union Meeting, December 6–10, 2002, San Francisco, CA.

Ye, Q., Y. Roh, J. Zhou, C. Zhang, T. J. Phelps, and M.W. Fields. 2002. Metal reduction and mineral formation by an alkaliphilic Fe(III)-reducing bacterium isolated from an alkaline leachate pond. American Geophysical Union Meeting, December 6–10, 2002, San Francisco, CA.

Roh, Y., R. J. Lauf, and T. J. Phelps. Utilization of Biomineralization Processes for Carbon Sequestration. Oak Ridge National Laboratory. Environmental Sciences Division Carbon Management Seminar Series, October 2002, Oak Ridge, Tennessee.

Ye, Q., M. Fields, J. Zhou, Y. Roh, T. J. Phelps, and C. L. Zhang. 2002. Isolation of an alkaliphilic metal-reducing bacterium from a saline pond containing high concentration of boron. Goldschmidt Conference. August 18–23, 2002. Davos, Switzerland. Geochimica et Cosmochimica Acta. 66(15A): A861. Suppl.

Ye, Q., Y. Roh, T. J. Phelps, J. Zhou, C. Zhang, and M. W. Fields. 2002. Ferric iron-reducing bacterium from alkaline leachate ponds containing salt and boric acid. The American Society for Microbiology 102th General Meeting, May 19–23, Salt Lake City, Utah.

Hazen, T., Y. Roh, and T. J. Phelps. 2002. Reducing Boron toxicity by microbial sequestration. AAAS Annual Meeting, February 14–16, 2002. Boston, MS.

Hazen, T., Y. Roh, and T. J. Phelps. 2001. Reducing Boron toxicity by microbial sequestration. ERLUF and Community College Institute for Biotechnology, Environmental Sciences and Computing. August 8, 2001, Oak Ridge, TN.

Roh, Y., T. J. Phelps, A. D. McMillan, C. Zhang, C. J. Rawn, and R. J. Lauf,. 2001. Microbial synthesis of metal-substituted magnetite nanoparticles using thermophilic Fe(III)-reducing bacteria. 38th Annual Meeting of The Clay Minerals Society, June 16–20, 2001, Madison, Wisconsin.

Roh, Y., H. Vali, R. D. Stapleton, T. J. Phelps, and J. Zhou. 2001. Single-domain magnetite formation by a psychrotolerant iron-reducing bacterium. The American Society for Microbiology 101th General Meeting, May 20–May 24, 2001, Orlando, Florida.

Roh, Y., A. McMillan, R. Lauf, and T. Phelps. 2001. Utilization of biomineralization processes with fly ash for carbon sequestration. First National Conference on Carbon Sequestration, May 15–17, 2000, Washington DC.

Zhou. J., Y. Roh, R. Stapleton, G. Li, H. Huang, A. Palumbo, T. Phelps, C. Zhang, A. Murray, and J. Tiedje. 2000. Iron reduction by extremophiles. Annual meeting American Geophysical Union, December 15–19, San Francisco, California (Invited talk for a session entitled “ Iron Cycling in the Natural Environment: Biogeochemistry, Microbial Diversity, and Bioremediation” for the AGU 2000 Fall meeting).

Roh, Y., A. McMillan, R. Lauf, and T. Phelps. 2000. Utilization of biomineralization processes for carbon sequestration. Annual meeting of American Geophysical Union, December 15–19, San Francisco, California.

Phelps, T. J., and Y. Roh. 2000. Applied microbiology for the coal ash environment. Western Region Ash Group Fall Meeting. November 14, 2000, Denver, Colorado.

Roh, Y., T. J. Phelps, J. Zhou, and C. Zhang. 2000. Metal reduction and mineral formation by iron-reducing bacteria. Annual Meetings of the Soil Science Society of America, Nov. 5–9, 2000,

Minneapolis, Minnesota. (Invited talk for a symposium entitled “Microbes-Minerals Interactions in Soils” for the ASA-CSSA-SSSA annual meetings).

Roh, Y., G. Li, H. Huang, T. J. Phelps, and J. Zhou. 2000. Metal reduction and mineral formation by thermophilic Fe(III)-reducing bacteria from deep subsurface environments. The American Society for Microbiology 100th General Meeting, May 21–25, 2000, Los Angeles, California.

Roh, Y., R. D. Stapleton, C.-L. Zhang, A. V. Palumbo, J.-Z. Zhou, and T. J. Phelps. 1999. Chemical and mineralogical characterization of iron carbonate formed by psychrophilic, mesophilic, and thermophilic bacteria. The 4th International Symposium on Subsurface Microbiology, August 1999, Vail, Colorado.

PATENTS

Lauf, R. J., T. J. Phelps, C. Zhang, and Y. Roh. 2002. Mixed oxide nanoparticles and method of making. U.S. Patent No. 6,444,453.

Lauf, R. J., T. J. Phelps, C. Zhang, and Y. Roh. 2002. Mixed oxide nanoparticles and apparatus for making same: Continuation-In-Part of Application No. 10/174,184. Filed, June, 2002.

BIOGEOCHEMICAL REMEDIATION OF AMMONIA DISCHARGES FROM POWER PLANTS

T. J. Phelps, R. J. Lauf, and Y. Roh
Oak Ridge National Laboratory

INTRODUCTION

Electric utilities often use a process of Selective Catalytic Reduction to reduce NOx emissions by reacting the NOx with ammonia. There is inevitably a small amount of unreacted ammonia in the wastewater. It is necessary to eliminate this ammonia loading before it discharges into rivers at levels that might be toxic to fish. During warm weather, nitrifying bacteria indigenous to the ponds appear to adequately accomplish ammonia detoxification (analogous to the nitrifying bacteria that control ammonia levels in an aquarium). However, these indigenous bacteria become relatively inactive in cold weather, leading to an increase in the level of ammonia being released into waterways constituting a significant concern to power plant operators and regulators. It is well known that in both freshwater and marine aquaria, a healthy nitrogen cycle operates; otherwise, rising levels of ammonia (from the animal wastes) would kill the fish and adversely impact the aquatic ecosystem.

GOALS AND EXPERIMENTAL APPROACH

The purpose of this project is to develop processes to mitigate ammonia discharges from ash ponds and related aqueous streams associated with ammonia inputs from coal use. The ammonia issue arises from implementation of the Selective Catalytic Reduction (SCR) process that removes NOx and SOx from flue effluents. With the advent of SCR's an ammonia stream is used as the electron donor meaning that excess ammonia is then discharged to fly ash ponds at concentrations of several ppm. The need for this research is because power plant effluents of even 1 ppm can rapidly kill fish in streams. Our research is focusing on ammonia pollution streams at an ammonia test facility, FoSCR Pilot Ponds at Tennessee Valley Authority's Paradise Fossil Plant in Kentucky. This research is closely linked with TVA and their Paradise generation plant. After several meetings with TVA personnel, a shared literature review and a review of previous TVA data we embarked on a field endeavor to track ammonia during the testing of ammonia discharges at the Paradise plant. Fly ashes and water samples at different locations in the fly ash pond 1, 3, and 50 ft from the fly ash slurry inputs at Paradise Fossil Plant were obtained to characterize water chemistry, fly ash mineralogy, chemical speciation and mass balances of ammonia in waters and solids prior to ammonia additions and post ammonia additions. Bench-scale studies have also been performed to develop strategies of ammonia removal and carbon sequestration using fly ash collected from the two pilot ponds at Paradise fossil plant.

TECHNIICAL PROGRESS

In FY 2002 Lauf and Phelps participated in a sampling event at the Paradise plant, near Crystal City, KY. Samples were retrieved by TVA at test ponds (Fig. 1) and made available for ORNL testing. Current testing is for biogeochemical parameters, chemical speciation and mass balances of waters and solids prior to ammonia additions, post ammonia additions and basin samples at different locations in the flay ash pond 1, 3, and 50 ft from the fly ash slurry inputs.

Fig. 1. Aerial photograph showing fly ash ponds and test ponds at Paradise Power Plant.

RESULTS

Analytical methods of determining fixed ammonium in fly ash sediments was developed and examined to ascertain a mass balance of ammonia. This is imperative for an understanding of ammonia removal mechanisms in fly ash ponds and would greatly complement TVA efforts as they have yet to account for the ammonia.

Table 1 shows chemical analysis of NH_4-N in fly ash slurry and fly ash pond water. To quantify NH_4-N concentration in fly ash sediment, KCl (2M) was used to extract NH_4-N from fly ash slurry (10 mL extractant/1 g of fly ash). The extraction method described involves equilibrium extraction in which the fly ash samples were extracted with an accurately measured volume of extractant for a specified time. After filtration using Whatman no. 42 filter paper, enough NaOH was added to extract and to keep

Table 1. Geochemical analysis of HN_4, total N, total C and pH of fly ash slurry and fly ash pond water from Paradise fossil plant ponds

Sample	Fly Ash Slurry					Fly Ash Pond Water	
	Total C (%)	Total N (%)	KCl (2M) Extractable NH_4-N (ppb)	Hot water (90°C) Extractable NH_4-N (ppb)	HCl (1M) Extractable NH_4-N (ppb)	pH	NH_4-N (ppb)
Sediment FGD Unit 2 End of Sluice Pipe	1.52	BD*	**5,810**	**4,856**	**6,314**	7.6	**100**
Sediment Upstream of NH_4 injection	1.15	0.008	**3,630**	**4,163**	**6,441**	10.9	**632**
Sediment Pond 1 Ash Delta	0.49	BD	**3,180**	**6,317**	**5,809**	12.2	**2,440**
Sediment Pond 1 Bottom Sediment	2.06	0.013	**3,685**	**5,064**	**4,416**	11.9	**1,571**
Water Pond 1 Water Station A	ND[#]	ND	**ND**	**ND**	**ND**	8.9	**927**
Sediment Pond 2 Surface Sediment	0.46	BD	**3,480**	**4,945**	**5,845**	ND[#]	**3,278**
Sediment Pond 2 Dike	0.71	0.002	**4,563**	**3,892**	**7,354**	ND	**1,807**
Water Pond 2 Water Station A	ND	ND	**ND**	**ND**	**ND**	8.9	**1,340**

*BD, Below detection limit.
[#]ND, Not determined.

pH 11.5 to 12.0. Indophenol Blue Method (Bremner, 1996) was use to analyze NH_3-N in the extractant using infrared spectroscopy. The limitation of sensitivity is 0.1 ppm.

XRD analysis of fly ash sampled at various points in ponds showed that major minerals are quartz (SiO_2), mullite ($3Al_2O_3{\cdot}2SiO_2$), silicon (Si), magnetite (Fe_3O_4), hematite (Fe_2O_3), and gypsum ($CaSO_4{\cdot}2H_2O$) (Table 2).

Bench-scale studies have been performed to develop strategies for ammonia removal and carbon sequestration using fly ash collected from the two pilot ponds at Paradise fossil plant. Fly ash collected at two points (Pond 1 bottom sediment and Pond 2 dike) in ponds were reacted with CO_2 (pCO_2 = 100%) and with N_2 in the presence of NH_4 (~105 ppm), 1 g of fly ash slurry with reacted with 15 mL deionized water containing NH_4 (~105 ppm) in a closed system using 26 mL anaerobic tubes. The headspace volume was 10 mL. Figure 2 shows that ammonia was sequestered into the fly ash under N_2 and CO_2 headspace.

These experiments indicate that fly ash slurry from Paradise Steam Power plant has NH_4 sequestration capacity of 68–111 mg NH_4/kg (8.5 to 13.3 % of total NH4 in the system) ash slurry under N_2 atmosphere and 82–116 mg NH_4/kg (10 to 13.9 % NH_4 in the system) ash slurry under CO_2

Table 2. Mineralogical analysis of fly ash slurry sediments used for bench-scale carbon sequestration and ammonia removal study

Sample	Mineralogy	
	Fly Ash Slurry from Paradise Plant	**Fly Ash Slurry from Paradise Plant (After reacting with 120 mM $NaHCO_3$)**
Sediment FGD Unit 2 End of Sluice Pipe	Gypsum ($CaSO_4 \cdot 2H_2O$)	Calcite ($CaCO_3$), Bassanite ($CaSO_4 \bullet 0.5\ H_2O$)
Sediment Upstream of NH_4 injection	Quartz (SiO_2), Mullite ($3Al_2O_3 \cdot 2SiO_2$), Silicon (Si), Magnetite (Fe_3O_4), hematite (Fe_2O_3)	Quartz (SiO_2), Calcite ($CaCO_3$), Mullite ($3Al_2O_3 \cdot 2SiO_2$), Silicon (Si), Magnetite (Fe_3O_4), hematite (Fe_2O_3)
Sediment Pond 1 Ash Delta	Quartz (SiO_2), Mullite ($3Al_2O_3 \cdot 2SiO_2$), Silicon (Si), Magnetite (Fe_3O_4), hematite (Fe_2O_3)	Quartz (SiO_2), Calcite ($CaCO_3$), Mullite ($3Al_2O_3 \cdot 2SiO_2$), Silicon (Si), Magnetite (Fe_3O_4), hematite (Fe_2O_3)
Sediment Pond 1 Bottom Sediment	Quartz (SiO_2), Mullite ($3Al_2O_3 \cdot 2SiO_2$), Silicon (Si), Magnetite (Fe_3O_4), hematite (Fe_2O_3)	Quartz (SiO_2), Calcite ($CaCO_3$), Mullite ($3Al_2O_3 \cdot 2SiO_2$), Silicon (Si), Magnetite (Fe_3O_4), hematite (Fe_2O_3)
Sediment Pond 2 Surface Sediment	Quartz (SiO_2), Mullite ($3Al_2O_3 \cdot 2SiO_2$), Silicon (Si), Magnetite (Fe_3O_4), hematite (Fe_2O_3)	Quartz (SiO_2), Calcite ($CaCO_3$), Mullite ($3Al_2O_3 \cdot 2SiO_2$), Silicon (Si), Magnetite (Fe_3O_4), hematite (Fe_2O_3)
Sediment Pond 2 Dike	Quartz (SiO_2), Mullite ($3Al_2O_3 \cdot 2SiO_2$), Silicon (Si), Magnetite (Fe_3O_4), hematite (Fe_2O_3)	Quartz (SiO_2), Calcite ($CaCO_3$), Mullite ($3Al_2O_3 \cdot 2SiO_2$), Silicon (Si), Magnetite (Fe_3O_4), hematite (Fe_2O_3)

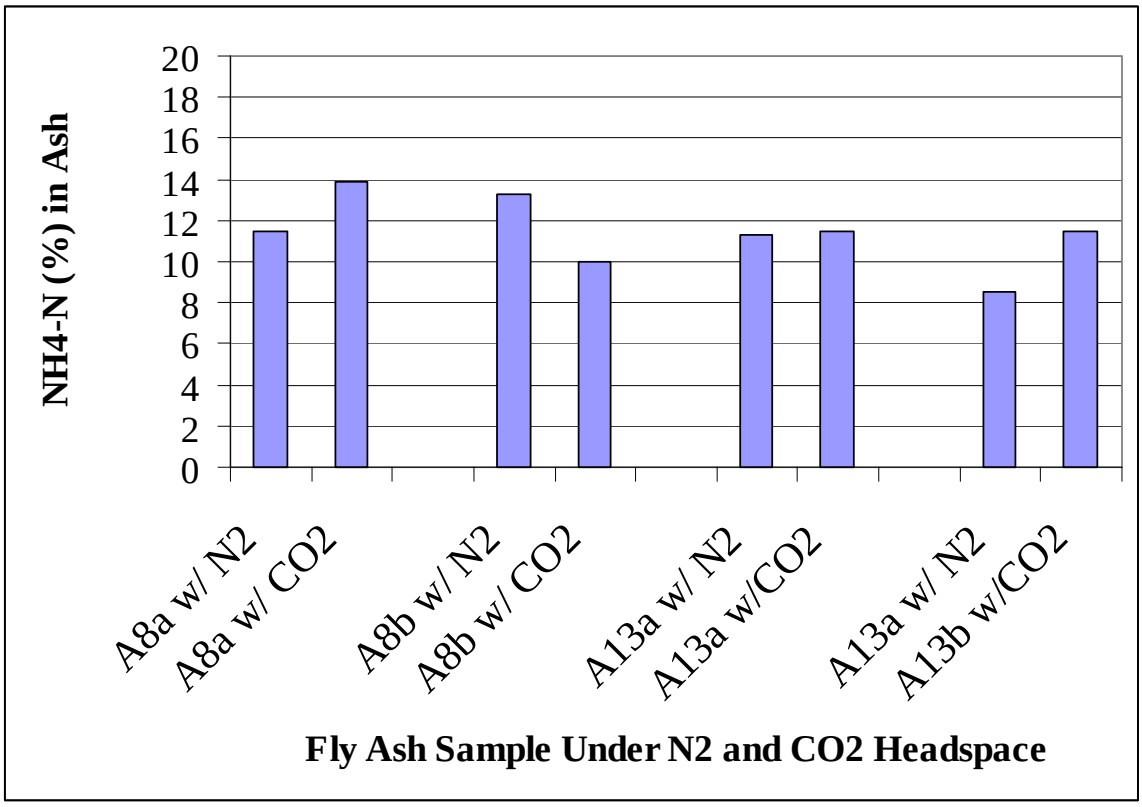

Fig. 2. Ammonia sequestered into fly ash sample obtained from Paradise plant under N_2 and CO_2 atmosphere.

atmosphere, likely sufficient to mitigate ammonia discharges from the ponds if that sequestration capacity were approached.

XRD analysis of ash sampled after reacting with CO_2 and NH_4 showed that increased pCO_2 (210 mM HCO_3^-) facilitated carbonate mineral (calcite, $CaCO_3$) formation (Table 3). Ammonia, to some extent, is also expected to be sequestered in carbonate minerals.

Table 3. Mineralogical analysis of fly ash slurry sediments used for bench-scale carbon sequestration and ammonia removal study

Sample	Mineralogy	
	Fly Ash Slurry from Paradise Plant	**Fly Ash Slurry from Paradise Plant (After reacting with 120 mM $NaHCO_3$)**
Sediment FGD Unit 2 End of Sluice Pipe	Gypsum ($CaSO_4 \cdot 2H_2O$)	**Calcite ($CaCO_3$)**, Bassanite ($CaSO_4 \bullet 0.5\ H_2O$)
Sediment Upstream of NH_4 injection	Quartz (SiO_2), Mullite ($3Al_2O_3 \cdot 2SiO_2$), Silicon (Si), Magnetite(Fe_3O_4), hematite(Fe_2O_3)	Quartz (SiO_2), **Calcite ($CaCO_3$)**, Mullite ($3Al_2O_3 \cdot 2SiO_2$), Silicon (Si), Magnetite(Fe_3O_4), hematite(Fe_2O_3)
Sediment Pond 1 Ash Delta	Quartz (SiO_2), Mullite ($3Al_2O_3 \cdot 2SiO_2$), Silicon (Si), Magnetite(Fe_3O_4), hematite(Fe_2O_3)	Quartz (SiO_2), **Calcite ($CaCO_3$)**, Mullite ($3Al_2O_3 \cdot 2SiO_2$), Silicon (Si), Magnetite(Fe_3O_4), hematite(Fe_2O_3)
Sediment Pond 1 Bottom	Quartz (SiO_2), Mullite ($3Al_2O_3 \cdot 2SiO_2$), Silicon (Si), Magnetite(Fe_3O_4), hematite(Fe_2O_3)	Quartz (SiO_2), **Calcite ($CaCO_3$)**, Mullite ($3Al_2O_3 \cdot 2SiO_2$), Silicon (Si), Magnetite(Fe_3O_4), hematite(Fe_2O_3)
Sediment Pond 2 Surface	Quartz (SiO_2), Mullite ($3Al_2O_3 \cdot 2SiO_2$), Silicon (Si), Magnetite(Fe_3O_4), hematite(Fe_2O_3)	Quartz (SiO_2), **Calcite ($CaCO_3$)**, Mullite ($3Al_2O_3 \cdot 2SiO_2$), Silicon (Si), Magnetite(Fe_3O_4), hematite(Fe_2O_3)
Sediment Pond 2 Dike	Quartz (SiO_2), Mullite ($3Al_2O_3 \cdot 2SiO_2$), Silicon (Si), Magnetite(Fe_3O_4), hematite(Fe_2O_3)	Quartz (SiO_2), **Calcite ($CaCO_3$)**, Mullite ($3Al_2O_3 \cdot 2SiO_2$), Silicon (Si), Magnetite(Fe_3O_4), hematite(Fe_2O_3)

IMPLICATIONS

Ammonia content of the pond water samples indicated that ammonia is likely being removed and/or (co)precipitated within feet and after minutes of entering the fly ash ponds. Effluents from the FGD sluice pipe are diluted ~1:6 with fly ash. Upstream of the ammonia and in the FGD effluent the ammonia concentration is far less than 1 ppm. After the 2 ppm ammonia injection both pond 1 and pond 2 waters exhibit 2–3 ppm ammonia. However, within feet of distance and minutes of travel time more than one half of the ammonia is lost within the system, likely bound in the sediments. By the time waters reached sampling station A in both ponds ~2/3 of the ammonia was lost within the system. Attempts to account for the ammonia in the sediments have not been sufficient to close a mass balance as the sediments represent less than a two percent slurry of solids. TVA data concurs that they are accounting for less than 25% of the ammonia in mass balances. While it is convenient to suggest that the lost ammonia is due to

biology, the fact that it occurred during cold climates within days of the restart of ammonia injection further heightens our speculation that ammonia is lost within the system. Chemical composition of the pond water and ash sediments indicated that Si, Al, Fe, Mg, Na, and other metals in the pond water are precipitated with fly ash sediments. The ammonia added to the pond water may be precipitated with these metals in the fly ash sediments.

FUTURE RESEARCH

Bench-scale studies are being performed to develop strategies of ammonia removal and carbon sequestration via biogeochemical processes using fly ash collected from the ponds at Paradise fossil plant. Analytical method for determining fixed ammonium in fly ash sediments is currently developing to ascertain a mass balance of ammonia. This would greatly complement TVA efforts as they have yet to account for the ammonia. Further bench-scale study may include biological components and/or may focus more on engineering aspects for enhanced geochemical removal/sequestration. Close collaborations with TVA will be important.

In collaborations with TVA we will pursue completing a mass balance for ammonia additions/losses from fly ash systems, far better than the current 20–50%. Importantly, we will scrutinize the impacts of ash, time, distance and flux of ammonia in the fly ash processing pond systems using closed headspace laboratory tests and relate to field studies.

ABSTRACTED PRESENTATION

Roh, Y., R. J. Lauf, and T. J. Phelps. “Utilization of Biomineralization Processes for Carbon Sequestration.” Oak Ridge National Laboratory. Environmental Sciences Division Carbon Management Seminar Series, October 2002, Oak Ridge, Tennessee.

HYDRATE FORMATION AND DISSOCIATION IN FIELD SAMPLES

T. J. Phelps and O. R. West
Oak Ridge National Laboratory

INTRODUCTION

The goal of this two-year research project is to characterize the thermodynamics and kinetics of natural gas hydrate formation and dissociation and biogeochemically characterize MH containing sediments. Characterization of samples from ODP Leg 204 and associated hydrated stability of drilling additives is the primary focus with minor efforts on analysis of coring from Mallik. Experiments are being conducted in the ORNL Seafloor Process Simulator at the ORNL hydrate research facility. Microbiological enrichments and time course characterizations are being conducted with properties correlated with hydrate thermodynamic and kinetic properties.

GOALS AND EXPERIMENTAL APPROACH

The goal of this project is to characterize the thermodynamics and kinetics of natural gas hydrate formation and dissociation and to biogeochemically characterize MH containing sediments. The approach will be to utilize the extraordinary potentials of the ORNL 70 liter SPS hydrate facility as well as smaller vessels to examine microbial, mineralogical, chemical and physical characteristics of host sediments. These characteristics will be correlated with hydrate thermodynamic and kinetic properties. Aspects of this work will be to characterize the ODP-Leg-204 cores as well as to develop an understanding of hydrate formation and stability in the sediments and a more applied aspect of this project is to examine hydrate nucleation and inhibition agents that are an ongoing concern to the safety of hydrate exploration. In that vein most of the second year effort in late FY 2003–2004 will examine hydrate formation and stability in sediment/drilling fluid/adjuvant mixtures to assess the ability of drilling fluid additives to enhance or inhibit hydrate nucleation in sedimentary environments.

TECHNICAL PROGRESS

Results from Mallik cores. Biological methane production from Mallik cores could not be detected even after more than three months of incubation under ambient conditions, enriched with acetate, hydrogen and or methanol. Despite analysis of more than 100 tubes, each containing 3–5 g of sediment from a time course study revealed considerable production of carbon dioxide from radiolabeled 14C-2-acetate but no radioactive methane (sensitivity of 200 dpm from 10,000,000 dpm of added 14CO2 or 14-acetate). Similarly, no increase in the methane concentrations within the headspace of test tubes were

detected (sensitivity of ~0.1%) during the >3 month time course experiment. Results corroborated those of R. Colwell (INEEL) and other investigators.

Analysis of cores from ODP. Successful core recovery, storing, shipping and handling procedures were developed and used for ODP Leg 204. Our on shore laboratories received at least 5 shipments of cored materials from the cruise, with most being received within days of recovery. Types of samples included ~20 small (<100 g) of samples frozen under liquid nitrogen that are currently stored at –80C, several kg of samples frozen samples stored at –20C, and several kg of fresh sediments used for time course activity and microbial enrichment experiments and some of which is stored at 4C. The first set of test samples were delayed a day in delivery and ship-board researchers quickly fixed the hurdles and subsequent shipments arrived in good time and in good quality. The Leg and the science were a huge success and we have had a very good response from DOE involvement in the cruise. Experiments are currently in progress. This constituted the successful accomplishment of the fall 2002 milestone.

Biological methane production from ODP Leg 202 cores past their final incubation point after more than three months with one set of incubations under ambient conditions, and two at near in situ temperatures of 4C. Some are enriched with acetate, hydrogen and or methanol. These tubes may be in stark contrast to those from Mallik where results revealed considerable production of carbon dioxide from radiolabeled 14C-2-acetate but no radioactive methane (sensitivity of 200 dpm from 10,000,000 dpm of added 14CO2 or 14-acetate). Similarly, no increase in the methane concentrations within the headspace of test tubes were detected (sensitivity of ~0.1%) during the >3 month time course experiment of the Mallik samples but considerable methane and radioactive methane are anticipated form the ODP cores. Results are being corroborated those of R. Colwell and M. Delwiche (INEEL) and other investigators. Now that Dr. Zatsepina is oriented to the ORNL laboratory system analyses of the samples will proceed promptly.

SPS hydrate formation results. A new procedure/method for enhancing the nucleation of hydrates that was recently discovered as part of this work was mentioned in the last quarterly report. After lengthy discussions with our intellectual property experts we determined that while the technology was indeed patentable in the classic sense of claims and exclusionary rights, it was impossible to detect its unauthorized utilization in its most sensitive mode. In other words, a simple ice machine could suffice for the enablement of the technology and no clear indication of its unauthorized use would be indicated. Instead of the patent disclosure we are advised and concur that we will share the technology with sponsors and through publications.

Nevertheless the discovery of cool water formerly present as ice, even if the cool waters are days removed from the frozen state leads to a 10–20-fold improvement in the amount of overpressure required for nucleation, from ~600 psi to ~30 psi. The new procedure was not expected from a review of the literature and the results were startling. In the range of 3–6C nucleation pressures greater than 1200 psi

are customary for nucleation to occur in the SPS. Similar to smaller vessels as noted in the literature there a significant memory effect is noted upon repeated formation of hydrates. If hydrates are dissociated and then reformed within hours a memory effect is observed and nucleation often occurs at far less overpressure. For example, in fresh water nucleation overpressures of ~600 psi are typical whereas if hydrates are formed again using the same water (even if there is a 24 hr lag time) the overpressure required to form hydrates is typically 200–300 psi. This memory effect represents a substantial energy savings from initial hydrate formation equilibria. Consequently any nucleation enhancer should lower the required overpressure far more than any observed memory effect. Our new process resulted in required overpressures of only 22 and 33 psi in two separate attempts with fresh water. This is nearly an order of magnitude better than nucleation enhancement of the well known memory effect. This phenomenal successful nucleation enhancement procedure may be more scalable and less expensive though at least as effective as our procedure documented previously that relied on chemical additives enhancing ice nucleation.

EFFECTS OF THAWED WATER, AGITATION, AND BUBBLES ON HYDRATE FORMATION

The formation of hydrates of gasses is an attractive process to several industries such as natural gas storage and transportation, as well as in separation technologies. The hydrated form of methane concentrates the gas approximately 160 times the concentration of gas phase methane per unit volume. An ability to concentrate fuels, therefore, makes an economic way to form hydrates an area of active research. Additionally, when water is taken up into the hydrate structure, dissolved ions are excluded, so hydrate formation is considered a possible desalinization technique. It has been published that the use of previously frozen water in experiments significantly lowers the hydrate nucleation overpressure (i.e., the amount of pressure above beyond the 3-phase equilibrium point necessary to form hydrate) (Vysniauskas et al., 1983; Takeya et al., 2000). In those experiments, however, the entire volume of water used in the experimental reactor was frozen and thawed. This method would be uneconomical for an industrial scale hydrate reactor. We have demonstrated experimentally that even if a relatively small amount of the reactor water was previously frozen, and if left in a cool thawed state for many hours, the overpressure required for hydrate formation is significantly lowered in the large volume SPS (Table 1). Additionally, our results demonstrated that the thawed water could be stored at room temperature (~25C) for 48 hours and the effect is preserved.

Nucleation experiments were performed by pressurizing the SPS reactor with the hydrate forming gas (in this case, methane), to a pressure below the hydrate equilibrium pressure and cooling the reactor to ~4–6C for several hours to saturate the water with gas. Gas is then injected into the water through a

Table 1. Methane Hydrate Nucleation Experiments With and Without the Use of Thawed Water

Description of experiment	Nucleation pressure (psi)	Nucleation temperature (°C)	Equilibrium pressure (psi)	Nucleation overpressure (psi)
1st nucleation no thawed water	1338	5.9	674	663
1st nucleation no thawed water	1195	4.5	584	610
2nd nucleation, no thawed water	951	5.3	631	320
2nd nucleation, no thawed water	740	3.9	552	188
1st nucleation, all thawed water	630	4.7	597	33
1st nucleation, 20% thawed water	557	4.0	555	22

diffuser and the gas bubbles rise through the water and terminate at the gas/water interface. The pressure relief valve on the vessel is closed during injection, so the vessel pressure increases at a rate of ~8 psi/min. Hydrate formation is detected visually by the presence of opaque hydrate-covered gas bubbles collecting and persisting at the gas-water interface. The pressure at which this occurs is called the nucleation pressure. For the experiments involving thawed water, the water was allowed to warm up to room temperature (~25C) after thawing for approximately 48 hours. In one experiment, all of the water in the vessel (~60 L) was frozen and thawed. In the other, approximately 20% of the water added to the vessel was previously frozen. In all of the 1st nucleation experiments, all of the water in the vessel was drained out to prevent any hydrate "memory effect." This memory effect is apparent by comparing the reduction in overpressure in the 2nd nucleation experiments (experiments where the water was not changed between hydrate nucleation experiments) with the 1st nucleation experiments.

Using the commercially available hydrate equilibrium program CSMHYD (Sloan, 1998), the equilibrium pressure can be calculated for the experimental temperature. The difference between the actual nucleation pressure and the equilibrium pressure is called the overpressure (Table 1). Several additives have been tested which also have been found to lower the hydrate nucleation overpressure, but none were found to be as effective as the use of thawed water. Example from our laboratory include the use of SNOMAX, a bacterially derived protein use commercially as a snow nucleator, as a possible hydrate nucleation promoter. It was found to lower the nucleation overpressure to an average of 182 ± 21 psi at concentrations of 20–30 mg/L. These results are similar to those found by Morgan et al. (1997). Bentonite, a clay mineral which is a common component of drilling muds was found to lower the overpressure to an average of 96 ± 11 psi at a concentration of 200 mg/L. While these additives do significantly lower the nucleation overpressure as compared to bulk water, neither are as effective or as economical as the use of recently thawed water.

Experiments are currently being conducted in a small pressure vessel (450-ml volume) to determine whether there is a volume dependent effect of the thawed water on nucleation (Fig. 1). Experiments are also being conducted on the effect of agitation and bubble formation on hydrate formation. Preliminary

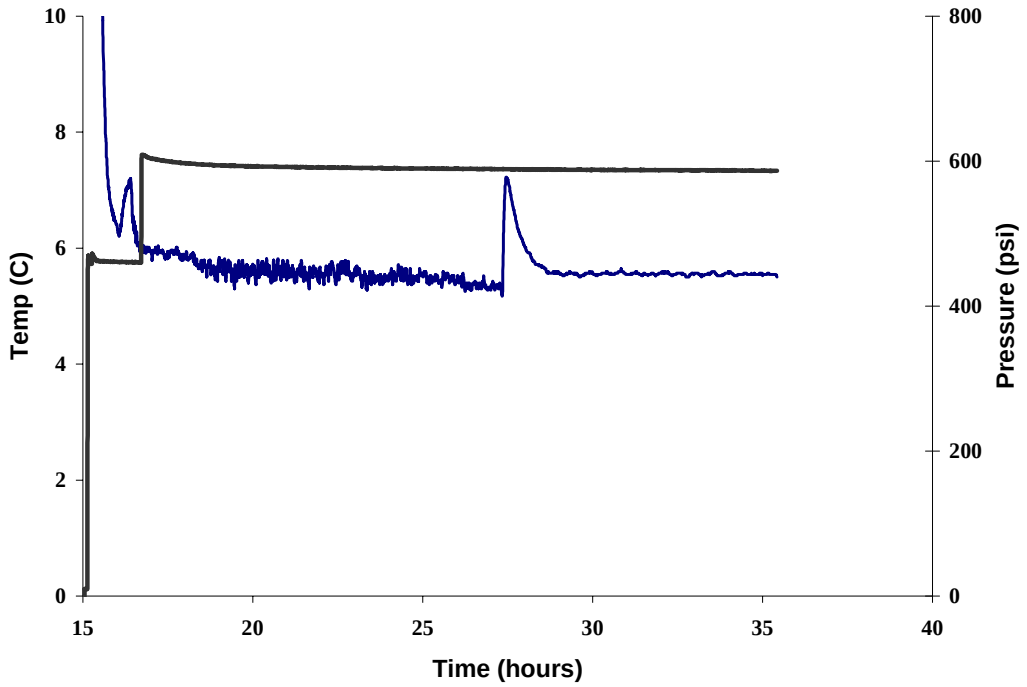

Fig. 1. Hydrate formation in the 450 ml vessel using distilled water (without thawed water, agitation, or bubble formation). Hydrate formation was detected approximately 10 hours after the vessel was pressurized to about 200 psi overpressure. Hydrate formation is detected by a spike in the vessel temperature, which is due to the exothermic nature of hydrate formation. Experiments are being conducted on the effects of thawed water, water agitation, as bubble formation on the onset of hydrate formation.

results have shown that the rapid agitation of the vessel fluid (via a spinning propeller at about 400 rpm) may decrease the induction time for hydrate formation and increase the amount of hydrate formed. Experiments have also been conducted in which the vessel was rapidly depressurized a small amount (but still within the hydrate 3-phase equilibrium pressure and temperature) after some hydrate had formed in the water phase. The depressurization causes the formation of small bubbles as gas is releases from solution. Hydrates rapidly form on the interfacial surface of the bubbles and the vessel was rapidly filled entirely with hydrate.

There are several potential uses for simple, inexpensive methods for the formation of hydrates. For example, when drilling through gas-rich sediments during oil and gas exploration, thawed water could be used to form hydrate and sequester the potentially explosive gasses that are transported to the surface through the drill hole. Another example is in the use of hydrate formation as a desalinization or dissolved chemical concentration method (dissolved species will become concentrated in the aqueous phase that has not been incorporated into the hydrate structure). The simple addition of thawed water would be cheaper and cleaner than the use of any additives to promote hydrate formation.

IMPLICATIONS

Implications of this research are directly related to hydrate occurrence and mechanism of accumulation; hydrate stability and uses in third party technologies; and maintaining hydrate stability during sub seafloor hydrocarbon exploration.

The lack of methanogenesis in Mallik cores is another line of evidence that hydrate accumulation in sediments may well be the result of transport, even if of biological origin. Biogenic methane will transport in subsurface environments such that hydrate accumulation may be spatially separated several km from the initial methane source and temporally separated by millions of years from the time the methane was produced. Accordingly the spatially and temporally separated methane production need have been subjected to the ~1/3 energetic penalty imposed by producing methane against a >100 partial pressure methane gradient nor would the methanogens need to have proliferated to a massive extent in low permeability silts formations. ODP cores are being examined to see if the hypothesis follows in these similarly silt environments poorly-hospitable for massive methanogenesis. Testing these hypotheses are important for methane hydrate exploration, explaining their occurrence and understanding their significance in U.S. energy derivation.

Another major implication of this work is the formation of hydrates as an attractive process to several industries such as natural gas storage and transportation, as well as in separation technologies. When water is taken up into the hydrate structure, dissolved ions are excluded, so hydrate formation is considered a possible desalinization technique, as exemplified in the seven patents of Michael Max). Interestingly, use of previously frozen water in experiments significantly lowers the hydrate nucleation overpressure (i.e., the amount of pressure above beyond the 3-phase equilibrium point necessary to form hydrate) (Vysniauskas et al., 1983; Takeya et al., 2000). In those experiments, however, the entire volume of water used in the experimental reactor was frozen and thawed and would be uneconomical for an industrial scale hydrate reactor. We have demonstrated experimentally that even if a relatively small amount of the reactor water was previously frozen, and if left in a cool thawed state for many hours, the overpressure required for hydrate formation is significantly lowered in the large volume SPS (Table 1). Additionally, our results demonstrated that the thawed water could be stored at room temperature (~25C) for 48 hours and the effect is preserved. This newly found process for routinely forming massive hydrates at low overpressures is spawning a new interest in using hydrates in separations chemistry and we are drafting another patent disclosure for improved CO2 separations using hydrates. Processes considered too energy intensive have now seen a 50% reduction in energy requirements making their reevaluation timely.

The major implication of this work will likely be in hydrate stability during hydrocarbon exploration in hydrate stability regions. We are collaborating with the JIP, ODP, NETL, and others to evaluate

hydrate nucleation and inhibition additives in the 70 liter SPS. Using the techniques described above we are uniquely suited for these large volume tests examining the ability of additives to enhance, forestall or inhibit nucleation processes. We will also examine characteristics of any formed hydrates and controls on their size, be they dispersed slurries or massive solids posing safety and pipeline clogging hazards.

FUTURE RESARCH

Biogeochemical and microbiological characterization of the ODP-LEG 204 samples is progressing well with future experiments to be directed at hydrate formation and stability.

ODP cores studies examining thermodynamic and hydrate kinetic experiments are being in progress. Sufficient materials or high quality are preserved for the planned experiments and other core materials are available from ODP.

Experiments are also in progress for the enhanced hydrate nucleation and inhibition materials. During the spring and summer 2002 DOE-GH workshops interest was expressed in the enhanced nucleation and in the inhibition of hydrates, particularly low cost additives for drilling fluids. Experiments are in progress with additives to bentonite drilling fluids and see if they enhance/inhibit hydrate formation. Based on our knowledge of hydrate nucleation we have reason to suspect that our additives may perform better and at lower or comparable costs to lecithin additives currently used in the drilling industry. Fluids and adjuvants were received by Phelps and experiments are planned for late FY 2003–2004 on the formation and inhibition/enhancement characteristics of drilling fluid components and determine if our procedures or simple adjuvants may better serve the drilling community. Experiments to date are already leading to at least one paper on enhanced hydrate nucleation materials, and papers on hydrate inhibition are to follow from planned experiments. These experiments are planned on hydrate inhibition/enhancement studies of drilling fluids and their additives from the in progress artic drilling campaign

PUBLICATIONS/PRESENTATIONS

Phelps was an invited participant in the International Pressure Coring Workshop sponsored by the ODP. The conference was in College Station, TX, February 5–7, 2003 and the topic of the presentation was on the SPS being an integral link to the accessing and R&D on cores recovered at temperature and pressure, exuded at temp and pressure and then examined in the native temperature and pressure regime. Work is underway between agencies to foster collaborations in pressure and temperature experiments.

The Marine Geology paper entitled, “Sediment Surface Effects on Methane Hydrate Formation and Dissociation,” authored by David Riestenberg, Olivia West, Sangyong Lee, Scott McCallum, and Tommy J. Phelps is officially in Press and galley proofs were returned to the editor in March 2003.

Publication is planned for a special Issue entitled, “Geosphere-Bioshpere,” hopefully in the April–May issue of Marine Geology.

A second paper on hydrate nucleation at low overpressures is currently being drafted.

Though the patent disclosure on improved procedures of hydrate formation has been stopped due to an inability to verify the use of a water cooling device (patent would not enforceable) we are instead refocusing DOE intellectual property efforts on enhanced chemical separations by hydrates, gaining advantage of the low overpressures required for hydrate formation.

MESOSCALE CHARACTERIZATION OF NATURAL AND SYNTHETIC GAS HYDRATES

Claudia J. Rawn (PI), Hsin Wang, Jane Howe, Michael Lance (Metals and Ceramics Division),
Bryan C. Chakoumakos (Condense Matter Sciences Division), and
Adam J. Rondinone (Chemical Sciences Division)
Oak Ridge National Laboratory
Camille Y. Jones
NIST Center for Neutron Research, Gaithersburg, MD 20899

INTRODUCTION

Clathrate hydrates are inclusion compounds where a variety of guest molecules can be occluded in a host lattice formed from an ice-like hydrogen bonded network arranged in such a way that polyhedral cavities are created. Two common atomic arrangements that result are cubic and designated as structure I and structure II with unit cell edges of approximately 12 and 17 Å, respectively.

Deposits of natural gas hydrates have been estimated to be several times that of known fossil fuel reserves. In addition to the idea that gas hydrates can be exploited as an energy resource issues surrounding uncontrolled release of the occluded gases into the atmosphere and risks to equipment and personnel resulting from either hydrate plugs in pipelines or reduction in the mechanical strength of the seafloor are of importance.

Prior to this project supported by Fossil Energy our group constructed a pressure cell [1] to synthesize gas hydrates from D_2O and gas and characterize the resulting structures with in-situ neutron powder diffraction with Laboratory Director Research and Development funds. As part of this prior effort we have studied the structure of laboratory synthesized clathrate hydrates of CO_2, CH_4, CH_4-C_2H_6, C_3H_8, TMO, and THF as a function of temperature [2–5]. These atomic structure studies of one or two phase materials (hydrate and ice VII) have aided in understanding the thermal expansion, motion of the occluded molecules, and guest-host interactions of clathrate hydrates. However, these experiments do not provide a complete understanding of the complex multiphase assemblages found in nature where hydrates with several types of gas molecules as the occluded guests are found in a mixture with ice and sediments present as additional phases.

The main emphasis of this project has been to characterize samples found in nature. Natural samples from two different Green Canyon (Gulf of Mexico) locations have been provided by Dr. Roger Sassen (Texas A&M University) and are designated by GC232 and GC234 in this report. Details of sample retrieval and previous characterization by Dr. Sassen and his colleagues can be found at http://www-gerg.tamu.edu/menu_RGD/index.asp.

In the current study, the gas hydrate specimens, GC232 and GC234, were harvested from the mound located at the Green Canyon (GC) in Gulf of Mexico continental slope, southwest of the Mississippi Delta. Visual inspection shows that GC232 contains significant amount of sediment (mud), which appears as white solid (hydrate) with dark gray streaks (sediment) while GC234 (see Fig. 1) is relative pure with little noticeable sediment.

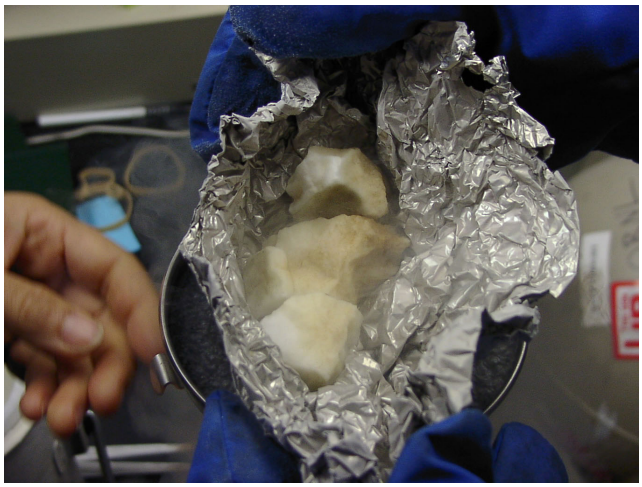

Fig. 1. Natural hydrate sample from Green Canyon in the Gulf of Mexico.

The following report describes characterization of GC232 and CG234 by in-situ x-ray powder diffraction, Small Angle Neutron Scattering (SANS), Inelastic Neutron Scattering (INS), thermal conductivity measurements, IR camera imaging, and Raman studies. Some data will be presented along with preliminary interpretation of the data. Also described are the preparations for a special issue of the American Mineralogist devoted to the clathrate hydrates.

LOW TEMPERATURE X-RAY DIFFRACTION STUDY OF NATURAL HYDRATE SAMPLES

Claudia J. Rawn

INTRODUCTION

We have used low-temperature x-ray powder diffraction to determine the phases present, decomposition temperatures, and the lattice parameters changes as a function of temperature to determine the instantaneous coefficient of thermal expansion in the natural samples designated GC232 and GC234 collected from the Green Canyon in the Gulf of Mexico. Most of the x-ray diffraction data has been analyzed using the Rietveld method which allows structural parameters that are used to calculate powder diffraction patterns to be refined by allowing the parameters to change for the calculated pattern to better fit the observed data. Resulting refined structural parameters include the atomic positions, lattice parameters, site occupancies, and atomic displacement parameters. Additional variables for calculating the diffraction pattern include both sample and instrumental parameters e.g. the peak shape.

EXPERIMENTAL

A laboratory x-ray diffractometer with a theta-theta goniometer has been modified with a closed-cycle He refrigeration unit, vacuum pumping station, and temperature controller. Samples G232 and 234 were loaded onto the low temperature stage in a flowing He glove bag to prevent frosting. The minimum temperature that can be obtained is approximately 12 K and the maximum temperature during loading can be kept under the decomposition temperatures.

The diffraction patterns were collected using CuKα radiation (45 kV and 40 mA) as step scans with a step size of 0.02 °2θ and a rate of 1 °2θ/min. The sample holder was fabricated from Cu with a deep well for the containment of the samples.

RESULTS AND DISCUSSION

The resulting x-ray powder diffraction patterns showed that both samples were structure II and that ice was present as a secondary phase. In some cases the intensity of the diffraction maxima was not well matched, however the peak positions clearly indicated structure II. Attempts were made to add structure I and the hexagonal form of clathrate hydrates to the calculated diffraction patterns to account for some of the intensity mismatches, however, calculated patterns with these additional phases did not fit well to the observed data. Most likely the discrepancy in intensities results from the inability to model various gas species in the cages. X-ray powder diffraction data were collected separately on sediments that were included in the samples and is shown in Fig. 2. Phases identified in the sediments included low quartz (SiO_2), aragonite ($CaCO_3$), and halite (NaCl).

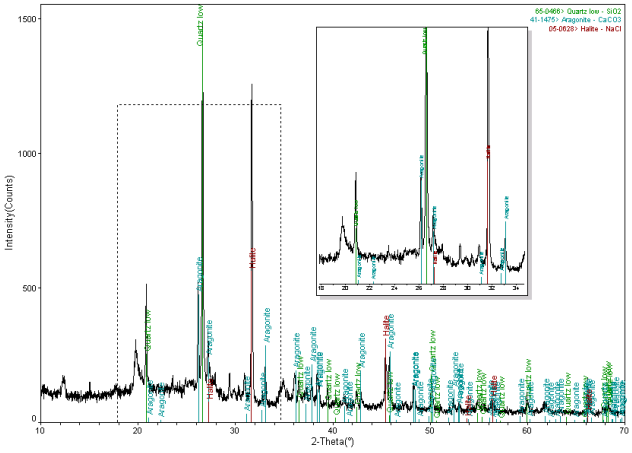

Fig. 2. Ambient temperature x-ray powder diffraction pattern of the sediments included in the natural hydrate samples.

The results shown below are preliminary and several more comparisons need to be made and discussed before any clear conclusions can be made. One result that seems clear is that the natural samples decompose at approximately 190 K. Figure 3 shows the refined *a* lattice parameter as a function of temperature for two separate runs of sample GC232. Figure 4 shows the wt% ice as a function of temperature for two separate runs of sample GC232 that remains constant at approximately 30 wt% until about 175 K.

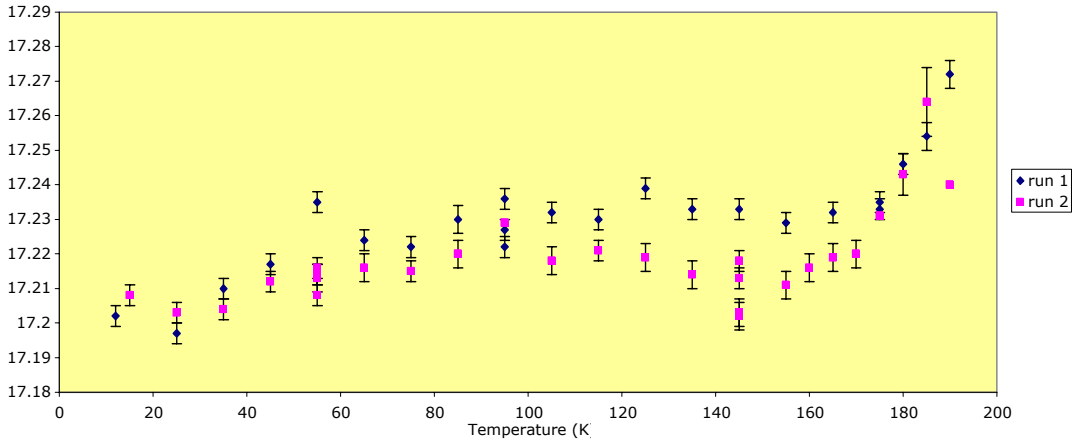

Fig. 3. Refined a lattice parameter as a function of temperature for two separate runs on sample GC232.

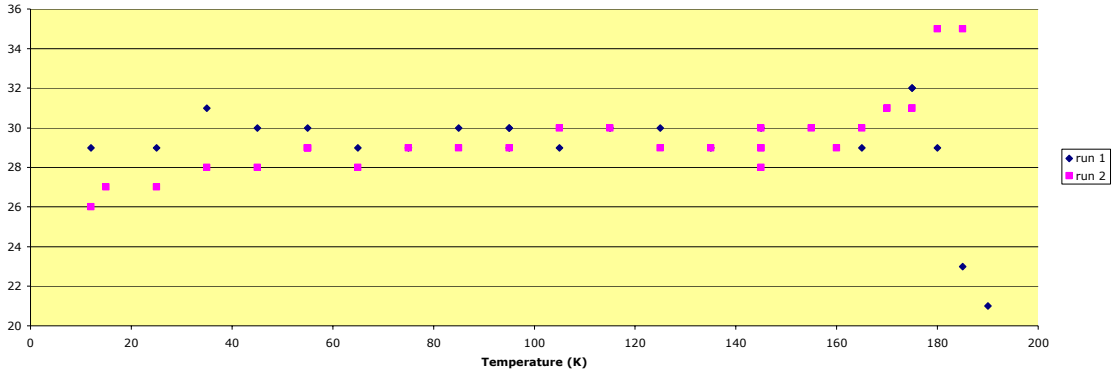

Fig. 4. Weight fraction of ice present as function of temperature for two separate runs on sample GC232.

From the lattice parameter as a function of temperature $\Delta a/a_0$ can be calculated and plotted against temperature and the data fit to a polynomial. By taking the derivate of the polynomial with respect to temperature the instantaneous coefficient thermal expansion can be calculated as shown in Fig. 5 for the two separate runs on sample GC232.

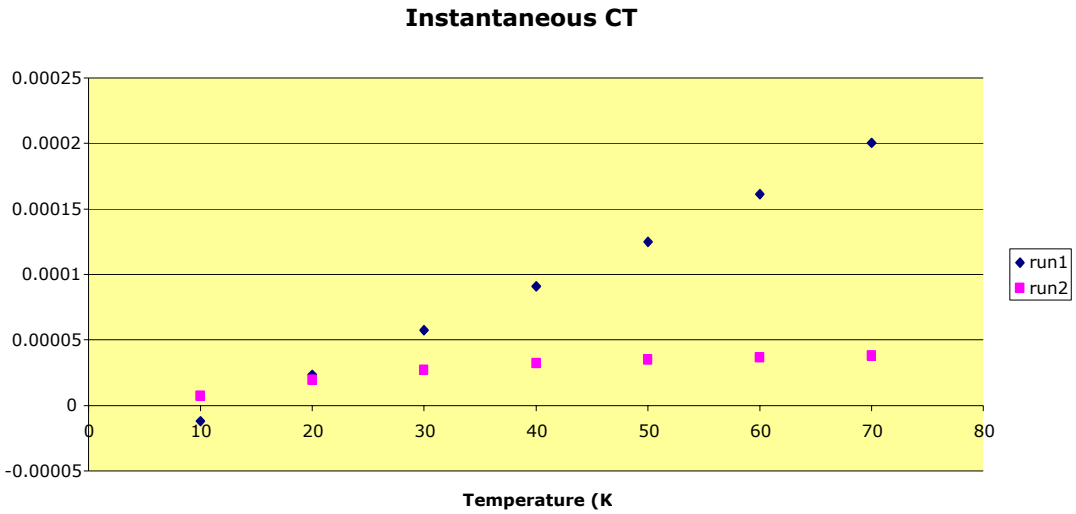

Fig. 5. Instantaneous coefficient of thermal expansion as a function of temperature up to 80 K.

THERMAL CONDUCTIVITY OF NATURAL CLATHRATE HYDRATES IN LIQUID NITROGEN

Hsin Wang

This study is directed at understanding the low temperature thermal transport properties of natural clathrate hydrates.

Two large natural samples were selected for thermal conductivity measurements. The main challenge was to prepare a natural sample with one flat surface, which became a difficult task since the natural samples are shaped like rocks with irregular surfaces, and they have to be kept at very low temperatures. We chose a larger natural sample and wrapped it with aluminum foil, exposing one relatively flat surface for polishing. The sample was quickly taken out of a liquid nitrogen bath and polished on 180 grit sand paper for about 5 seconds and then returned into the liquid nitrogen bath to prevent melting. After repeated polishing cycles, a flat surface was obtained as shown in Fig. 6. In additional to the natural

Fig. 6. Preparation of a flat sample for thermal conductivity measurements.

samples, we also tested ice and TMO structure I samples at liquid nitrogen temperature and compared results with literature values.

THERMAL CONDUCTIVITY MEASUREMENTS

For thermal conductivity measurements, a small piece of Styrofoam and a C-clamp were used to hold the sample and the Hot Disk sensor together. The assembly was then immersed into a liquid nitrogen bath, as shown in Fig. 7, for testing. For the TMO-I and natural samples, only single-side tests were performed, however, for the ice a double–sided test was performed.

Fig. 7. Styrofoam and a C-clamp securing the sample to the Hot Disk sensor with entire assembly submerged into a liquid nitrogen bath.

RESULTS AND DISCUSSIONS

THERMAL CONDUCTIVITY OF ICE

In the first test, the standard Hot Disk method was used where the Kapton sensor/heater was sandwiched between the two ice specimens. The test conditions were: 0.5 Watt and 10 seconds and at –34°C the average thermal conductivity was 2.39 W/mK. For measuring the thermal conductivity near –194°C the sample holder was placed into a liquid nitrogen bath. The average thermal conductivity for ice in a liquid nitrogen bath is 8.45 W/mK. The results are plotted with published thermal conductivity values [6] in Fig. 8. The increase in thermal conductivity at lower temperatures is typical behavior for crystalline materials. The test of ice proved that the Hot Disk method could be used at liquid nitrogen temperatures.

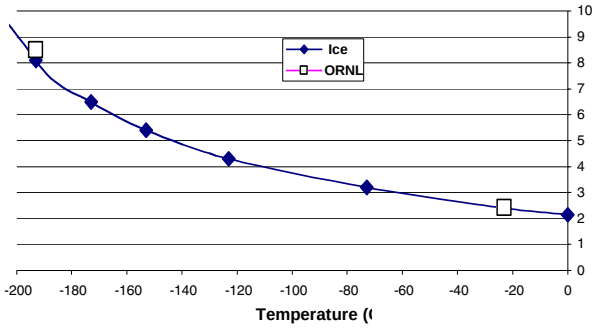

Fig. 8. Thermal conductivity of ice at low temperatures.

TMO-I AND NATURAL SAMPLES

A TMO-I sample was used in the single-side test backed by Styrofoam. The thermal conductivity tests conducted at –34°C showed a value of 0.58 W/mK. At liquid nitrogen temperature, –194°C, the average thermal conductivity was 0.49 W/mK. The decrease in thermal conductivity as a function of temperature is consistent with THF hydrate in the literature [7]. The literature values of THF is shown in Fig. 9 as a reference since no such TMO-I thermal conductivity values were available to us.

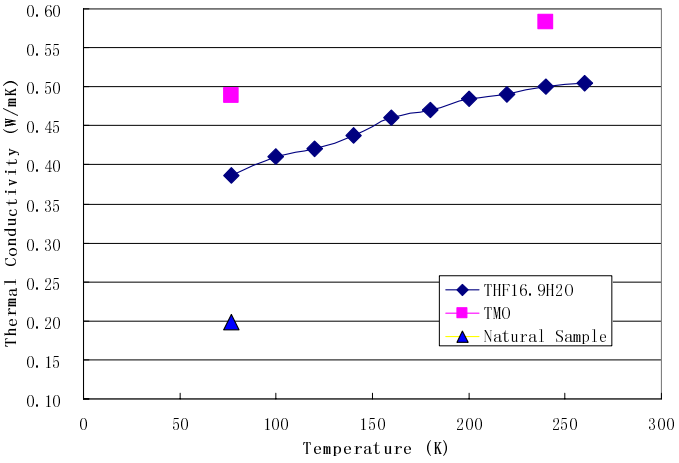

Fig. 9. Thermal conductivity of TMO-I and natural samples.

The natural samples showed an even lower thermal conductivity at liquid nitrogen temperature. The average value was 0.20 W/mK with relatively large scatter (15–20%). This was due to the fact that thermal conductivity of natural sample is comparable to the backing Styrofoam and the reduced thermal conductivity contrast resulted more uncertainty in the measurements. The ideal condition will be testing two natural samples using the standard Hot Disk method. The only two larger natural samples (collected from two different sites) did not match well in size for the standard test.

INFRARED TEMPERATURE MONITORING OF NATURAL CLATHRATE HYDRATE SAMPLES UNDER HIGH PRESSURE

Hsin Wang

Proper handling natural of samples is the key to characterization efforts. Since the melting temperature of the natural samples are well below ambient temperature, the control of temperature during measurements, transport and handling becomes very important. Currently, the natural samples are stored at liquid nitrogen temperature and a small amount of sample is taken out for data collection. There has been no effective temperature monitoring during the measurements other than cell or environment temperatures. We employed an infrared camera to monitor sample temperatures in a high-pressure sapphire cell. The following are some preliminary IR images and analysis.

EXPERIMENTS

The high-pressure cell has been described in other reports related to this study [1]. The cell is made of sapphire, which is an infrared transparent material. We used a Raytheon, Radiance HS, IR camera in this study. The IR camera has a 256×256 pixel Focal Plane Array InSb detector, which is sensitive to 3–5 micron thermal radiation. At room temperature, the 12-bit digital image gives a temperature resolution of 0.015°C. For this preliminary study temperature calibration was not performed since it

requires more experimental effort and we are only interested in relative temperature changes at this stage. The integration time of the IR camera was 1 ms.

Typical IR monitoring consists 3–4 minutes continuous temperature measurements at 1 Hz. The digital image sequences were played back and analyzed by Image Desk software.

During the experiment, a small piece of natural sample was taken from a liquid nitrogen bath and quickly inserted into the cell. Once the cell top was secured, high pressure was applied to keep the sample from melting. The IR camera started collecting images from a distance. This type of non-contact temperature measurement can be used while conducting other measurements.

RESULTS AND DISCUSSION

Figure 10 shows the temperature images of a natural sample under pressure (a) in the beginning, (b) 4 minutes later. The plots on the right are line-temperature-profiles indicated by the black lined going through the sample. The temperature was not calibrated for emissivity. The background, room temperature, intensity was about 1700. For a material with emissivity close to 1, 1°C = 30 intensity units. Using this estimate, the sample temperature in Fig. 10(a) was at least 12°C below room temperature. Note in Fig. 10(b) the sample was partially melted and the temperature scale increased 100 units (at least 3°C).

In Fig. 11, a small circular area, “1” was monitored over time, the maximum, minimum, and average temperatures in that area were plotted on the right. All three temperatures showed a jump after 40 seconds. This was because a step-increase in cell pressure. Even at constant pressure, the IR camera still observed melting of the sample, especially in the areas in contact with the cell wall and the support.

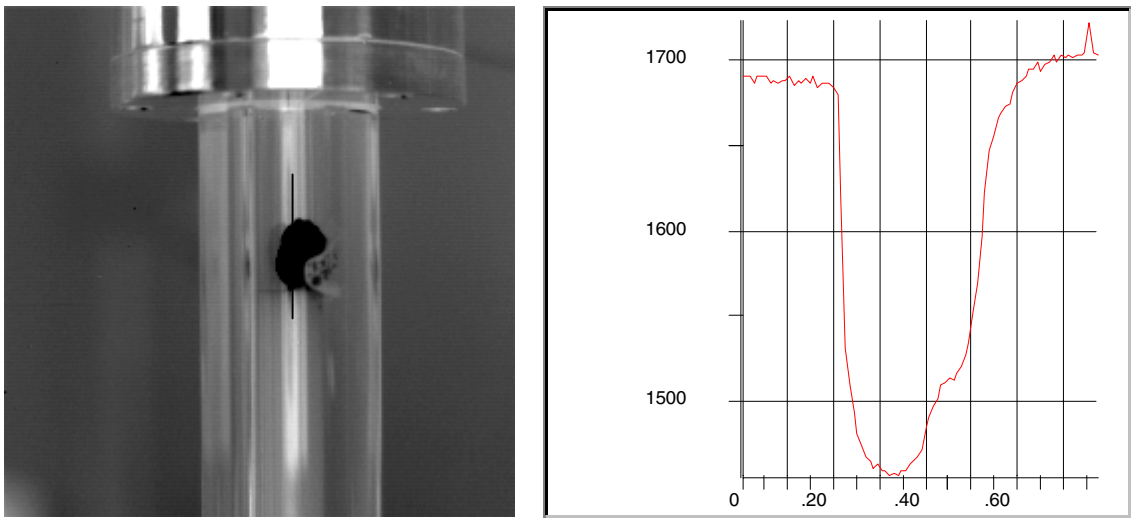

Fig. 10 (a) Natural sample in a high pressure sapphire cell. Temperature is shown in uncalibrated IR intensity scale.

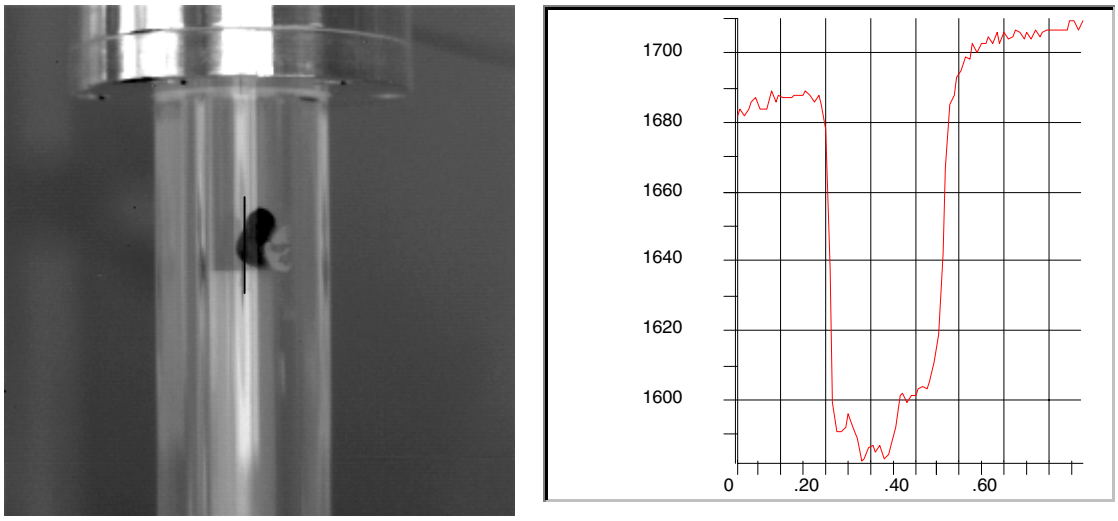

Fig. 10 (b) Same natural sample 4 minutes later. About half of the sample has melted away. The temperature of the sample increased 100 unit (3–4 degree C).

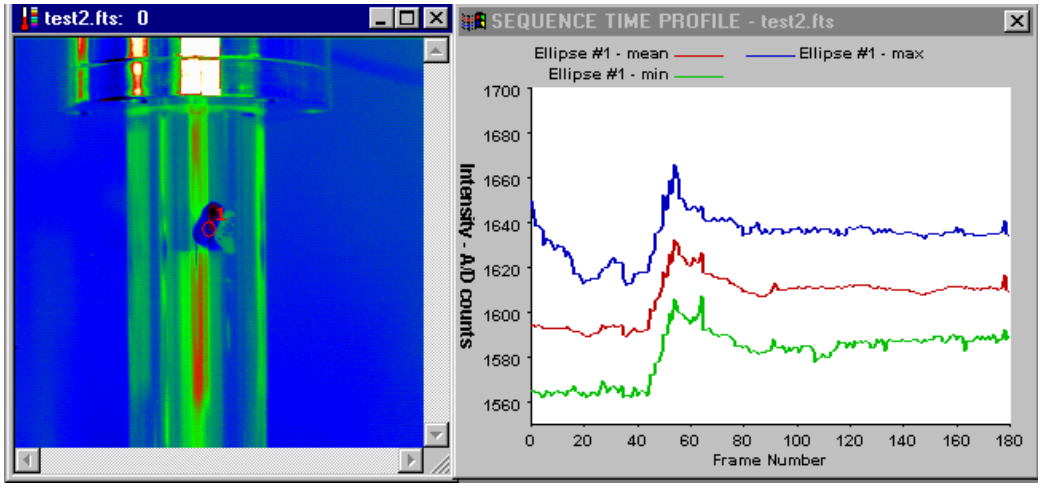

Fig. 11. Temperature changes (max, min and average) of a natural sample under pressure over a period of 3 minutes (imaging speed at 1 Hz) in a circular area "1". The temperature jump after 40 seconds was due to a step increase in cell pressure.

Figure 12 shows the temperature change of a natural sample when the cell pressure was released. A single point temperature, "2", was traced and plotted on the right. The sample temperature kept dropping for at least 25 seconds after the pressure release.

Other than, pressure change in the cell, the sample temperature was also affected by direct contact with the cell wall and supporting rod. The heat transfer from contact is one source of continuous melting of the sample even when the sample is under constant pressure. Detailed study requires careful calibration and control of the experiments.

Fig. 12. IR imaging of natural sample melting after pressure release. The sample temperature kept dropping for 25 seconds.

SUMMARY

This was a preliminary study to explore the feasibility of using IR imaging in our study of natural sample. The results showed this method can be used as an effective tool to monitor sample temperature changes during data collection. The time-stamped temperature maps will help us in explaining experimental results of the natural samples.

AMERICAN MINERALOGIST CLATHRATE HYDRATE SPECIAL ISSUE

Bryan C. Chakoumakos

Through discussions with the Editor, Lee Groat, from the University of British Columbia, the American Mineralogist has embraced the idea to publish a special issue devoted to clathrate hydrates. The publication date is set to be October 2004, with a manuscript submission deadline of October 2003. Roughly thirty hydrate researchers have agreed to contribute, from a solicitation of over 400 researchers worldwide. The American Mineralogist, the premier International Journal of Earth and Planetary Sciences and the official publication of the Mineralogical Society of America, publishes the results of original research in the general fields of mineralogy, crystallography, petrology, and geochemistry. Journal details and information for authors are available at http://www.minsocam.org/MSA/AmMin/AmMineral.html. Each manuscript submission will be subject to the same peer review process as regular articles. The special issue will have space to accommodate 20 to 30 articles. Bryan Chakoumakos (Oak Ridge National Laboratory) will act as a managing editor.

Topics that will be included for this special issue are crystal structure, physical property measurements, kinetic studies, thermodynamical properties, phase equilibria, natural occurrence descriptions, synthetic analogs, high pressure studies, experimental methods, theoretical modeling, carbon dioxide sequestration, etc.

INELASTIC NEUTRON SCATTERING OF CLATHRATE HYDRATES

Bryan Chakoumakos

Vibrational spectroscopy of clathrate hydrates links the microscopic properties to the macroscopic properties, such as thermal conductivity. Vibrational spectroscopy done by inelastic neutron scattering (INS) generally offers poorer resolution than FTIR or Raman, but it has no selection rule restrictions. Examples INS spectra of a clatharte hydrate (TMO structure I) collected on a triple-axis spectrometer at several temperatures are show in Fig. 13. The incoherent scattering is so much larger for the hydrogen as compared to the other constituent atoms of typical clathrate hydrates that it overwhelmingly dominants the contribution to the spectra. Consequently, for a synthetic sample prepared with a deuterated host lattice, the INS spectrum will emphasize those vibrational modes involving the hydrogenous guest molecule. In contrasting synthetic samples prepared with and without a deuterated host lattice, Fig. 14, some modes shift in frequency whereas others do not, which in principle should help to identify which modes are associated with the guest molecule, host lattice, or both. Our preliminary experiments of synthetic samples show that in the low energy transfer region (0–50 meV) there are prominent modes connected to the guest host coupling. We have examined two natural structure II methane hydrates from Green Canyon in the Gulf of Mexico over the 0–50 meV energy transfer range. As these samples are hydrogenous, and contain small amounts of higher

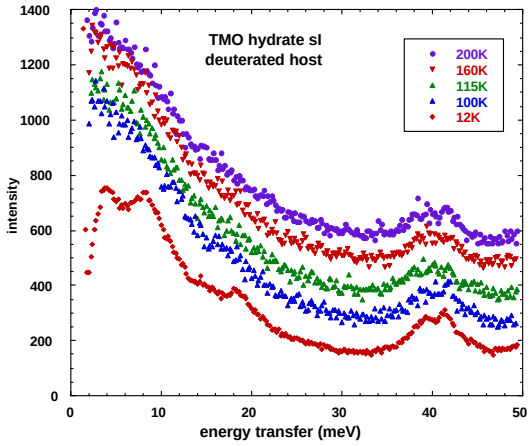

Fig. 13. Inelastic neutron scattering spectra for trimethylene oxide (TMO) hydrate sI as a function of temperature. The host lattice is deuterated and the guest molecule is hydrogenous. The spectra are offset along the vertical axis for clarity. Data collected on the HB1 triple-axis spectrometer at the HFIR, ORNL.

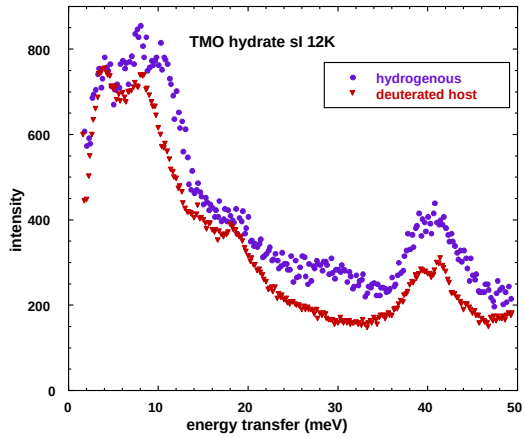

Fig. 14. Inelastic neutron scattering spectra for trimethylene oxide (TMO) hydrate sI at 12K comparing a fully hydrogenous sample with one that has only a deuterated host lattice. The spectra are offset along the vertical axis for clarity. Data collected on the HB1 triple-axis spectrometer at the HFIR, ORNL.

weight hydrocarbon molecules, the INS do not show as much detail as the purely synthetic samples [Fig 15(a) and (b)]. Nevertheless, the spectra do exhibit changes as a function of temperature and some structure at the lowest energy transfers. To fully identify the various vibrational modes in the spectra, it will be necessary to undertake higher resolution scans with different neutron spectrometers, correlate the spectra with Raman and IR measurements, and examine more synthetic samples (both deuterated and hydrogenous). This month, Yoshi Ishii is undertaking new INS of a fully hydrogenous sI methane hydrate freshly synthesized by the U.S. Geological Survey (Stern et al.) on a higher resolution spectrometer at the Japan Atomic Energy Research Institute. His results will be integrated into the interpretation of our own preliminary measurements, and devising the most appropriate instrument design for future measurements. Ultimately, we can expect to further elucidate the underlying lattice dynamical picture of the glass-like thermal conductivity exhibited by the gas clathrate hydrates.

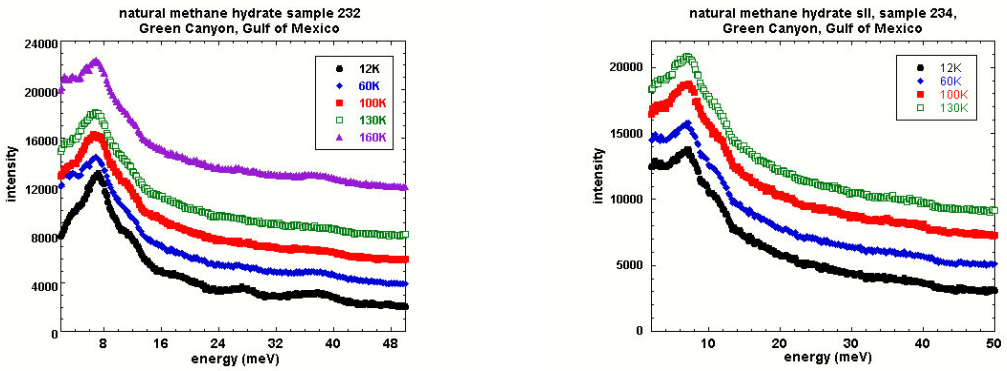

(a) **(b)**

Fig. 15. Inelastic neutron scattering spectra for methane hydrate sII samples (a) 232 and (b) 234 from Green Canyon, Gulf of Mexico. The spectra are offset along the vertical axis for clarity. Data collected on the HB1 triple-axis spectrometer at the HFIR, ORNL.

RAMAN SCATTERING MEASUREMENTS

Michael Lance and Adam J. Rondinone

Raman microscopy is extremely useful in characterizing gas hydrates since it can directly measure the vibrational energies of the interstitial gas molecules non-destructively. Also, since the Raman spectroscopy is a scattering spectroscopy, spectra can be obtained through a clear pressure cell for in-situ measurements at various temperatures and pressures. In addition, the spot size is ~2 μm, which allows one to probe around microstructural features of natural samples.

Raman spectra were obtained with a DilorXY800 triple stage Raman microprobe (JY, Inc., Edison, NJ) using a Innova 308C Ar^+ ion laser (Coherent Laser Group, Santa Clara, CA) at 5145 Å and 100mW output power. The spot diameter and penetration depth were both ~2 μm in size. Both a high pressure cell (Sam O. Colgate, Inc., Gainesville, FL) and a low temperature stage (THMS 600, Linkam, Inc.), were used to create and analyze gas hydrates.

The high-pressure cell has a maximum pressure of 10,000 psi at 25°C and can be cooled to –20°C. A thermocouple inside the cell measures the temperature and a magnetic stirrer ensures a well-mixed solution. The initial test showed that we successfully created the methane hydrate at 5100 psi and 4°C. The peak from the methane hydrate structure I and a shoulder from structure II (see Fig. 16) were clearly visible showing that we successfully created gas hydrate. The peak positions compared well with values reported in the literature.

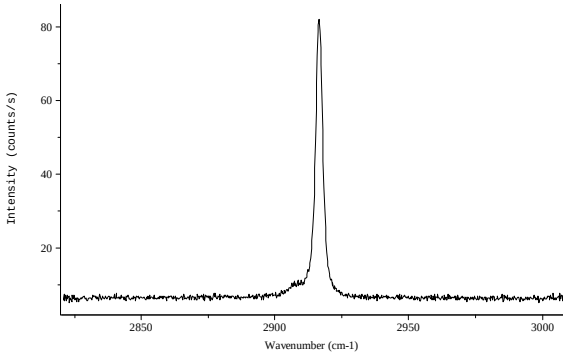

Fig. 16. Raman spectrum obtained from methane hydrate at 2100 psi and 16ºC.

Natural hydrate samples (GC232 and GC234) were analyzed at low temperatures using the cooling stage. Sample GC232 had more petroleum deposits and visually looked dirtier than sample GC234. This resulted in a slightly higher background for this sample but Raman spectra could still be acquired. The effect of temperature on the Raman peak position of the structure I methane hydrate is shown in Fig. 17. The peak shifts only ~0.5 cm^{-1} over a 60°C temperature range which shows that the temperature where we choose to measure will have little effect on our measured peak positions and so can be compared to literature values.

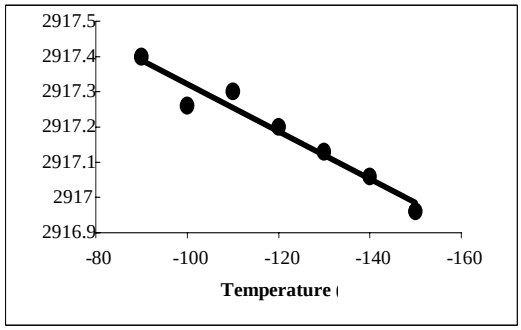

Fig. 17. Effect of temperature on the peak position of the structure I methane hydrate.

The spectra obtained from sample GC234 is shown in Fig. 18(a) and (b) for the spectral ranges associated with C-H vibrations and with C-C vibrations, respectively. Numerous peaks are observed which are related to various gases and are summarized in Table 1. Methane and ethane were the predominant gases along with trace amounts of isobutene and trans-butane. The methane and ethane were observed in both structures I and II. Raman bands from sample GC232 are essentially identical to those from sample GC234.

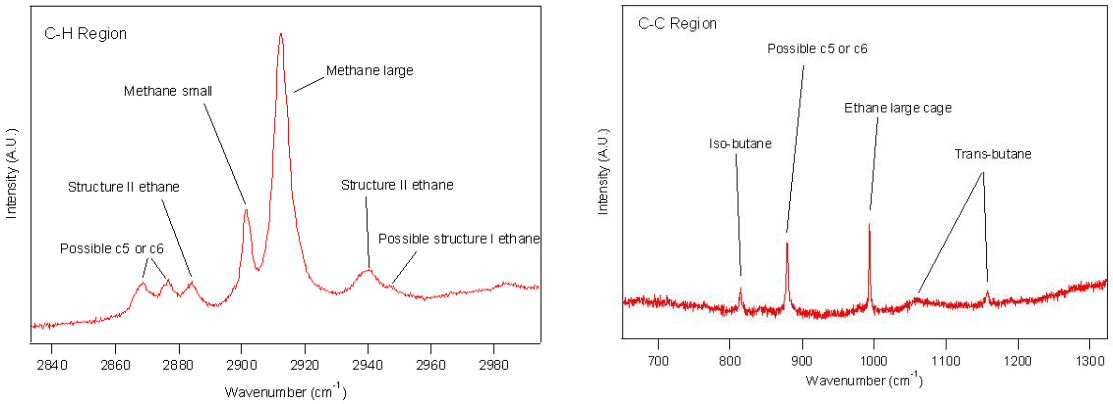

Fig. 18. Raman spectrum from natural sample GC234 in the spectral region associated with (a) C-H vibrations and (b) C-C vibrations.

Table 1. Assignment of Raman bands to different gas hydrates in natural samples

Possible Clathrate 1st Guess	*Measured Peak Position (cm^{-1})*	*From Literature*
C5 or C6	2868.49	
C5 or C6	2876.71	
C2H6 in SII 5(12)6(2) Large	2884.34	2887.3
CH4 in SII 5(12)6(4) Large	2898.77	2903.72 +/– 0.28
CH4 in SI 5(12)6(2) Large	2901.73	2904.85 +/– 0.33
CH4 in SII 5(12) Small	2912.32	2913.73 +/– 0.76
CH4 in SI 5(12) Small	2917.14	2915.04 +/– 0.58
C2H6 in SII 5(12)6(2) Large	2939.47	2942.3
C2H6 in SI 5(12)6(2) Large	2947.46	2946.2
???	2982.53	

SMALL-ANGLE NEUTRON SCATTERING OF NATURAL CLATHRATE HYDRATES

Jane Y. Howe and Camille Y. Jones

EXPERIMENTAL PROCEDURES

Small Angle Neutron Scattering (SANS) experiments were carried out at National Center for Neutron Research at National Institute of Standard and Technology, Gaithersburg, MD. Data were collected on the NG3, a 30-m SANS instrument equipped with a helium closed-cycle refrigerator (CCR), with a monochromatic neutron influx at wavelength of 6.0 Å, and a momentum transfer Q from 0.004 to 0.47 $Å^{-1}$. The sample holder is made of aluminum with a path length of 1 mm. Data was collected on sample GC234 at 25, 50, 75, 100, and 125 K and on samle GC232 hydrates at 25, 75, and 125 K. Scattering from the empty cell was measured at 25 and 125 K. Data was also collected on sediment samples from the vicinities of both the GC232 and GC234 mounds. These samples were dried in air around 340 K and ground to fine powder prior to the SANS study. The sediment part of the GC232

sample, which remained after the decomposition of the hydrates and gases, was also studied. The SANS data of mud and sediment samples were collected at 283 and 298 K with 1 mm path length. SANS data analysis was carried out using the SANS Analysis Package with IGOR, developed by S.R. Kline which is available at NIST's website [8].

RESULTS AND DISCUSSION

SANS data of GC232 and GC234 hydrates, plotted in log-log format, are complied in Figs. 19 and 20. These data were collected from 0.002 to 0.32Å^{-1} that covers the structural characteristics in the mesoscale range (~2 to 300 nm). Both samples show the temperature independence of small-angle scattering. And both samples have the power-law relationship; the slope of the power-law fit is 3.4 for GC234 and 3.3 for GC232 (Table 2). This indicates that the samples are surface fractal with a surface fractal dimension of 2.6 and 2.7 respectively.

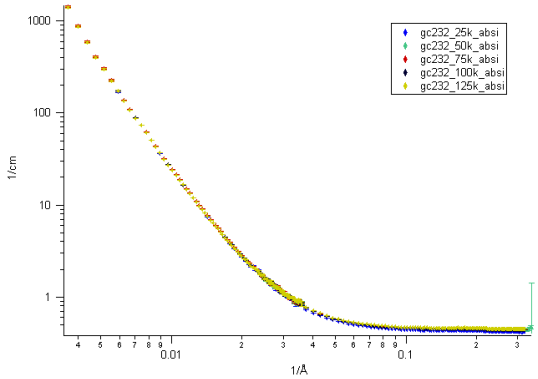

Fig. 19. SANS data of GC232 taken at 25 to 125K.

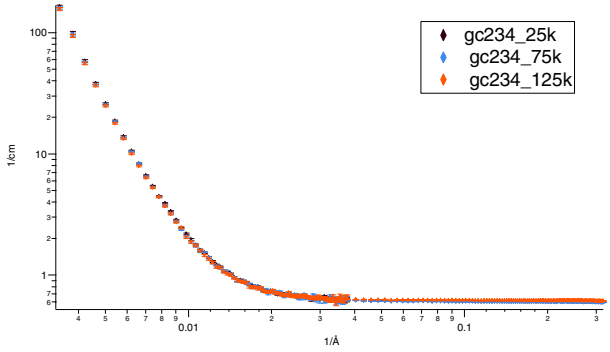

Fig. 20. SANS data of GC234 taken at 25, 75 and 125K, which indicates the temperature independence.

Table 2. SANS data Analysis

	Two-phase model Cor. Length (nm)	χ^2	Power-Law α	Fractal D_s (6-α)
GC234-25K	68	5.6	3.4	2.6
GC234-75K	72	4.5	3.4	2.6
GC234-125K	72	3.4	3.4	2.6
GC232-25K	23	96.3	3.3	2.7
GC232-75K	22	120.6	3.3	2.7
GC232-125K	22	119.8	3.3	2.7

GC234 is the sample with little sediment. XRD reveals that it is a mix of type II hydrate and ice in 70:30 wt ratio. Hence, it is reasonable to describe the small-angle data using the Debye-Bueche model.

The correlation length is calculated to be 68, 72, and 72 nm for GC234 at 25, 75, and 125 K, respectively (Table 2). The value of χ^2 quantifies the goodness of a fit. The small value of χ^2 for the GC234 data suggests that the model and experimental results agrees quite well.

Figure 21 contains plots of GC232 and GC234 data taken at 25 K. The scattering intensity of the GC232 extends to a higher Q-range, suggesting that the structural feature is smaller that of GC234. The GC232 data were fitted to the two-phase Debey-Bueche model and the correlation length was estimated to be 22 nm. The fitness of the data is poor as the value of χ^2 is 120, implying that GC232 is not a two-phase system and that a more complicated model needs to be used.

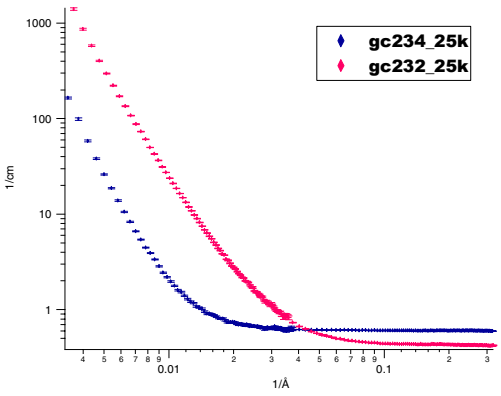

Fig. 21. The SANS data of GC232 and GC234 taken at 25 K.

The SANS data of the sediment and the GC232 are compared in Fig. 22. Data analysis indicates that the sediment sample has smaller correlation length at 14 nm. A better interpretation of the SANS data is possible once the structural information and chemical composition (XRD and ND results) becomes available.

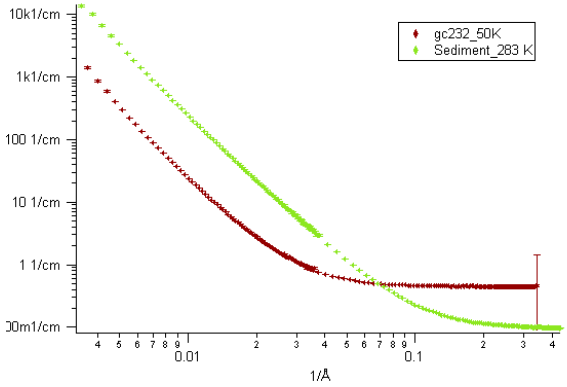

Fig. 22. The SANS data of GC232 hydrate and its sediment.

SUMMARY

GC234 is a two-phase system of hydrate and ice mix and well described using the Debye-Bueche model. The correlation length is calculated to be 70 nm. The correlation length of the GC232 is 22 nm, though the fitting of the Debye-Bueche model is relatively poor.

REFERENCES

1. A. J. Rondinone, C. Y. Jones, S. L. Marshall, B. C. Chakoumakos, C. J. Rawn, and E. Lara-Curizo, "A Single-Crystal Sapphire Cell for in situ Neutron Diffraction Study of Gas-Hydrate," in press *Can. J. Phys.* (2002).
2. C. J. Rawn, A. J. Rondinone, B. C. Chakoumakos, S. Circone, L. A. Stern, S. H. Kirby, and Y. Ishii, "Neutron Powder Diffraction Studies as a Function of Temperature of Structure II Hydrate Formed from Propane," in press *Can. J. Phys.* (2002).

3. B. C. Chakoumakos, C. J. Rawn, A. J. Rondinone, L. A. Stern, S. Sircone, S. H. Kirby, Y. Ishii, C. Y. Jone, B. H. Toby, and D. C. Dender, "Temperature Dependence of Polyhedral Cage Volumes in Clathrate Hydrates," in press *Can. J. Phys.* (2002).
4. C. Y. Jones, S. L. Marshall, B. C. Chakoumakos, C. J. Rawn, and Y. Ishii, "Structure and Thermal Expansivity of Tetrahydrofuran Deuterate Determined by Neutron Powder Diffraction," accepted *J. Phys. Chem. B* (2002).
5. C. J. Rawn, A. J. Rondinone, B. C. Chakoumakos, S. L. Marshall, L. A. Stern, S. Circone, S. H. Kirby, C. Y. Jones, B. H. Toby, and Y. Ishii, "Neutron Powder Diffraction Studies as a Function of Temperature of Structure II Hydrate Formed from a Methane + Ethane Gas Mixture," *Proceedings of the Fourth International Conference on Gas Hydrates* (2002), p. 595.
6. G. A. Slack, "Thermal Conductivity of Ice," *Physic. Rev. B.* **22**(6), 3065–3071, 1980.
7. H. Suga, "Calorimetric Studies of Some Energy-Related Materials," *Thermochimica Acta,* **328**, 9–17, 1999.
8. S.R. Kline, SANS Analysis with IGOR http://www.ncnr.nist.gov/programs/sans/manuals/data_anal.html

NEW ACOUSTIC WAVE PIPE INSPECTION SYSTEM

Venugopal K. Varma, Raymond Tucker, Steve Kercel,
Thomas Thundat, and Ali Passian
Oak Ridge National Laboratory

Joseph Rose and Xiaoliang Zhao
Pennsylvania State University

INTRODUCTION

The safety of the Unites States' natural gas supply is of prime importance since 30% of the energy produced in the country is derived from it. Natural gas is supplied through a million miles of vast pipeline network. Pipeline companies have an impressive safety record due to the proactive role of standards and inspection of pipelines. Since the pipelines are getting old, there is a great need to identify corrosion, cracks, and other defects that can cause potential problems.

Stress corrosion cracking (SCC) can occur under a range of pipeline field conditions including soil type, stress, cathode potential, coating conditions and temperature. This type of defect is usually oriented along the lengthwise direction of the pipe. If not found and conditions persist, the cracks may grow and/or coalesce and eventually result in a leak or pipe rupture. There are also other types of defects that can occur in pipe structures. They are either critical to the safety of the pipeline like corrosion, welding cracks, pits etc or benign stringer-like internal inclusions. Non-destructive Inspection (NDI) systems are strongly needed to be able to locate the defects early without false alarms from benign inclusions, and to characterize and size the defects for repair or replacement management.

Many technologies have been developed for pipe inspections, but they are limited to detecting certain types of defects. For example, Axial-field Magnetic Flux leakage (MFL) in-line inspection smart pipe-inspection-gears (PIGs), extensively used for pipeline inspection, are good for detecting corrosion damage or circumferentially oriented defects inside a pipe. It is not suitable for detecting flaws or cracks in the axial direction.

In this project, ultrasonic guided waves are being studied for the feasibility of detecting many kinds of defects that occur in pipes. One major benefit of guided waves is their rapid global inspection capabilities which enables them to inspect a structure line-by-line instead of point-by-point. However, defect classification and sizing by guided waves are still a major problem under investigation due to the complexity of the wave propagation characteristics.

MODELING

2D MODELING

BEM (Boundary Element Method) analysis is used to model the flaws and study the effect of guided shear waves impinging on the flaw. The dispersion curves of the circumferential guided.

Shear (SH) waves were calculated to arrive at the EMAT settings for generating n1 mode. Comparison of the dispersion curves with those of a flat plate shows that a large diameter thin walled pipe can be approximated as a plate locally (see Fig. 1). The transmission and reflection coefficient for the shear wave incident on a crack 1/8 in. wide are as shown in Fig. 2. These were calculated using 2-D BEM analysis.

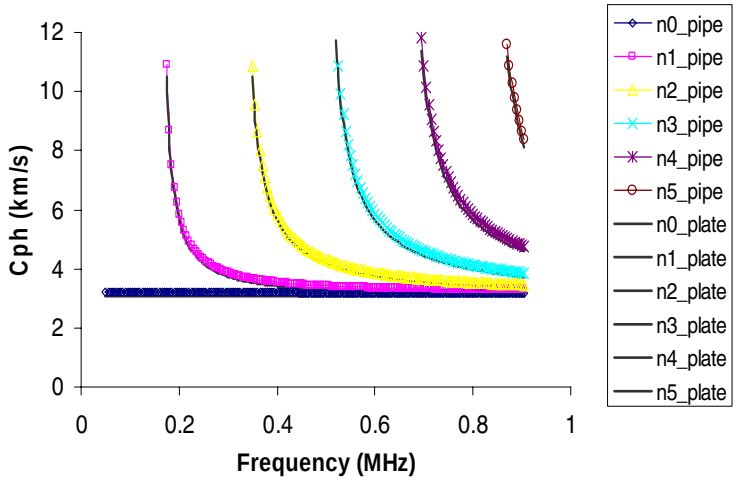

Fig. 1. Phase velocity dispersion curves for SH wave in the circumferential direction of a 10 in. schedule 40 steel pipe and plate of same thickness (9.271 mm).

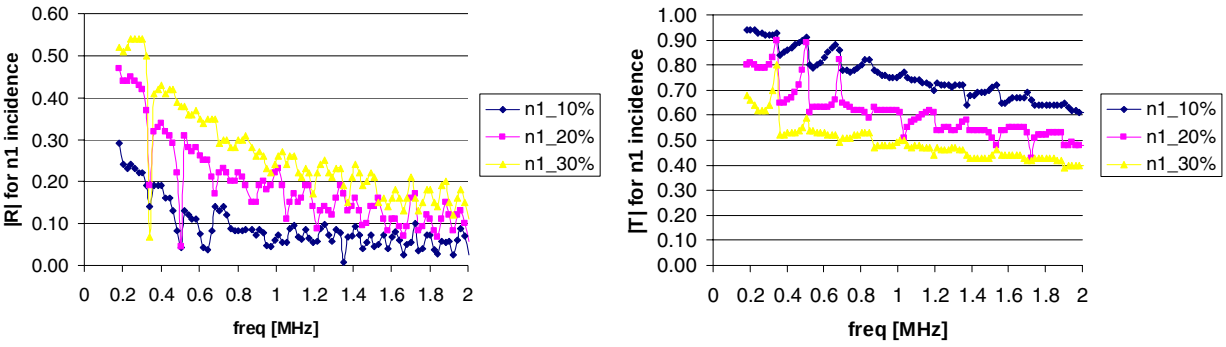

(a) **(b)**

Fig. 2. (a) The reflection coefficient and (b) transmission coefficient of n1mode for n1mode SH wave incident into 1/8 in. wide cracks with 10%, 20%, and 30% through wall depth. The pipe wall is 9.272 mm thick.

3D MODELING OF FLAWS

The geometry for the 3-D problem can be shown in Fig. 3. A cylindrical coordinate system is attached to the center of the meshed disc region, with the z = 0 plane being the mid-plane of the plate. A commercial Finite Element Analysis package called IDEAS was used to mesh the surface of the disc with defects. Quadrilateral 2-D elements were used. The software package can output the coordinates of each corner points and the connectivity relation between elements and corner points were also given. This information can be input to the 3-D BEM code as geometry mesh. Consider a time-harmonic SH plane wave incident from the left, the scattered wave field may consists Lamb waves and SH waves.

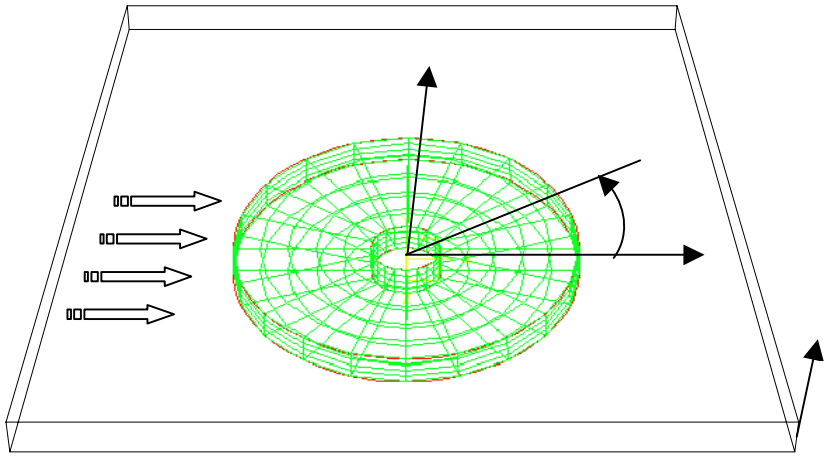

Fig. 3. An example mesh for three-dimensional defects in an infinite plate and the coordinate system set-up. A plane SH wave is incident onto the defect region.

BEM CALCULATION OF SCATTERED GUIDED WAVE FIELD FROM A THROUGH-PLATE HOLE

The hybrid boundary element normal mode expansion technique was applied to the calculation of the scattered wave field from a circular through-plate hole in a plate (see Fig. 3). Note that this defect can be substituted by any arbitrary shaped 3-D defect without jeopardizing the validity of the code. The geometry mesh used here is just for testing the concept with an easy mesh. Considering a plane shear horizontal wave propagating in the positive x direction, it impinges onto the defect and will be scattered back. The scattered wave consists of all propagating as well as non-propagating modes of both the Shear Horizontal wave and the mode converted Lamb wave. The non-propagating waves do not carry away any energy flux and die out within several wavelengths. Thus only propagating modes exist beyond the virtual boundary, which was chosen to be far enough (usually much larger than a wavelength) from the defect. Figure 4 (a), (b), and (c) show the x, y, and z component of the scattered wave particle displacement amplitude on the outer cylindrical surface, respectively. In each figure, the amplitude curves of three frequency points were displayed. The red dot-dash line with an arrow still shows the positive x direction.

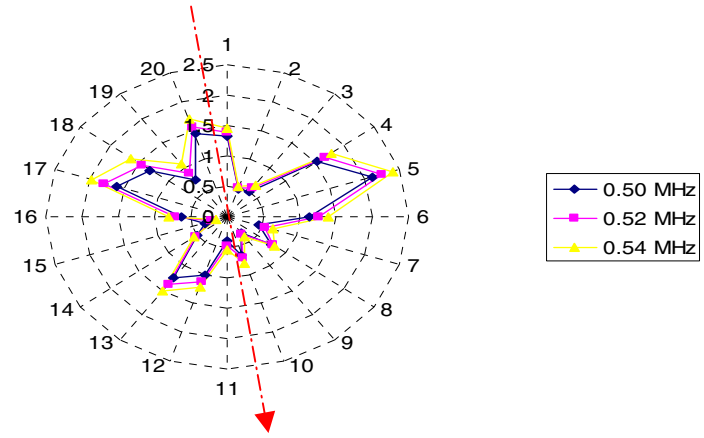

(a)

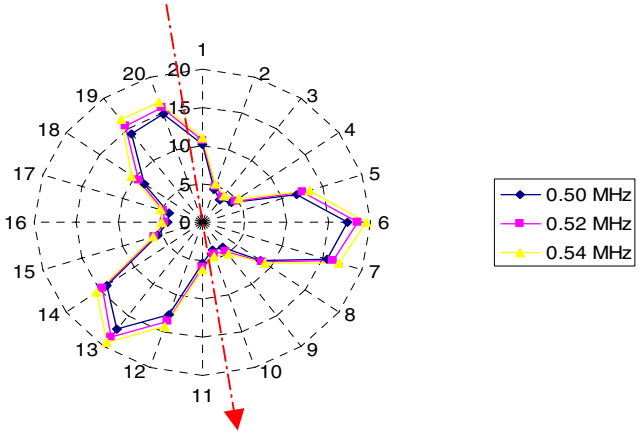

(b)

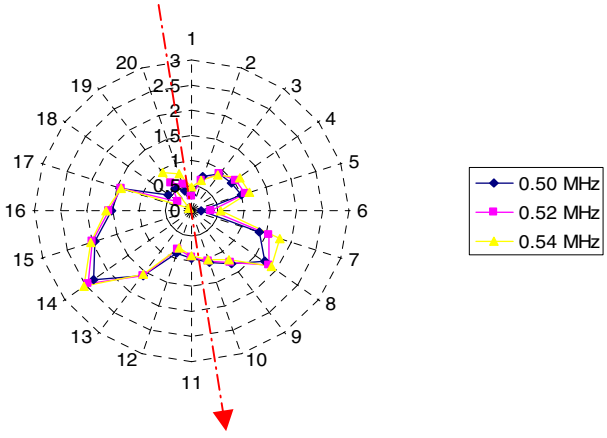

(c)

Fig. 4. (a) x component of the scattered wave particle displacement amplitude on the outer cylindrical surface. The red dot-dash line with an arrow shows x direction. (b) y component of the scattered wave particle displacement amplitude on the outer cylindrical surface. The red dot-dash line with an arrow shows x direction. (c) z component of the scattered wave particle displacement amplitude on the outer cylindrical surface. The red dot-dash line with an arrow shows x direction.

It is seen the displacement components are not strictly symmetric with respective to the x axis anymore. This might due to the asymmetric boundary conditions. Further studies will be conducted on this. The three curves of different but close frequency show similar scatter patterns, which may indicate good stability of the code developed. Further study will be carried out to decompose the scattered field into normal modes and to give the scattering or mode conversion coefficients.

EMAT EXPERIMENTAL SET-UP

EMAT sensors were designed for 10 in. and 12 in. pipe geometry with hardware fabricated for attaching them on to the inside walls of the pipe. The anchoring mechanism had provisions to vary the gap between the pipe wall and the EMAT. With wheels/ball rollers, the EMATS could be positioned anywhere inside the pipe. Figure 5 shows the circumferential and axial EMATS developed for pipeline inspection.

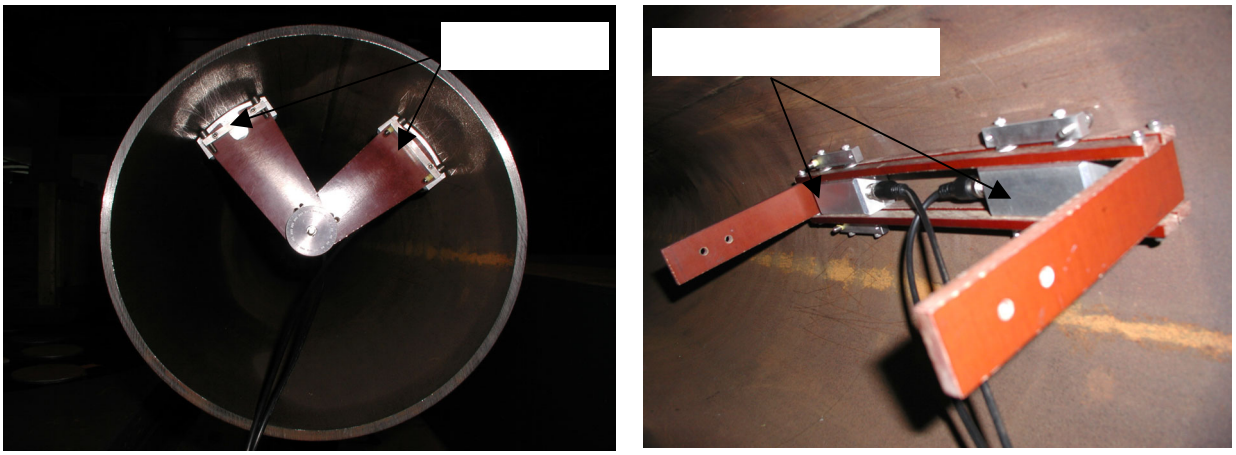

Fig. 5. Axial and Circumferential EMATs.

1/8 in., 1/4 in., and 0.006 in. wide cuts with varying depths were fabricated on the pipe walls to determine whether the EMATS are able to detect these flaws. Most tests were performed using horizontal n1 mode shear wave. By utilizing the through transmission mode whereby the distance between the EMATs is fixed, better correlation was obtained for the effect of flaws. A sample of the windowed receiver pulse signal for the case of no-flaw and flaws on the pipe walls is given in Fig. 7. As can be seen from the figure, the signal is strongest when there is no flaw and reduces in amplitude when it encounters a flaw. The multiple pulses in Stress Corrosion Cracks (SCC) flaw data is due to the smaller section of the pipe (18 in. instead of 6 ft) used for this case. These pulses correspond to the reflections from the pipe ends and are separated by larger time intervals when the pipe section used is long. Number of EMATs required to characterize the entire diameter of the pipe was determined by assessing the propagation angle

that does not affect the quality of the signal for preset EMAT separation. Fixture in Fig. 6 was used to perform these experiments.

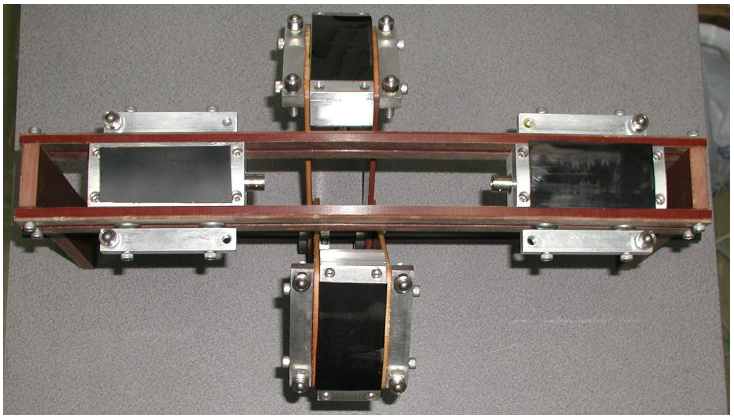

Fig. 6. Fixture for attaching both circumferential and Axial EMATs.

Attenuation or changes in amplitude in the time domain data (see Fig. 7) are not a useful feature for identifying flaws. Despite the fact that such changes are obvious in laboratory data collected under carefully controlled conditions, their reliability does not hold up for data collected in less controlled field conditions. Too many other mechanisms besides a flaw in the medium of propagation can lead to attenuation in field data. The only reliable features for flaw detection are those that depend on the change imposed by the flaw on the shape rather than the amplitude of the signature.

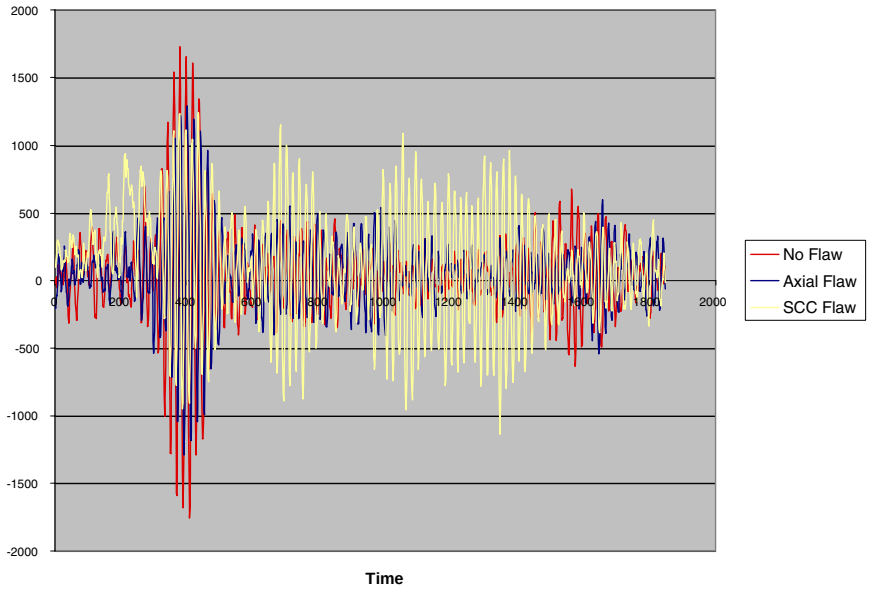

Fig. 7. Amplitude Versus Time for Flaw and No-flaw Receiver EMAT Signal.

SIGNAL ANALYSIS

To find features that distinguish the presence of a flaw, the signal must be analyzed, or literally broken apart. Since the EMAT-induced ultrasonic signature is an oscillating transient burst of energy, and the problem is to consider how a flaw in the propagation medium disrupts the pattern of the burst. A reasonable approach is to break up the signal into pieces that are themselves oscillating transient bursts. Discrete wavelet transform was used for this analysis.

The idea in pattern recognition is that the "no-flaw" signals will all be similar to each other. They will concentrate in a bounded region of feature space relatively close to a cluster center. In the case of an N-dimensional feature space, if the feature dimensions were on the same scale, the feature vectors for the "no-flaw" signals would form a cluster inside some N-dimensional hypersphere whose center is the "cluster center," and is located at the mean of the feature vector values of all the no-flaw samples. "Flaw" signals will have feature vectors that are scattered all over the feature space and at some distance from the "no-flaw" cluster center, outside the hyperspherical "decision surface."

The feature space can be transformed by rotating its coordinate axes to align with the eigenvectors of the covariance matrix of the "no-flaw" features and rescaling all axes to the same scale. As a result, the distance of any feature vector from the cluster center can then be represented as a single number, conventionally known as the Mahalanobis distance (Fig. 8).

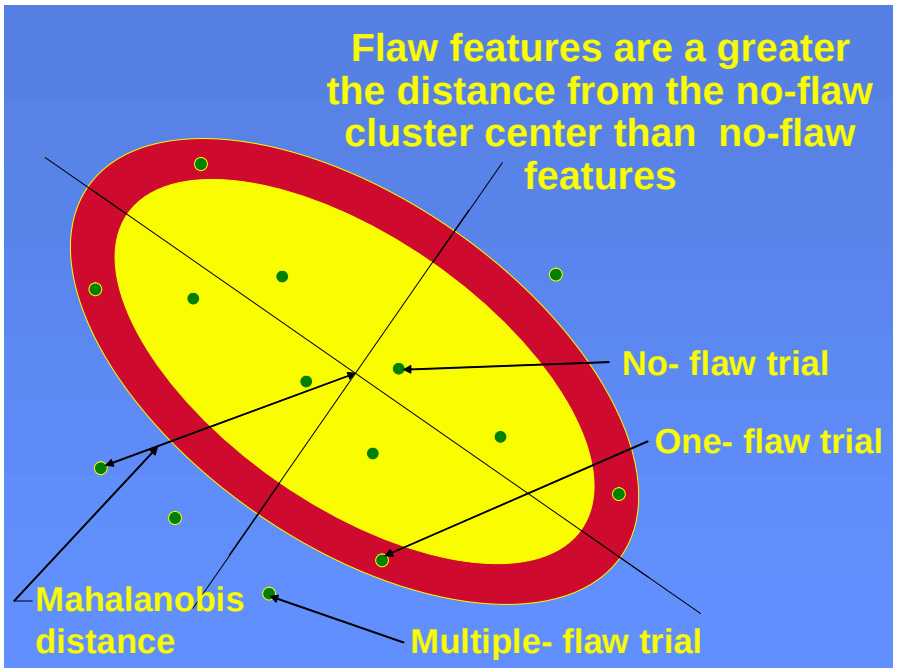

Fig. 8. Clustering of Features.

The above wavelet analysis was performed on the data obtained using shear EMATs on 10 in. and 12 in. diameter pipes with fabricated flaws. Figure 9 shows the classification SCC flaws. The horizontal axis is the fraction of signal energy retained in wavelet-packet space for the analysis. The vertical axis is the squared Mahalanobis distance of the feature vector from the cluster center of the "No Flaw" samples. There is one line on the graph for each trial. The line represents the Mahalanobis distance of the feature vector from the "no flaw" cluster center, as a function of retained energy.

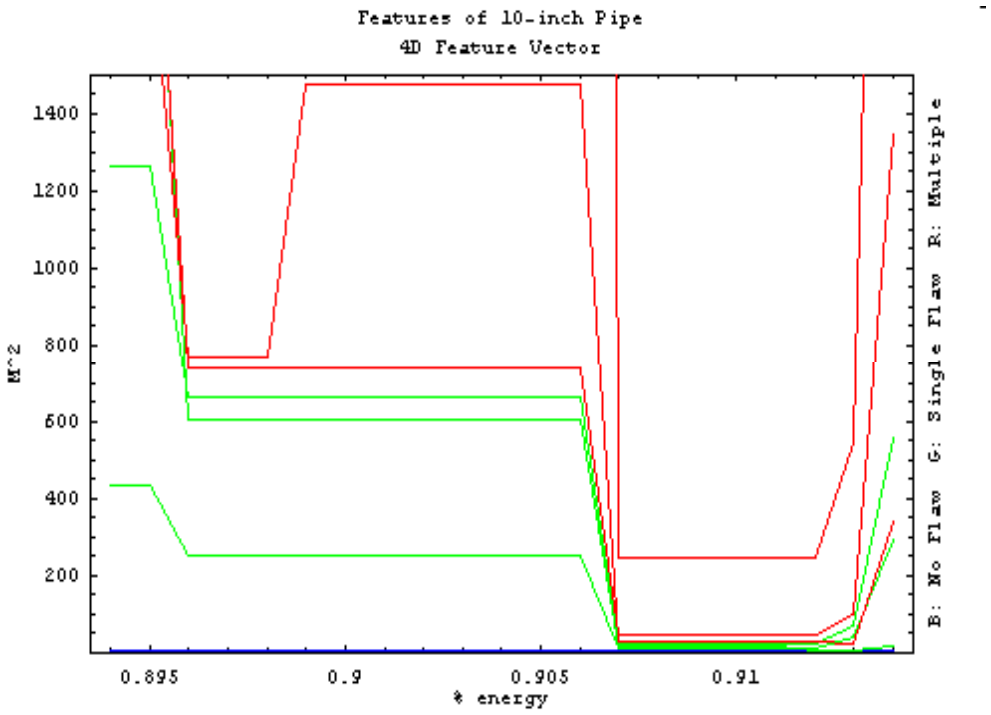

Fig. 9. Mahalanobis distance for SCC Flaws.

Signatures for the 10-in. pipe were fully distinguished into three classes (no flaw, single flaw, and multiple flaws) by an analysis similar to that described above. The wavelet filter used for processing is an 8-coefficient Least Asymmetric Wavelet.

MICROCANTILEVER LEAK DETECTION

A novel MEMS-based acoustic sensor that uses an array of high Q microcantilevers, such as those used in atomic force microscopy is being developed for internal and external acoustic detection of ultrasound emitted from defects (holes and cracks) in pressurized gas systems such as gas pipelines. It is essential to monitor the integrity of commercial pipelines for defects that can cause potential problems in the future, as well as to identify existing defects that are currently causing problems. It is conceivable that detecting and characterizing the flaws will help determine potential leakage in a pipe, but a sensor tuned

to the sound frequency generated by the gases escaping from the pipe gives a positive identification of the leak. Modern leak-detection systems for pipelines are usually bulky, expensive and rely upon often inaccurate or time consuming detection methods such as flow rate analysis, mass difference calculations or trace gases. In comparison, a system utilizing microcantilevers would occupy a smaller footprint either within the pipeline, or outside it and will enable the integrity of the pipe to be assessed without evacuation.

Acoustic detection using microcantilevers can be accomplished using a micromachined silicon cantilever with typical dimensions of 100 μm length, 20 μm width, 0.3–1 μm thickness, with a Q-factor of 100. The fundamental resonance frequency, **f**, of an oscillating cantilever can be easily shown to be expressed by $\omega = (k/m_e)^{1/2}$, where **k** is the equivalent spring constant and m_e is the effective mass of the cantilever beam. The spring constant is determined by the geometrical and material properties of the beam. For a rectangular cantilever, response to acoustic energy occurs primarily along the axis parallel to a normal to the cantilever. This translates into directionality capabilities as shown in the results presented below.

In order to determine the resonance frequency of the cantilever, we monitor the cantilever response, and the driving signal to the acoustic transducer simultaneously on a spectrum analyzer. By frequency sweeping the driving voltage (<1 volt peak-to-peak) of the transducer from the signal generator in the initial interval 15–100 kHz at a rate of 2 KHz per second, and an iterative reduction of this interval centered at the observed frequency response of the cantilever, the fundamental resonance frequency was determined at the maximum of the Q factor. With a bias voltage of V = 5 volts, a nominal cantilever resistance of R_c = 2.2 kΩ, and with the transducer plane parallel to the cantilever plane and positioned 20 cm away, the fundamental resonance frequency in air at room temperature was measured. This is summarized in Fig. 10. As the width of the sweeping in Fig. 10a is reduced, the resonance peak of the cantilever is measured from the sharp peak in Fig. 10b. As can be seen, for this cantilever, the peak is at f = 22.50 kHz, and therefore the quality factor $Q = f/(\Delta f)|_{FWHM}$ can be determined at FWHM of ≈128 Hz to be Q = 176. We note here that the FWHM of the driving voltage to the transducer was less than 40 Hz. The peaks for most examined cantilevers appear to be in the range 22 < f < 50 kHz, i.e., in the ultrasound region.

The maximum amplitude of each frequency peak of the cantilever in Fig. 10 is directly proportional to the amplitude of the effective driving force F exerted by the pressure fluctuations in the driving acoustic field.

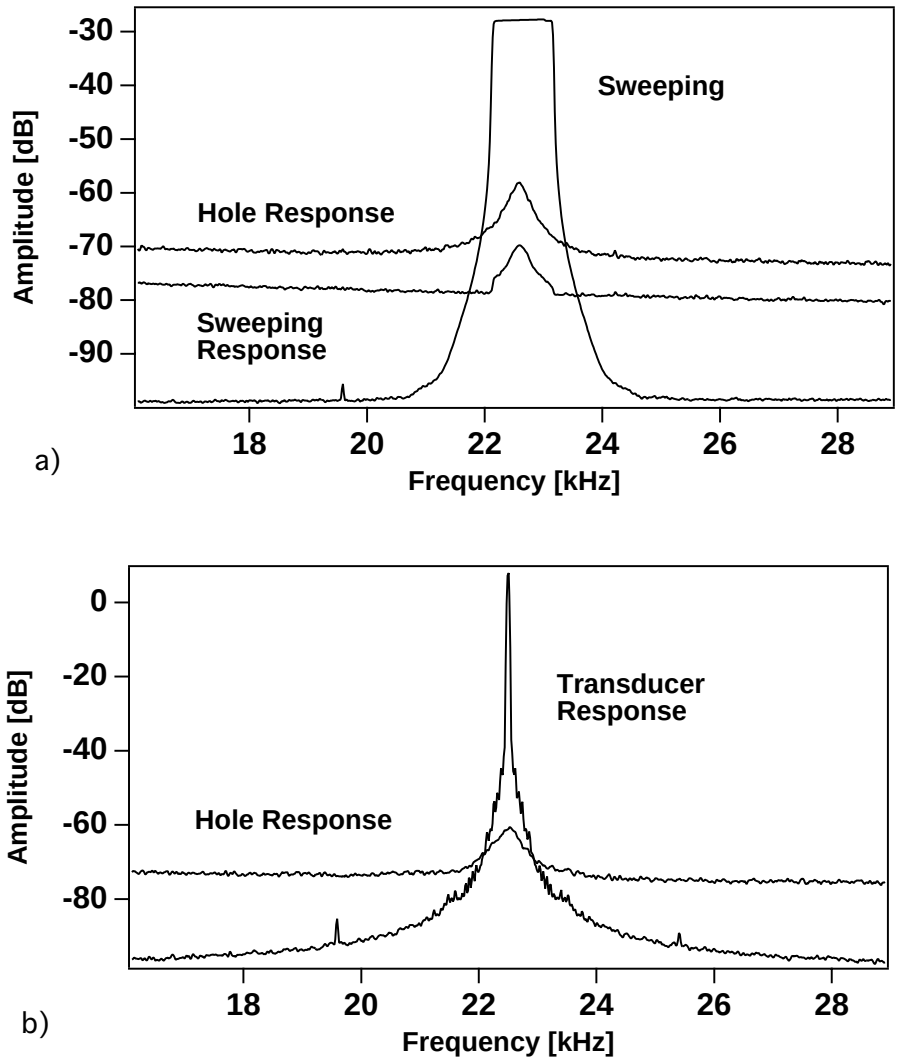

Fig. 10. Frequency response of the cantilever.

REFERENCES

Passian, A., Evans, P. G., Varma, V. K., Ferrell, T. L., and Thundat, T., "Piezoelectric detection of acoustic waves," Review of Scientific Instruments, Vol.74, No.2, February, 2003.

Tucker, R. W., Kercel, S. W., and Varma, V. K., "Characterization of gas pipeline flaws using wavelet analysis," QCAV (Quality Control Using Artificial Intelligence), Gatlinburg, TN, May 2003.

Kercel, S. W, Tucker, R. W., and Varma, V. K, "Pipeline flaw detection with wavelet packets and Gas," SPIE 2003.